Stability and optimal control of time-periodic flows - application to a pulsed jet

Léopold Shaabani-Ardali

To cite this version:

Léopold Shaabani-Ardali. Stability and optimal control of time-periodic flows - application to a pulsed jet. Fluids mechanics [physics.class-ph]. Université Paris Saclay, 2018. English. ⟨NNT : ⟩. ⟨tel-02192727⟩

HAL Id: tel-02192727
https://hal.science/tel-02192727v1
Submitted on 24 Jul 2019

université
PARIS-SACLAY

NNT : 20XXSACLXXXX

Thèse de doctorat

ÉCOLE POLYTECHNIQUE
UNIVERSITÉ PARIS-SACLAY

ONERA
THE FRENCH AEROSPACE LAB

Stability and optimal control of time-periodic flows — application to a pulsed jet

Stabilité et contrôle optimal des écoulements périodiques en temps — application au jet pulsé

Thèse de doctorat de l'Université Paris-Saclay
préparée à l'École polytechnique

Ecole doctorale n°579
Sciences mécaniques et énergétiques, matériaux et géosciences (SMEMaG)
Spécialité de doctorat : Mécanique des fluides

Thèse présentée et soutenue à Meudon, le 26 novembre 2018, par

LÉOPOLD SHAABANI ARDALI

Composition du Jury :

Ivan Delbende	
Maître de Conférences, LIMSI et Sorbonne Université	Rapporteur
David Fabre	
Maître de Conférences, IMFT–Université Paul Sabatier	Rapporteur
Aimee Morgans	
Professeur, Department of Mechanical Engineering, Imperial College	Examinatrice
Jean-Christophe Robinet	
Professeur, DynFluid, Arts et Métiers ParisTech	Examinateur
Nicolas Triantafyllidis	
Professeur, LMS, École polytechnique	Examinateur
Lutz Lesshafft	
Chargé de Recherche, LadHyX, École polytechnique–CNRS	Directeur de thèse
Denis Sipp	
Directeur de Recherche, ONERA	Directeur de thèse

STABILITY AND OPTIMAL CONTROL OF TIME-PERIODIC FLOWS — APPLICATION TO THE PULSED JET

LÉOPOLD SHAABANI ARDALI

Stabilité et contrôle optimal d’écoulements périodiques en temps — application au jet pulsé

Léopold Shaabani Ardali: *Stability and optimal control of time-periodic flows — application to the pulsed jet*, Stabilité et contrôle optimal d’écoulements périodiques en temps — application au jet pulsé.

CONTENTS

1

INTRODUCTION

In 1628, on her maiden voyage, the *Vasa* ship (figure 1.1) sank in the bay of Stockholm after less than one nautical mile of sailing. This happened because of a mistaken load balance between the top and lower decks. The upper decks were too high and too heavily built compared to the hull amount below the waterline. This placed the centre of gravity too high, providing very little righting moment to stabilise the ship. Hence, a wind gust was enough to provoke her sinking. This tragic event stemmed from the combination of pressure from King Gustav II Adolf, incompatible technical requirements and the premature death of the master shipwright, which led to the *Vasa* being conceived almost unstable.

An *unstable system* is a system in which initial perturbations are amplified as times advances. An example of such a system is the inverted vertical pendulum. Conversely, when a *stable system* is perturbed, disturbances eventually decay to zero. For instance, the regular pendulum is stable: a displacement from its vertical position leads to oscillations that are eventually damped because of air friction.

When studying the stability of the regular or inverted pendulum, one focuses on perturbations around a steady equilibrium state, the vertical position. However, other systems are characterised by a time-periodic motion: after a period $T > 0$, the

Figure 1.1: The *Vasa* ship, which sank in 1628. In the twentieth century, the ship was salvaged and restored, and today it is exposed in the *Vasa museum* in Stockholm. Taken from Wikipedia.

system returns to an identical state[1].

This thesis investigates the stability and the optimisation of time-periodic flows. In a similar way as steady flows (section 1.1), time-periodic flows can sustain instabilities (section 1.2). The mathematical framework to explore such instabilities is the Floquet theory (section 1.3). In particular, this thesis focuses on pulsed jets, detailed in section 1.4.

1.1 STABILITY OF STEADY FLOWS

Traditionally, flow stability describes the behaviour of perturbations around steady solutions of the Navier–Stokes equations. In the incompressible case, a steady solution $\mathbf{Q_0}(\mathbf{x}) = (\mathbf{U_0}(\mathbf{x}), P_0)$ verifies

$$\left(\mathbf{U_0} \cdot \nabla\right) \mathbf{U_0} = -\nabla P_0 + \frac{1}{Re}\Delta \mathbf{U_0}, \qquad \nabla \cdot \mathbf{U_0} = 0. \tag{1.1}$$

For simplicity, the general Navier-Stokes equations for a flow $\mathbf{q}$ are rewritten as

$$\frac{\partial \mathbf{q}}{\partial t} = F(\mathbf{q}), \tag{1.2}$$

with F a nonlinear function. The steady solution $\mathbf{Q_0}(\mathbf{x})$ verifies $F(\mathbf{Q_0}(\mathbf{x})) = 0$.

The stability analysis of steady flows can be divided into two categories, depending on the time-range that is considered: modal analysis (section 1.1.1) describes the long-term behaviour of perturbations, while non-modal analysis (section 1.1.2) focuses on transient effects or on continuous perturbations of the system.

1.1.1 *Modal analysis*

Let us consider a perturbation $\mathbf{q}'$ to the base solution $\mathbf{Q_0}$. The total flow $\mathbf{Q_0} + \mathbf{q}'$ verifies

$$\frac{\partial \left(\mathbf{Q_0} + \mathbf{q}'\right)}{\partial t} = \frac{\partial \mathbf{q}'}{\partial t} = F(\mathbf{Q_0} + \mathbf{q}') = F(\mathbf{Q_0}) + \left.\frac{\partial F}{\partial \mathbf{q}}\right|_{\mathbf{Q_0}} \mathbf{q}' + o(\|\mathbf{q}'\|) = \mathcal{L}\mathbf{q}' + o(\|\mathbf{q}'\|), \tag{1.3}$$

with the linearised flow operator

$$\mathcal{L} = \left.\frac{\partial F}{\partial \mathbf{q}}\right|_{\mathbf{Q_0}}. \tag{1.4}$$

As a consequence, the linearised perturbation equations can be written as

$$\frac{\partial \mathbf{q}'}{\partial t} = \mathcal{L}\mathbf{q}', \tag{1.5}$$

which has the solution

$$\mathbf{q}'(t) = e^{\mathcal{L}t}\mathbf{q}'(t=0). \tag{1.6}$$

---

[1] By convention, this period is always chosen as small as possible.

Therefore, the initial linear partial differential equations are recast into linear ordinary differential equations.

Modal analysis considers the long-term behaviour of $\mathbf{q}'$, when $t \to \infty$. This behaviour is controlled by the eigenvalue spectrum of $\mathcal{L}$.

On the one hand, if all its eigenvalues λ have a negative real part, the flow is stable; all perturbations eventually decay to zero, at a rate given (in the most general case) by the least stable eigenvalue $\max_\lambda \mathcal{R}(\lambda)$, with $\mathcal{R}(x)$ being the real part of x.

On the other hand, if there exists an eigenvalue λ with a positive real part, the flow is unstable; in the most general case, an arbitrarily small perturbation will grow in amplitude.

In early years, because of computational limitations, modal analysis focused on the stability of infinite parallel flows, enabling the decomposition of the perturbation into streamwise and spanwise Fourier components. This reduces the perturbation shape to a function of only one spatial coordinate. An introduction to this approach, called *local stability analysis*, can be found in Drazin and Reid (2004).

In the framework of local analysis, an important distinction has been made between absolute and convective instabilities. In a *convectively* unstable setting, a localised perturbation grows exponentially with time, but is at same time convected in such way that the perturbation at the initial disturbance location decays to zero in time. On the contrary, in an *absolutely* unstable setting, a localised initial perturbation gives rise to exponential temporal growth at the disturbance location.

Thanks to computational power advances, it has become possible to relax the parallel flow assumption and directly study the fully non-parallel $\mathcal{L}$ operator. For two-dimensional problems, modal stability analysis has been performed in numerous applications. This approach is now commonly called *global stability analysis* (Theofilis, 2011). In three dimensions, global stability analysis without decomposing the flow in spanwise Fourier modes is performed today (Loiseau et al., 2014; Marquet and Larsson, 2015), but still remains a very challenging task.

1.1.2 *Non-modal analysis*

As long as modal stability is concerned, the *Vasa* ship was stable, as any other ship sailing today. On paper, any small perturbation of its vertical position decays in the long run. However, we understand that this stability was weak for the *Vasa*. Is there a linear framework to characterise such a weakness?

In other words, this brings the question of transient dynamics: what happens between the initial time and the long run? *"In the long run we are all dead"*, said Keynes (1923). Can we characterise what happens before?

Non-modal analysis tackles such questions (Schmid, 2007). Mathematically, this concept is linked to the question of non-normality of operators. An operator $\mathcal{L}$ is defined as being *normal* if and only if it commutes with its hermitian transpose $\mathcal{L}^*$

$$\mathcal{L}\mathcal{L}^* = \mathcal{L}^*\mathcal{L}. \tag{1.7}$$

The importance of non-normality in fluid mechanics has been brought up in the early 1990s, when researchers tried to explain the discrepancies observed between the critical Reynolds number predicted in linear analysis and experimental observations. In most open flows, the experimental destabilisation occurs earlier than predicted by linear analysis. For instance, Couette flow is supposed to be stable at all Reynolds numbers, but undergoes transition to turbulence around Reynolds number 350 (Trefethen et al., 1993). A deeper mathematical discussion about non-modality can be found in Trefethen and Embree (2005).

1.1.2.1 *Transient growth*

A first method to characterise non-modal behaviour of $\mathcal{L}$ is to study its *transient growth*. We are no longer interested in the flow behaviour in the long term; instead, we calculate the maximal energy that a perturbation can reach over a given finite-time t

$$\max_{\|\mathbf{q}'\|=1} \left\| e^{\mathcal{L}t}\mathbf{q}' \right\|. \tag{1.8}$$

For a normal operator $\mathcal{L}$, this quantity is given at all times by the growth rate of the least stable eigenvalue. On the contrary, when $\mathcal{L}$ is non-normal, this transient growth is uncorrelated with the long-term behaviour of the flow. Certain perturbations in stable flows can achieve very large transient growth rates (Chomaz, 2005; Schmid, 2007).

The non-normality of the linearised Navier–Stokes operator arises from its convective term (Trefethen et al., 1993). Transient growth explains the discrepancies between the theoretical and experimental critical parameters for the onset of turbulence. If perturbations, even stable in the long run, can be amplified by a factor of a thousand or a million, then the small perturbation assumption used in the linearisation assumption is no longer valid and nonlinear dynamics takes over, which may trigger a transition to turbulence (Trefethen et al., 1993).

1.1.2.2 *Resolvent analysis*

In order to improve the characterisation of the *Vasa*'s weak stability, one could study its response to wind gust. More formally, by imposing upcoming wind gusts of different frequency and amplitude $\hat{\mathbf{f}}e^{i\omega t}$, its frequency response can be characterised. Building upon the formalism of section 1.1.1, one can force the linearised system (1.5):

$$\frac{\partial \mathbf{q}'}{\partial t} = \mathcal{L}\mathbf{q}' + \hat{\mathbf{f}}e^{i\omega t}. \tag{1.9}$$

In this case, the perturbation $\mathbf{q}'$ converges towards a periodic state $\hat{\mathbf{q}}'e^{i\omega t}$ that evolves at the same pace as the forcing. This state is computed as

$$\hat{\mathbf{q}}' = (i\omega - \mathcal{L})^{-1}\hat{\mathbf{f}}. \tag{1.10}$$

This defines the resolvent operator $(i\omega - \mathcal{L})^{-1}$ that characterises the linear frequential response of the system. One can then look for the forcing that induces the largest response in the systems:

$$\max_{\|\hat{\mathbf{f}}\|=1} \left\| (i\omega - \mathcal{L})^{-1}\hat{\mathbf{f}} \right\|. \tag{1.11}$$

Numerically, these optimal forcing distributions and their associated flow responses are computed by singular value decomposition of the resolvent operator. In the case of the *Vasa*, such an analysis would have displayed frequencies with large responses close to the natural rolling frequencies of the ship.

In fluid mechanics, such an analysis can be carried out to evaluate the most responsive frequencies of a stable system. The first resolvent analysis in a global framework, to my knowledge, was carried out for a laminar boundary layer flow (Alizard, Cherubini, and Robinet, 2009).

Moreover, in turbulent cases, the resolvent analysis is applied around mean flows to predict the dominant coherent structures of the flow. Indeed, by decomposing the flow as the sum of a mean flow $\overline{\mathbf{U_0}}$ and fluctuations $\mathbf{u}'$, the equations for fluctuations can be written as

$$\frac{\partial \mathbf{q}'}{\partial t} = \overline{\mathcal{L}}\mathbf{q}' + \mathcal{N}(\mathbf{q}', \overline{\mathbf{Q_0}}), \tag{1.12}$$

with $\overline{\mathcal{L}}$ the linearisation operator around the mean flow and $\mathcal{N}$ a nonlinear operator. In this equation, instead of modelling $\mathcal{N}(\mathbf{q}', \overline{\mathbf{Q_0}})$ to close the system, we can treat it as an external forcing term $\hat{\mathbf{f}}e^{i\omega t}$, leading to a resolvent analysis (1.11). This *mean-flow resolvent analysis* is now an important tool to characterise perturbations around an averaged flow (Beneddine et al., 2016; Garnaud et al., 2013; Semeraro et al., 2016; Sipp and Lebedev, 2007).

1.2 SOME EXAMPLES OF TIME-PERIODIC FLOWS AND THEIR INSTABILITIES

Steady flows are not the only ones that can sustain instabilities: this is also the case for time-periodic flows. We now review several examples of such flows, classified according to two criteria.

A first distinction can be made between flows that are strictly periodic, in the sense that the condition $\mathbf{u}(t+T) = \mathbf{u}(t)$ is enforced at every time step, and flows that are periodic in a phase-averaged sense, *i.e.* flows for which $\mathbf{u}(t) = \overline{\mathbf{u}}(t) + \mathbf{u}'(t)$, with $\overline{\mathbf{u}}(t)$ T-periodic and $\mathbf{u}'(t)$ random uncorrelated fluctuations. The former are generally laminar whereas the latter are mostly turbulent flows.

The second distinction is between flows in which time-periodicity results from an external forcing and flows in which this period arises naturally as an intrinsic phenomenon.

1.2.1 *Laminar or turbulent time-periodic flows*

1.2.1.1 *Laminar time-periodic flows*

In this section, we review two prominent examples of laminar time-periodic flows: the wake behind a cylinder and heart-pulsed blood flow.

CYLINDER FLOW One of the most-documented time-periodic flows is the von Kármán vortex street (see figure 1.2) behind a cylinder. At low Reynolds number, the flow around a cylinder is steady, before transitioning at Reynolds number 46.6 (Sipp and Lebedev, 2007) to a two-dimensional time-periodic vortex shedding wake.

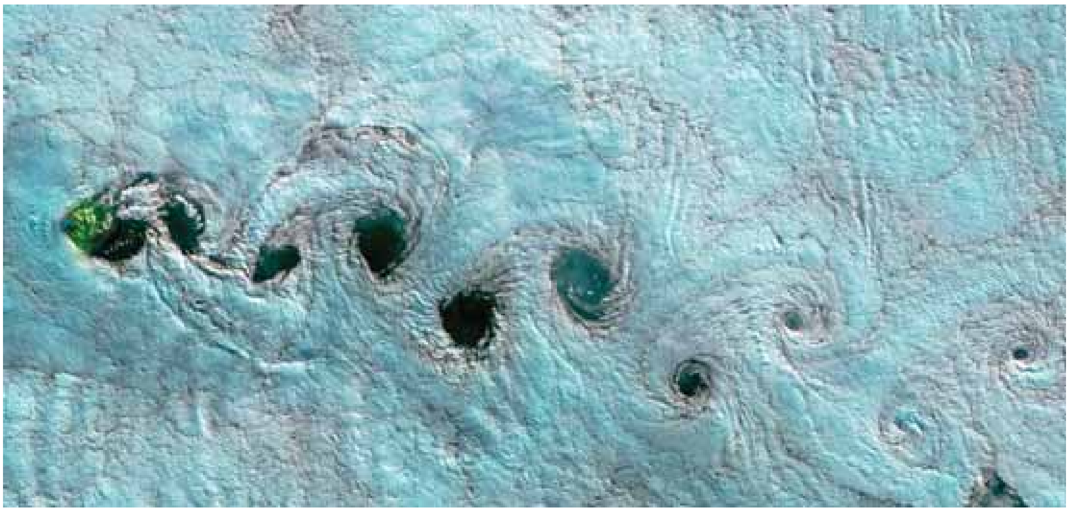

Figure 1.2: Von Kármán vortex street past the *Tristan da Cunha* island, in the South Atlantic Ocean. Taken from the NASA Earth Observatory website.

At larger Reynolds number, this time-periodic two-dimensional wake is itself unstable to three-dimensional perturbations of two kinds. Barkley and Henderson (1996), using Floquet theory (section 1.3), demonstrated that this wake is first unstable at Reynolds number $Re_2 = 188$ to large spanwise perturbations that scale with the vortex core. Then, at Reynolds numer $Re'_2 = 259$, smaller-scale pertubations of the order of the braid shear layer also become unstable, as summarised in the neutral stability curves displayed in figure 1.3. This was confirmed experimentally by Williamson (1996).

The instability of the two-dimensional vortex shedding in a cylinder wake with respect to spanwise disturbances has been one of the first fundamental time-periodic flows whose stability has been investigated.

More recently, this analysis has been extended to more complex behaviours involving cylinders, such as the oscillating cylinder (Gioria et al., 2009), or square cylinders tilted to break symmetries (Blackburn and Sheard, 2010).

BLOOD FLOW Blood is a non-Newtonian fluid that is pulsed regularly in arteries. In normal conditions, this flow is laminar. However, complex geometries, such as *stenosis* — the narrowing of arteries due to atherosclerosis — can trigger transition to turbulence (Ku, 1997).

In their papers, Sherwin and Blackburn (2005) and Blackburn, Sherwin, and Barkley (2008) model a stenotic flow as a Newtonian flow in a pipe with a constriction. They consider both the modal and non-modal stability of the axisymmetric base pulsating flow. They show the existence of a critical Reynolds number above which instabilities occur for different pulsating shapes. Their results also indicate that a large transient growth occurs in these configurations.

1.2.1.2 *Turbulent phase-averaged time-periodic flows*

Turbulent phase-averaged time-periodic flows, mostly encountered in industrial applications, are not periodic in a strict way but only in an phase-averaged manner:

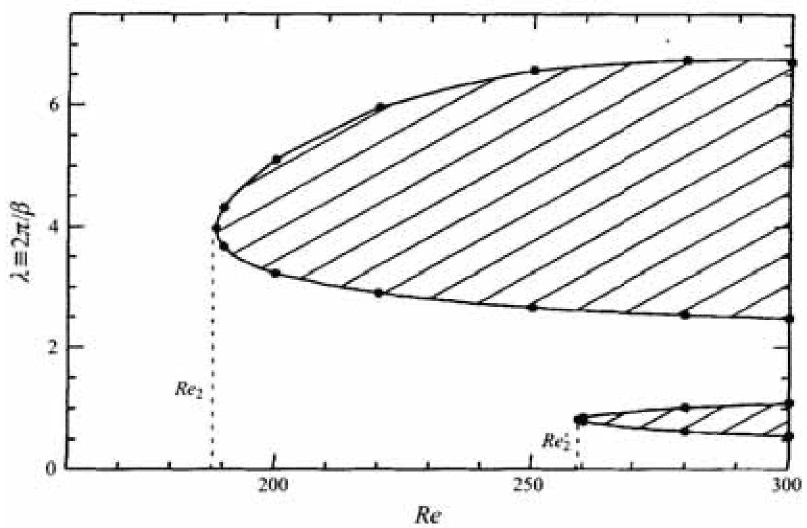

Figure 1.3: Neutral stability curves of the two-dimensional cylinder wake in the Reynolds–spanwise perturbation wavelength plane. The shaded regions represent unstable configurations. From Barkley and Henderson (1996).

the flow $\mathbf{u}(t)$ can be decomposed as the sum of a T-periodic phase-average $\overline{\mathbf{u}}(t)$ and random uncorrelated fluctuations $\mathbf{u}'(t)$. Time-periodicity generally arises from the angular frequency of boundary conditions. The system is then characterised by the phase-averaged periodic flow $\overline{\mathbf{u}}$.

NON-REACTING FLOWS The computation of a phase-averaged flow field $\overline{\mathbf{u}}$ is a challenge in itself (Sicot, 2009). Several numerical techniques have been developed to perform this calculation, such as the harmonic balance (Hall, Thomas, and Clark, 2002) or the time-spectral method (Sicot, Dufour, and Gourdain, 2012). On the one hand, the Harmonic Balance Method decomposes the periodic flow into Fourier components, and solves for these components in the frequency domain. On the other hand, the Time-Spectral Method perform similar computations in the time domain. These methods have been applied, for example, to study turbomachinery flows (Hall, Thomas, and Clark, 2002; Sicot, Dufour, and Gourdain, 2012; Van Der Weide, Gopinath, and Jameson, 2005), to characterise fluid-structure instabilities such as pitching airfoils and wings (Gopinath and Jameson, 2005), to optimise the shape of helicopter wings (Nadarajah and Jameson, 2007) or to design vertical axis wind turbine (Vassberg, Gopinath, and Jameson, 2005).

With these time-periodic base flows in hand, the next step would be to assess the stability of the computed periodic orbits. This is a difficult task that has never been carried out, to the best of our knownledge, for industrial applications. In the laminar case, concerning turbine blades, Abdessemed, Sherwin, and Theofilis (2009) analyse both the modal and non-modal stability of the periodic flow around such blades for moderate Reynolds numbers. Very quickly after a transition from a steady flow to a two-dimensional wake at a critical Reynolds number of 906, this wake becomes itself unstable (in a Floquet sense) to three-dimensional perturbations. However, Sharma et al. (2011) show that transient growth mechanisms totally dominate such transitions.

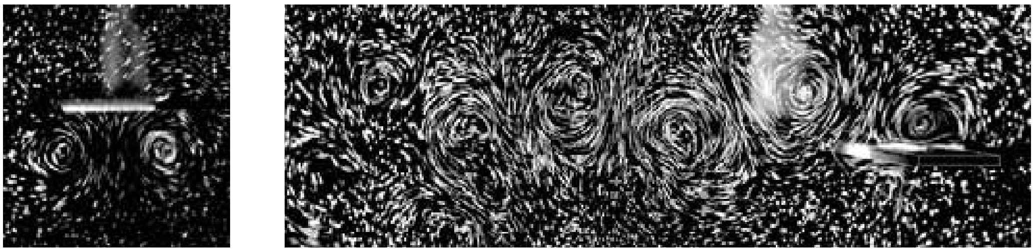

(a) Flapping airfoil before the critical Reynolds number. The flow is symmetric.

(b) Flapping airfoil above the critical Reynolds number. The symmetry is broken and a propulsive wake emerges.

Figure 1.4: Destabilisation of the symmetrical flow around a flapping airfoil. From Vandenberghe, Zhang, and Childress (2004).

COMBUSTION INSTABILITIES Open flames are generally stable. However, they are strong noise amplifiers (Juniper and Sujith, 2018). In most industrial applications, flames are confined inside a combustion chamber. This configuration is prone to the occurrence of an acoustic feedback loop: perturbations at the flame inlet are amplified, leading to the generation of acoustic waves; instead of being radiated into the free space, these waves are reflected at the flame enclosure, triggering the flame back again. This feedback may lead to resonance, that generally saturates into a limit-cycle. Predicting such limit-cycle oscillations is, as in the non-reactive case, of primary importance, but the presence of reaction makes this even more difficult. Han, Li, and Morgans (2015) developed a methodology to predict the characteristics of such limit-cycle oscillations, in a turbulent case.

When these finite-amplitude limit-cycles are determined, control strategies have been developed to damp them (Dowling and Morgans, 2005). These strategies can rely either on active control, stabilizing unstable modes (Morgans and Stow, 2007), or on passive control, for instance by introducing Helmholtz resonators in a Rijke tube (Zhao and Morgans, 2009).

1.2.2 *Forced or intrinsic time-periodicity*

1.2.2.1 *Periodicity fixed by an external forcing*

We now provide two examples of time-periodic flows induced by a forcing, flapping airfoils and pitching airfoils, which have respectively been studied physically and mathematically.

FLAPPING AIRFOILS Vandenberghe, Zhang, and Childress (2004) consider a symmetric wing with no pitch that undergoes an imposed up-and-down flapping motion. This wing is free to move in the horizontal direction. At low Reynolds number (based on the forcing frequency), the flow around the wing is symmetric and the wing remains at the same horizontal position, as shown in figure 1.4a. However, the authors experimentally demonstrate that above a critical Reynolds number, a symmetry-breaking bifurcation occurs, introducing a horizontal propulsive force that moves the wing, as shown in figure 1.4b. By varying the forcing frequency, the authors show that one can cross the critical Reynolds threshold and demonstrate the presence of a hysteresis phenomenon.

Alben and Shelley (2005) further analyse the physical mechanisms of the transition between these two states. Two stages are identified: the flow symmetry is first broken, which then leads to an asymmetric vortex array that propels the wing.

PITCHING AIRFOILS Jallas, Marquet, and Fabre (2017) consider a pitching airfoil with an imposed flapping motion. It is shown that, above a critical frequency, the airfoil wake becomes asymmetric, leading to a non-zero mean lift and thrust.

This transition is explained using a Floquet modal analysis (section 1.3), the unstable periodic base flow being stabilised by imposing spatio-temporal symmetries.

TURBINE WAKES Horizontal axis wind turbines, in a similar way as helicopter rotors, produce several helical vortices in their wake, this number depending on their number of blades (Vermeer, Sørensen, and Crespo, 2003). The time-periodicity of these vortices is fixed by the rotation speed of the wind turbine.

This helical wake, before being dissipated, can sustain several instabilities. Indeed, in a similar way as vortex rings in jets (section 1.4.1), these vortices can merge together (Delbende, Piton, and Rossi, 2015). Recently, Selçuk, Delbende, and Rossi (2017b) studied the linear and nonlinear dynamics of two and three helical vortices. Their approach combines a steady-flow formulation in a co-moving reference frame and the use of quasi-equilibrium states as base flows (Selçuk, Delbende, and Rossi, 2017a). They demonstrate events of vortex-leapfrogging and merging confirmed by linear analysis, as shown in figure 1.5.

1.2.2.2 *Intrinsic time-periodicity*

We now provide three examples of intrinsic time-periodic flows, which occur without any external forcing.

INTERNAL GRAVITY WAVES Internal gravity waves are encountered in density-stratified flows, such as oceans or atmosphere (Staquet and Sommeria, 2002). This stratification can result from gradients of temperature, salinity or pressure. In these media, internal waves typically arise from flow over a topography.

The linear stability of these waves has been first studied by Mied (1976) and this works have been generalised by Klostermeyer (1982).

VISCOUS FILM RUNNING DOWN FIBERS When a steady viscous film flows down a vertical fiber, as shown in figure 1.6a, absolute instabilities can be sustained if the flow rate is sufficiently low, as demonstrated by Duprat et al. (2007). In this case, primary instabilities saturate by forming equispaced drop-like structures. Close to the entrance valve, the configuration obtained is periodic in both space and time.

However, at some downstream position, this periodic state is destabilised through coalescence — drops merging two by two — and repulsion as shown in figure 1.6b.

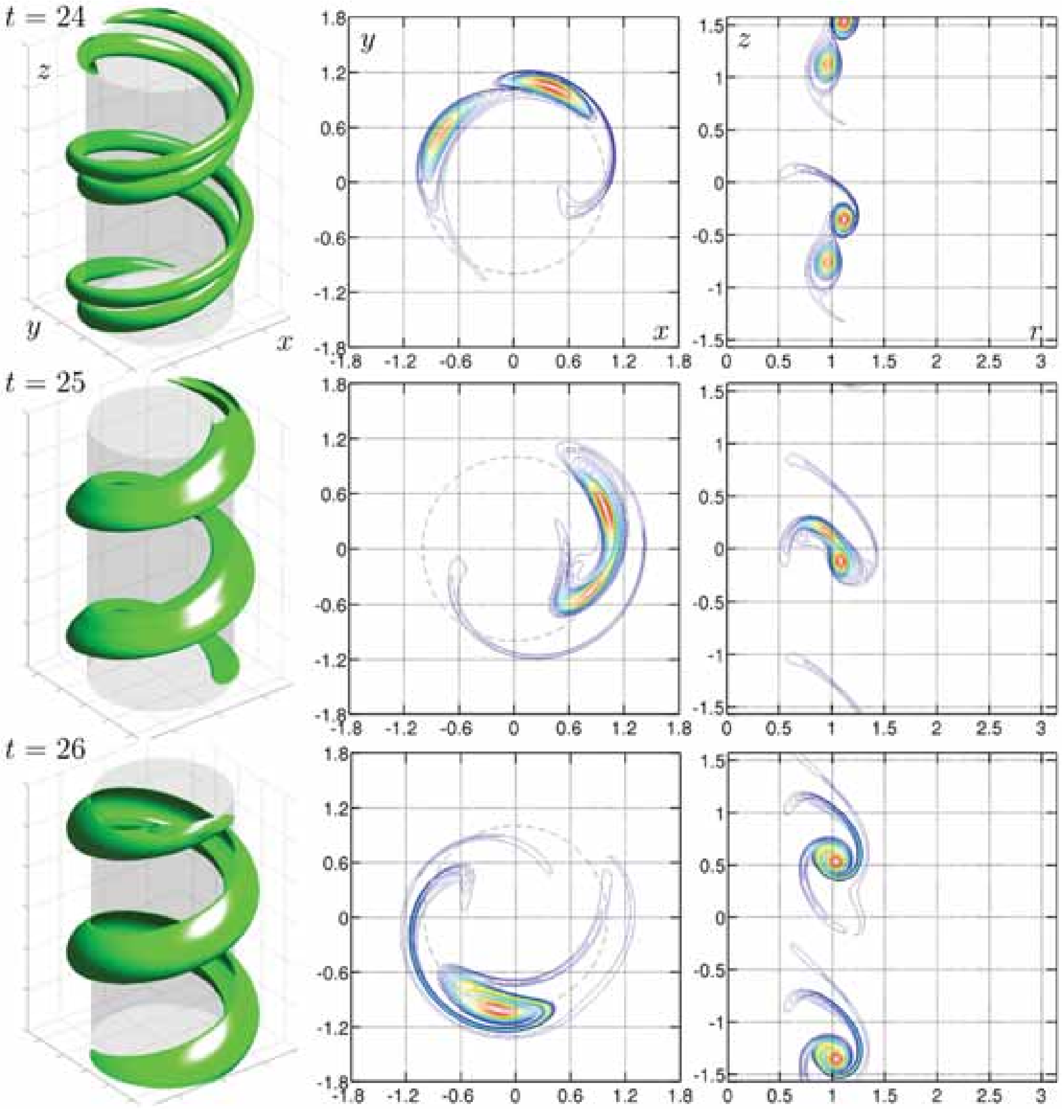

Figure 1.5: Vorticity isocontours (left) along with vorticity cut in a horizontal (middle) and a meridional (right) plane representing a merging sequence of two helical vortices perturbed with the most unstable mode. From Selçuk, Delbende, and Rossi (2017b).

A partial theoretical explanation for this instability is provided in Duprat et al. (2009).

THE CUBICAL LID-DRIVEN CAVITY The lid-driven cavity flow, in both two and three dimensions, is a canonical example of a confined flow. Concerning the cubic lid-driven cavity, it has been demonstrated that the steady flow becomes linearly unstable above a critical Reynolds number between 1914 (Feldman and Gelfgat, 2010; Loiseau, Robinet, and Leriche, 2016) and 1919.5 (Kuhlmann and Albensoeder, 2014). Above this critical Reynolds number, a time-periodic orbit emerges, displayed in figure 1.7. However, as demonstrated in (Kuhlmann and Albensoeder, 2014; Loiseau, Robinet, and Leriche, 2016; Lopez et al., 2017), in direct

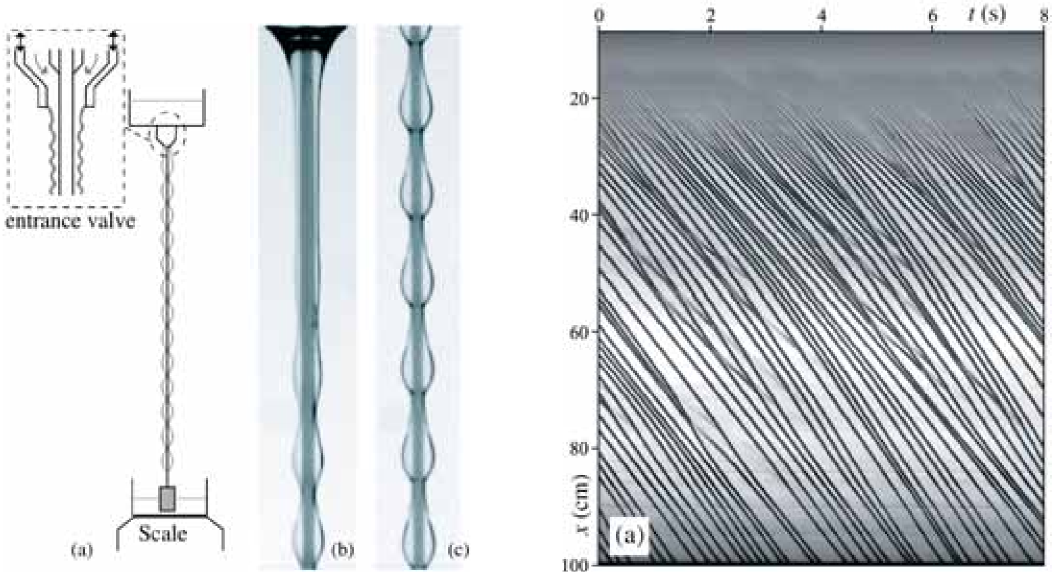

(a) From left to right, the experimental setup used in fiber experiments and two close-up pictures of running films, the first one after the entrance valve and the second one 10 centimeters below. From Duprat et al. (2007).

(b) Spatiotemporal diagram displaying the successive stages of droplet coalescence. From Duprat et al. (2009).

Figure 1.6: A time-periodic film running down a fiber (left) which undergoes instabilities (right).

numerical simulations, this periodic state can experience *intermittent chaos*, with sudden "bursts" in the cavity.

1.3 MATHEMATICAL FORMULATION OF THE MODAL STABILITY OF TIME-PERIODIC FLOWS

This section introduces Floquet theory (Floquet, 1883), which characterises the linear stability of periodic orbits.

1.3.1 *Problem formulation*

Let us consider a T-periodic solution $\mathbf{Q} = (\mathbf{U}, P)$ of the Navier–Stokes equations

$$\frac{\partial \mathbf{U}}{\partial t} + (\mathbf{U} \cdot \nabla)\,\mathbf{U} = -\nabla P + \frac{1}{Re}\Delta \mathbf{U}, \qquad \nabla \cdot \mathbf{U} = 0, \tag{1.13}$$

with appropriate boundary conditions. This solution is defined as a base flow solution. In this section, the mathematical Floquet theory (Floquet, 1883) to formalise the stability of such solution is summarised along with some computational considerations.

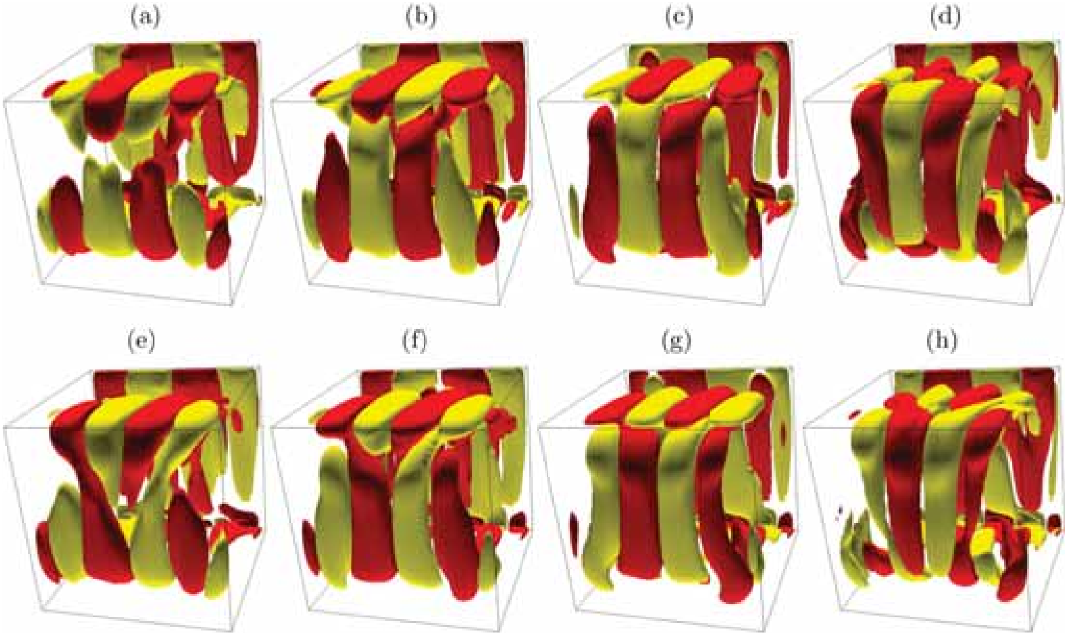

Figure 1.7: Successive helicity perturbation $\mathcal{H} - \overline{\mathcal{H}}$ snapshots in one period of the time-periodic orbit observed in the cubical lid-driven cavity at Reynolds number 1930. The helicity is defined as $\mathcal{H} = \mathbf{u} \cdot (\nabla \times \mathbf{u})$ and is averaged over one period as $\overline{\mathcal{H}}$. From Lopez et al. (2017).

To discuss the stability of the base flow, let us introduce a flow perturbation $\mathbf{q} = (\mathbf{u}, p)$; without any further assumption, the perturbation equation can be written as

$$\frac{\partial \mathbf{u}}{\partial t} + (\mathbf{u} \cdot \nabla)\,\mathbf{U} + (\mathbf{U} \cdot \nabla)\,\mathbf{u} + (\mathbf{u} \cdot \nabla)\,\mathbf{u} = -\nabla p + \frac{1}{Re}\Delta \mathbf{u}, \qquad \nabla \cdot \mathbf{u} = 0, \quad (1.14)$$

since the base flow equation is solution of (1.13). By further assuming that the perturbations are small compared to the base flow, the *linearised* equations for perturbations can be derived as

$$\frac{\partial \mathbf{u}}{\partial t} + (\mathbf{u} \cdot \nabla)\,\mathbf{U} + (\mathbf{U} \cdot \nabla)\,\mathbf{u} = -\nabla p + \frac{1}{Re}\Delta \mathbf{u}, \qquad \nabla \cdot \mathbf{u} = 0, \quad (1.15)$$

the $(\mathbf{u} \cdot \nabla)\,\mathbf{u}$ term being of second-order in $\mathbf{u}$.

In a more formal way, the equations can be cast as a linear problem

$$\frac{\partial \mathbf{q}}{\partial t} = \mathcal{L}(t)\mathbf{q}, \quad (1.16)$$

with $\mathcal{L}(t)$ a linear T-periodic operator that contains space-derivatives. An initial condition is also provided as

$$\mathbf{q}(t = 0) = \mathbf{q_0}. \quad (1.17)$$

1.3.2 *Floquet theory*

The linear stability theory used for periodic orbits is the Floquet theory (Floquet, 1883), which is reminded in this section. An English-written reference can be found in Arnold (1973).

According to the Cauchy-Lipschitz theorem (Arnold, 1973), there exists a unique solution $\mathbf{q}(t)$ of (1.16) verifying the initial condition (1.17). This solution is defined on $\mathbb{R}$, because the linear operator $\mathcal{L}(t)$ has a finite norm at every time t.

Now, it is possible to define the operator Ψ^t that maps an initial condition $\mathbf{q_0}$ to its solution of (1.16) at time t

$$\mathbf{q}(t) = \Psi^t(\mathbf{q_0}). \tag{1.18}$$

Note that because of the linearity of the original equation, this operator Ψ^t is linear in $\mathbf{q_0}$. Moreover, because of the T-periodicity of $\mathcal{L}$, one can easily demonstrate that

$$\Psi^{t+T} = \Psi^t \Psi^T. \tag{1.19}$$

Now, let us focus on the particular operator Ψ^T. This operator is invertible, since any perturbation field at time T can be traced back to an initial perturbation at time 0 (by considering the backward problem $\partial_t \mathbf{q} = -\mathcal{L}(t)\mathbf{q}$). Therefore, there exists a linear operator A such that

$$\Psi^T = e^{AT}. \tag{1.20}$$

We then define the linear operator $P(t)$ as $P(t) = \Psi^t e^{-At}$, which leads to

$$\Psi^t = P(t)e^{At}. \tag{1.21}$$

$P(0)$ is the identity operator and $P(t)$ is T-periodic, since, using (1.19)

$$P(t+T) = \Psi^{t+T}e^{-A(t+T)} = \Psi^t\Psi^T e^{-A(t+T)} = \Psi^t e^{AT} e^{-A(t+T)} = \Psi^t e^{-At} = P(t). \tag{1.22}$$

All these results now easily lead to a stability criterion. Indeed, for every time t,

$$\|\mathbf{q}(t)\| \leq \|P(t)\| \, \|e^{At}\| \, \|\mathbf{q_0}\|. \tag{1.23}$$

Since $P(t)$ is continuous and time-periodic, this operator $P(t)$ is bounded uniformly in time. Therefore, the flow perturbation is stable if and only if the operator e^{At} is stable, *i.e.* if and only if all the eigenvalues of e^{AT} have an absolute value lower than 1.

1.3.3 *Computing Floquet stability in practice*

For practical applications in large time-periodic systems, two methods exist to implement Floquet analysis.

The first one, in light of the harmonic balance and time-spectral methods, consists in simultaneously perturbing either the Fourier modes of the periodic base flow or the time steps computed in the time-spectral method. This leads to a very large eigenvalue problem, the solution of which imposes high memory requirements. Formally, this procedure is equivalent to adding another spatial dimension to the problem. This method is described in Lazarus and Thomas (2010).

The second one remains closer to the proof detailed in section 1.3.2. It relies on the successive time-stepping of flow perturbations over one period to approximate the e^{AT} operator. This method, despite consuming more CPU time, has much lower memory requirements. This method is described in more detail in Chapter 3.

Due to the limited memory on available local clusters, the stability techniques we will describe in this thesis rely on the second method.

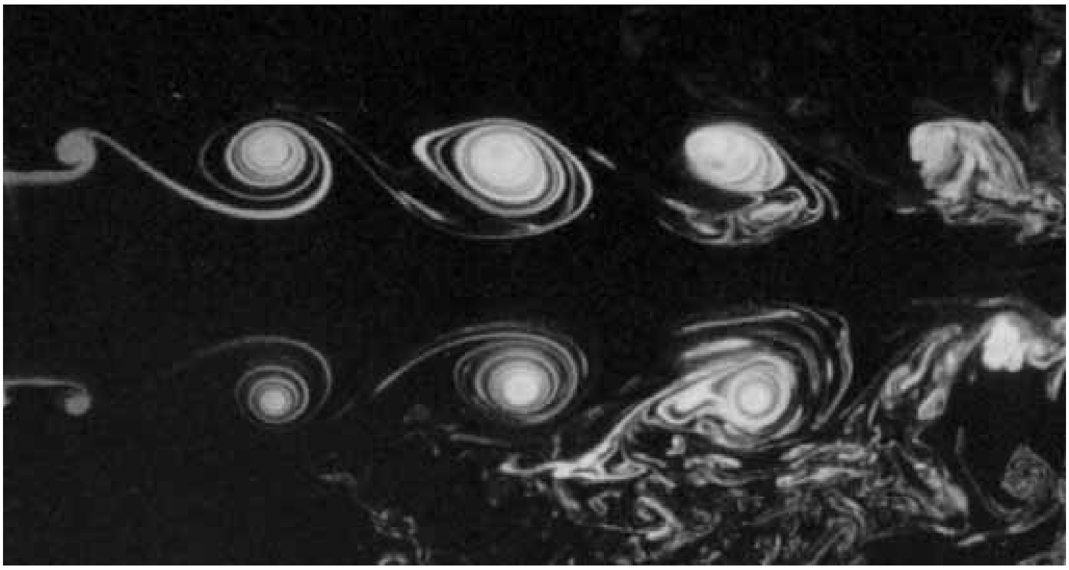

Figure 1.8: Experimental visualisation of a pulsed jet, with the formation of vortex rings. Taken from Parekh, Reynolds, and Mungal (1987).

1.4 DYNAMICS OF PULSED JETS

Jets are generally used in practice for two main reasons. First, for generating thrust, as at the rear of a combustion engines. Second, to mix inhomogeneous fluids; this inhomogeneity can arise from a composition difference, as in a combustion chamber, or from a temperature difference, like Kercher et al. (2003) use vortex rings to better cool electronic devices. In this thesis, our physical objective focuses on the improvement of the jet mixing properties. To do so, we consider using one of the strongest coherent features they exhibit: the vortex rings.

These vortex rings arise from a primary instability of jet shear layer. Indeed, jets are known to be large noise amplifiers (Jordan and Colonius, 2013): they display strong convective instabilities, meaning that smallest inlet disturbances are largely amplified while being convected downstream. A primary instability triggered by these perturbations is the vortex roll-up, in which the axisymmetric shear layer rolls up and detaches, forming vortex rings.

To better control the generation of these rings, regular pulsing is applied at the inflow. In this case, because of the time-periodic forcing, the jet shear layer rolls up regularly and vortex rings are generated in a periodic fashion, as in figure 1.8. In experiments, this pulsation can be acoustic (through loudspeakers) or hydrodynamic (through flow injection or wind tunnel fan).

Before being dissipated by the turbulence, these vortices can undergo two kinds of instabilities: *vortex pairing* or *jet bifurcation or blooming*.

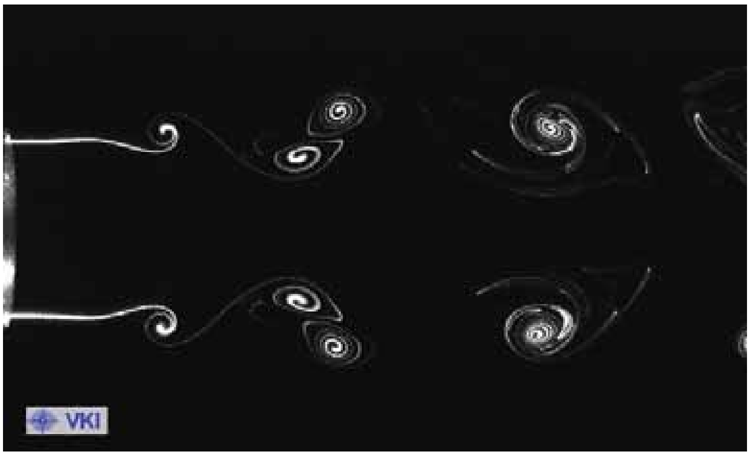

Figure 1.9: Experimental visualisation of pairing in a jet, snapshot of a movie by Schram (2003).

1.4.1 *Vortex pairing*

The first instability, *vortex pairing* is an *intrinsic* one. As documented by Hussain and Zaman (1980) and Zaman and Hussain (1980), for certain parameter conditions, generated ring vortices can merge two by two after being convected downstream. An example of such fusion is displayed in figure 1.9.

At first, this phenomenon seems counter-intuitive: in nonlinear dynamics, when a flow is forced at ω one is used to the onset of harmonic frequencies, such as 2ω or 3ω. However, in this case, merged vortices evolve at the frequency $\omega/2$, and can sometimes even merge again, evolving at $\omega/4$.

In other cases, pairing, despite forcing, does not occur, and, in the laminar case, the flow evolves at ω.

In the 1980s and 1990s, vortex pairing has been extensively studied (Broze and Hussain, 1994; Hussain and Zaman, 1980; Monkewitz, 1988; Zaman and Hussain, 1980) from both an experimental and a theoretical point of view. However, most of these studies explain pairing *from the paired state point of view*. Indeed, they explain the behaviour of the subharmonic Fourier component in the flow, *i.e.* the pairing component, focusing on predicting the pairing location or the growth rate of this mode. Conceptually, they rely on mode interaction and resonance theories, but they do not provide explanations on the very simple existence of this subharmonic mode. They might explain its growth, but not its presence in the first place.

In the classification developed in section 1.2, vortex pairing in jets is triggered by an external pulsation but occurs in both laminar and turbulent regime. In this thesis, one of our goals is to explain this pairing occurrence *from the unpaired state point of view*. In this view, we ask the following questions: why can we not observe unpaired vortex streets for all parameters? How does this subharmonic mode arise? How do the large noise amplification properties of the jet influence the flow?

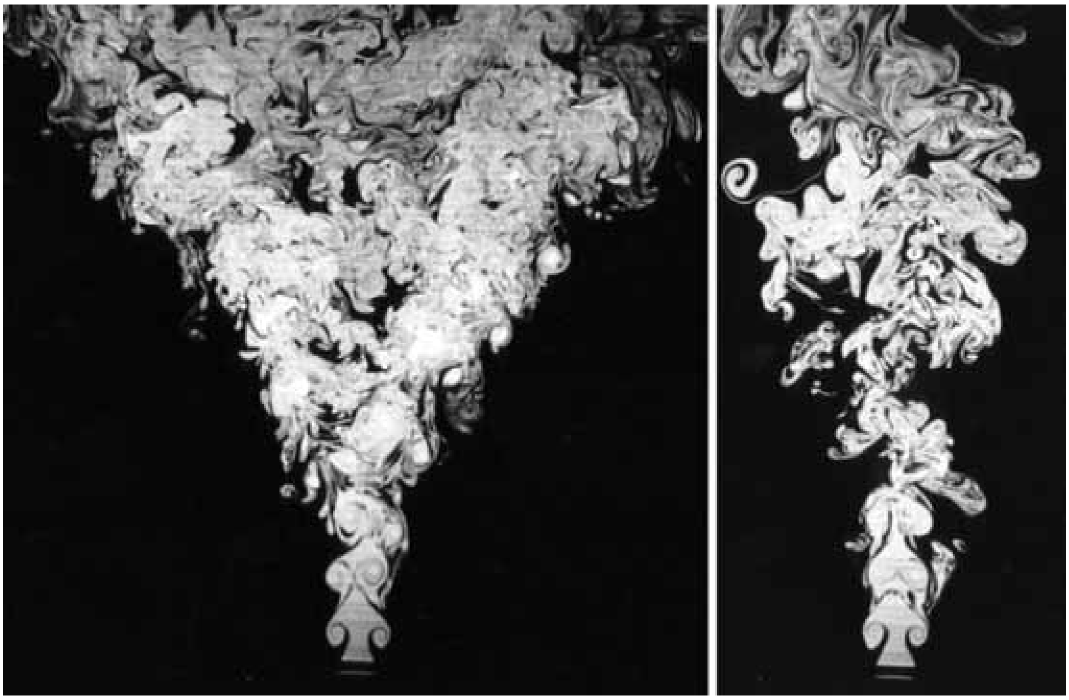

Figure 1.10: Bifurcating (left) and bisecting (right) plane views of a bifurcating jet at $Re = 4300$ with $R_f = 2$. From Lee and Reynolds (1985).

1.4.1.1 *Bifurcating and blooming jets*

The second instability we focus on is an *extrinsic* one, the bifurcating and blooming jet. When an additional helical perturbation is added to the axisymmetric inlet forcing, its effect on the flow depends on the ratio R_f between the axisymmtric and the helical forcings.

When this ratio is equal to 2, a *bifurcating* jet is obtained. As explained by Lee and Reynolds (1985) and Parekh, Leonard, and Reynolds (1988), because of the subharmonic helical forcing, the vortices are slightly shifted and tilted off-axis. Then, by mutual induction, they further depart from the jet axis. The resulting bifurcating jet displays spectacular spreading and increased mixing properties in a preferential plane, the *bifurcating plane*, as shown in figure 1.10. In the normal plane (the *bisecting plane*), no significant increase of the spreading can be observed.

When this ratio is equal to 3, a *trifurcating* jet is obtained, displaying three branches Gohil, Saha, and Muralidhar (2015). However, the achieved spreading is less pronounced than in the bifurcating case.

On the contrary, when these forcing frequencies are not in simple proportion, a *blooming jet* is obtained. There is no longer a preferred plane in which vortices are shifted and tilted, leading to a large flaring in all directions, the flow envelope displaying a conical shape, as shown in figure 1.11.

In the classification developed in section 1.2, bifurcating and blooming jets periodicity is triggered by an external forcing, but it occurs in both laminar and

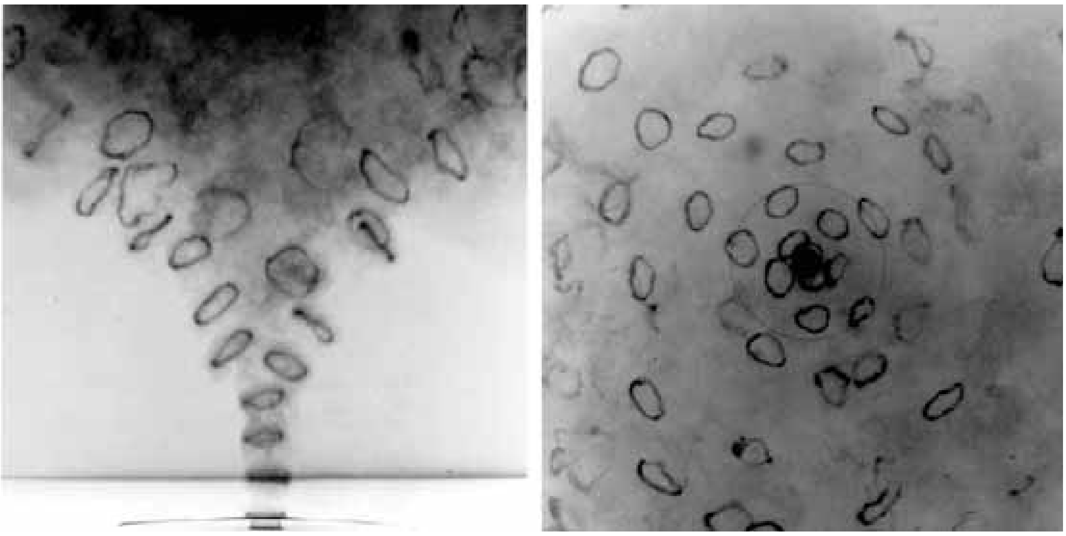

Figure 1.11: Side (left) and top (right) view of a blooming jet at $Re = 4300$ with $R_f = 2.4$. From Lee and Reynolds (1985).

turbulent regimes. In this thesis, we will restrict ourselves to laminar bifurcating jets. Our objective is to optimise the inlet helical forcing in order to maximise the spreading and mixing properties of bifurcating jets.

1.5 ORGANISATION OF THE THESIS

This thesis discusses the stability and optimisation of time-periodic flows, choosing the pulsed jet as an example. To do so, it is divided into three main parts.

Chapter 2 describes a time-delayed feedback technique to compute unstable periodic orbits. Compared to others, this method is very simple to implement. It has been applied to the axisymmetric forced jet in order to cancel pairing. Several improvements are proposed in order to reduce the memory burden of the technique and to deal with unstable orbits of unknown period, the latter being applied to the cubic lid-driven cavity exposed in section 1.2.2.2 to cancel bursting.

Chapter 3 studies the pairing phenomenon in axisymmetric jets as the result of a global Floquet instability. Following section 1.4.1, this analysis is carried out *from the unpaired state point of view*. To do so, the modal and non-modal stability of the periodic unpaired base flow computed in chapter 2 is calculated. After a parametric study exploring the role of the different flow parameters in this phenomenon, we demonstrate that the modal instability accurately predicts pairing occurrence. Transient growth analysis provides an intense bifurcation mechanism from the unpaired to the paired flow, with optimal growth rate of order 3 over one pulsing period, compared to 1 to 1.2 for modal growth.

The tools introduced in this chapter are generic and can be used to carry out the modal and transient growth analysis of any periodic base flow.

Chapter 4 focuses on the optimisation of the bifurcating jet. Following the physical scenario exposed in section 1.4.1.1, we look for the linear helical perturbation that maximally shifts the vortices off-axis. To do so, we introduce an optimisation norm based on vortex displacements. We then plug the resulting optimal forcing into three-dimensional direct numerical simulations and compare the results with those obtained from simpler *ad hoc* forcings. Our optimal forcing triggers a much stronger bifurcation across a larger Strouhal band.

The optimisation framework developed in this chapter can be adapted to other periodic flows.

Chapter 5 concludes and discusses open perspectives.

In Appendices A and B, the stability of vicinal surface growth in crystals is investigated. These results, from a collaboration with Laurent Guin, PhD candidate in the *Laboratoire de Mécanique des Solides* (École Polytechnique) and Prof. Michel Jabbour and Prof. Nicolas Triantafyllidis, from the same laboratory, are presented, about the stability of vicinal surfaces.

2

A TIME-DELAYED FEEDBACK TECHNIQUE FOR SUPPRESSING INSTABILITIES IN TIME-PERIODIC FLOW

CONTEXT

As explained in the previous chapter, in this thesis, our main physical objective consists in finding ways of improving the jet mixing properties, relying on vortex rings through two mechanisms: vortex pairing as well as jet bifurcation or blooming. We begin our study with the pairing phenomenon. Indeed, this current chapter provides us with an axisymmetric base flow that will be useful both for the stability analysis of chapter 3 and to optimise the more promising blooming phenomenon in chapter 4.

Vortex pairing in a pulsed jet only occurs in a limited parameter range, as discussed in chapter 3. Outside of this range, the resulting flow is a simple array of vortices, without pairing. However, the existence of a *paired state* seems confusing at first. Indeed, pairing means that, when the flow is forced at a fundamental frequency ω, it responds at the subharmonic frequency $\omega/2$. However, nonlinear phenomena have got us used to the emergence of *harmonic* responses such as 2ω or 3ω, not to *subharmonic* ones. Therefore, as the *unpaired state* seems more "natural", at least from a dynamical system point of view, than the paired one, we can postulate that such an unpaired state exists for all parameter values. In order to understand pairing, chapter 3 will therefore investigate the links between paired and unpaired states.

Yet, such an unpaired flow cannot be easily observed by simple direct numerical simulation. Among several possibilities to circumvent this problem, including Newton-like solvers, harmonic balance, linear filters, we decided to develop a stabilisation method based on a time-delayed feedback because of its simplicity as well as lower memory and computational footprints. Therefore, similarly to what the *selective frequency damping* method did for stabilising steady flows (Åkervik et al., 2006), this chapter presents an easy way of stabilising unstable time-periodic orbits. This setting has been optimised to damp $\omega/2$ frequencies, but it can be easily tuned to damp other frequencies.

The work in this chapter has been published in *Physical Review Fluids* (Shaabani-Ardali, Sipp, and Lesshafft, 2017).

ABSTRACT

A numerical method is presented that allows to compute time-periodic flow states, even in the presence of hydrodynamic instabilities. The method is based on filtering non-harmonic components by way of delayed feedback control, as introduced by Pyragas (1992). Its use in flow problems is demonstrated here for the case of a

periodically forced laminar jet, subject to a subharmonic instability that gives rise to vortex pairing. The optimal choice of the filter gain, which is a free parameter in the stabilisation procedure, is investigated in the context of a low-dimensional model problem, and it is shown that this model predicts well the filter performance in the high-dimensional flow system. Vortex pairing in the jet is efficiently suppressed, so that the unstable periodic flow state in response to harmonic forcing is accurately retrieved. The procedure is straightforward to implement inside any standard flow solver. Memory requirements for the delayed feedback control can be significantly reduced by means of time interpolation between checkpoints. Finally, the method is extended for the treatment of periodic problems where the frequency is not known *a priori*. This procedure is demonstrated for a three-dimensional cubic lid-driven cavity in supercritical conditions.

2.1 INTRODUCTION

Any analysis of linear flow instability first requires the definition of an unperturbed basic flow state. An obvious problem is that such flow states, if indeed they are unstable, cannot be recovered as asymptotic solutions by simple time-stepping. In the context of *steady* flow, several methods exist that allow the computation of unstable steady states. Newton–Raphson iteration (Sipp and Lebedev, 2007) or recursive projection (Campobasso and Giles, 2004; Shroff and Keller, 1993) are efficient in many such configurations, although they may require deep modifications of numerical flow solvers, and their convergence is often problematic. A robust alternative, which furthermore is convenient to integrate into an existing time-stepping simulation code, has been proposed by Åkervik et al. (2006) under the name of “selective frequency damping” (SFD). This technique has since been used for a wide variety of steady flow configurations.

Time-periodic flows constitute a distinct class of instability problems, and interest in the computation of periodic states is furthermore not limited to the purpose of instability analysis. Examples include vortex shedding in shear flows (Henderson and Barkley, 1996), pulsating flow in blood vessels (Sherwin and Blackburn, 2005), and complex flow in turbomachines (Sicot, Dufour, and Gourdain, 2012).

Even when a flow settles into an asymptotically stable time-periodic state in the long-time limit, its computation by time-stepping may be costly if long transient dynamics prevail. This difficulty can be overcome by use of the “harmonic balance” technique (Hall, Thomas, and Clark, 2002; Thomas, Dowell, and Hall, 2002), which consists in the simultaneous computation of all or many temporal Fourier components of a given periodicity. A pseudo-time is typically employed in order to make all Fourier components converge. This approach is widely used today both in fundamental and in applied contexts. Several improvements of the method address specific issues: if the fundamental period is not known a priori, a “gradient-based variable time period” algorithm (Gopinath and Jameson, 2006; McMullen, Jameson, and Alonso, 2006; McMullen, Jameson, and Alonso, 2002; Spiker et al., 2006) allows to identify it as an additional unknown of the problem; if the flow is simultaneously forced at several frequencies, the method can be generalised (Ekici and Hall, 2008).

Some strategies for control and shape optimisation have also been devised on this basis (Nadarajah, McMullen, and Jameson, 2003; Nadarajah and Jameson, 2007).

Yet time-periodic flows may sustain hydrodynamic instabilities. In particular, the growth of *subharmonic* perturbations is observed in many such cases. Prominent examples are the pairing of vortices in shear flows (Zaman and Hussain, 1980) and the parametric subharmonic instability (PSI) of internal waves in stratified media (Bourget et al., 2013). Such instabilities may arise from linear dynamics, tractable in the framework of Floquet theory, or from nonlinear effects, as in the case of PSI. It may be possible to retrieve unstable periodic states through harmonic balance, as long as no harmonics of the fundamental flow frequency are involved in the instability, but to the best of our knowledge, this has never been attempted. Shooting methods have been designed to this effect (Lust and Roose, 1998; Roose et al., 1995), and these have been used successfully in the context of some flow problems (Sánchez and Net, 2010; Sánchez et al., 2004). However, their implementation requires a considerable overhead around a given flow solver.

The objective of this study is to present an easy-to-implement filtering technique, similar in spirit to the SFD method (Åkervik et al., 2006) used for steady flow, that allows the exact computation of time-periodic orbits in stable as well as unstable situations. To this end, an artificial forcing is added to the Navier–Stokes equations, which is required to leave the dynamics of the fundamental flow frequency and of all its higher harmonics unaffected, such that the simulation converges in time towards a periodic solution of the unforced equations. A *delayed feedback control* (Pyragas, 1992) achieves this objective. Such time-delay filters have been extensively used in the context of controlling chaotic dynamics in systems with a low number of degrees of freedom. In a recent study (Jallas, Marquet, and Fabre, 2017), a similar technique is applied in a high-dimensional flow problem, in order to suppress spatio-temporal asymmetries in wakes. In the present chapter, the use of time-delayed feedback for flow stabilisation is explored.

The phenomenon of vortex pairing in an axisymmetrically forced jet is chosen to illustrate the procedure. It is demonstrated how the artificial damping efficiently suppresses the growth of subharmonic perturbations, and thereby the onset of vortex pairing, so that unstable periodic solutions of the Navier–Stokes equations can be obtained. The feedback optimally eliminates subharmonic components, letting the fundamental and its harmonic components unaffected, while all non-harmonic frequencies experience damping. We will show that in weakly stable settings, the feedback can be used to accelerate the convergence towards the asymptotic state. However, this method, due to the full period storage, can be memory-consuming; to severely reduce the memory requirements, we will show how spline interpolation between checkpoints in time can be used, without affecting much the convergence properties of the algorithm.

When flow periodicity arises from intrinsic dynamics, as opposed to external forcing, the period length of the asymptotic state is not known *a priori*. We will show that the stabilisation method for such cases can be extended to identify the period length through iterative adjustment, as will be demonstrated for a cubic lid-driven cavity. Due to their broad range of application, cavities are well-studied flow systems, which can sustain several types of instabilities (Shankar and Deshpande, 2000). A configuration is chosen that is known to give rise to co-existing limit-cycles and intermittently chaotic dynamics (Feldman and Gelfgat, 2010; Kuhlmann and Albensoeder, 2014; Loiseau, Robinet, and Leriche, 2016).

This chapter is organised as follows. The jet flow example is introduced in section 2.2, and the occurrence of vortex pairing in the absence of artificial damping is discussed. The stabilisation method is presented in section 2.3. A single free parameter needs to be chosen; its optimal value is found in the context of a simple model problem. Section 2.4 documents the performance of the technique for an unstable vortex street, with a discussion of the optimal parameter choice. It is further shown how the same technique accelerates the convergence in stable situations, and how the memory requirements may be reduced through check-pointing and interpolation. Details on the simulation technique are provided here. Section 2.5 extends the stabilisation procedure to periodic flows with an unknown period.

2.2 AN EXAMPLE OF SUBHARMONIC INSTABILITY: VORTEX PAIRING IN JETS

Axisymmetric harmonic forcing at the nozzle of a laminar round jet excites, over a wide range of frequencies, a shear instability of the steady flow state, leading to exponential growth of the perturbation amplitude along the axial direction. As the amplitude reaches nonlinear levels, the shear layer rolls up into a regular street of vortex rings, which form and convect at the frequency of the applied forcing. Depending on flow parameters and forcing frequency (more details given in section 2.4.1), these vortices may undergo subsequent pairing (Ho and Huerre, 1984), and if the ambient flow is sufficiently quiet and the harmonic forcing is well-controlled, this pairing takes place in a perfectly regular fashion. The numerical method is detailed in section 2.4.1.

In cases where pairing occurs, two neighboring vortices merge into one, such that the passage frequency of vortices downstream of the pairing location is exactly half that of the imposed forcing. If the forcing is characterised by the time period T, such that $\omega_f = 2\pi/T$, the "paired state" is globally 2T-periodic (T-periodic upstream of the pairing and $2T$-periodic downstream). The velocity field of a paired state will be denoted $\mathbf{u}^p$. An example, obtained by direct numerical simulation, is shown in figure 2.1a.

Another case at different parameter settings, where no pairing is found to occur, is shown in figure 2.1b. Vortices roll up close to the nozzle and advect downstream, until they are dissipated by viscosity. Such a flow state is (globally) T-periodic and will be called hereafter an "unpaired state". Its velocity field will be denoted $\mathbf{u}^u$.

The purpose of this study is to show how, for each paired state, a corresponding unpaired state can be recovered, defining two valid periodic solutions of the Navier–Stokes equations at the same parameter setting.

2.3 SUBHARMONIC STABILISATION

In this section, after a brief presentation of filtering techniques (section 2.3.1), a simple model problem is introduced in order to determine the coefficients of a

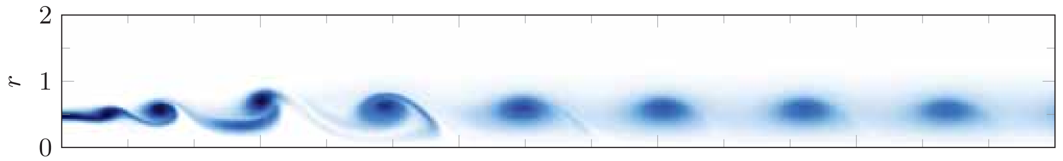

(a) Paired state at $St = 0.6$ and $Re = 2000$.

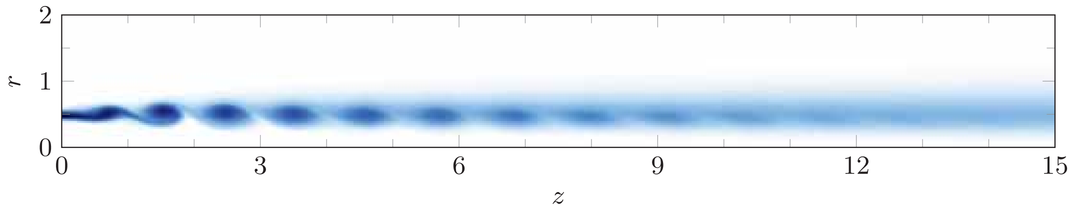

(b) Unpaired state at $St = 0.6$ and $Re = 1300$.

Figure 2.1: Vorticity snapshots of paired and unpaired states, obtained without stabilisation for two different parameter settings. Reynolds and Strouhal numbers are defined in section 2.4.1.

time-delayed feedback — here an additional term added to the momentum equation — so that the forced Navier–Stokes simulation converges towards a T-periodic state.

2.3.1 *Time-delayed feedback*

A fully synchronised paired state can be decomposed into components that are T-periodic and those that are only $2T$-periodic,

$$\mathbf{u}^p(\mathbf{x}, t) = \sum_n \mathbf{u}_n^T(\mathbf{x}) \exp\left(\mathrm{i} n \omega_f t\right) + \sum_n \mathbf{u}_n^{2T}(\mathbf{x}) \exp\left(\mathrm{i}\frac{2n+1}{2}\omega_f t\right), \tag{2.1a}$$
$$\text{with} \quad n = 0, \pm 1, \pm 2, \dots, \pm N.$$

An unpaired state, in contrast, is purely T-periodic,

$$\mathbf{u}^u(\mathbf{x}, t) = \sum_n \mathbf{u}_n^T(\mathbf{x}) \exp\left(\mathrm{i} n \omega_f t\right). \tag{2.1b}$$

The objective is to design a filter that will damp all $2T$-periodic components under the second sum in (2.1a), while leaving any T-periodic flow state unaffected. Of course, this filter should also lead to a stable global system.

A first approach might be to consider a standard linear band-stop filter H that cuts around the subharmonic frequency $\omega_f/2$ (*i.e.* gain $|H(\omega_f/2)| \ll 1$), while preserving the steady component and the fundamental frequency ($H(0) = H(\omega_f) = 1$). However, in order to achieve such characteristics, a very high-order filter is needed: in logarithmic scale, $\omega_f/2$ and ω_f are apart by only $\log(2) = 0.69$, whereas the gains are separated by $-\log(|H(\omega_f/2)|) \gg 1$. This filter would be cumbersome to implement, and it would require a careful stability and pole placement analysis, as described for example by Åström and Murray (2008), or by Doyle, Francis, and Tannenbaum (1992). Furthermore, such a filter could not satisfy all requirements:

the gain at $\omega_f/2$ cannot be strictly zero, and no constraint can be imposed on the higher $2T$-periodic harmonics ($\pm\frac{3}{2}\omega_f, \pm\frac{5}{2}\omega_f, \ldots$).

A better approach, that will be adopted here, is to use time-delayed feedback (TDF), as described by Pyragas (1992). When the flow at time t is compared with the flow at time $t-T$, components of period T and of period $2T$ are clearly distinguished.

The $2T$-periodic components in a paired state (2.1a), which are the target of artificial damping, are thus isolated as

$$\mathbf{u}^p(\mathbf{x},t) - \mathbf{u}^p(\mathbf{x},t-T) = 2\sum_n \mathbf{u}_n^{2T}(\mathbf{x}) \exp\left(\mathrm{i}\frac{2n+1}{2}\omega_f t\right), \tag{2.2}$$

whereas a T-periodic unpaired state satisfies

$$\mathbf{u}^u(\mathbf{x},t) - \mathbf{u}^u(\mathbf{x},t-T) = 0. \tag{2.3}$$

Then, adding a forcing term of the form

$$\mathbf{f} = -\lambda(\mathbf{u}(t) - \mathbf{u}(t-T)) \tag{2.4}$$

to the right-hand side of (2.12) allows to control $2T$-periodic fluctuations without any forcing on T-periodic dynamics. In this framework, λ is a forcing parameter that needs to be prescribed (see section 2.3.2).

The Laplace transform of this forcing term is

$$\mathcal{L}\{f\} = -\lambda\left(1 - e^{-\omega T}\right)\mathcal{L}\{u\}, \tag{2.5}$$

so that its gain for a given frequency ω is found as

$$\frac{\|\mathcal{L}\{f\}\|}{\|\mathcal{L}\{u\}\|}(i\omega) = \lambda\sqrt{2 - 2\cos(\omega T)}. \tag{2.6}$$

The resulting transfer function is plotted in figure 2.2. The time-delayed feedback damps all frequencies that are not harmonics of ω_f, with maximum effect on the subharmonic frequency $\omega_f/2$ and on its odd harmonics $(n+1/2)\omega_f$. It is neutral with respect to the mean flow, the fundamental frequency ω_f and its harmonics $n\omega_f$.

If the forced system converges towards a T-periodic unpaired state, the forcing will vanish, such that the recovered state is a consistent solution of the unforced Navier–Stokes equations.

2.3.2 *Choice of the feedback parameter λ*

At first glance, it might be expected from (2.6) that larger values of λ will always lead to more efficient non-harmonic damping. This however is not the case, similar to what has been demonstrated in the context of low-dimensional chaotic systems (Pyragas, 1992).

In order to guide the choice of the feedback parameter λ for the present purpose, a model problem is proposed. The dynamics of a two-frequency oscillator is considered,

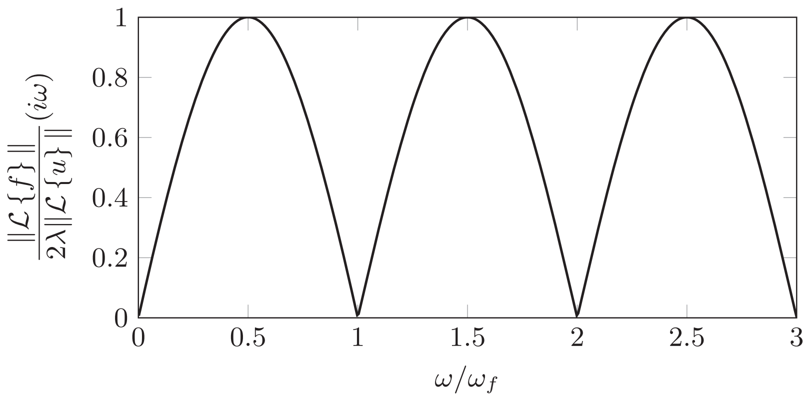

Figure 2.2: Gain of the delayed feedback transfer function.

$$\frac{\mathrm{d}}{\mathrm{d}t}\begin{pmatrix} x^s \\ \tilde{x}^s \\ x^h \\ \tilde{x}^h \end{pmatrix} = \begin{pmatrix} 0 & \frac{\omega_f}{2} & 0 & 0 \\ -\frac{\omega_f}{2} & 0 & 0 & 0 \\ 0 & 0 & 0 & \omega_f \\ 0 & 0 & -\omega_f & 0 \end{pmatrix}\begin{pmatrix} x^s \\ \tilde{x}^s \\ x^h \\ \tilde{x}^h \end{pmatrix} - \lambda \begin{pmatrix} x^s(t) - x^s(t-T) \\ \tilde{x}^s(t) - \tilde{x}^s(t-T) \\ x^h(t) - x^h(t-T) \\ \tilde{x}^h(t) - \tilde{x}^h(t-T) \end{pmatrix}, \tag{2.7}$$

with $T = 2\pi/\omega_f$ the period of the fundamental mode. Unlike the flow problem, the two frequencies ω_f and $\frac{1}{2}\omega_f$ in this model are uncoupled. After non-dimensionalisation, $\omega_f t \to t$ and $\lambda/\omega_f \to \lambda$, the system can be diagonalised as

$$\frac{\mathrm{d}}{\mathrm{d}t}\begin{pmatrix} y^s \\ \tilde{y}^s \\ y^h \\ \tilde{y}^h \end{pmatrix} = \begin{pmatrix} \frac{i}{2} & 0 & 0 & 0 \\ 0 & -\frac{i}{2} & 0 & 0 \\ 0 & 0 & i & 0 \\ 0 & 0 & 0 & -i \end{pmatrix}\begin{pmatrix} y^s \\ \tilde{y}^s \\ y^h \\ \tilde{y}^h \end{pmatrix} - \lambda \begin{pmatrix} y^s(t) - y^s(t-2\pi) \\ \tilde{y}^s(t) - \tilde{y}^s(t-2\pi) \\ y^h(t) - y^h(t-2\pi) \\ \tilde{y}^h(t) - \tilde{y}^h(t-2\pi) \end{pmatrix}. \tag{2.8}$$

In a general linear problem with time-delayed feedback, the eigenvalues are not found in closed form, and their number is infinite (Michiels and Niculescu, 2007). In contrast, exact eigensolutions of the uncoupled problem (2.8) can be found analytically. Introducing exponential modes, the following system is obtained:

$$y^s \propto e^{\alpha^s t} \quad \Rightarrow \quad \alpha^s = \frac{i}{2} - \lambda\left(1 - e^{-2\pi\alpha^s}\right), \tag{2.9a}$$

$$\tilde{y}^s \propto e^{\tilde{\alpha}^s t} \quad \Rightarrow \quad \tilde{\alpha}^s = -\frac{i}{2} - \lambda\left(1 - e^{-2\pi\tilde{\alpha}^s}\right), \tag{2.9b}$$

$$y^h \propto e^{\alpha^h t} \quad \Rightarrow \quad \alpha^h = i - \lambda\left(1 - e^{-2\pi\alpha^h}\right), \tag{2.9c}$$

$$\tilde{y}^h \propto e^{\tilde{\alpha}^h t} \quad \Rightarrow \quad \tilde{\alpha}^h = -i - \lambda\left(1 - e^{-2\pi\tilde{\alpha}^h}\right). \tag{2.9d}$$

As long as real values are chosen for λ, the solutions of equations (2.9a)-(2.9d) come in complex conjugate pairs, $\tilde{\alpha}^s = \bar{\alpha}^s$ and $\tilde{\alpha}^h = \bar{\alpha}^h$. It is therefore sufficient to consider equations (2.9a), (2.9c) and their closed-form solutions

$$\alpha_j^s = \frac{i}{2} - \lambda + \frac{1}{2\pi} W_j \left(-2\pi\lambda e^{2\pi\lambda} \right), \tag{2.10a}$$

$$\alpha_j^h = i - \lambda + \frac{1}{2\pi} W_j \left(2\pi\lambda e^{2\pi\lambda} \right), \qquad j \in \mathbb{Z}. \tag{2.10b}$$

W_j denotes the j^{th} branch of the Lambert W function, which is the inverse relation of the complex function $z \mapsto ze^z$ (Corless et al., 1996). An infinite number of solutions (2.9a), (2.9c) exist, corresponding to individual branches of the Lambert function. In particular, W_0 gives $\alpha_0^h = i$ for any value of λ, preserving the harmonic dynamics. For the purpose of flow stabilisation, only the real part of the α values is of interest, as these govern the growth or decay of fluctuations. If, for a given λ, there exists at least one j such that the real part of α_j^s or of α_j^h is positive, then the system is unstable. Therefore, λ must meet two criteria:

1. It should provide the most efficient damping in the subharmonic component equation (2.9a). For a given λ, it is always sufficient to consider the least stable mode among all possible solutions, *i.e.* the mode α_j^s with the largest real part in equation (2.10a). The optimal value of λ leads to maximal decay in the least stable mode.

2. At the same time, λ must not create any instability in the fundamental equation (2.9c); the real part of α_j^h must be negative for every $j \in \mathbb{Z}$. While the neutral fundamental mode $\alpha_0^h = i$ exists irrespective of λ, it must not be dominated by any unstable mode.

In order to identify the optimal λ according to these requirements, the following result is demonstrated in appendix 2.A: if, for a given value of λ, equations (2.9a) or (2.9c) have unstable solutions, the branch j on which this solution lies is such that

$$|j| < 2\lambda + 1. \tag{2.11}$$

As will be seen later, optimal subharmonic damping is found to be achieved within the range $0 < \lambda < 2$; consequently, the stability of the fundamental component must be ascertained for this range of λ, and the branches $-4 \leq j \leq 4$ are to be considered.

Figure 2.3 shows that no fundamental modes on these branches are unstable for any value of λ. As expected, the neutral eigenvalue $\alpha_0^h = i$ is always recovered, which is consistent with the premise that the applied forcing does not modify the fundamental dynamics. Therefore, the stability requirement for the fundamental modes (criterion 2) does not restrict the choice of λ.

Figure 2.4 demonstrates that the subharmonic modes on branches $-2 \leq j \leq 2$ experience damping for any value of λ. The same is observed for branches $|j| = 3, 4$. Therefore, all the subharmonic modes are stable. The least stable modes among these correspond to $j = 0$ and $j = -1$. The real parts of α_0^s and α_{-1}^s are identical for $\lambda > 0.04432$. This is identified as the optimal λ value, as it provides the strongest stabilisation of α_0^s.

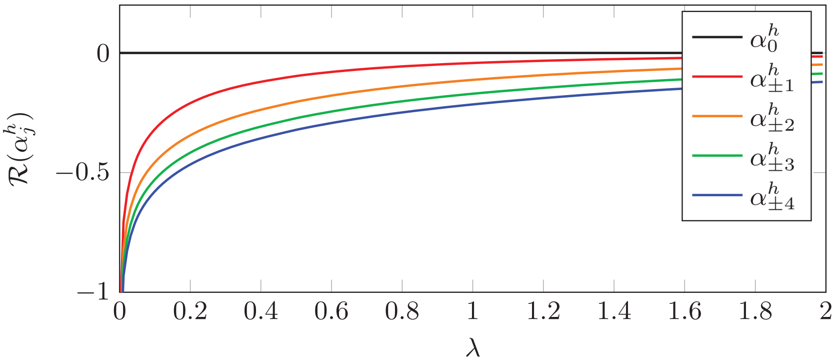

Figure 2.3: Real part of eigenvalues α_j^h for $-4 \leq j \leq 4$, pertaining to fundamental oscillations, as functions of λ. It is found numerically that α_j^h and α_{-j}^h always have the same real part. The system is neutrally stable for any value of λ, with the neutral mode $\alpha_0^h = i$.

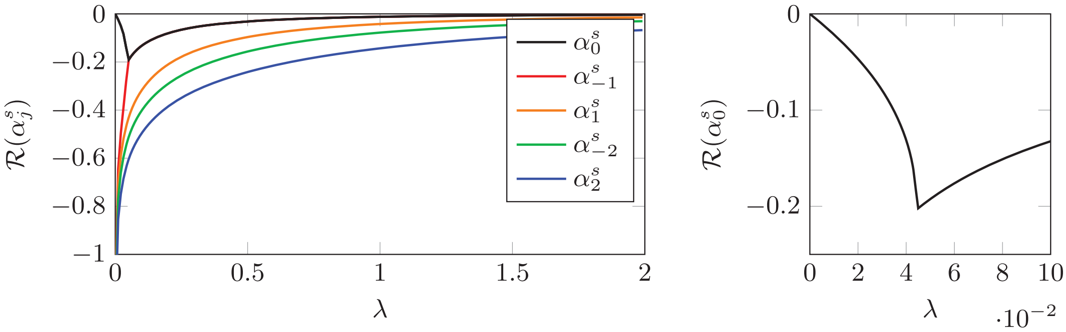

Figure 2.4: Real part of eigenvalues α_j^s, pertaining to subharmonic oscillations, as functions of λ. On the left, eigenvalues for $-2 \leq j \leq 2$; on the right, zoom on small λ values only for $j = 0$. All these eigenvalues are stable, but least so for the $j = 0$ branch. Higher eigenvalues than those shown are even more stable.

It is now examined whether the damped value $\alpha_0^s = -0.203 + 0.501i$ is still the least stable across all j branches. It is demonstrated in appendix 2.A that, if such a mode exists, it must stem from a branch j such that $|j| < 1 + \left(1 + e^{2\pi 0.203}\right)\lambda$. For $\lambda < 2$, this criterion restricts the search interval to $-10 \leq j \leq 10$. It can be reported that α_0^s is indeed the least stable eigenvalue of the stabilised system. Consequently, $\lambda = 0.04432$ is the optimal value of the damping parameter, leading to a system where the maximum subharmonic growth rate is -0.203.

2.4 STABILISED VORTEX STREET

In this section, the TDF technique presented in section 2.3 is applied to the case of vortex pairing. The configuration and the numerical code used in this chapter (section 2.3.1) is first described in some more detail. Then, in section 2.4.2, it is demonstrated that adding a time-delayed feedback makes a Navier–Stokes simulation converge towards the unstable unpaired state when initialised with the natural paired state. In section 2.4.3, it is confirmed that the simple model problem provides the optimal coefficient in the present vortex pairing case. Finally, in section 2.4.4, the technique is shown to also provide an efficient means to accelerate convergence in the case of a stable unpaired state.

2.4.1 *Simulation Method*

Direct numerical simulations were carried out using *NEK5000*, an incompressible spectral element code. An axisymmetric laminar jet is described in cylindrical coordinates (z, r), z being the main flow direction and r being the radial distance from the jet axis. The flow is assumed to be governed by the incompressible Navier–Stokes equations with zero azimuthal velocity, written in dimensionless form as

$$\frac{\partial \mathbf{u}}{\partial t} + (\mathbf{u} \cdot \nabla)\,\mathbf{u} = -\nabla p + \frac{1}{Re}\Delta \mathbf{u}, \qquad \nabla \cdot \mathbf{u} = 0. \tag{2.12}$$

The velocity $\mathbf{u}$ has axial and radial components u and v, and p denotes pressure. The jet diameter D and the inlet centerline velocity U_0 are used to render the flow problem nondimensional, defining the Reynolds number as $Re = U_0 D/\nu$, with ν the kinematic viscosity. The computational domain extends over 15×5 diameters in the axial and radial directions, respectively, and it is discretised with 6600 spectral elements, each containing 64 mesh points. Mesh convergence has been validated by comparing results for different spectral polynomial orders ($n = 4$, 6, 8 and 10; 8 being the standard). Boundary conditions are specified as follows.

1. In the inlet plane, $z = 0$, a hyperbolic-tangent velocity profile is imposed. In dimensionless form, its amplitude is modulated in time as

$$\mathbf{u}(r,t) = \frac{1}{2}\left\{1 - \tanh\left[\frac{1}{4\theta_0}\left(r - \frac{1}{4r}\right)\right]\right\}\left(1 + A\cos\left(\omega_f t\right)\right)\mathbf{e_z}, \tag{2.13}$$

   where $A = 0.05$ is the forcing amplitude of the jet, $\theta_0 = 0.025$ is the initial dimensionless mixing layer thickness and ω_f is the axial forcing frequency. The periodic nature of the flow is imposed with the periodic inlet forcing, similar as in Jacobs and Durbin (2001). The forcing period is given by $T = 2\pi/\omega_f$, and the Strouhal number is defined as $St = \omega_f D/(2\pi U_0)$.

2. On the centerline of the jet, $r = 0$, axisymmetric boundary conditions are imposed,

$$\frac{\partial u}{\partial r} = v = \frac{\partial p}{\partial r} = 0. \tag{2.14}$$

3. in the outlet plane, $z = 15$, and on the lateral boundary, $r = 5$, a stress-free outflow condition is applied:

$$-p\mathbf{n} + \frac{1}{Re}\left(\nabla \mathbf{u} + \nabla \mathbf{u}^t\right)\mathbf{n} = 0. \tag{2.15}$$

The flow configuration is thus characterised by the Reynolds number Re, the Strouhal number St, the dimensionless mixing layer thickness θ_0 and the forcing amplitude A.

2.4.2 *Computation of an unstable unpaired state*

The stabilisation technique described in section 2.3.1 is now applied, by adding a time-delayed feedback term

$$\mathbf{f}(t) = -\lambda\omega_f\left(\mathbf{u}(t) - \mathbf{u}(t-T)\right) \tag{2.16}$$

to the right-hand side of the Navier–Stokes equations (2.12). The parameter setting $Re = 2000$ and $St = 0.6$ has previously been found to exhibit synchronised vortex pairing in the absence of stabilisation (figure 2.1a), and will serve as example case. The action of the feedback is measured by tracing a norm of non-harmonic (in the sense of non-T-periodic) fluctuations, defined as

$$e(t) = \frac{1}{2}\sqrt{\int_z\int_r r\|\mathbf{u}(t) - \mathbf{u}(t-T)\|^2\,\mathrm{d}r\,\mathrm{d}z}. \tag{2.17}$$

This quantity measures the residual during the stabilisation process.

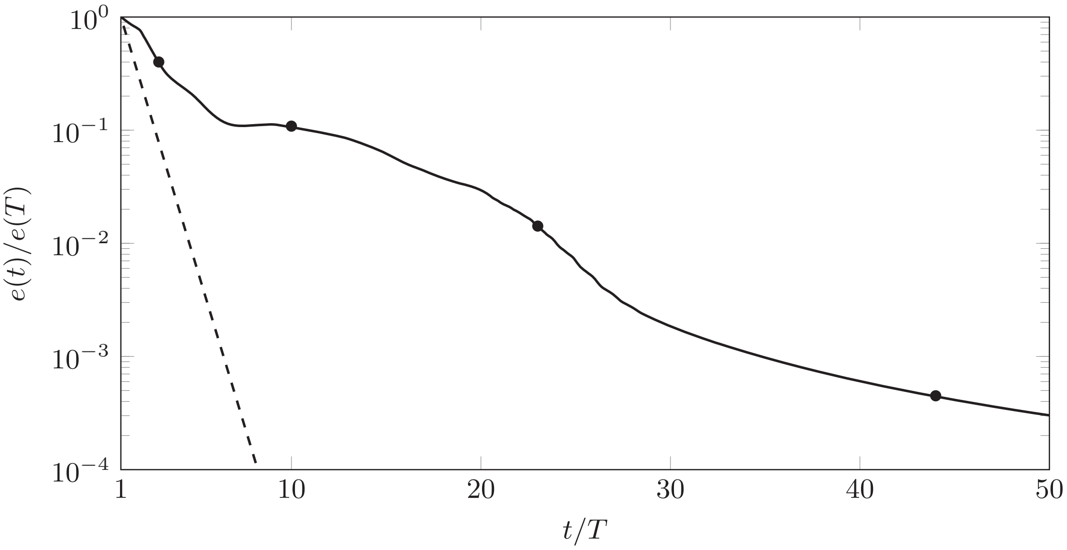

Figure 2.5: Evolution of the residual norm $e(t)$ (equation (2.17)), in a jet simulation with $Re = 2000$, $St = 0.6$ and $\lambda = 0.04432$. Dashed line: decay rate found in the model problem. Markers indicate the instances of snapshots shown in figure 2.6.

The simulation is started at $t = 0$ from the paired state represented in figure 2.1a, and the optimal value $\lambda = 0.04432$ as identified in section 2.3.2 is used first. Feedback is switched on at $t = T$, because one flow period needs to be recorded before the TDF term can be evaluated. The evolution of $e(t)$ is plotted in figure 2.5; four phases in the stabilisation process can be distinguished.

During the first phase, the applied forcing quenches the $2T$-periodic paired vortices. The distinct vortex structures downstream of the pairing location are thus replaced by a diffuse band of vorticity, as seen by comparing figures 2.6a and 2.6c. The magnitude of the non-harmonic component, $\|\mathbf{u}(t) - \mathbf{u}(t-T)\|$, which is proportional to the magnitude of the instantaneous forcing, is displayed in figure 2.6d: the forcing at this stage is active in the entire paired region, but not in

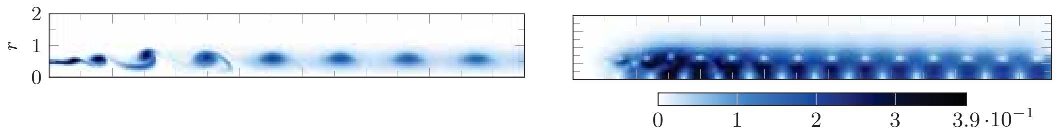

(a) Vorticity at $t = T$. (b) Non-harmonic component at $t = T$.

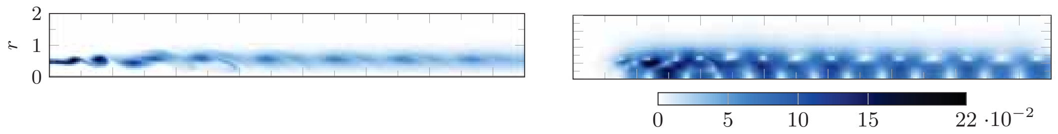

(c) Vorticity at $t = 3T$. (d) Non-harmonic component at $t = 3T$.

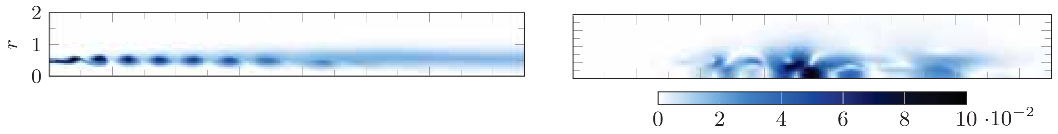

(e) Vorticity at $t = 10T$. (f) Non-harmonic component at $t = 10T$.

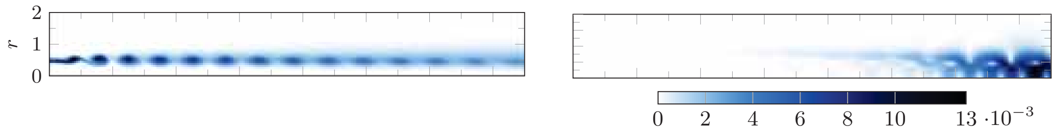

(g) Vorticity at $t = 23T$. (h) Non-harmonic component at $t = 23T$.

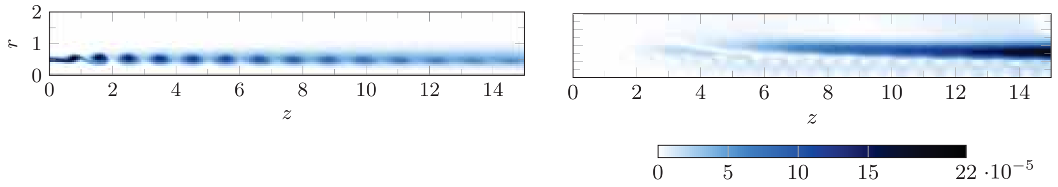

(i) Vorticity at $t = 44T$. (j) Non-harmonic component at $t = 44T$

Figure 2.6: Vorticity and non-harmonic component magnitude $\|\mathbf{u}(t) - \mathbf{u}(t - T)\|$ for $\lambda_{opt} = 0.04432$. The vorticity colorbar is in figure 2.1b.

the region of initial vortex roll-up. This behaviour is typical for $0 < t < 5T$, when the decay of the non-harmonic component is fastest, according to figure 2.5. This stage of the stabilisation process is conceptually similar to the subharmonic damping in the model problem of section 2.3.2. However, the damping rate observed in the jet is smaller than predicted by the model. This may be explained by the inherent positive subharmonic growth in the jet, which the damping has to overcome, whereas no such growth was assumed in the model problem.

During the following phase, the flow domain is gradually re-populated by a street of unpaired vortices, essentially by convection, as shown in figure 2.6e. This interpretation is consistent with the map in figure 2.6f, where non-harmonic fluctuations are seen to be concentrated around the trailing end of the emerging vortex array. This behaviour dominates the plateau region around $t = 10T$ in figure 2.5.

The third phase begins as the unpaired vortex street reaches the downstream end of the domain, when the flow visually appears to have reached a periodic state, displayed in figure 2.6g. The non-harmonic fluctuations at the trailing end of the vortex street leave the domain at this point, as seen in figure 2.6h, and this leads to a second sudden drop in the residual norm $e(t)$ in figure 2.5.

In the final phase, the flow is globally synchronised, and no visible difference between subsequent periods is observed anymore. Figure 2.6i shows the flow state at $t = 44T$. The residual norm continues to slowly decay in time as residual fluctuations are suppressed. These fluctuations are located far from the jet inlet, see figure 2.6j, and they do not present any spatial structure that can be associated with vortex pairing.

2.4.3 *Validation of the optimality of the feedback parameter λ*

In the preceding section, λ has been prescribed as the optimal value derived in the context of a model problem. The optimality for the present flow problem is now to be assessed. The simulation from section 2.4.2 is repeated, over a time horizon of $250T$, with sixteen different values of λ between 0.01 and 2. The time evolution of $e(t)$ is documented in figures 2.7a and 2.7b for each value $0.01 \leq \lambda \leq 0.5$. Larger values give poor results and are not reported.

Comparable results are achieved with $0.03 \leq \lambda \leq 0.2$; all curves in this range display the same characteristic phases of convergence, albeit with different efficiencies over short times. The long-time residual $e(t \gg T)$ is seen in figure 2.8 to be insensitive to the choice of λ within these limits. However, an optimal λ value may be identified that induces the fastest convergence towards the final phase, *i.e.* the λ for which the end of the third phase defined in section 2.4.2 is reached in the shortest time. Figures 2.7a and 2.7b show that the optimal value in this sense, among all values tried, is indeed $\lambda = 0.04432$, the one obtained in section 2.3.2.

2.4.4 *Convergence acceleration in a stable setting*

In the context of steady flows, selective frequency damping is effective in stabilising unstable settings, but it also provides accelerated convergence towards a steady state in weakly stable situations (Åkervik et al., 2006). Time-delayed feedback may achieve the same for weakly stable periodic flow. The case of a jet at $Re = 1300$, forced at $St = 0.6$, is chosen for a demonstration. The stable periodic solution in this setting is the unpaired state presented in figure 2.1b. This case is close to the onset of a pairing instability, as the same configuration with $Re = 1400$ settles into a stable paired state. Convergence of the final periodic unpaired state at $Re = 1300$ is slow as a consequence.

A converged steady laminar state without inflow forcing is chosen as initial condition, and harmonic inflow forcing (2.13) is started at $t = 0$. Simulations are then performed with and without time-delayed feedback; the non-harmonic component norm $e(t)$ is plotted as a function of time for both runs in figure 2.9.

Without damping, pairing sets in quickly several diameters downstream of the inlet. The paired vortex is then convected downstream, while repeated pairing takes place at almost the same location, such that the global norm of non-T-periodic components continue to grow (dashed line in figure 2.9). This growth

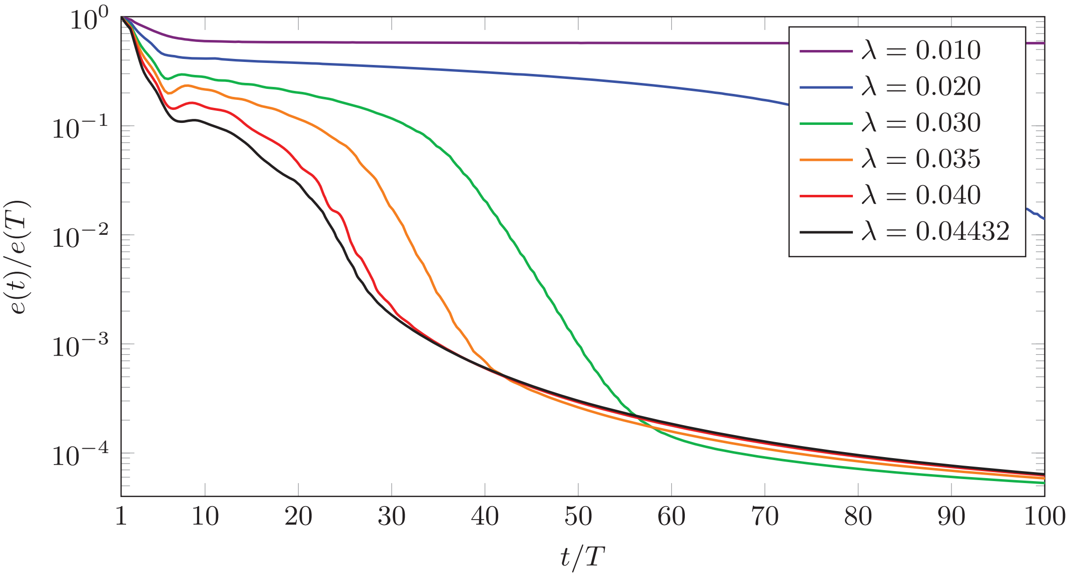

(a) Here, $\lambda \leq 0.0432$.

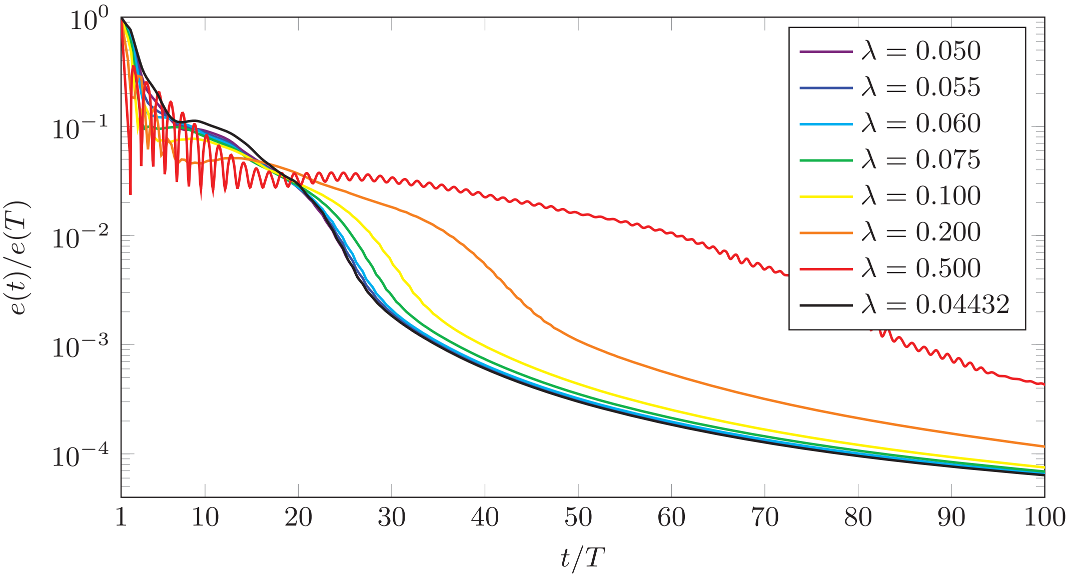

(b) Here, $\lambda \geq 0.0432$.

Figure 2.7: Residual norm as a function of time for several values of λ. Curves for $\lambda = 0.0425$, 0.0475 are omitted for clarity. At values $\lambda > 0.5$, the convergence is increasingly ill-behaved, displaying huge oscillating behaviour, and results are not reported.

ends at $t = 14T$, when the first paired ring reaches the outlet, as can be seen in figures 2.10a and 2.10b. Subsequently, $e(t)$ decays as the pairing location moves slowly downstream. At the end of the simulation, at $t = 200T$, pairing still takes place near the downstream end of the domain, as shown in figures 2.10c and 2.10d. Evacuation of the transient pairing through convection is a very slow process in this setting.

In the presence of time-delay feedback, pairing is never observed, and the convergence is significantly accelerated. According to figure 2.9, subharmonic fluctuations

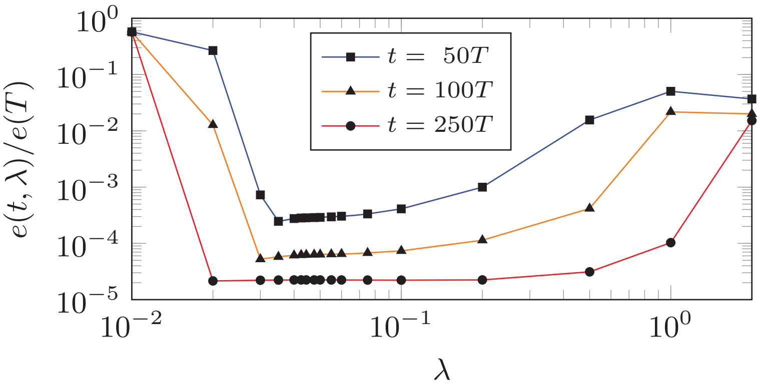

Figure 2.8: Residual norm $e(t)$ at $t = 50T$, $100T$ and $250T$ as a function of λ.

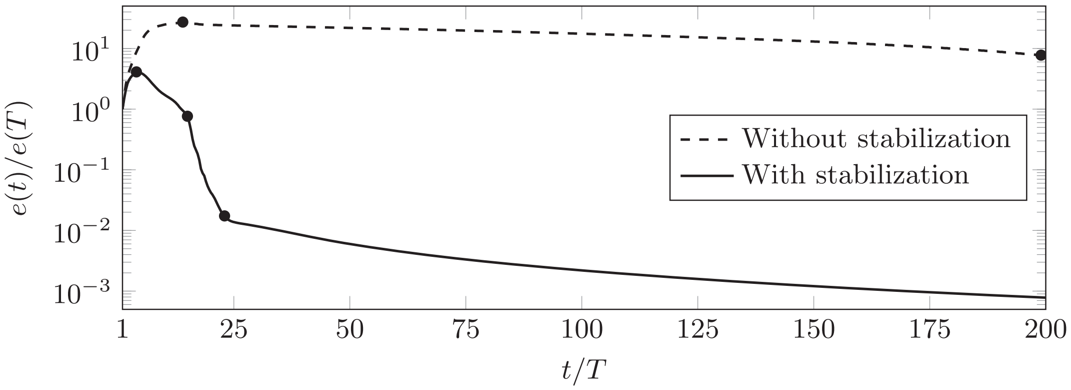

Figure 2.9: Evolution of the residual norm $e(t)$ with and without stabilisation applied. The different time-steps defined in section 2.4.4 are reported.

are reduced to residual levels within 20 forcing periods, which corresponds to the convection time of vortices through the domain. Snapshots of vorticity and of non-harmonic components are shown in figure 2.11 for three notable instances, as marked in figure 2.9.

2.4.5 *Reducing the memory requirements through time interpolation*

The TDF method described so far, although easy to implement, needs the storage of one full flow period, which can be resource-intensive, especially in the case of three-dimensional simulations. A remedy may be to store all flow variables and their time-derivatives only at N equispaced instants over one period, and to approximate all intermediate time steps through interpolation.

A first interpolation technique could rely on Fourier methods, since the converged flow is T-periodic. However, since the algorithm is based on the damping of *non-periodic* components, accurate reconstruction of these component precludes the use of Fourier series.

A spline interpolation is tried instead: each period is composed of $N_{\Delta t}$ time steps, and N equispaced time steps of the previous running period are stored in memory, *i.e.* one time step every $N_{\Delta t}/N$ time steps. The time derivative $\mathbf{u}_t$ of the velocity at

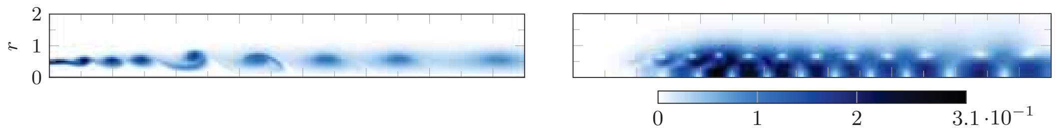

(a) Vorticity at $t = 14T$.

(b) Non-harmonic component at $t = 14T$.

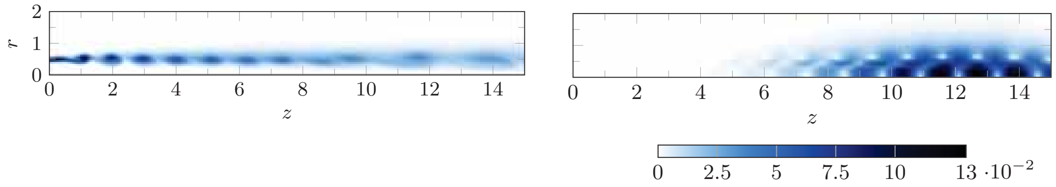

(c) Vorticity at $t = 200T$.

(d) Non-harmonic component at $t = 200T$.

Figure 2.10: Vorticity and non-harmonic component magnitude $\|\mathbf{u}(t) - \mathbf{u}(t-T)\|$ without feedback applied. The vorticity colorbar is in figure 2.1b.

each time step, computed with a centered-difference scheme, is also stored. Then, to reconstruct the flow at $t - T$, if $t_i \leq t - T \leq t_{i+1}$, with t_i and t_{i+1} time steps where the flow is stored, the following spline interpolation formula is used:

$$\begin{aligned}\tilde{\mathbf{u}}(r,z,t-T) = \left(1-t'\right)^2\left(1+2t'\right)\mathbf{u}(r,z,t_i) \;+\; t'\left(1-t'\right)^2\frac{T}{N}\mathbf{u}_t(r,z,t_i) \;+\\ t'^2\left(3-2t'\right)\mathbf{u}(r,z,t_{i+1}) \;+\; t'^2\left(t'-1\right)\frac{T}{N}\mathbf{u}_t(r,z,t_{i+1}),\end{aligned} \tag{2.18}$$

with the normalized time

$$t' = \frac{t-T-t_i}{t_{i+1}-t_i}. \tag{2.19}$$

This interpolation technique yields interpolated values, continuous up to the first time-derivative, that match the true velocity and acceleration at every checkpoint. Therefore, the forcing used in the Navier–Stokes equations (2.12) is now taken as

$$\tilde{\mathbf{f}}(t) = -\lambda\omega_f\left(\mathbf{u}(t) - \tilde{\mathbf{u}}(t-T)\right). \tag{2.20}$$

In traditional check-pointing techniques, such as the one used in direct-adjoint optimisation schemes (Hinze, Walther, and Sternberg (2006) and Schmid (2007)), a new simulation is run from the checkpoint to avoid errors from interpolation. This strategy cannot be applied in the present case, due to endless interdependency between periods: the time-delayed feedback at $t - T$ requires the knowledge of the flow at $t - 2T$, which in turn depends on the flow state at $t - 3T$, and so forth.

The reconstruction technique has been evaluated for the paired jet case at parameters $Re = 2000$ and $St = 0.60$. Each period of the flow is composed of 1000 time steps, with $\Delta t = 5/3 \times 10^{-3}$. Four cases have been investigated and compared to the results obtained without interpolation: $N = 50$, 20, 10 and 5. These cases respectively need 10, 25, 50 and 100 times less memory than the full-storage method (as memory is needed for the flow and its derivative).

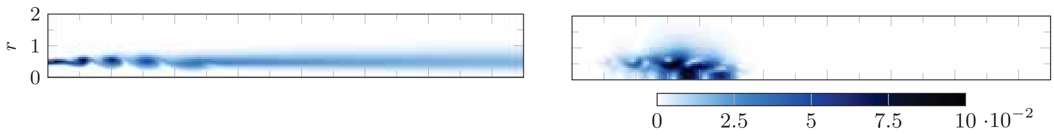

(a) Vorticity at $t = 4T$.

(b) Non-harmonic component at $t = 4T$.

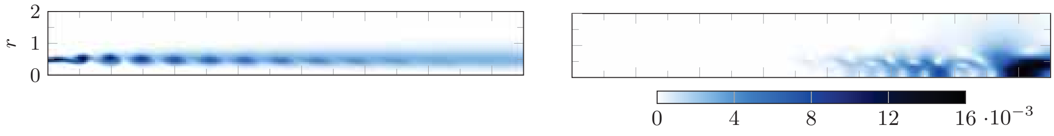

(c) Vorticity at $t = 15T$.

(d) Non-harmonic component at $t = 15T$.

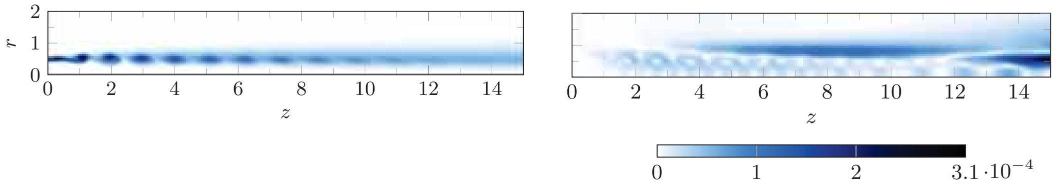

(e) Vorticity at $t = 23T$.

(f) Non-harmonic component at $t = 23T$.

Figure 2.11: Vorticity and non-harmonic component magnitude $\|\mathbf{u}(t) - \mathbf{u}(t-T)\|$ with time-delayed feedback applied. The vorticity colorbar is in figure 2.1b.

In order to evaluate the convergence performance of the algorithm for various values of N, two residuals are used. The first one, denoted $\tilde{e}_N(t)$, is based on the interpolated velocity $\tilde{\mathbf{u}}$ at $t - T$:

$$\tilde{e}_N(t) = \frac{1}{2}\sqrt{\int_z \int_r r\|\mathbf{u}(t) - \tilde{\mathbf{u}}(t-T)\|^2 \,\mathrm{d}r\,\mathrm{d}z}. \tag{2.21}$$

The second one, denoted $e_N(t)$, is based on the true velocity $\mathbf{u}$ at $t - T$, as defined in equation (2.17). $\tilde{e}_N(t)$ is the only available residual when interpolation is applied in general, whereas $e_N(t)$ is the true residual, which is normally unknown. For each N, the evolution of each of these two residuals is compared to the evolution of the residual $e(t)$ obtained with the full-storage version (see section 2.4.2).

The convergence results with the interpolated residual $\tilde{e}_N(t)$ are depicted in figure 2.12a. In every case, the residual first decreases in the same way as the uninterpolated stabilised flow. However, for $N < 50$, the residual starts to oscillate at a critical residual threshold. These oscillations have a maximum peak value $\tilde{E}_N$, which depends on N, and they descend in *all* cases to the same residual level E that is found in the full-storage solution (black line). The oscillation period corresponds to the interpolation period T/N. It is found that at the precise instants where snapshots are stored, the residual $\tilde{e}_N(t)$ is of the same order as the reference residual E.

In order to understand the meaning of this residual peak $\tilde{E}_N$, the maximum error between the interpolated and the real flow field as a function of t and N has been computed for the stabilised unpaired case. This maximum error occurs at $t = (t_i + t_{i+1})/2$ and is listed in table 2.1. For each N, the values obtained are of

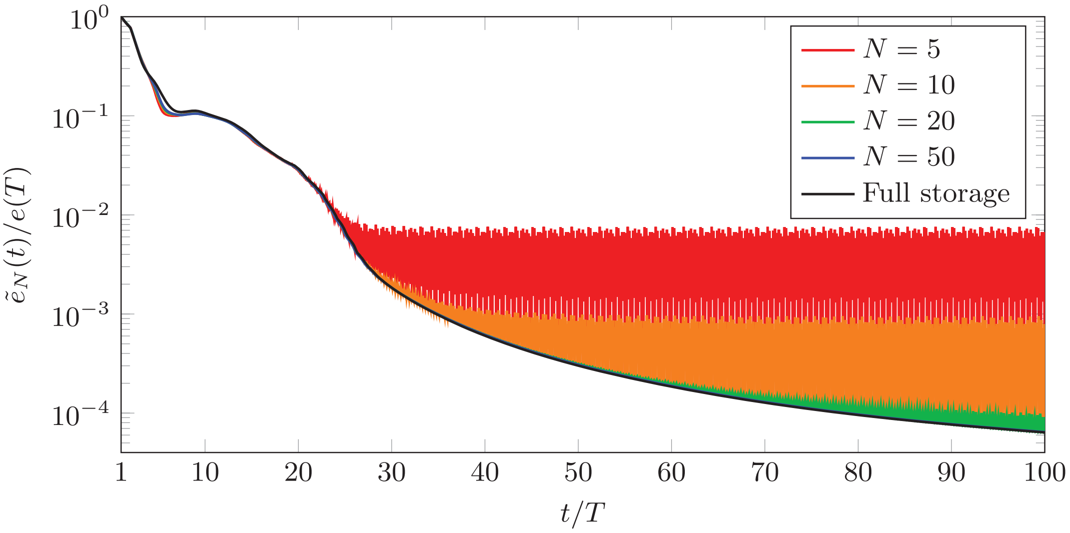

(a) Residual norm based on the interpolated velocity $\tilde{e}_N(t)$ as a function of time for different N and comparison to full-storage residual $e(t)$.

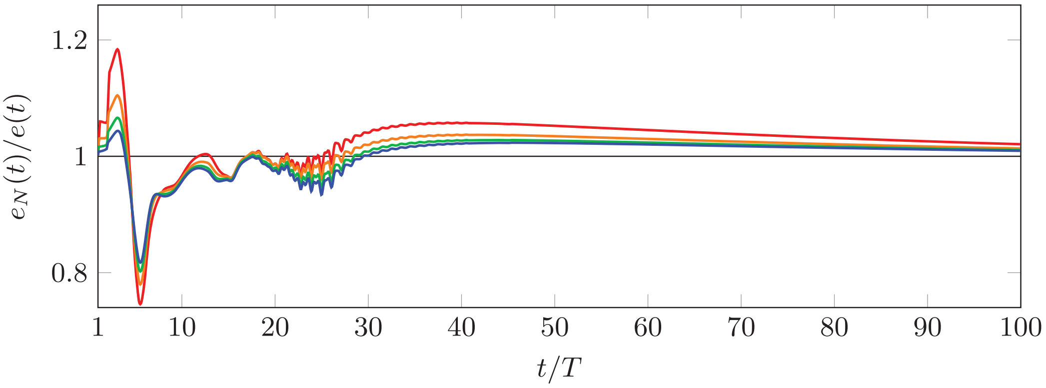

(b) Ratio between the exact residual $e_N(t)$ and the residual obtained with full storage $e(t)$ as a function of time for different N.

Figure 2.12: Convergence analysis of the stabilisation procedure with interpolation, for different storage requirements N. For $N = 5$, 10 and 20, $\tilde{E}_N$ is defined as the maximum peak of $\tilde{e}_N(t)$ when the residual starts oscillating. For $N = 50$, no oscillations are observed.

the same order as $\tilde{E}_N$ from figure 2.12a. For $N = 50$, the value $3.6 \cdot 10^{-6}$ is one order of magnitude smaller than $\min_t \tilde{e}_{50}(t) = 6 \cdot 10^{-5}$, which explains why oscillations are not encountered in this case. The residual from the interpolated velocity $\tilde{e}_N(t)$ can then be understood as the sum of two components: the non-T-periodic component of the flow $e_N(t)$ and the interpolation error of the flow at $t - T$. At large times, the interpolation error component seems to dominate the interpolated residual $\tilde{e}_N(t)$. We will now prove this statement and show that interpolation does not affect the overall precision of the reconstructed flow.

For this, figure 2.12b displays the evolution of the ratio between the residual $e_N(t)$ computed with the exact flow field for each interpolation level N and the residual $e(t)$ from the full-storage reference case. For $t > 30T$, in the final phase of

N	50	20	10	5
$\dfrac{\max\limits_t \lVert \mathbf{u}(t) - \tilde{\mathbf{u}}(t) \rVert}{e(T)}$	$3.6 \cdot 10^{-6}$	$1.3 \cdot 10^{-4}$	$1.5 \cdot 10^{-3}$	1.1×10^{-2}

Table 2.1: Maximum normalised error between the interpolated and the real flow as a function of N for a fully stabilised unpaired flow at $Re = 2000$ and $St = 0.60$.

stabilisation (see figure 2.12a), the exact residual with interpolation $e_N(t)$ is only slightly above the residual from full-storage calculations. As N increases, the interpolation improves and $e_N(t)$ approaches the reference value. It is found that the stabilised flow state obtained with checkpointing, even for $N = 5$, is about as accurate as the full-storage solution, despite large residual values $\tilde{e}(t)$ between checkpoints. When interpolation is used and only $\tilde{e}_N(t)$ is available, the convergence of the algorithm should therefore be only assessed at times t that corresponds to checkpoints at $t - T$.

2.5 STABILISATION OF LIMIT CYCLES WITH UNKNOWN FREQUENCIES – THE LID DRIVEN CAVITY EXAMPLE

When the frequency of the limit cycle is not known *a priori*, unlike the jet example, some techniques have been developed in the harmonic balance technique to overcome this issue, such as the Gradient-Based Variable Time Period (Gopinath and Jameson, 2006; McMullen, Jameson, and Alonso, 2006; McMullen, Jameson, and Alonso, 2002; Spiker et al., 2006). This technique is based on considering the residual as a function of not only t but also T, and to choose T as an extremum of this residual. This method, based in their case on gradient computations, can easily be transposed to our stabilisation procedure:

- A starting guess T_g of the period T_0 of the limit cycle is required.
- TDF is then applied with this T_g. Both the term $\mathbf{u}(t - T_g)$ and the dimensional λ depend on T_g, see equation (2.16).
- At $t = t_1$, when initial transients are stabilised, *i.e.* when $e(t_1, T_g)$ is small enough (for instance, $e(t_1, T_g) < 0.01\lVert \mathbf{u}(t_1) \rVert$), a new value for T_g is identified as the minimum

  $$T_g = \underset{T' \in \left[0.8T_g; 1.2T_g\right]}{\arg\min} \; e(t_1, T'), \tag{2.22}$$

  with the residual $e(t, T)$ as defined in equation (2.17). This global search, almost inexpensive since $\mathbf{u}(t)$ and $\mathbf{u}(t - T')$ are already stored, is restricted to $\left[0.8T_g; 1.2T_g\right]$ in order to avoid abrupt variations of T_g.
- The stabilisation procedure is applied again with the new T_g over a time-horizon equal to T_g.
- The global search is regularly carried out at $t_{i+1} = t_i + T_g$.

	Re_c	ω_c
Feldman and Gelfgat (2010)	1914.0	0.575
Kuhlmann and Albensoeder (2014)	1919.5	0.586
Loiseau, Robinet, and Leriche (2016)	1914.0	0.585

Table 2.2: Review of the critical Reynolds number and frequency of the linear unstable mode at Re_c for the cubic lid-driven cavity.

We prefer performing regular global searches for T_g instead of calculating $\partial e / \partial T$, because the full storage of the past period allows to perform a cheap and quick optimisation over a full range of T_g values ($[0.8T_g; 1.2T_g]$) and because of the superior robustness provided by global methods compared to local methods.

As the limit-cycle frequency in the forced jet is prescribed by the applied forcing, it would be contrived to treat it as an unknown. The flow in a $3D$ cubic lid-driven cavity is chosen instead for a demonstration. It has been shown that the steady solution of such a flow, above a critical Reynolds Re_c, is no longer stable (Feldman and Gelfgat, 2010; Kuhlmann and Albensoeder, 2014; Loiseau, Robinet, and Leriche, 2016), and that it bifurcates towards a limit cycle in a slightly subcritical fashion (Kuhlmann and Albensoeder, 2014). The bifurcated state is unsteady and, close to Re_c, it evolves at the frequency ω_c predicted by linear stability theory. Critical Reynolds number and frequency are listed in table 2.2. However, as shown in Kuhlmann and Albensoeder (2014) and Loiseau, Robinet, and Leriche (2016), this limit cycle is not stable since it experiences *intermittent chaos*: short bursts occur that destabilise the cycle before disappearing. Therefore, without applying any stabilisation technique, it cannot be expected that this cycle will converge naturally.

These simulations have been carried out again with Nek5000, on the same mesh as used in Loiseau, Robinet, and Leriche (2016). The driving velocity and the cube side length are used to non-dimensionalise the problem. A Reynolds number of 1930 – above the critical limit – is chosen. At this Reynolds number, the limit-cycle frequency is kept unchanged at $\omega_0 = 0.585$ (Loiseau, Robinet, and Leriche (2016)). The time step was fixed to $\Delta t = 2.0 \cdot 10^{-3}$. In this study, all time steps have been stored (the method described in section 2.4.5 was not applied). At $t = 0$, the cavity is at rest: $\mathbf{u}(t = 0) = \mathbf{0}$.

To understand the performance of the algorithm, several cases have been investigated:

- with no forcing,
- with forcing applied at the fixed frequency of the limit cycle, $\omega_0 = 0.585$.
- with variable-frequency forcing applied, starting form an initial guess. Five guess values have been tried: $\omega_g = 0.50$, 0.55, 0.60, 0.65, and 0.585. The frequency interval covered is $\omega_0 \pm 15\%$.

The results are reported in figure 2.13. First, it can be stated that the method works for every ω_g studied: the convergence is improved by at least two orders of magnitude compared to the time-stepping without stabilisation. Moreover, the convergence of the flow and ω is achieved whatever ω_g studied, which shows the

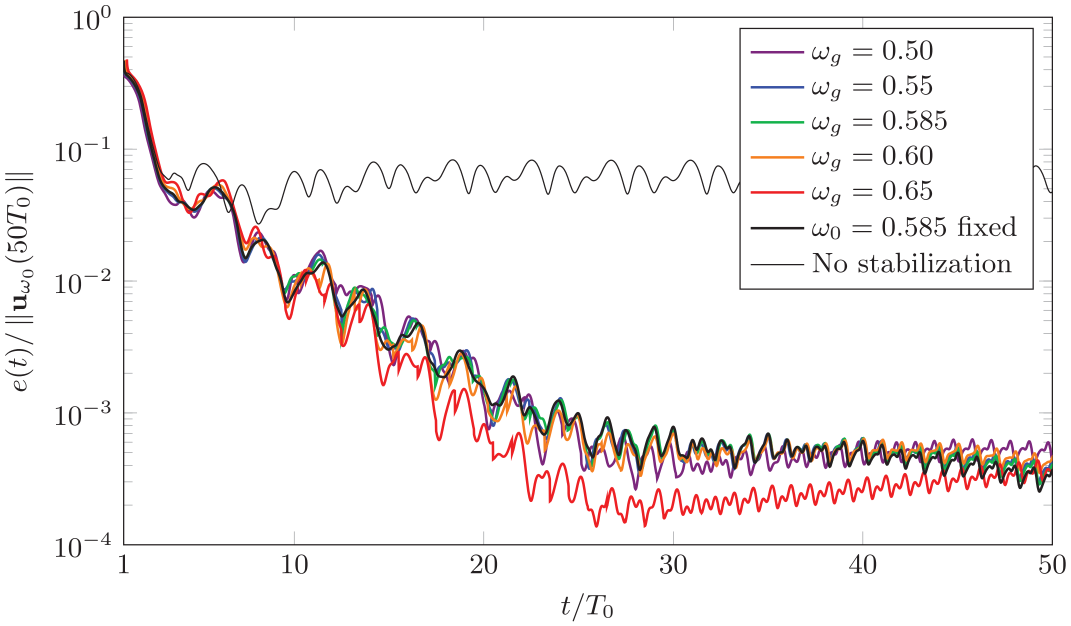

(a) Norm of the residual component as a function of time for the different cases studied normalized with the total velocity norm at $t = 50T_0$ of the fixed ω_0 case.

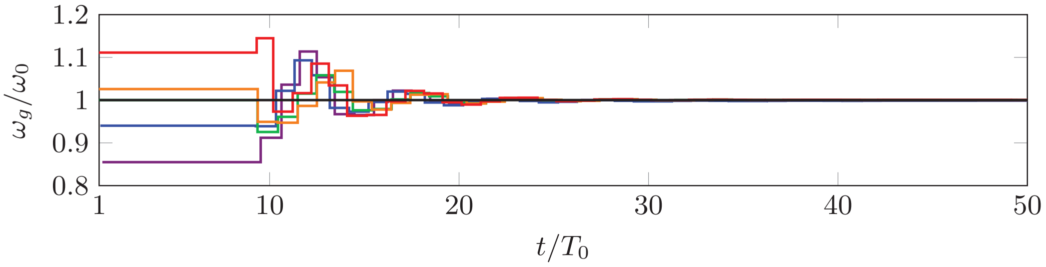

(b) Evolution of the global frequency guess for each case as a function of time.

Figure 2.13: Convergence analysis of the lid-driven cavity.

robustness of the technique. Convergence is achieved in about $25T_0$ whatever ω_g, which is the same physical time needed for the case with fixed ω_0 to settle. Therefore, the frequency search does not augment significantly the computational cost. However, contrary to the unpaired jet, the decrease of the residual is not monotonic, which can be linked to the fact that the cavity flow is not receptive to $\omega_0/2$ perturbations but to other frequencies (Loiseau, Robinet, and Leriche, 2016).

2.6 CONCLUSION

A time-delayed feedback method, introduced by Pyragas (1992) in the context of ODEs with few degrees of freedom, has been applied to a flow problem for the purpose of computing unstable time-periodic states. It has been demonstrated that spontaneous vortex pairing in a harmonically forced jet is efficiently suppressed by this method, such that an unpaired vortex street, synchronised at the frequency of the prescribed inflow forcing, is recovered. In this final converged flow state, the stabilising feedback term vanishes, and the recovered state is therefore a true solution of the flow equations, uncompromised by artificial damping. The one free numerical parameter for this procedure has been chosen based on a simple model problem, where the optimal value could be determined analytically. It has then been found that the same value provides optimal convergence also in the jet calculations.

The same technique has been shown to be useful also in weakly stable situations, where uncontrolled time-stepping converges towards a T-periodic state, but only slowly so. Artificial damping through time-delay feedback greatly increases the rate of convergence in this case.

The described method is very easy to implement with a given flow solver, as it only requires the addition of a simple source term, as well as the storage of one full cycle of the flow. The latter aspect may be memory resource-intensive. An interpolation method has been proposed in order to overcome this limitation. In the jet example, the storage requirement could thus be reduced by a factor 100, without significant loss of accuracy, and at negligible additional cost.

The suppression of vortex pairing in the present example enables a stability analysis of the recovered unpaired state, and the results of such analysis will be reported in a forthcoming study.

The time-delayed feedback method has finally been adapted to stabilise limit cycles in unforced flows, where the frequency is not known *a priori*. This was demonstrated for a lid-driven cubic cavity case with intermittent chaos. The procedure has been found to be very effective, enabling limit-cycle stabilisation at the correct frequency. The iteration identification of the limit-cycle frequency, as an additional unknown, did not lead to prolonged simulations in the cavity example. As in the harmonically forced jet, the recovered state is a true solution of the flow equations.

2.A STABILITY OF SOLUTIONS TO EQUATIONS (2.9a) AND (2.9c)

Consider the equation

$$\alpha = ki - \lambda \left(1 - e^{-2\pi\alpha}\right), \tag{2.23}$$

with both k and λ having positive real values. Solutions (Corless et al., 1996) are found as

$$\alpha_j = ki - \lambda + \frac{1}{2\pi} W_j \left(2\pi\lambda e^{2\pi(\lambda - ik)}\right), \quad j \in \mathbb{Z}. \tag{2.24}$$

The j^{th} solution involves the j^{th} branch W_j of the Lambert function. Assuming that there exists a branch W_j such that $\mathcal{R}(\alpha_j) > \beta$ for a given λ, where $\mathcal{R}(z)$ and $\mathcal{I}(z)$ respectively denote the real and imaginary parts of z, the triangular inequality, applied to equation (2.23), guarantees

$$|\alpha_j| \leq |ki| + \lambda |1 - e^{-2\pi\alpha_j}| \leq k + \left(1 + e^{-2\pi\beta}\right)\lambda. \tag{2.25}$$

The imaginary part of (2.24) is evaluated as

$$\mathcal{I}(\alpha_j) = k + \frac{1}{2\pi} \mathcal{I}\left[W_j\left(2\pi\lambda e^{2\pi(\lambda - ik)}\right)\right]. \tag{2.26}$$

Positive and negative integer values of j need to be considered separately.

2.A.1 *Case $j > 0$*

In this case, from (Corless et al., 1996), as $\mathcal{I}(W_j(z)) > 0$ for all complex number z and $k > 0$:

$$|\mathcal{I}(\alpha_j)| = k + \frac{1}{2\pi}\mathcal{I}\left[W_j\left(2\pi\lambda e^{2\pi(\lambda - ik)}\right)\right], \tag{2.27}$$

so that, as $|\alpha_j| \geq |\mathcal{I}(\alpha_j)|$:

$$|\alpha_j| \geq k + \frac{1}{2\pi}\mathcal{I}\left[W_j\left(2\pi\lambda e^{2\pi(\lambda - ik)}\right)\right]. \tag{2.28}$$

Therefore, combining (2.25) and (2.28):

$$\mathcal{I}\left[W_j\left(2\pi\lambda e^{2\pi(\lambda - ik)}\right)\right] \leq 2\pi\left(1 + e^{-2\pi\beta}\right)\lambda. \tag{2.29}$$

From the properties of the Lambert function (Corless et al., 1996), and because $j > 0$, $\mathcal{I}\left(W_j\left(z\right)\right) > 2\pi\left(j-1\right)$ for all complex z. Therefore a necessary condition for $\mathcal{R}(\alpha_j) > \beta$ with $j > 0$ is:

$$|j| < 1 + \left(1 + e^{-2\pi\beta}\right)\lambda. \tag{2.30}$$

2.A.2 *Case $j < 0$*

In this case, from (Corless et al., 1996), as $\mathcal{I}(W_j(z)) < 0$ for all complex number z and $k > 0$:

$$|\mathcal{I}(\alpha_j)| = k - \frac{1}{2\pi}\mathcal{I}\left[W_j\left(2\pi\lambda e^{2\pi(\lambda - ik)}\right)\right], \tag{2.31}$$

so that, as $|\alpha_j| \geq |\mathcal{I}(\alpha_j)|$:

$$|\alpha_j| \geq k - \frac{1}{2\pi}\mathcal{I}\left[W_j\left(2\pi\lambda e^{2\pi(\lambda - ik)}\right)\right]. \tag{2.32}$$

Therefore, combining (2.25) and (2.32):

$$-\mathcal{I}\left[W_j\left(2\pi\lambda e^{2\pi(\lambda - ik)}\right)\right] \leq 2\pi\left(1 + e^{-2\pi\beta}\right)\lambda. \tag{2.33}$$

From the properties of the Lambert function (Corless et al., 1996), and because $j < 0$, $\mathcal{I}\left(W_j\left(z\right)\right) < 2\pi\left(j+1\right)$ for all complex z. Therefore a necessary condition for $\mathcal{R}(\alpha_j) > \beta$ with $j < 0$ is:

$$|j| < 1 + \left(1 + e^{-2\pi\beta}\right)\lambda. \tag{2.34}$$

2.A.3 *Conclusion*

The two cases $j \lessgtr 0$ leads to the same conclusion, which is also valid for $j = 0$. Therefore, for a given λ, any mode α_j such that $\mathcal{R}(\alpha_j) > \beta$ must derive from branches W_j with:

$$|j| < 1 + \left(1 + e^{-2\pi\beta}\right)\lambda. \tag{2.35}$$

This criterion is strict and holds for any value of k.

In particular, for a given λ, the unstable modes, if they exist, must derive from branches W_j with $|j| < 1 + 2\lambda$.

3

VORTEX PAIRING IN JETS AS A GLOBAL FLOQUET INSTABILITY: MODAL AND TRANSIENT DYNAMICS

CONTEXT

In the previous chapter 2, a method to recover unpaired periodic orbits has been developed, relying on a time-delayed feedback to suppress the related instability.

Numerous previous works have investigated pairing *from the paired stated point of view*: why does the paired state have its given shape? Why does pairing occur at this given location? In this view, the dominant explanation of pairing occurrence links the growth of the subharmonic mode to the phase speed equality between the fundamental and the subharmonic Fourier mode in a paired flow. However, these studies have a dead angle: they do not resolve the dilemma we observed at the beginning of chapter 2, i.e. they do not explain why, for some parameter ranges, unpaired states are not observed.

The methods introduced in chapter 2 allow to to compute the unpaired flow for all parameter values. This allows us to focus on the *unpaired state point of view*: under which conditions is it a stable state? *A priori*, the instability of this state can stem both from a linear or a nonlinear mechanism. Through this chapter, relying on the Floquet framework, we explain that the linear mechanisms are at stake here: in particular, the dynamical system is subject to a bifurcation in which both *modal* and *non-modal* growth play a role.

This analysis, together with the results of chapter 2, enables us to build a complete toolbox fully adapted to study both modal and non-modal stability of time-periodic orbits.

The work in this chapter is currently under review for the *Journal of Fluid Mechanics* (Shaabani-Ardali, Sipp, and Lesshafft, 2018).

ABSTRACT

The spontaneous pairing of rolled-up vortices in a laminar jet is investigated as a global secondary instability of a time-periodic spatially developing vortex street. The growth of subharmonic perturbations, associated with vortex pairing, is analysed both in terms of modal Floquet instability and in terms of transient growth dynamics. This chapter has the double objective to outline a toolset for global analysis of time-periodic flows, and to leverage such an analysis for a fresh view on the vortex pairing phenomenon.

Axisymmetric direct numerical simulations (DNS) of jets with single-frequency inflow forcing are performed, in order to identify combinations of the Reynolds and Strouhal numbers for which vortex pairing is naturally observed. The same DNS calculations are then repeated with an added time-delay control term, which

artificially suppresses pairing, so as to obtain time-periodic unpaired base flows for linear stability analysis. It is demonstrated that the natural occurrence of vortex pairing in nonlinear DNS coincides with a linear subharmonic Floquet instability of the underlying unpaired vortex street. However, DNS results suggest that the onset of pairing involves much stronger temporal growth of subharmonic perturbations than what is predicted by modal Floquet analysis, as well as a spatial distribution of these fast-growing perturbation structures that is inconsistent with the unstable Floquet mode. Singular value decomposition of the phase-shift operator (the operator that maps a given perturbation field to its state one flow period later) is performed for an analysis of optimal transient growth in the vortex street. Non-modal mechanisms near the jet inlet are thus found to provide a fast route towards the limit-cycle regime of established vortex pairing, in good agreement with DNS observations.

It is concluded that modal Floquet analysis accurately predicts the parameter regime where sustained vortex pairing occurs, but that the bifurcation scenario under typical conditions is dominated by transient growth phenomena.

3.1 INTRODUCTION

When the shear layer of a jet is subjected to low-level forcing at the nozzle, perturbations within a band of unstable frequencies are amplified as they travel downstream (Michalke, 1971). When the perturbation amplitude reaches nonlinear levels, the shear layer rolls up into vortices. In the case of laminar jets, forced axisymmetrically at a single frequency, a regular street of ring vortices is formed, where the passage frequency of vortices is controlled by the nozzle forcing. It has long been observed that such vortices may, in certain parameter regimes, spontaneously undergo regular *pairing*: two neighboring vortices then merge into one, such that a new vortex street is formed, with a periodicity that corresponds to the subharmonic of the applied forcing frequency. This scenario is illustrated in figure 1.9, which shows a flow visualisation from the experiments by Schram (2003). The first systematic studies of the pairing scenario have been conducted by Zaman and Hussain (1980) and Hussain and Zaman (1980). While the merging of two vortices is clearly a nonlinear process, it remains to be clarified to what extent the occurrence of regular vortex pairing is governed by linear mechanisms, and how such linear dynamics may be properly formalised.

Numerous past studies have sought to explain the pairing phenomenon by investigating the consistency of the paired flow state itself. Monkewitz (1988) developed a theoretical framework based on weakly nonlinear interaction between the forced fundamental instability wave and its subharmonic. His formalism leads to a phase-relation criterion for subharmonic resonance, which has subsequently been validated experimentally by Husain and Hussain (1989), Raman and Rice (1991), Paschereit, Wygnanski, and Fiedler (1995) and others.

A different approach consists in considering the bifurcation process from a harmonic unpaired to a subharmonic paired state. This viewpoint leads to the question whether an array of vortices convecting at the imposed forcing frequency is unstable with respect to subharmonic perturbations. In forced jets, vortex pairing occurs as a self-sustained process, and the pairing location is stationary in a spatially non-periodic flow. Therefore, the appropriate framework will have to be based on either locally absolute/convective, or fully global analysis. Brancher and Chomaz (1997) investigate the absolute nature of pairing instability in a periodic array of Stuart vortices, as a model for a rolled-up two-dimensional plane shear layer. In order to apply the notion of absolute/convective instability (Huerre and Monkewitz, 1990), commonly used for steady configurations, they conduct their analysis in a co-moving frame of reference, where the vortices are stationary. By varying the concentration factor of the vortices, they show that the required backflow rate for absolute instability decreases as the vortex concentration increases. This formalism pertains to a spatially periodic array of vortices and does not account for viscous effects.

In the present study, we aim to describe the onset of vortex pairing as a secondary instability in a *global* analysis framework. As the underlying basic state, the unpaired vortex street resulting from the primary shear instability, is time-periodic, a classical Floquet formalism is employed. Modal instability as well as transient growth scenarios will be explored within this framework. Global instability analysis has become a standard approach in the context of *steady* base flows (Theofilis, 2011). Linearisation of the governing flow equations around a steady base flow yields an autonomous operator; the spectrum of this operator indicates the possibility of perturbation growth in the long-time limit. However, the base flow in our case is not steady but *periodic* in time, the periodicity being controlled by the harmonic forcing of the jet. Therefore, the global analysis method must be adapted to account for this periodicity, by use of the Floquet theorem (Floquet, 1883). A global Floquet formalism has been successfully applied by Barkley and Henderson (1996) to the secondary instability of a cylinder wake around $Re = 200$ and more recently by Jallas, Marquet, and Fabre (2017) to a study of secondary instabilities in wake flows.

Another possible scenario for the onset of instability would be through transient growth; this phenomenon has first been described in parallel flows by Trefethen et al. (1993): if the linearised flow operator is non-normal, then, even though the system is stable, in the sense that at an infinite time horizon any perturbation decays towards zero, intial perturbations can be greatly amplified over a short time. For stationary jets, Nichols and Lele (2011) and Garnaud et al. (2013) studied this phenomenon and shown its significant role in the bifurcation. However, we aim at studying transient growth of a time-periodic jet. Several authors (Arratia, Caulfield, and Chomaz, 2013; Barkley, Blackburn, and Sherwin, 2008; Blackburn, Sherwin, and Barkley, 2008; Johnson, Brion, and Jacquin, 2016) applied direct-adjoint looping in order to identify finite-time optimal perturbations in unsteady base flows. In the present chapter, we use a technique that allows us to retrieve optimal perturbations based on direct time-stepping alone, and which takes full advantage of the time-periodicity of the underlying base flows.

As a prerequisite for our analysis, periodic base flow states *without* vortex pairing must be computed even in situations where such pairing arises naturally. Standard methods for the computation of periodic flow states may be based on *Newton–Picard shooting* methods, as described in Lust and Roose (1998) and Roose et al. (1995) and applied to several flows in Sánchez and Net (2010) and Sánchez et al. (2004).

One alternative is the *harmonic balance* technique, in which several temporal Fourier components of a given periodicity are calculated simultaneously (Hall, Thomas, and Clark, 2002; Thomas, Dowell, and Hall, 2002). In a recent publication (Shaabani-Ardali, Sipp, and Lesshafft, 2017), we describe how subharmonic fluctuations in time-stepping simulations can be efficiently suppressed by way of time-delayed feedback control ; this technique is employed here in order to construct the periodic base states.

This chapter is organised as follows: a comprehensive literature review is provided in section 3.2, in order to delineate the context of our investigation. Section 3.3 presents a systematic study of the parameter regimes where vortex pairing is observed in direct numerical simulations (DNS) of laminar jets at moderate Reynolds numbers. Modal Floquet analysis is performed in section 3.4, and it is shown that the Floquet-unstable parameter regime coincides with the observation of pairing in the DNS. Non-modal transient growth dynamics are investigated in section 3.5, and their relevance for the bifurcation scenario is demonstrated.

3.2 REVIEW OF THE LITERATURE ON VORTEX PAIRING

3.2.1 *Discovery*

The pairing of vortex rings in jets was described for the first time by Becker and Massaro (1968): in jet experiments at moderate Reynolds number, acoustic single-frequency forcing was observed to give rise to regular vortex formation and subsequent pairing. Winant and Browand (1974) investigated the same phenomenon in a plane mixing layer: pairing was found to occur intermittently in these experiments, punctuated by occasional “shredding” events, *i.e.* the destruction of vortex cores by a subharmonic strain field, which interrupt the pairing process. The authors proposed a phenomenological model based on Stuart vortices. In the context of jets, Petersen (1978) examined the influence of higher Reynolds numbers, and they inferred an argument on the basis of wave dispersion intended to predict the location of vortex pairing.

More detailed experimental investigations of vortex pairing in jets were carried out by Zaman and Hussain (Hussain and Zaman, 1980; Zaman and Hussain, 1980). These authors considered high Reynolds number ($Re = O(10^4)$) jets with a thin initial mixing layer, forced at a single frequency. Pairing was found to arise in two distinct frequency bands, one around $St_\theta = f\theta/U \approx 0.012$ and the other around $St_D = fD/U \approx 0.85$. These Strouhal numbers are formed with the jet exit velocity U, forcing frequency f, and either the initial shear layer thickness θ or the jet diameter D. According to their characteristic scaling, the two bands were identified with a “mixing layer mode” and a “jet column mode”, respectively. In the former case, the vortices are very thin and dissipate quickly, whereas in the latter case, their radial extent is comparable to the jet radius, and their viscous dissipation takes place over a much longer travel distance. Both articles describe in much detail the vortex dynamics, their trajectories and velocities, as well as the transition to turbulence. When turbulence sets in close to the nozzle, the pairing becomes intermittent. High-quality flow visualisations of vortex pairing in jets, at Reynolds number 2300, are shown by Meynart (1983).

Vortex pairing is also a common event in *plane shear layers*. Ho and Huang (1982) found that very low-amplitude subharmonic forcing in their shear layer experiments led to a vigorous flow response in the form of regular pairing, associated with a strongly increased spreading of the mean flow. Intermittently, simultaneous coalescence of several vortices occurred, and was described as "collective interaction". Similar observations had been made in jet experiments by Kibens (1980). Ho and Huang (1982) established experimentally that spatial growth of the subharmonic component only occurs in situations where its phase velocity is equal to that of the fundamental flow perturbation.

3.2.2 *Interpretation in terms of wave interaction*

Prior to theoretical explanations, Arbey and Ffowcs Williams (1984) demonstrated experimentally the importance of the phase difference between fundamental and subharmonic perturbations for the onset of vortex pairing. A jet at Reynolds number 17500 was forced at moderate amplitude (about 2% of the centreline velocity) at two frequencies ω and $\omega/2$. The spatial growth of perturbations at both frequencies was found to be strongly dependent on the relative phase of the applied forcing. Thanks to a numerical model, Mankbadi (1985) argued that pairing arises when the subharmonic component acquires sufficient energy, both from the fundamental wave and from the mean flow, to become the largest-amplitude perturbation in the jet. He observed that one or more stages of subsequent pairing can occur; in his framework, the number of stages and their spatial localisation depends on the Strouhal number.

A deeper theoretical understanding of the wave interaction involved in vortex pairing was reached by Monkewitz (1988), who formulated a weakly nonlinear model for the spatial development of fundamental and subharmonic instability waves in a parallel mixing layer. This model reflects the role of the phase shift between the two waves in triggering resonance, resulting in either pairing or "shredding" of vortices. It was predicted that the fundamental wave needs to reach a critical amplitude before subharmonic perturbations may phase-lock and grow. The same conclusions are supported by the more general theory of Cheng and Chang (1992).

The model of Monkewitz (1988) was confirmed experimentally by numerous studies: in a mixing layer, Husain and Hussain (1989) showed that simultaneous forcing of a fundamental frequency and its subharmonic could either enhance or attenuate the pairing and shredding phenomena. Subsequently, detailed statistical analysis of experimental data was performed, first for uncontrolled "natural" perturbations in a mixing layer (Hajj, Miksad, and Powers, 1992), then for explicitly forced fundamental and subharmonic waves in the same setup (Hajj, Miksad, and Powers, 1993). These two studies gave clear evidence of a parametric resonance, determined by the phase difference between both waves. Husain and Hussain (1995) carried out similar investigations of jets with a very thin shear layer, confirming that pairing was amplified for a large band of phase differences, but attenuated for a narrow band of phase differences. Moreover, these authors studied the influence of a slight frequency detuning in the subharmonic forcing, finding that the occurrence of vortex pairing depended on the instantaneous phase difference in the forcing. A parametric experimental study of pairing in jets was conducted by Raman and Rice (1991), who varied the Strouhal number, phase difference and forcing amplitude for both the fundamental and the subharmonic instability wave. Consistent with the theoretical predictions, it was shown that a critical fundamental amplitude was necessary to trigger subharmonic resonance, the growth rate being controlled by the phase difference at small forcing amplitude. When the forcing was strong enough, however, the subharmonic growth became independent of the phase difference. Paschereit, Wygnanski, and Fiedler (1995) confirmed these results, and further demonstrated that the subharmonic growth draws its energy from the mean flow, whereas the fundamental wave merely acts as a catalyst. In all these studies, explicit forcing of the subharmonic wave controlled the location of vortex pairing in turbulent jets.

The modal interaction framework was used by Bradley and Ng (1989) to study interactions between more than two frequencies, or between frequencies different from the fundamental ω and its subharmonic $\omega/2$. These authors experimentally studied a jet forced either at ω and $\omega/2$ or at ω and $\omega/3$ and studied the influence of frequency, amplitude ratio and phase shift. In the ω and $\omega/3$ forcing case, they found more diverse behaviour, with collective interactions, or pairing between vortices of different sizes.

3.2.3 *Further developments on pairing*

3.2.3.1 *Chaotic behaviour*

In less controlled configurations, vortex pairing events are often observed to be irregular and intermittent. Broze and Hussain (1994, 1996) conducted jet experiments with single-frequency excitation; depending on the Strouhal number St_D and on the forcing amplitude a_f, different types of behaviour were reported, as summarised in figure 3.1. Regular dynamics were found to arise over large parameter regions, namely no pairing (FO regime in figure 3.1), stable pairing (SP) and stable double pairing (SDP), the latter referring to the occurrence of two successive stages of vortex pairing. Irregular dynamics were observed either in the mild form of "aperiodic modulations" of the first (AM) or the second pairing stage (SPMQ), or in more erratic ways, categorised as intermittency, chaos (QCA) and "nearly-periodic modulations" (NPMP).

The results of Broze and Hussain (1996) do not appear to depend significantly on the Reynolds number within their operating conditions of $11000 \leq Re \leq 90000$. Drawing on chaos theory, the authors characterised the pairing dynamics in terms of attractors. For irregular scenarios, it was demonstrated that the occurrence of pairing of two vortices is strongly influenced by previous pairing events, implying that upstream-directed feedback is involved in the subharmonic growth. This observation is fully consistent with the wave-interaction model discussed in section 3.2.2. Narayanan and Hussain (1997) attempted to stabilise the pairing dynamics in chaotic regimes.

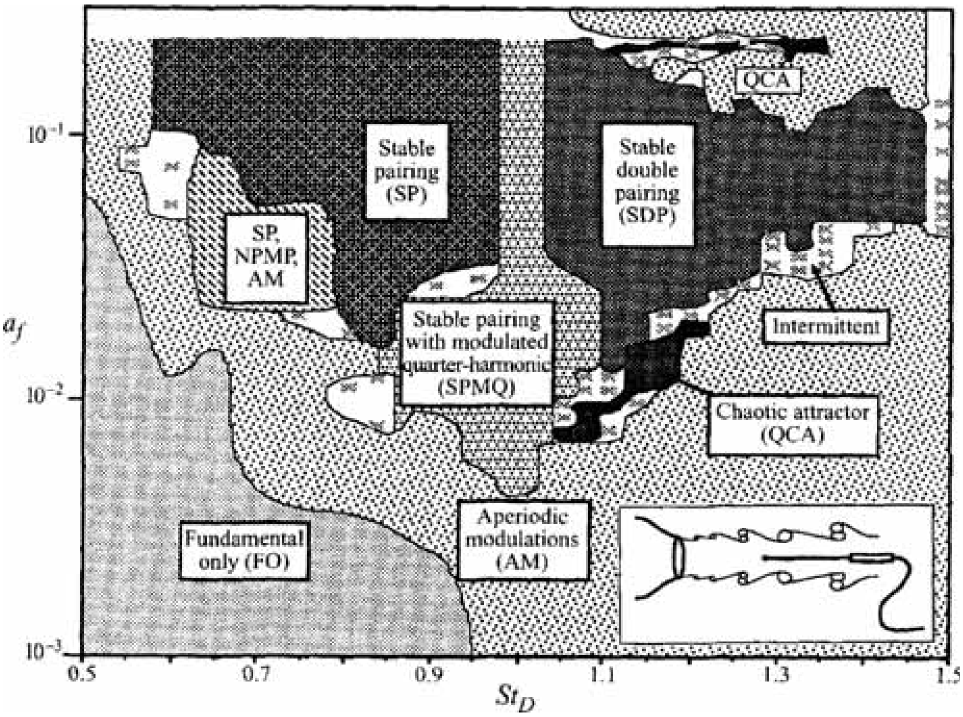

Figure 3.1: Pairing dynamics observed experimentally in turbulent jets at $Re = O(10^4)$, forced at a Strouhal number St_D with amplitude a_f. No subharmonic forcing is applied. From Broze and Hussain (1996).

3.2.3.2 *Pairing-related jet noise*

High-speed jets are potent sources of noise, and the role of vortex pairing as an aeroacoustic source mechanism has received much attention. Bridges and Hussain (1987) determined that the radiated noise is dominated by pairing events only in cases where the initial shear layer is laminar; in fully turbulent jets, vortex pairing appears to be acoustically unimportant. The dominant role of vortex pairing in laminar jet noise was further analysed numerically by Bogey and Bailly (2010). A detailed description of sound generation from vortex interaction in jets was given by Inoue (2002), and model-based predictions of radiated sound levels were derived by Schram et al. (2005).

3.2.3.3 *Kinematical modelling of vortex-ring interaction*

Vortex interaction can be conveniently modelled by use of the Biot–Savart law. An account of early applications of such approaches to vortex rings is given by Shariff and Leonard (1992); these studies were largely concerned with the initial roll-up or with the collective motion of a limited number of co-axial vortices. A common representation characterises a vortex ring by its core centre position and core radius, from which a semi-analytical induction law can be derived (Saffman, 1992). Contrary to vortex elements in a two-dimensional plane, axisymmetric vortex rings move at a self-induced velocity, which becomes infinitely large as the core radius approaches zero. Some simplifications arise from the assumption that the core radius is much smaller than the ring radius.

Within the limiting assumptions of inviscid flow and compact cores, such a conceptual model then yields low-dimensional systems representing the mutually induced motion of a collection of vortex rings. The “leapfrogging” interaction between two rings, when one passes through the other, corresponds to the early nonlinear stage of pairing in a jet before actual merging occurs. A model of a *plane* jet, consisting of counter-rotating vortex pairs, was studied by Tophøj and Aref (2013), who formulated a linear stability criterion for the occurrence of leapfrogging. Similarly, Borisov, Kilin, and Mamaev (2013) and Borisov et al. (2014) derived stability criteria for sets of two and three co-axial vortex rings, and validated these with respect to numerical simulations of viscous flow at high Reynolds number. Their work was completed by Cheng, Lou, and Lim (2015), who explicitly portrayed parameter regions in which leapfrogging could occur, depending on the Reynolds number and the aspect ratio of the vortex arrangement. Meunier et al. (2002) discovered a merging criterion for two co-rotating vortices in a two-dimensional plane.

3.3 VORTEX PAIRING IN SIMULATIONS AT VARIOUS REYNOLDS AND STROUHAL NUMBERS

In this section, we give a general overlook of the vortex pairing phenomenon in axisymmetric laminar jets. After explaining the numerical simulation details, we show that, depending on the jet parameters and the forcing considered, vortex pairing can occur or not. When it does, we take a close look on a pairing sequence. Eventually, we finish with a parametric study to characterise its occurrence domain.

3.3.1 *Setup of direct numerical simulations*

Simulations were carried out using *NEK5000*, an incompressible spectral element code. A perfectly axisymmetric jet is described in cylindrical coordinates (z, r), z being the main flow direction and r being the radial distance from the jet axis. The flow is assumed to be governed by the incompressible axisymmetric Navier–Stokes equations with zero azimuthal velocity, written in dimensionless form as

$$\frac{\partial v}{\partial t} + v\frac{\partial v}{\partial r} + u\frac{\partial v}{\partial z} = -\frac{\partial p}{\partial r} + \frac{1}{Re}\left(\frac{1}{r}\frac{\partial}{\partial r}\left(r\frac{\partial v}{\partial r}\right) - \frac{v}{r^2} + \frac{\partial^2 v}{\partial z^2}\right), \tag{3.1a}$$

$$\frac{\partial u}{\partial t} + v\frac{\partial u}{\partial r} + u\frac{\partial u}{\partial z} = -\frac{\partial p}{\partial z} + \frac{1}{Re}\left(\frac{1}{r}\frac{\partial}{\partial r}\left(r\frac{\partial u}{\partial r}\right) + \frac{\partial^2 u}{\partial z^2}\right), \tag{3.1b}$$

$$\frac{1}{r}\frac{\partial (rv)}{\partial r} + \frac{\partial u}{\partial z} = 0, \tag{3.1c}$$

where the velocity $\mathbf{u}$ has axial and radial components u and v, and p denotes pressure. The jet diameter D and the inlet centerline velocity $\overline{U}$ are used to render the flow problem nondimensional, leading to a definition of the Reynolds number as $Re = \overline{U}D/\nu$, with ν the kinematic viscosity. The computational domain extends, unless specified otherwise, over 40×5 diameters in the axial and radial directions, respectively, and it is discretised with 17600 spectral elements, each containing 64 mesh points.

Boundary conditions are specified as follows. In the inlet plane, $z = 0$, a hyperbolic tangent velocity profile is imposed. Its amplitude is modulated in time as

$$\mathbf{u}(z=0,r,t) = \frac{1}{2}\left\{1-\tanh\left[\frac{1}{4\theta_0}\left(r-\frac{1}{4r}\right)\right]\right\}\left(1+A\cos\left(\omega_f t\right)\right)\mathbf{e}_z, \qquad (3.2)$$

where A is the forcing amplitude, $\theta_0 = 0.025$ is the initial non-dimensional shear layer thickness and ω_f is the forcing frequency. The forcing period is given by $T = 2\pi/\omega_f$, and the Strouhal number is defined as $St_D = \omega_f D/(2\pi\overline{U})$.

On the jet centreline, axisymmetric boundary conditions are imposed as

$$\frac{\partial u}{\partial r} = v = \frac{\partial p}{\partial r} = 0 \quad \text{at } r = 0. \qquad (3.3)$$

In the outlet plane, $z_{max} = 40$, and on the lateral boundary, $r_{max} = 5$, the standard outflow formulation provided by NEK5000 is employed. This prescribes a stress-free condition

$$\frac{1}{Re}\frac{\partial v}{\partial r} - p = \frac{\partial u}{\partial r} = 0 \text{ at } r = r_{max} \quad \text{and} \quad \frac{1}{Re}\frac{\partial u}{\partial z} - p = \frac{\partial v}{\partial z} = 0 \text{ at } z = z_{max}. \qquad (3.4)$$

The flow configuration is thus characterised by the Reynolds number Re, the Strouhal number St_D, the initial shear layer thickness θ_0 and the forcing amplitude A. A single value $\theta_0 = 0.025$ is used throughout this study.

3.3.2 *Two distinct behaviours*

Depending on flow parameters and forcing Strouhal number, rolled-up vortices may spontaneously undergo subsequent pairing. In the absence of free-stream turbulence, and if the harmonic forcing is well-controlled, this pairing takes place in a perfectly regular fashion.

In cases where pairing occurs, two neighboring vortices merge into one, such that the passage frequency of vortices downstream of the pairing location is exactly half that of the imposed forcing. An example, obtained by direct numerical simulation with parameters $Re = 2000$, $St_D = 0.6$ and $A = 5\%$, is shown in figure 3.2a. If the forcing is characterised by the time period T, the "paired state" is globally $2T$-periodic. The velocity field of a paired state will be denoted $\mathbf{u}^p$.

A different behaviour is observed when the Reynolds number is lowered to $Re = 1300$, as shown in figure 3.2b. Vortices roll up close to the nozzle and advect downstream, until they are dissipated by viscosity, but no spontaneous pairing is observed at this parameter setting. Such a flow state is globally T-periodic and will be called hereafter an "unpaired state". Its velocity field will be denoted $\mathbf{u}^u$.

When the natural time-asymptotic flow state for a given set of parameters involves pairing, it is still possible to recover an unpaired state as an alternative solution of the flow equations, by use of time-delayed feedback control (see section 3.4.1 and Shaabani-Ardali, Sipp, and Lesshafft (2017)). The unpaired state obtained in such a way for the previous configuration with $Re = 2000$ is shown in figure 3.2c. This solution is an exact solution of the Navier-Stokes equations without the time-delayed feedback.

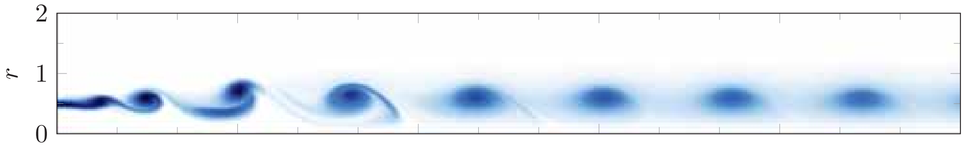

(a) Paired state ($2T$-periodic) at $St_D = 0.6$, $Re = 2000$ and $A = 5\%$ at $t = 3T/2$. This is the same state as in figure 3.3d.

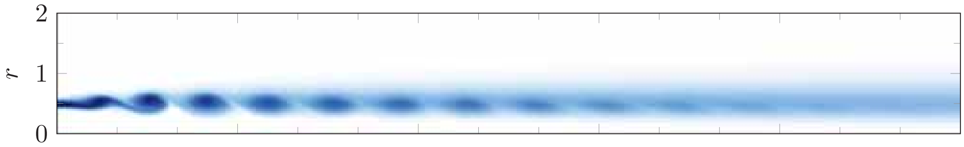

(b) Unpaired state (T-periodic) at $St_D = 0.6$, $Re = 1300$ and $A = 5\%$ at $t = T/2$.

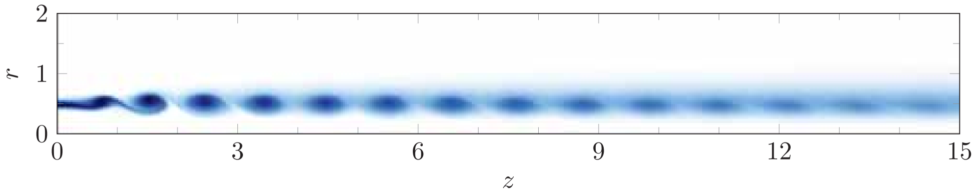

(c) Unpaired state (T-periodic) stabilised using time-delayed feedback control, defined in section 3.4.1, at $St_D = 0.6$, $Re = 2000$ and $A = 5\%$ at $t = T/2$.

Figure 3.2: Vorticity snapshots of the periodic paired and unpaired states, obtained naturally for two different parameter settings. Forcing amplitude, Reynolds and Strouhal numbers are defined in section 3.3.1.

3.3.3 *The dynamics of vortex pairing*

The process of the pairing of two vortices is inspected from snapshots of the vorticity, presented in figure 3.3, at four different phases of one pairing cycle. At $t = 0$ (figure 3.3a), two successive vortices, located around $z = 1$ and 2, have rolled up due to the primary shear instability. One half-cycle of the forcing period later (figure 3.3b), the leading vortex has slightly expanded radially, while the trailing one has contracted. This movement is accompanied by a deceleration of the expanding vortex, and inversely an acceleration of the contracting vortex, through the influence of the vortex ring radius on its self-induced propulsion. The same process continues at $t = T$ (figure 3.3c), when the trailing vortex begins to pass through the interior of the leading vortex. At $t = 3T/2$ (figure 3.3d), both vortices are in the process of merging into one, which is largely achieved at the end of the cycle (figure 3.3a).

Conceptual arguments for the occurrence of vortex pairing in the literature are typically based on the interaction between fundamental and subharmonic fluctuations, and the possibility of energy transfer to the latter (Monkewitz, 1988). Spatial energy variations of the fundamental ω_f and the subharmonic $\omega_f/2$ Fourier modes are readily extracted from the present numerical simulations. These are presented in figure 3.4, for the configuration $Re = 2000$, $St_D = 0.6$ and $A = 5\%$, in the form of radially integrated kinetic energy. This plot allows the distinction

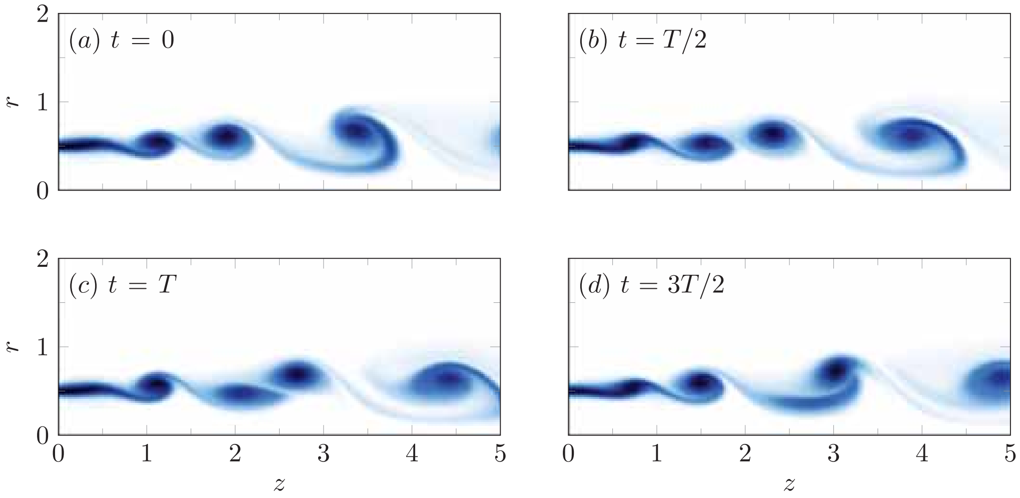

Figure 3.3: Vorticity snapshots of a paired case at $Re = 2000$ forced harmonically at $St_D = 0.60$ and $A = 5\%$. Only the region near the inlet is shown. The colour coding is the same as in figure 3.2c.

of various stages in the pairing process. Immediately downstream of the inlet, the fundamental mode grows from its forced initial amplitude to its peak value at $z = 1.4$. This streamwise position may be identified with the shedding of a fully formed vortex (see figure 3.3). The subharmonic component experiences strong exponential growth over the same interval, starting from a much lower level, as the boundary condition imposes zero amplitude at the inlet. Subharmonic growth continues down to $z = 3.1$, where figure 3.3(*d*) shows strong pairing dynamics. The energy of the fundamental mode decreases over the distance $1.4 < z < 3.1$, although a local maximum is found at the peak location of the subharmonic mode. As pairing is accomplished, at $z > 3.1$, both the fundamental and the subharmonic mode decay slowly in z, both at a similar rate, due to viscous dissipation of the convecting vortices.

Consistent with these observations, Monkewitz (1988) argued that a growth of subharmonic perturbations must be fed by energy transfer from the fundamental mode, which requires that both modes propagate at the same phase velocity. Phase velocities of fundamental and subharmonic fluctuations in the present simulation are compared in figure 3.5 as solid and dashed lines. The reported phase velocities are measured, for each streamwise location, at the radial distance where each respective Fourier mode has its maximum amplitude along r. The values for both modes match quite closely throughout the relevant interval upstream of the pairing location. They continue to match in the downstream region, but this is only the result of the fundamental mode being slaved to its subharmonic counterpart as a passive harmonic.

For comparison, energy and phase velocity results obtained for the fundamental mode of the corresponding stabilised (unpaired) flow are also presented in figures 3.4 and 3.5 (dotted lines), alongside the values found in the paired state. Upstream of the roll-up location, the fundamental modes show identical energy growth in both configurations. Between the roll-up and the pairing locations, the fundamental energy decay in the paired case is stronger than in the unpaired case,

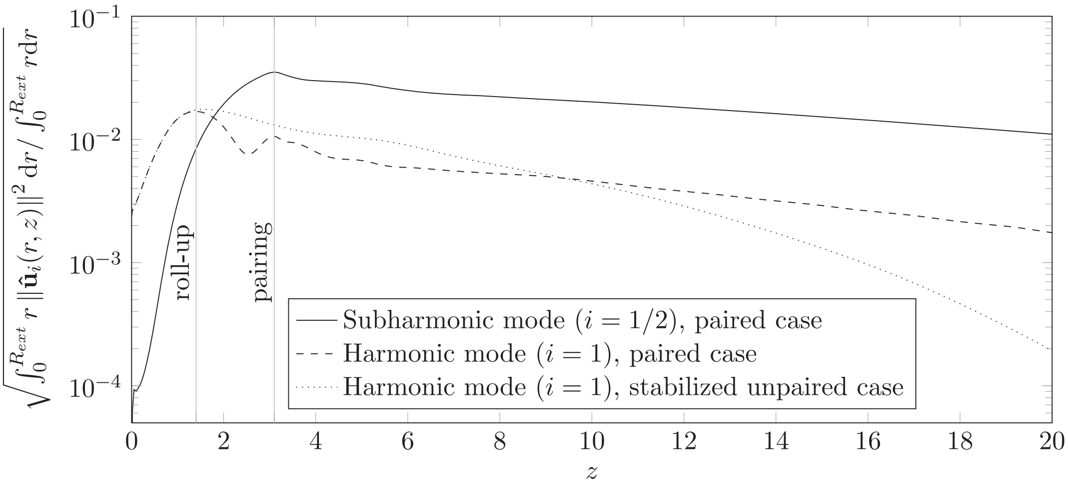

Figure 3.4: Total energy of the fundamental $\hat{\mathbf{u}}_1$ and subharmonic $\hat{\mathbf{u}}_{1/2}$ Fourier components in each plane $z = const.$ as a function of z at $St_D = 0.6$, $Re = 2000$ and $A = 5\%$.

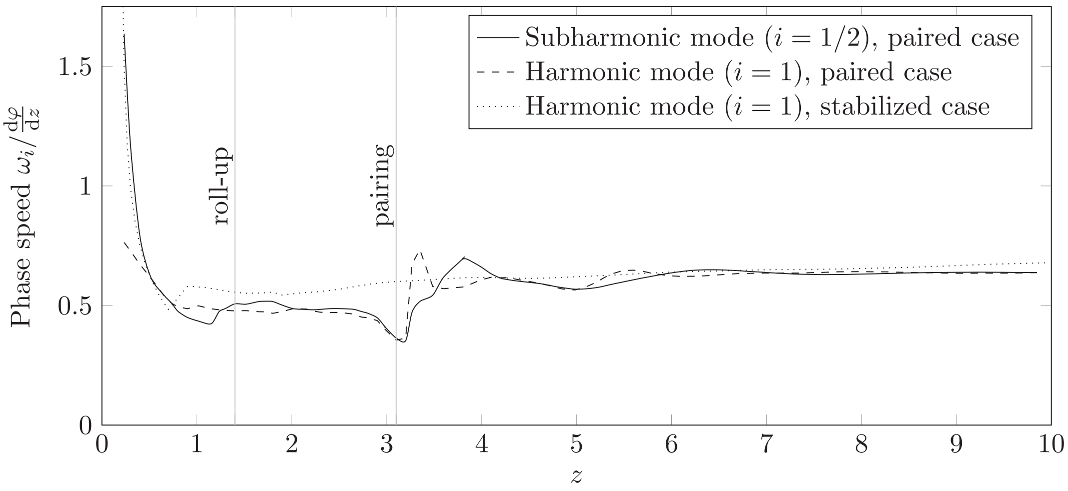

Figure 3.5: Phase speed along the line of maximum subharmonic mode of the subharmonic and fundamental modes of a paired jet at $(Re = 2000, St_D = 0.60)$, and comparison with the phase speed of the fundamental mode along the lime of maximum fundamental mode of the corresponding stabilised (unpaired) jet. The phase of the Fourier mode is denoted as φ.

which again indicates that the growth of subharmonic perturbations feed on the energy of the fundamental mode. However, downstream of the pairing location, the fundamental mode in the stabilised case decays significantly faster, and at an increasing rate. This difference is also visible when one compares figures 3.2a and 3.2c: it appears that the lower frequency and the stronger circulation of the paired vortices hinders their diffusion and allow them to be sustained longer. When comparing the phase velocities in figure 3.5, it is seen that the unpaired fundamental mode propagates faster than its paired counterpart upstream of the pairing location, whereas their velocities are again equal in the downstream region. The discrepancy upstream of the pairing can be linked to different positions of the vortices: in the paired case, the vortices are radially more expanded than in the unpaired case,

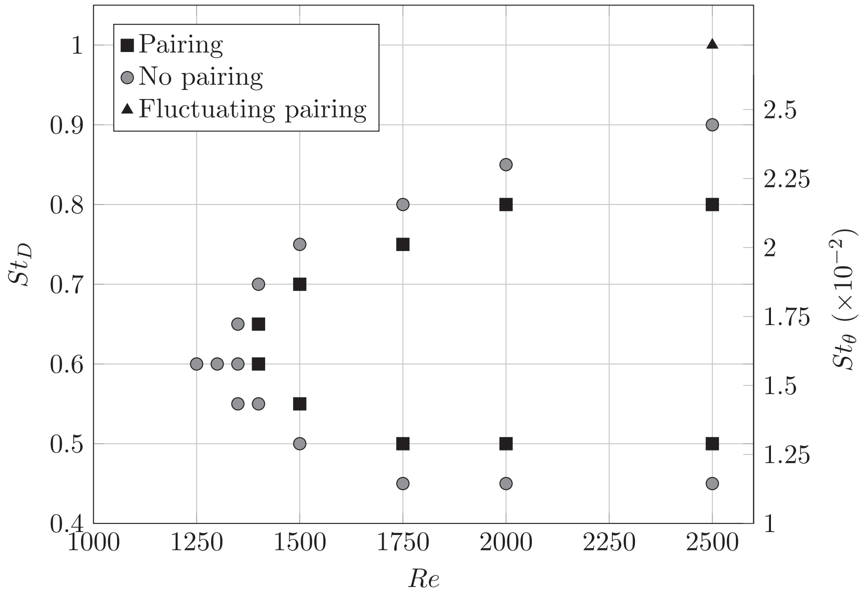

Figure 3.6: Occurrence of vortex pairing as a function of Reynolds number and Strouhal number for configurations with forcing amplitude $A = 5\%$ and initial shear layer thickness $\theta_0 = 0.025$. Only points near the pairing boundary are represented.

therefore moving at a slower speed. Vortex pairing does not only influence the flow downstream, but also upstream.

3.3.4 *Parametric study*

All simulations presented in this section were carried out on a reduced domain with $z_{max} = 15$ in order to save computational resources. Test runs with $z_{max} = 40$ were performed for selected cases, showing no effect of domain truncation on the results presented here.

3.3.4.1 *Effect of Reynolds number and Strouhal number*

The effect of Reynolds and Strouhal numbers on the onset of vortex pairing is investigated first, for a fixed forcing amplitude $A = 5\%$. Direct numerical simulations were run, first in an exploratory fashion for many (Re, St_D) combinations. After an initial transient phase, the flow settles into an asymptotic time-periodic state. Asymptotic states that involve regular vortex pairing were found in a restricted region in the (Re, St_D) plane, and the boundary of that region was then determined more accurately by running simulations well into the asymptotic regime. Results of these simulations are mapped in figure 3.6. Pairing is found to occur first around a critical Reynolds number $Re_c = 1375$, for the fundamental forcing Strouhal number $St_D = 0.6$. Up to $Re = 2500$, the maximum value considered in this study, vortex pairing at asymptotic times is restricted to the band $0.5 \leq St_D \leq 0.8$. With increasing Reynolds number, the pairing becomes more vigorous, and its location gradually shifts nearer to the inlet.

Close to the instability thresholds, it becomes difficult to precisely characterise the flow behaviour, because of the long simulation times needed to achieve convergence. When the Reynolds number is about 1350, computations were run on full-length domains ($40D$), and even after several hundred forcing periods, the paired or unpaired nature of the final flow state cannot be determined. For instance, at $St_D = 0.6$, the final state for $Re = 1350$ is unpaired, for $Re = 1400$ it is paired. For intermediate values $Re = 1360$, 1372 or 1375 (close to threshold $Re_c = 1371$ predicted in section 3.4.4), the pairing location moves gradually downstream as time evolves, but with no indication whether it will eventually become stationary. These ambiguous data points are not displayed in figure 3.6.

As mentionned in section 3.2.1, a first parametric study of vortex pairing in terms of Reynolds and Strouhal numbers has been carried out experimentally by Zaman and Hussain (1980), for Reynolds numbers greater than 10^4 and thin initial mixing layer $\theta/D \approx 0.25\%$). They found that pairing could occur in *two* frequency bands, one characterised by a Strouhal number $St_\theta = f\theta/U$ based on the shear layer thickness, the other by a Strouhal number $St_D = fD/U$ based on the jet diameter. Pairing has been reported for St_θ around 0.012 and for $0.75 \leq St_D \leq 1.0$. With our choice of the initial shear layer thickness being 5% of the diameter, these two regimes are only weakly separated, which explains why our findings of a single band of instability at a given Reynolds is coherent; both scalings are indicated in figure 3.6.

Again for Reynolds numbers greater than 10^4, and for a 5% forcing amplitude, Broze and Hussain (1994), found several flow regimes depending on St_D (see figure 3.1): no pairing for $St_D < 0.52$, aperiodic modulations and coexistence of different states (stable or modulated pairing) for $0.52 < St_D < 0.77$, stable pairing for $0.77 < St_D < 0.97$, stable pairing with quarter-harmonic modulations for $0.97 < St_D < 1.02$ and stable double pairing for $St_D > 1.02$, with some intermittent cases. The St_θ-dependance is not documented in that study. In our computations, we do not encounter such a richness of scenarios, because our inlet condition is fully laminar and time-periodic, and because our Reynolds number is one decade lower; however, the occurrence of pairing, reported in figure 3.6, is consistent with the experiments of Broze and Hussain (1994). Multiple stages of successive pairing are never observed in our computations, even at $St_D > 1$. This difference with respect to the experiments is certainly owing to the lower Reynolds number, as Cheng, Lou, and Lim (2015) demonstrated that viscosity inhibits pairing. However, the modulated states described by Broze and Hussain (1994) for $St_D \approx 1$ may be linked to our observation of fluctuations of the pairing position (triangle in figure 3.6).

Cheng, Lou, and Lim (2015) investigated the leapfrogging of coaxial vortex rings: for a system of two adjacent vortices, these authors carried out a parametric study, computing the occurrence of this phenomenon as a function of Reynolds number and vortex separation. The Reynolds number, defined as the ratio of the ring vorticity over the viscosity and chosen of the order of 10^3 is related to the product between Reynolds and Strouhal numbers in our present notation. The ratio of the vortex spacing and the ring radius is related to the inverse of the Strouhal number as defined here. Cheng *et al.* found that leapfrogging occurs only above

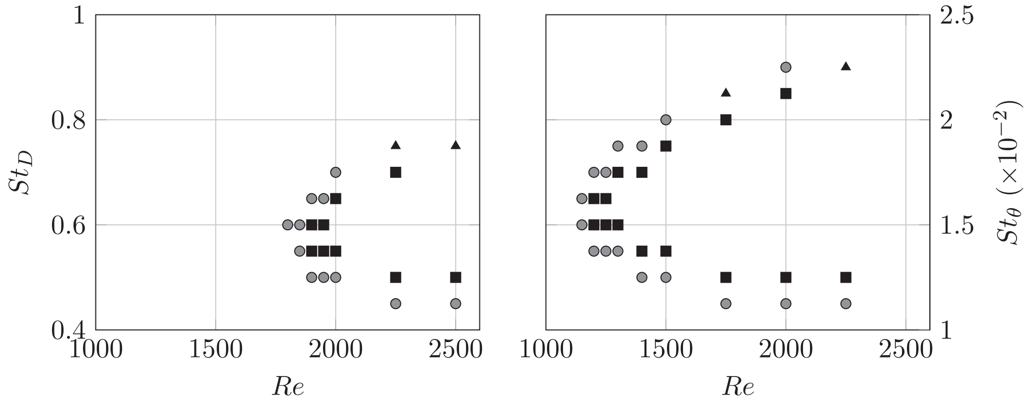

(a) $A = 1\%$.

(b) $A = 10\%$.

Figure 3.7: Occurrence of vortex pairing as a function of the Reynolds and the Strouhal number for two different forcing amplitudes $A = 1\%$ and 10%. The same symbols as in figure 3.6 are used.

a critical Reynolds number, and for a narrow Strouhal band that increases with Reynolds number. This is consistent with our findings (figure 3.6), as pairing can be understood as an advanced stage of leapfrogging (figure 3.3).

3.3.4.2 *Effect of forcing amplitude*

The effect of forcing amplitude is investigated by including computations with two additional values, $A = 1\%$ and 10%. Instability maps in the (Re, St_D) plane for these configurations are displayed in figures 3.7a and 3.7b. An increase in the forcing amplitude is seen to shift the onset of pairing towards lower Reynolds number values.

Another effect of increasing A is to move the roll-up and pairing locations upstream, as can be seen in figure 3.8. In the same way as discussed for figure 3.4, the energy of the fundamental mode in all cases grows from the inflow towards its maximum at the roll-up location, whereas the subharmonic mode peaks at the location of pairing. Increasing the fundamental amplitude at the inflow reduces the distance needed before roll-up, and it catalyses the subharmonic mode, inducing an earlier pairing.

However, by comparing the difference between the modes at $A = 1\%$ and 5%, and between the modes at $A = 5\%$ and 10% in figure 3.8, it is anticipated that a further increase in A will only marginally change the paired flow behaviour. This is consistent with Broze and Hussain (1994): as shown in figure 3.1, increasing the forcing amplitude above 5% does not induce significant topological changes in the final state, but below 1% forcing, no stable pairing is observed in the experiments. Raman and Rice (1991) also found that a critical minimal amplitude of the fundamental forcing was required to trigger pairing. Therefore, an expansion of the study to *lower* amplitude levels $A < 1\%$ could be of interest; however, this would require higher values of Re to be considered, rendering the assumption of laminar flow increasingly doubtful.

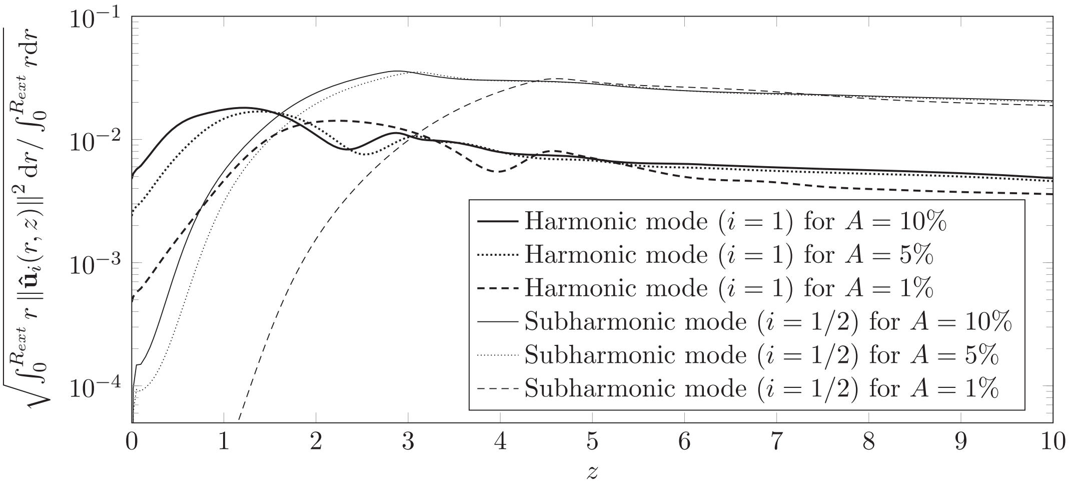

Figure 3.8: Total energy of the fundamental and subharmonic modes in each plane $z = const$ as a function of z at $St_D = 0.6$ and $Re = 2000$. Three values of the inlet forcing amplitude are considered, $A = 1\%$, 5% and 10%.

In their leapfrogging study of two vortex rings, Cheng, Lou, and Lim (2015) varied the vortex thickness, and thereby the vortex concentration, which is similar to varying the amplitude of forcing. Consistent with the present study, they concluded that stronger vortices undergo pairing at lower Reynolds numbers.

3.3.4.3 *Effect of inlet noise*

In configurations where vortex pairing does not arise intrinsically, the flow may still be receptive to low-level subharmonic extrinsic perturbations, in the sense of a "slightly damped oscillator" (Huerre and Monkewitz, 1990), and exhibit vortex pairing in their presence. In the following, this receptivity is probed by imposing a random noise in addition to the fundamental forcing at the inlet, such that the inflow condition is prescribed as

$$\mathbf{u}(r,t) = \frac{1}{2}\left\{1 - \tanh\left[\frac{1}{4\theta_0}\left(r - \frac{1}{4r}\right)\right]\right\}\left(1 + A\cos\left(\omega_f t\right) + \epsilon_{noise}(t)\right)\mathbf{e_z}, \quad (3.5)$$

with ϵ_{noise} a white noise, constant in r, with a specified standard deviation. Four Reynolds number values are selected, $Re = 500$, 750, 1000 and 1300, and two values of the standard deviation $A_\epsilon = \sqrt{\langle \epsilon_{noise}, \epsilon_{noise} \rangle} = 0.1\%$ and 1% are tested. The latter are chosen such as not to exceed the level of coherent forcing A. The fundamental forcing in all cases is prescribed with $St_D = 0.6$ and $A = 5\%$.

Four distinct types of the flow response are observed:

1. At low Reynolds number, the noise barely impacts the flow behaviour. For instance, at $Re = 500$ and for both noise levels, no significant departure from the purely harmonically forced jet is observed.

2. The noise induces a subharmonic modulation of the vortices, but the flow diffuses too quickly for pairing to occur, for instance in the case $Re = 750$ and $A_\epsilon = 0.1\%$.

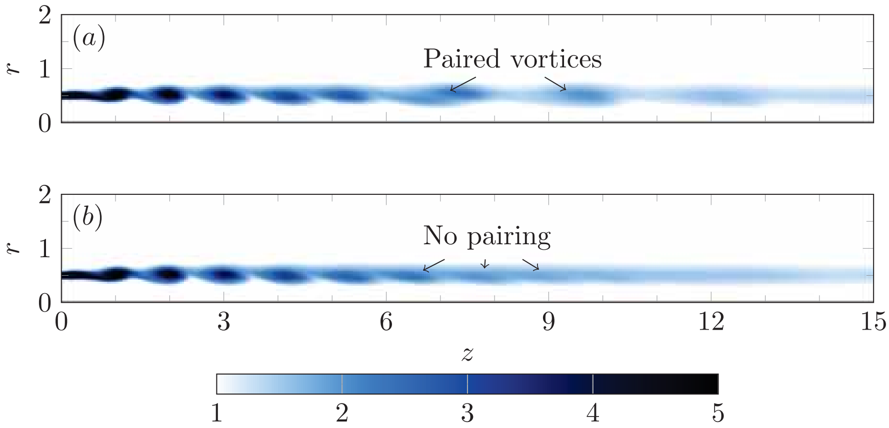

Figure 3.9: Vorticity snapshots at $Re = 750$, $St_D = 0.60$ and $A = 5\%$ with $A_\epsilon = 1.0\%$ taken at two different times, and both at the same phase. Pairing is intermittent, occurring in (a) and not in (b). The colorbar is rescaled compared to figure 3.2b, to magnify the behaviour of downstream vortices.

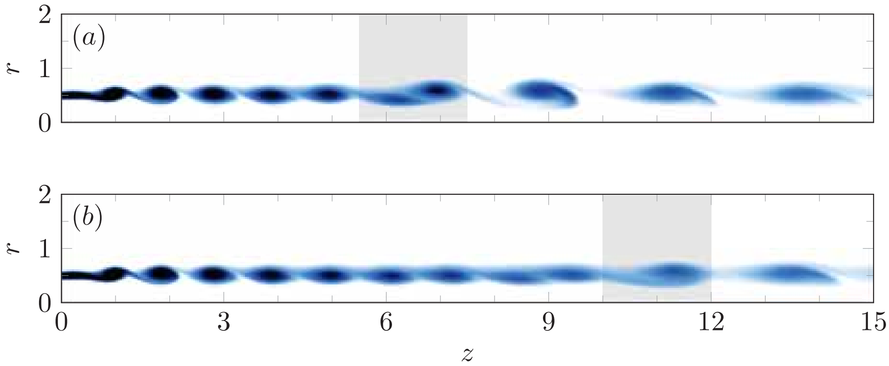

Figure 3.10: Vorticity snapshots at $Re = 1300$ and $St_D = 0.60$ with $A_\epsilon = 0.1\%$ taken at two different times, and both at the same phase. This shows the pairing location fluctuation, emphasised in grey, in this setup. The colorbar is in figure 3.9.

3. Intermittent pairing is triggered, for instance at $Re = 1000$ and $A_\epsilon = 0.1\%$, or at $Re = 750$ and $A_\epsilon = 1.0\%$ (figure 3.9). In the latter case, pairing occurs far downstream, where the vortices are indistinct due to diffusion.

4. Continuous pairing is sustained by noise input, but its location fluctuates in time. This is observed for $Re = 1000$ with $A_\epsilon = 1\%$, and for $Re = 1300$ with $A_\epsilon = 0.1\%$ (figure 3.10) as well as 1.0%. As described experimentally by Ho and Huang (1982) and Husain and Hussain (1989), other phenomena such as *shredding*, where one single vortex “escapes” between two successful pairing events, or *collective interaction*, where more than two vortices interact at once, can be observed, for instance in figure 3.11.

3.4 VORTEX PAIRING AS AN UNSTABLE GLOBAL FLOQUET MODE

In this section, it is investigated whether the onset of vortex pairing can be described as the manifestation of a global Floquet instability of the periodic unpaired state.

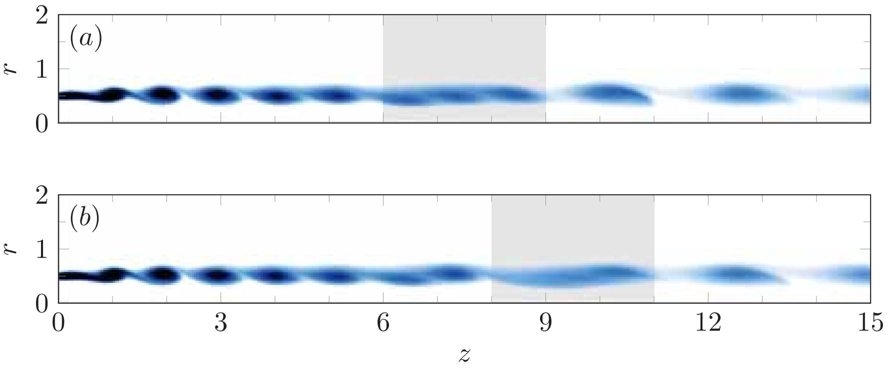

Figure 3.11: Vorticity snapshots at $Re = 1000$ and $St_D = 0.60$ with $A_\epsilon = 1.0\%$: (b) is taken two forcing periods after (a). The three vortices located in the shaded are on (a) merge altogether, as an example of collective interaction. The colorbar is in figure 3.9.

This unpaired state must first be computed for a given combination of flow parameters (section 3.4.1). After a short reminder of Floquet theory (section 3.4.2), and a presentation of the numerical implementation (section 3.4.3), the linear Floquet stability of the unpaired vortex street is analysed (section 3.4.4), and the instability characteristics are compared to the observations documented in the previous section.

3.4.1 *Computation of T-periodic states without vortex pairing*

Periodic flow states are obtained through direct numerical simulation, as described in section 3.3.1. In order to suppress vortex pairing in configurations where it naturally arises, subharmonic fluctuations are actively damped by means of time-delayed feedback control. A short description of this method follows, for details the reader is referred to Shaabani-Ardali, Sipp, and Lesshafft (2017).

A fully synchronised *paired* state can be decomposed into one component that is T-periodic and another that is only $2T$-periodic,

$$\mathbf{u}^p(\mathbf{x},t) = \sum_n \mathbf{u}_n^T(\mathbf{x}) \exp\left(\mathrm{i}n\omega_f t\right) + \sum_n \mathbf{u}_n^{2T}(\mathbf{x}) \exp\left(\mathrm{i}\frac{2n+1}{2}\omega_f t\right), \quad \text{with} \quad n = 0, \pm1, \pm2, \dots, \pm N. \tag{3.6}$$

In a T-periodic *unpaired* state, the second sum is zero. Time-delayed feedback control is applied by adding a forcing term of the form

$$\mathbf{f} = -\lambda(\mathbf{u}(t) - \mathbf{u}(t-T)) \tag{3.7}$$

to the right-hand side of the governing equations (3.1a)–(3.1c). Such forcing attenuates all $2T$-periodic fluctuations, but leaves T-periodic components unaffected. The simulations converge towards a purely T-periodic state, in which the artificial forcing term vanishes. This solution is therefore a full solution of the Navier-Stokes equations. An example of such a stabilised unpaired state is shown in figure 3.2c.

The value of λ in equation (3.7) affects the convergence of the stabilisation procedure. In a previous publication (Shaabani-Ardali, Sipp, and Lesshafft, 2017), it has been demonstrated that very small values of λ do not lead to convergence, as the resulting damping is insufficient to counteract the natural instability of the system. Similarly, too large values of λ result in overshooting of the damping force, which also inhibits convergence. An optimal value $\lambda = 0.0432\omega_f$ was derived from a model problem, and has been used in the present calculations.

3.4.2 *Floquet framework*

The Floquet stability problem for a T-periodic unpaired base flow $(\mathbf{U}^{\mathbf{u}}(t), P^u(t))$ is set up by superposing small-amplitude perturbations $(\mathbf{u}', p')$, which are governed to leading order by the linear equations

$$\frac{\partial \mathbf{u}'}{\partial t} + \left(\mathbf{U}^{\mathbf{u}}(t)\cdot\nabla\right)\mathbf{u}' + \left(\mathbf{u}'\cdot\nabla\right)\mathbf{U}^{\mathbf{u}}(t) = -\nabla p' + \frac{1}{Re}\Delta\mathbf{u}', \qquad \nabla\cdot\mathbf{u}' = 0. \tag{3.8}$$

The following boundary conditions are implemented. In the inlet plane, the flow is unperturbed, $\mathbf{u}'(r, z = 0, t) = \mathbf{0}$. We do not allow perturbations directly at the inlet, since we consider only the behaviour of *intrinsic* perturbations. On the centreline of the jet, $r = 0$, axisymmetric boundary conditions as in the nonlinear case are imposed, $\partial_r u' = v' = \partial_r p' = 0$. In the outlet plane $z = 40$ and on the lateral boundary $r = 5$, stress-free conditions (3.4) are chosen.

The equations are written in compact form as

$$\frac{\partial \mathbf{q}'}{\partial t} = \mathcal{L}(t)\mathbf{q}', \tag{3.9}$$

where $\mathbf{q}' = (\mathbf{u}', p')$ represents the perturbation state vector.

According to Floquet theory (Floquet, 1883), one may seek modal solutions of (3.9) in the form

$$\mathbf{q}'(t) = P(t)e^{At}\mathbf{q}'(0), \tag{3.10}$$

with $P(t)$ a T-periodic and A a constant matrix. Noting that

$$\mathbf{q}'(T) = e^{AT}\mathbf{q}'(0), \tag{3.11}$$

due to $P(T) = P(0) = Id$, the time-shift operator $\Phi = e^{AT}$ is introduced, such that

$$\mathbf{q}'(nT) = \Phi^n\mathbf{q}'(0). \tag{3.12}$$

The eigenvalues μ_i of Φ are known as *Floquet multipliers*, and the associated eigenmodes v_i are the *Floquet modes* of the system (3.9). For a modal perturbation $\mathbf{q}'(0) = (\tilde{\mathbf{v}}_{\mathbf{i}}, \tilde{p}_i)$, the Floquet multiplier μ_i such that $\mathbf{q}'((n+1)T) = \mu_i\mathbf{q}'(nT)$ represents the complex amplitude gain over one cycle period. Therefore, the stability of the system is indicated by the modulus of μ_i: if all Floquet multipliers have a modulus lower than unity, all perturbations decay at long time and the system is stable. Floquet modes with an associated $|\mu_i| > 1$ experience exponential temporal growth.

The complex phase of a Floquet multiplier, $\arg(\mu_i)$, characterises the time-periodicity of its associated mode. At zero phase, the mode evolves with the same periodicity as the base flow, and may be qualified as being *harmonic*. A phase of $\arg(\mu_i) = \pi$, indicates that two base flow periods are needed to complete one perturbation cycle, and the mode therefore evolves as $\omega_f/2$. Such a mode is qualified as being *subharmonic*. As vortex pairing is a $2T$-periodic phenomenon, subharmonic Floquet modes are expected to arise. Floquet multiplier phases that are not integer multiples of π characterise modes with periodicities unrelated to that of the base flow.

A standard result of Floquet theory applied to the linearised Navier-Stokes equations is that the time derivative of the base flow, $(\partial_t \mathbf{U}^{\mathbf{u}}, \partial_t P^u)$, represents a neutral Floquet mode of the system, with $\mu = 1$. However, such a mode does not exist in the present problem, because it is inconsistent with the boundary conditions. While the base flow is periodically forced at the inlet boundary, according to equation (3.2), linear perturbations are prescribed to be zero there.

3.4.3 *Numerical implementation*

The evolution of the linearised system (3.9) is calculated using a fully implicit finite-difference time-stepping scheme of second order implemented in FreeFem++ (Hecht, 2012). The mesh has the same size and resolution as the one used in the NEK5000 calculations. $P2$ finite elements are used for the velocity perturbation whereas $P1$ finite elements are used for the pressure.

In the numerical implementation of the Floquet mode calculation, only the velocity perturbation $\mathbf{u}'$ is considered. This is possible in incompressible flow, since the full state $\mathbf{q}' = (\mathbf{u}', p')$ is fully determined by $\mathbf{u}'$ alone. Therefore, the standard projection operator $P_{\mathbf{q}\to\mathbf{u}}$ from the $\mathbf{q}$-space to the $\mathbf{u}$-space can be defined, as well as its inverse $P_{\mathbf{u}\to\mathbf{q}}$. The operator $\Phi' = P_{\mathbf{q}\to\mathbf{u}} \Phi P_{\mathbf{u}\to\mathbf{q}}$ maps a given velocity perturbation to its value after one flow period. The modal stability properties of Φ' are the same as those of Φ, and Φ' will be considered in what follows.

By use of a block-Arnoldi method (Saad, 2011), it is possible to construct a matrix representation of Φ' in a reduced orthonormal basis, generated by power iterations. A N_{vec}-vector block-Arnoldi is iterated over N stages, each stage consisting in time-integration of the linear flow equations over one flow period. Contrary to the standard Arnoldi algorithm, where the image of only one vector is calculated in each iteration stage, N_{vec} vectors are advanced simultaneously in the block-Arnoldi method. A value $N_{vec} = 30$ was used in all calculations presented in this section. Eigenvalues of the resulting matrix, of reduced dimension $NN_{vec} \times NN_{vec} = 750 \times 750$, may then be obtained. Concretely, the algorithm involves the following steps:

1. An orthonormal basis of N_{vec} initial velocity perturbation vectors $\hat{\mathbf{u}}_i^0$ is built, with $i = 1, \ldots, N_{vec}$. Orthonormalisation of these vectors with respect to the energy scalar product

$$\langle \mathbf{u}, \mathbf{v} \rangle = \iint_\Omega r \mathbf{u}(r,z) \cdot \mathbf{v}(r,z) \mathrm{d}r \mathrm{d}z \tag{3.13}$$

   is enforced.

2. At iteration $n \in [1, N-1]$, the images $\Phi \hat{\mathbf{u}}_i^{n-1}$ of each vector $\hat{\mathbf{u}}_i^{n-1}$ after one flow period are computed simultaneously by time-stepping.

3. The Gram–Schmidt algorithm is employed to extract and normalise the component $\hat{\mathbf{u}}_i^n$ of $\Phi' \hat{\mathbf{u}}_i^{n-1}$ for $1 \leq i \leq N_{vec}$ that is orthogonal to the already existing set of vectors $\{\hat{\mathbf{u}}_{i'}^j\}$, with $1 \leq i' \leq N_{vec}$ when $0 \leq j \leq n-1$ and $1 \leq i' < i$ when $j = n$. Thereby, the orthonormal basis $\{\hat{\mathbf{u}}_i^j\}$ is augmented by dimension N_{vec} in every iteration n.

4. In the end, after N iterations over one flow period, a fully orthonormal Krylov basis $\{\hat{\mathbf{u}}_i^0, \ldots, \hat{\mathbf{u}}_i^{N-1}\}$ and their images $\{\Phi' \hat{\mathbf{u}}_i^0, \ldots, \Phi' \hat{\mathbf{u}}_i^{N-1}\}$ after one period of time-stepping are obtained. Let R denote the matrix of this basis,

$$R = \left[\hat{\mathbf{u}}_1^0, \ldots, \hat{\mathbf{u}}_{N_{vec}}^0, \ldots, \hat{\mathbf{u}}_1^{N-1}, \ldots, \hat{\mathbf{u}}_{N_{vec}}^{N-1} \right], \tag{3.14}$$

which is of dimension $N_{dof} \times N N_{vec}$, with N_{dof} the number of degrees of freedom of the initial velocity perturbation. It is then possible to construct the projection $\tilde{\Phi}$ of the infinite-dimensional operator Φ' onto the finite-dimensional space spanned by R. $\tilde{\Phi}$ is represented by the matrix

$$\tilde{\Phi}_{n N_{vec}+i, n' N_{vec}+i'} = \langle \Phi' \hat{\mathbf{u}}_{i'}^{n'}, \hat{\mathbf{u}}_i^n \rangle \quad \text{or} \quad \tilde{\Phi} = R^T M \left(\Phi' R \right), \tag{3.15}$$

with M the mass matrix associated with the scalar product (3.13).

5. By computing the eigenvalues μ_k and eigenvectors $\boldsymbol{\alpha}^k$ of $\tilde{\Phi}$, defined such as $\dim(\boldsymbol{\alpha}^k) = N N_{vec}$, the Floquet multipliers μ_k are obtained directly, and the Floquet modes $\mathbf{v}_k$ can be reconstructed as

$$\mathbf{v}_k = \sum_{n=0}^{N-1} \sum_{i=1}^{N_{vec}} \alpha_{n N_{vec}+i}^k \hat{\mathbf{u}}_i^n = R \boldsymbol{\alpha}^k. \tag{3.16}$$

As pointed out by Saad (2011), the orthonormalisation step (iii) is essential for the recovery of non-dominant eigenmodes in the n^{th} iteration amidst the numerical noise on the level of round-off error.

The above algorithm is designed to maximise numerical efficiency in combination with a linear flow solver based on implicit time-stepping. As the base flow is time-dependent, a linear operator is constructed and factorised at each time step. It would not be economical to use this factorised operator for the time advancement of one single state vector; by use of the block-Arnoldi method, N_{vec} vectors can be advanced in time simultaneously, thus lowering significantly the numerical burden of constructing a high-dimensional Krylov subspace.

A minimum of $N = 25$ flow-period iterations has been used to generate the following results. This number was increased in steps of 5 as necessary in order for the dominant eigenvalue to converge to four significant digits.

The list of all examined flow configurations is given in table 3.1; the influence of the Reynolds number, the Strouhal number and the forcing amplitude may thus be characterised. For high values of St_D, a larger number of block-Arnoldi iterations are required in order to achieve convergence. Two competing time scales characterise the dynamics: the forcing period, which decreases with increasing St_D, and the convection time, which is constant in all cases. Therefore, a constant number of iterations at high Strouhal number corresponds to a shorter convection time.

Re	St_D	A	N	Re	St_D	A	N	Re	St_D	A	N
500	0.60	5%	25	1750	0.60	5%	25	2000	0.85	5%	35
750	0.60	5%	25	2000	0.60	5%	25	2000	0.90	5%	40
1000	0.60	5%	25	2250	0.60	5%	25	2000	0.95	5%	40
1300	0.60	5%	25	2000	0.45	5%	25	2000	1.00	5%	40
1350	0.60	5%	25	2000	0.50	5%	25	2000	1.10	5%	45
1375	0.60	5%	25	2000	0.70	5%	30	2000	0.60	1%	25
1400	0.60	5%	25	2000	0.75	5%	35	2000	0.60	10%	25
1500	0.60	5%	25	2000	0.80	5%	35				

Table 3.1: Parameter combinations for which Floquet analysis is performed.

3.4.4 *Floquet instability modes*

As shown in table 3.1, nearly all calculations have been performed for constant forcing amplitude $A = 5\%$, and with fixed values of either $St_D = 0.6$ or $Re = 2000$, in order to track the isolated influence of Strouhal and Reynolds number on the instability behaviour. In nearly all cases, one strictly subharmonic Floquet mode is identified, characterised by a negative real Floquet multiplier μ. This mode is observed to be unstable over certain ranges of St_D and Re, where μ falls below -1. The absolute value $|\mu| = -\mu$ for $St_D = 0.6$ and $A = 5\%$ is plotted as a function of Re in figure 3.12a: by linear interpolation of the critical Reynolds at which $\mu_c = -1$, instability in this case is found to arise for $Re \geq 1371$. This is to be compared to the critical band $Re \in [1350; 1400]$, above (resp. below) which sustained pairing was found to occur (resp. not to occur) in the DNS, as discussed in section 3.3.4.1. The paired and unpaired regimes, as identified in the DNS, are indicated in figure 3.12a by black and grey bars, in order to highlight the agreement with the onset of subharmonic Floquet instability.

Results for variations in St_D, at fixed values $Re = 2000$ and $A = 5\%$, are presented in the same manner in figure 3.12b. A finite band of subharmonically unstable Strouhal numbers is identified, again in agreement with the prevalence of vortex pairing as observed in the DNS. Two values of μ reported in this diagram are distinct from the others: at $St_D = 0.75$, the Floquet multiplier of the most unstable mode appears as a complex conjugate pair with small imaginary parts, as indicated in the figure. This mode is therefore nearly subharmonic, but not strictly so, and further iterations of the block-Arnoldi procedure do not change this result. Higher deviations from the negative real axis are found in the stable case $St_D = 0.9$. For $St_D = 0.75$, the unstable mode is slightly detuned, but the DNS does not display any irregular behaviour.

The effect of the forcing amplitude A on the instability is demonstrated for a single setting $Re = 2000$ and $St_D = 0.6$. As shown in table 3.2, a higher amplitude leads to stronger instability, consistent with the DNS observations discussed in section 3.3.4.2. Vortex pairing was found to occur in all three configurations.

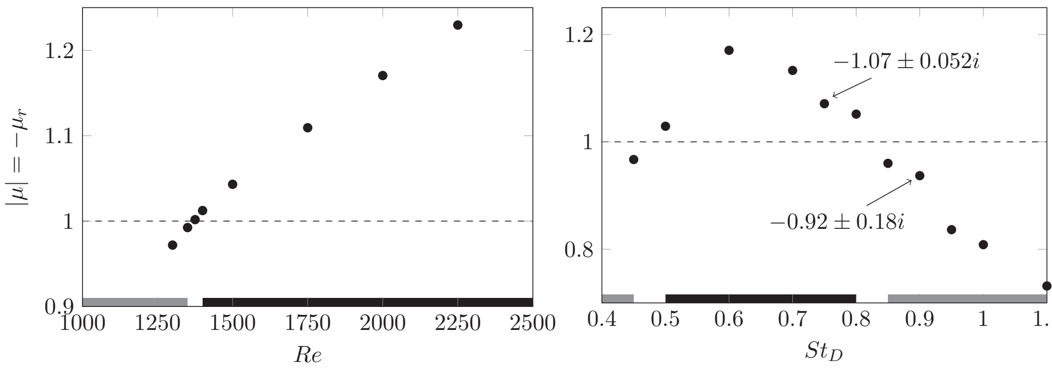

(a) $St_D = 0.6$.

(b) $Re = 2000$.

Figure 3.12: Absolute value of the dominant subharmonic Floquet multiplier for different (Re, St_D), obtained for $A = 5\%$. When the system is unstable, the most unstable mode is always subharmonic (e.g. real negative), except for the two labeled cases in (b), where the most unstable mode is almost subharmonic. When the system is stable, the represented mode are the least stable of the subhamonic domain. Black and grey bars represent parameter regimes with and without vortex pairing, according to uncontrolled DNS (see figure 3.6).

Forcing amplitude	1%	5%	10%
Most unstable Floquet multiplier	$-1.06 \pm 0.069i$	-1.17	-1.19

Table 3.2: Evolution of the most unstable Floquet multiplier with the forcing amplitude for $Re = 2000$ and $St_D = 0.60$.

The spatial shape of an unstable subharmonic Floquet mode is presented in figure 3.13, for parameters $Re = 2000$, $St_D = 0.6$ and $A = 5\%$, associated with an unstable Floquet mode $\mu = -1.17$. A snapshot of perturbation vorticity is shown. Its axial wavelength corresponds to twice the spacing between vortices in the unpaired base flow, and its amplitude maximum occurs far downstream, around $z = 20$. The latter seems rather surprising, because the base flow vortices at this position are already quite diffuse, as can be seen in figure 3.2c. Furthermore, vortex pairing in the unstabilised flow is observed around $z = 3$.

In order to demonstrate the effect of this modal shape onto the unpaired base flow, the two are superposed, with a perturbation amplitude that is chosen *ad hoc*. The resulting vorticity field is shown in figure 3.14. It is seen that the perturbation indeed displaces the vortices around $z = 20$ in a fashion that indicates pairing. However, the picture is very distinct from that of the fully developed paired state shown in figure 3.2a.

It might be speculated that a different, non-dominant Floquet mode could be responsible for the onset of pairing. Indeed, a second unstable mode exists at this parameter setting, characterised by a Floquet multiplier value $-1.03 \pm 0.14i$, and its vorticity distribution is given in figure 3.15. It displays the same spatial pattern as the first Floquet mode, but shifted several diameters further downstream, and this shift presumably accounts for its weaker growth. As this mode is not

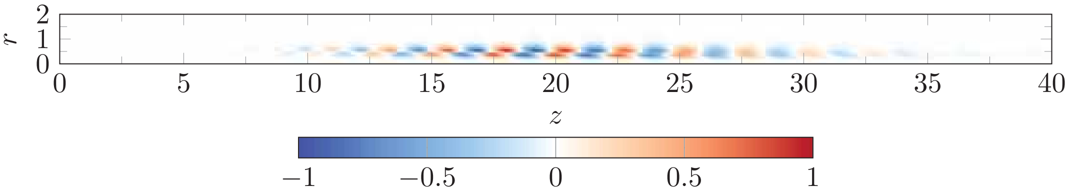

Figure 3.13: Vorticity component of the most unstable Floquet mode at $Re = 2000$ and $St_D = 0.60$. It peaks far downstream.

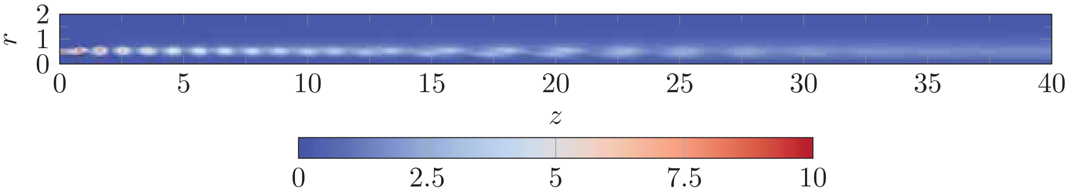

Figure 3.14: Vorticity snapshot of the base periodic unpaired flow at $Re = 2000$ and $St_D = 0.6$ slightly perturbed by the most unstable Floquet mode: $\mathbf{u}' = \mathbf{U^u} + \epsilon\tilde{\mathbf{v}}_1$, with $\epsilon = 0.2$.

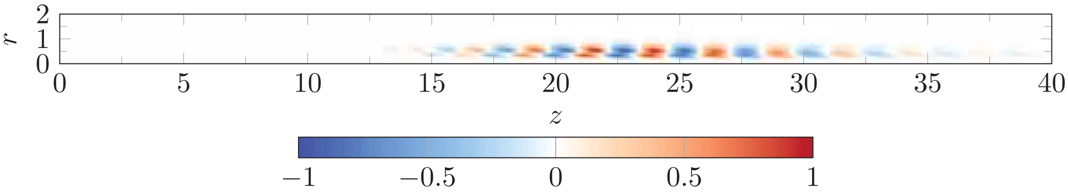

Figure 3.15: Real part of the vorticity component of the second most unstable Floquet mode at $Re = 2000$ and $St_D = 0.6$. Its peak is located far downstream.

strictly subharmonic, it does not evolve precisely at $\omega_f/2$; still its growth may trigger subharmonic pairing in the nonlinear regime. However, this mode does not provide a more plausible interpretation of the observed vortex pairing much further upstream.

3.5 TRANSIENT GROWTH ANALYSIS

In this section, we show that the transient dynamics is essential to understand the bifurcation from an unpaired unstable flow to a paired flow. Indeed, it will be demonstrated that even though the stability analysis predicts in which parameter range pairing occurs, the transition from an unpaired state arises much faster and much closer to the inlet that what modal theory predicts. In contrast, transient dynamics predicts more accurately the transition rate and the perturbation structures, and it allows to explain the occurrence of intermittent phenomena in sub-critical but noisy jets shown in section 3.3.4.3.

3.5.1 *Growth of random initial perturbations*

The jet at $Re = 2000$, forced at $St_D = 0.6$ with 5% amplitude is considered throughout this section. The natural state in this case is the paired one, shown in figure 3.6,

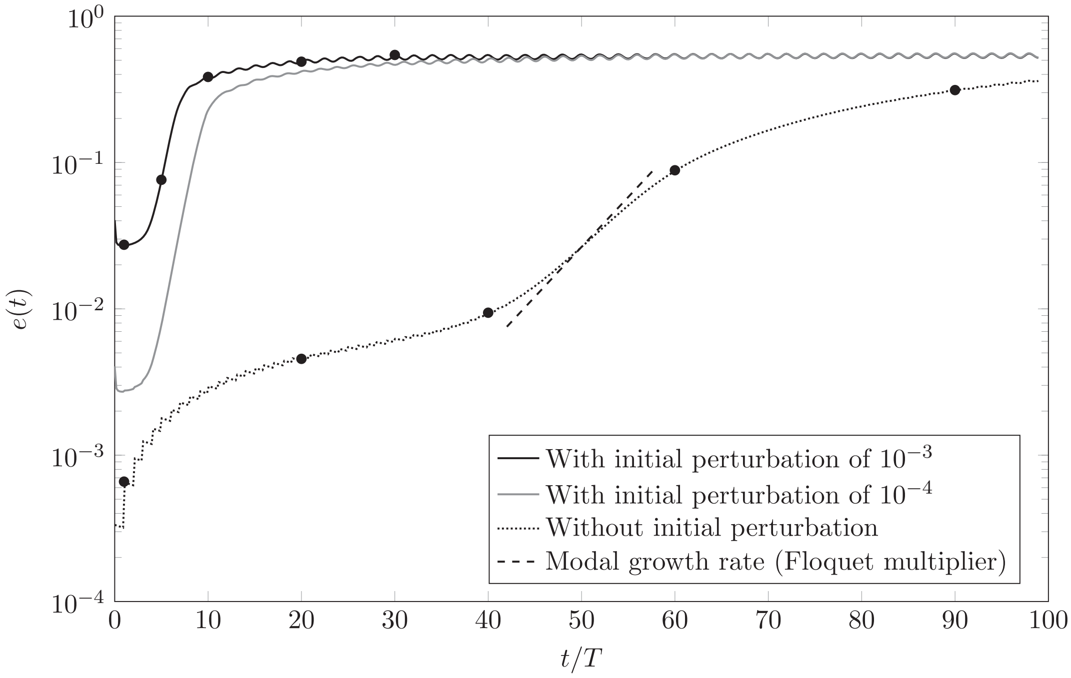

Figure 3.16: Growth of non-harmonic components in simulations with and without added initial noise. The modal Floquet growth rate is indicated for comparison.

consistent with an unstable Floquet multiplier $\mu = -1.17$ as discussed in section 3.4.4. Direct numerical simulation results are presented here, which aim to show how pairing is triggered in the unstable unpaired flow.

A first simulation is performed starting from the stabilised unpaired state, displayed in figure 3.2c, as initial condition. Residual non-T-periodic components $(u(t) - u(t-T))/2$ in this flow state are of the order of 0.01% of the reference jet velocity.

Two additional simulations have been carried out with the same state, but with added white noise velocity perturbations, $\mathbf{u}(r, z, t = 0) = \mathbf{U^u}(r, z, t = 0) + \boldsymbol{\epsilon}(r, z)$. This noise exhibits zero spatial mean $\overline{\boldsymbol{\epsilon}} = \mathbf{0}$, and two different standard deviations $\sqrt{\overline{\boldsymbol{\epsilon}^2}} = (10^{-3}, 10^{-3})^T$ and $(10^{-4}, 10^{-4})^T$ are prescribed in the two simulations.

Non-harmonic components of the flow state at any given time are measured by a norm defined as

$$e(t) = \frac{1}{2}\sqrt{\iint \|\mathbf{u}(t) - \mathbf{u}(t-T)\|^2 r \,\mathrm{d}r \,\mathrm{d}z}. \tag{3.17}$$

The time evolution of this norm is traced in figure 3.16 for the three different initial conditions. While all three cases evolve into the same paired attractor state, they arrive there along different trajectories.

3.5.1.1 *Modal growth from very low perturbation amplitude*

Starting from the unpaired state, as it has been obtained through flow stabilisation, without any added random noise, the initial perturbation that may give rise to a growing subharmonic component is given by the residual non-T-periodicity that

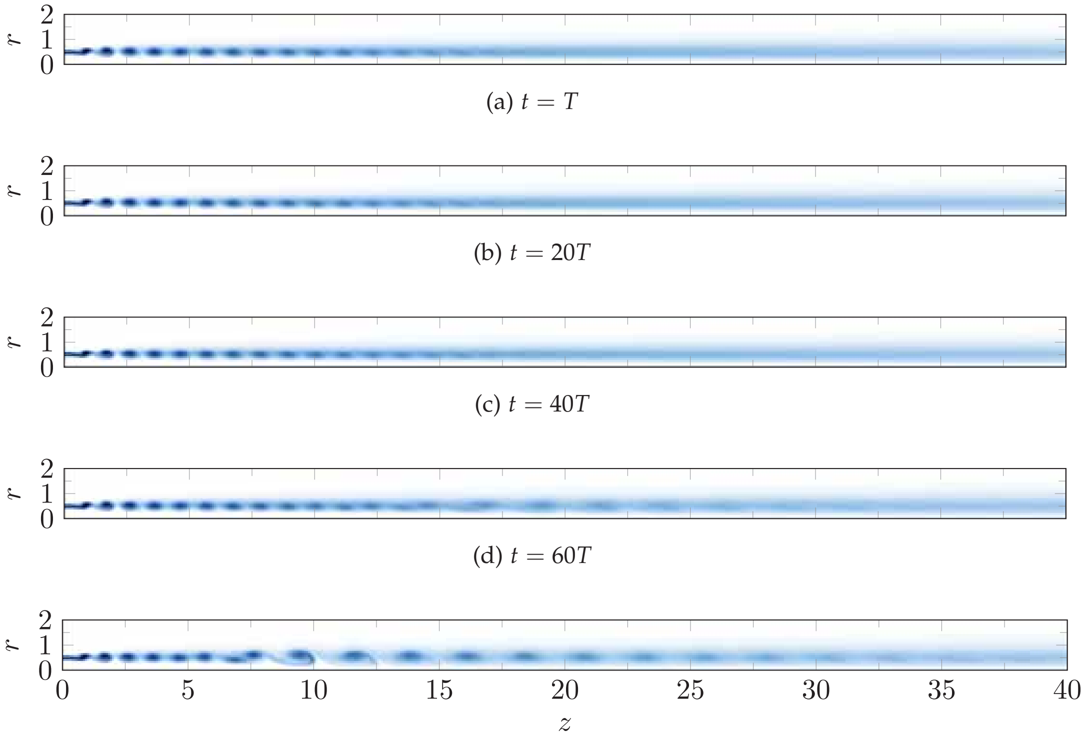

(a) $t = T$

(b) $t = 20T$

(c) $t = 40T$

(d) $t = 60T$

(e) $t = 90T$

Figure 3.17: Vorticity snapshots at five different instances without added initial noise. The colour coding is the same as in figure 3.2b.

remained when the stabilised calculation was halted. The total vorticity after one period T is shown in figure 3.17a, and the magnitude of the non-T-periodic residual at the same instant is presented in figure 3.18a. Note that this residual is computed by comparing the state at time t with that from time $t - T$; therefore time-stepping over one period is required before the stabilisation effect can be evaluated.

Over the first forty periods, the subharmonic perturbation is dominated by a slow growth of the residual structure, but at such small amplitude that the total vorticity field in figures 3.17b and 3.17c is not noticeably affected. Then, as can be seen by comparing figures 3.18c and 3.18d with figure 3.13, the exponentially growing unstable Floquet mode becomes manifest. Its amplitude growth per flow period, between $t = 40T$ and $60T$, is estimated from figure 3.16 as a factor 1.14, to be compared to the absolute value 1.17 of the computed Floquet multiplier. The spatial structure of this perturbation, displayed in figure 3.19, exhibits a similar structure as the one of the corresponding Floquet mode, shown in figure 3.13. Beyond $t = 60T$, a nonlinear saturation of the subharmonic perturbation sets in (figure 3.16), accompanied by a change in its spatial shape. At $t = 90T$, as the flow approaches the asymptotic periodic regime, the maximum perturbation amplitude has moved upstream to $z \approx 10$ (figure 3.18e), where a pronounced pairing of vortices is observed in figure 3.17e. This pairing location still moves further upstream with time, until it will finally stabilise near $z = 3$, in the natural asymptotic paired state shown in figure 3.2a.

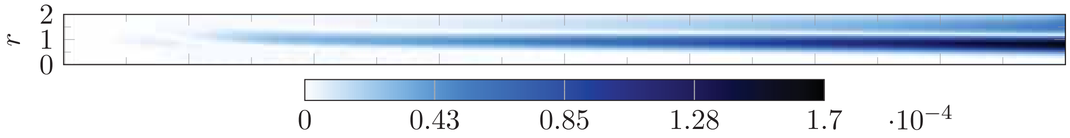

(a) $t = T$

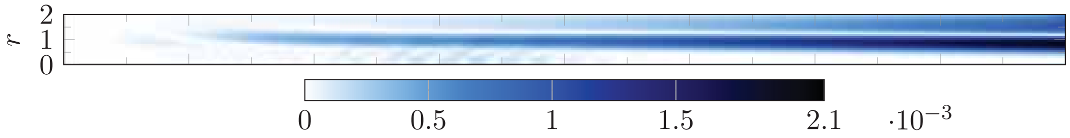

(b) $t = 20T$

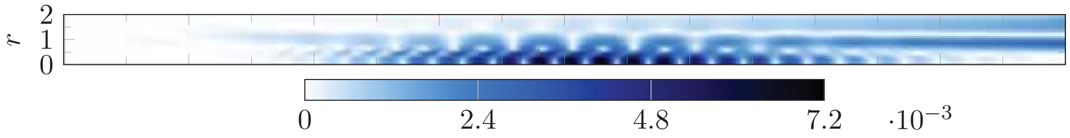

(c) $t = 40T$

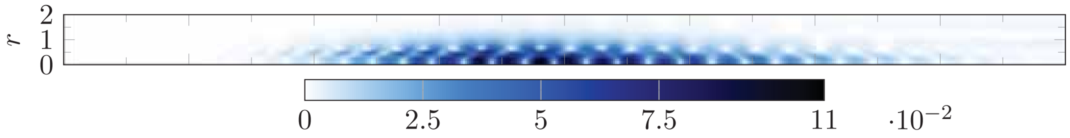

(d) $t = 60T$

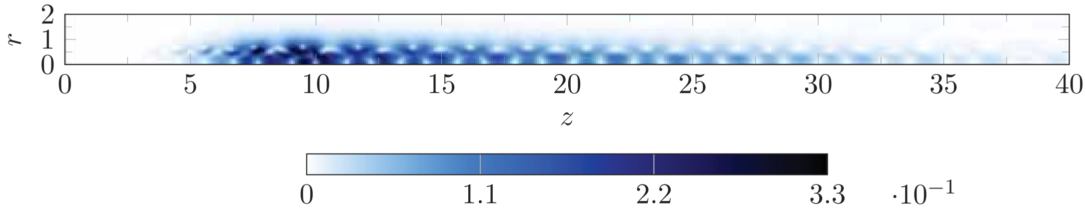

(e) $t = 90T$

Figure 3.18: Perturbation magnitude $\|\mathbf{u}(t) - \mathbf{u}(t-T)\|$ at five different instances without added initial noise.

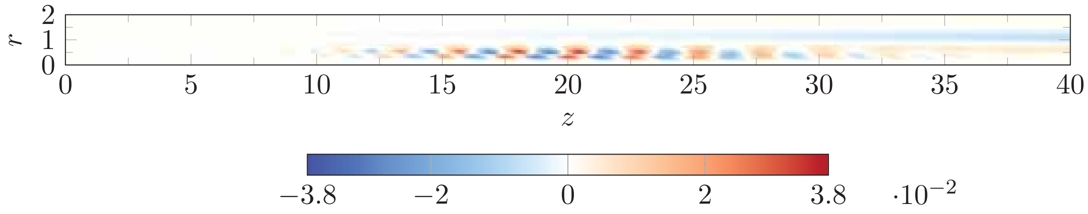

Figure 3.19: Vorticity field of the perturbation without any forcing applied at $t = 40T$.

3.5.1.2 *Non-modal growth from initial white noise*

The simulations with added white noise in the initial condition (solid lines in figure 3.16) show a much faster convergence to the final paired flow state than the

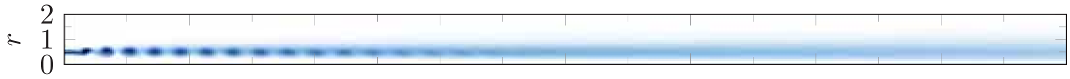

(a) $t = T$

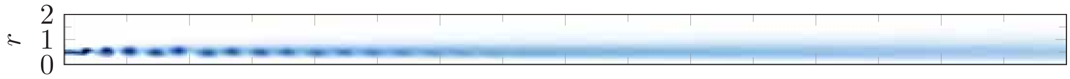

(b) $t = 5T$

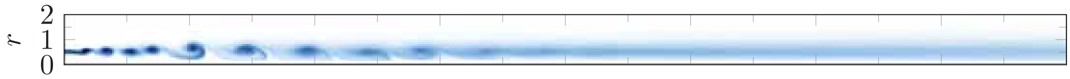

(c) $t = 10T$

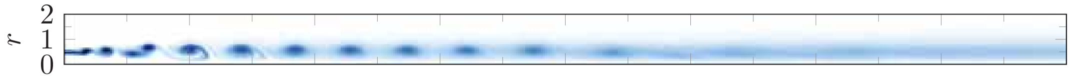

(d) $t = 20T$

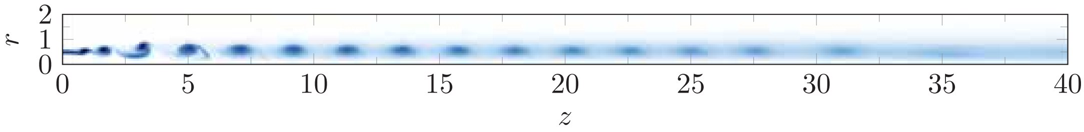

(e) $t = 30T$

Figure 3.20: Five snapshots of vorticity, evolving out of initial white noise level 10^{-3}. The colour coding is the same as in figure 3.2b.

case discussed in the preceding section (dotted line in figure 3.16). In particular, the initial growth of $e(t)$ in these two cases is markedly stronger than that of the unstable Floquet mode.

The time development from an initial condition with $\sqrt{\epsilon^2} = (10^{-3}, 10^{-3})^T$ (thick solid line in figure 3.16) is visualised in figure 3.20 by successive snapshots of the total vorticity. It is seen that vortex pairing not only sets in faster than in the previous case of figure 3.17, but also much further upstream. Corresponding non-periodic perturbations are again displayed in figure 3.21: the smallest scales of the random initial condition are quickly dissipated (figure 3.21a), and a growing coherent perturbation structure is evident after a few period cycles (figure 3.21b). The maximum perturbation growth in this phase, as measured from figure 3.16, corresponds to a factor 2.01 per period, much stronger than the modal growth factor 1.17. Persistent vortex pairing is fully established at $t = 10T$ (figure 3.21c); subsequently, the pairing location slowly moves upstream, and stabilises around $z = 3$.

Vorticity perturbations after five flow periods, in these simulations with added initial noise, are represented in figure 3.22. At this early stage, their dynamics may still be regarded as linear; however, the perturbations are now located close to the inlet, and their spatial distribution bears no resemblance with the unstable Floquet

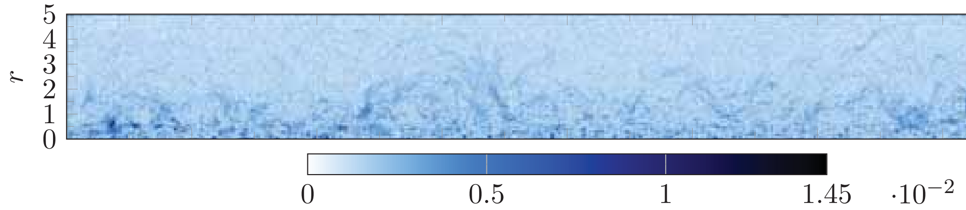

(a) $t = T$

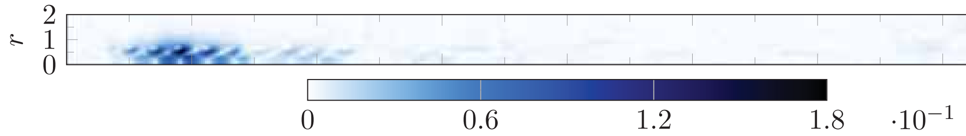

(b) $t = 5T$

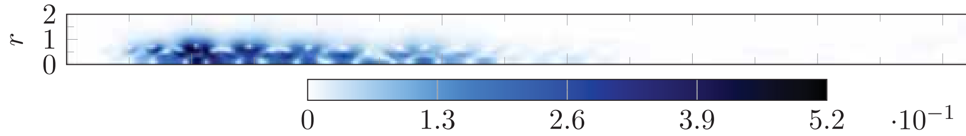

(c) $t = 10T$

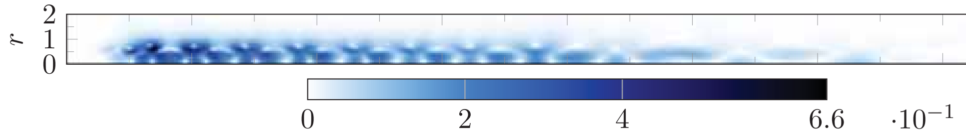

(d) $t = 20T$

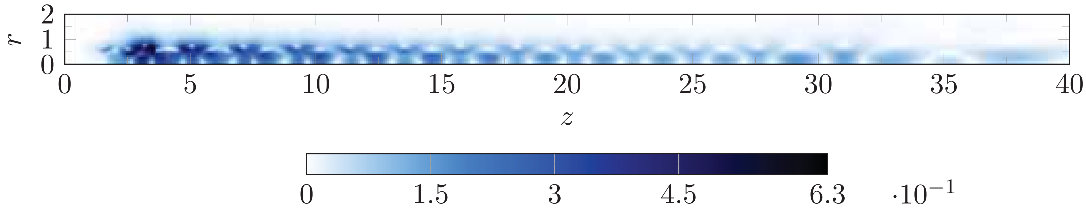

(e) $t = 30T$

Figure 3.21: Perturbation magnitude $\|\mathbf{u}(t) - \mathbf{u}(t - T)\|$ at five different instances evolving out of initial white noise level 10^{-3}.

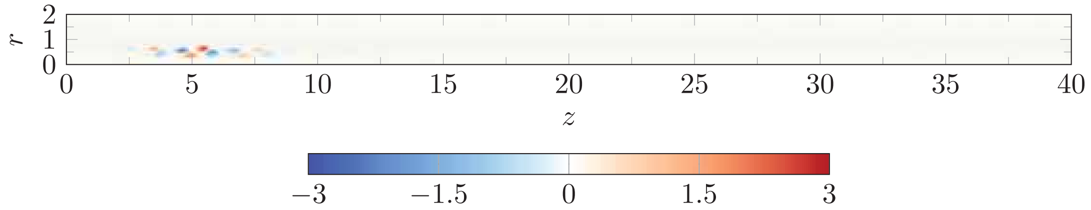

Figure 3.22: Vorticity field of the perturbation with random forcing (level 10^{-3}) at $t = 5T$.

mode (figure 3.13). Therefore, a non-modal mechanism is expected to underpin this growth.

Simulations with a lower initial noise level of 10^{-4} show a similar behaviour, although slightly delayed (figure 3.16). The exponential phase is longer, since the amplitude takes more time to saturate, and the maximum growth rate is 2.16 per forcing period.

3.5.2 *Optimal linear perturbation growth over one cycle*

In order to further analyse and understand the mechanism behind the non-modal onset of vortex pairing, as observed in section 3.5.1.2, the *optimal* growth of sub-harmonic perturbations is now investigated. One cycle period T is chosen as the time horizon over which optimisation is performed. As discussed in the context of (3.11), perturbations are propagated over one cycle by the time-shift operator Φ'. The optimal perturbation is then found as the solution to the maximisation problem

$$\|\mathbf{u}_{opt}(T)\| = \max_{\mathbf{u}'(t=0)} \frac{\|\mathbf{u}'(t=T)\|}{\|\mathbf{u}'(t=0)\|} = \max_{\mathbf{u}'(t=0)} \frac{\|\Phi'\mathbf{u}'(t=0)\|}{\|\mathbf{u}'(t=0)\|}, \tag{3.18}$$

The norm used in the following is derived from the standard real $\mathbf{u}$-scalar product in cylindrical coordinates (equation (3.13)). This scalar product defines a full norm for $\mathbf{u}$, but only a semi-norm for $\mathbf{q}$, because the separation condition is not fulfilled. The solution of the maximisation problem (3.18) is given by the norm of the operator Φ'.

To evaluate this norm, the orthonormal basis $\{\hat{\mathbf{u}}_i^n\}$ calculated in the context of modal analysis (section 3.4.3) is once more exploited. Instead of maximising the norm of Φ', a infinite-dimensional operator, we maximise the norm of its projection $\tilde{\Phi}$, of finite dimension, onto this basis.

A perturbation state $\mathbf{u}'$ is projected onto $\{\hat{\mathbf{u}}_i^n\}$ as

$$\mathbf{u}' = \sum_{n=0}^{N-1}\sum_{i=1}^{N_{vec}} \beta_{nN_{vec}+i}\hat{\mathbf{u}}_i^n + \mathbf{r}', \tag{3.19}$$

$$\text{with } \beta_{nN_{vec}+i} = \langle \mathbf{u}', \hat{\mathbf{u}}_i^n\rangle \quad \text{such that} \quad \boldsymbol{\beta} = R^T M\mathbf{u}'.$$

The residual $\mathbf{r}'$ is orthogonal to the basis $\{\hat{\mathbf{u}}_i^n\}$, such that $\|\mathbf{u}'\|^2 = \|\boldsymbol{\beta}\|^2 + \|\mathbf{r}'\|^2$. Therefore,

$$\begin{aligned} \Phi'\mathbf{u}' &= \sum_{n=0}^{N-1}\sum_{i=1}^{N_{vec}} \beta_{nN_{vec}+i}\left(\Phi'\hat{\mathbf{u}}_i^n\right) + \Phi'\mathbf{r}' \\ &= \sum_{n=0}^{N-1}\sum_{i=1}^{N_{vec}} \left(\tilde{\Phi}\boldsymbol{\beta}\right)_{nN_{vec}+i}\hat{\mathbf{u}}_i^n + \Phi'\mathbf{r}', \end{aligned} \tag{3.20}$$

and

$$\|\Phi'\mathbf{u}'\|^2 = \|\tilde{\Phi}\boldsymbol{\beta}\|^2 + \|\Phi'\mathbf{r}'\|^2 + 2\left\langle \sum_{n=0}^{N-1}\sum_{i=1}^{N_{vec}} \left(\tilde{\Phi}\boldsymbol{\beta}\right)_{nN_{vec}+i}\hat{\mathbf{u}}_i^n, \Phi'\mathbf{r}'\right\rangle, \tag{3.21}$$

with the norm of $\tilde{\Phi}\boldsymbol{\beta}$ calculated in a finite-dimensional space of dimension NN_{vec}. Therefore, maximising $\|\Phi'\mathbf{u}'\|$ is equivalent to maximising the right-hand side of the previous equation. However, the $\hat{\mathbf{u}}_i^n$-basis has not been chosen randomly: being constructed from the successive iterations of a single group of random vectors, it selects numerically the fastest-growing modes of the full system, in a similar way as power iterations (Saad, 2011). These modes are then gradually excluded from the residual space of $\mathbf{r}'$, and the norm of the image of $\mathbf{r}'$ through Φ' decreases as the number N of Krylov subspace iterations is increased. On the right-hand side of equation (3.21), the first term becomes dominant as N increases ; the second and third terms are bounded by $\|\Phi'\mathbf{r}'\|^2$ and $\|\tilde{\Phi}\boldsymbol{\beta}\|\|\Phi'\mathbf{r}'\|$, respectively. Therefore, the approximation $\|\Phi'\mathbf{u}'\| \approx \|\tilde{\Phi}\boldsymbol{\beta}\|$ is valid for large N. This explains why, for a given value of NN_{vec}, a trade-off needs to be found between N and N_{vec}: N must be large enough to capture the salient flow dynamics whereas N_{vec} must be sufficiently large to make the block-Arnoldi calculations computationally efficient.

The norm $\|\tilde{\Phi}\boldsymbol{\beta}\|$ is evaluated by use of the singular value decomposition (SVD)

$$\tilde{\Phi} = \tilde{U}\Sigma\tilde{V}^T, \tag{3.22}$$

with Σ a real positive diagonal matrix, and $\tilde{U}$ and $\tilde{V}$ real unitary matrices. Columns $\tilde{\mathbf{v}}_k$ and $\tilde{\mathbf{u}}_k$ represent forcing and response pairs in the orthonormal basis of the $\{\hat{\mathbf{u}}_i^n\}$. Σ contains the singular values ordered in descending order, such that $\tilde{\Phi}\tilde{\mathbf{v}}_k = \sigma_k\tilde{\mathbf{u}}_k$ with $\sigma_k \geq \sigma_{k+1} \geq 0$.

Note that the Krylov base constructed in section 3.4.3 is orthonormal with respect to the scalar product (3.13). Therefore, the optimal initial perturbations or responses in the reduced space correspond to the optimal initial perturbations or responses in the full-state space, using the R matrix to change basis. For a given optimal initial perturbation (resp. response) $\tilde{\mathbf{v}}_k$ (resp. $\tilde{\mathbf{u}}_k$) in this reduced basis, the corresponding full-state initial perturbation velocity (resp. response velocity) $\mathbf{v}_k$ (resp. $\mathbf{u}_k$) is obtained as $\mathbf{v}_k = R\tilde{\mathbf{v}}_k$ (resp. $\mathbf{u}_k = R\tilde{\mathbf{u}}_k$). The corresponding matrices of optimal initial perturbations and responses are $V = R\tilde{V}$ and $U = R\tilde{U}$. Because of this preserved optimality, the maximum linear gain achievable over one period in the full-state is still σ_1, obtained by perturbing the velocity field at $t = 0$ with $\mathbf{v}_1$. After one period, the perturbation velocity field is given by $\mathbf{u}_1$.

This method is computationally efficient, as it is entirely based on the results already available from the modal analysis. This is in contrast with the additional computations required in a direct-adjoint approach. Moreover, with the direct-adjoint approach, the optimisation is carried out for a single time horizon T_f. In this section, only $T_f = T$ has been chosen ; however, as will be seen in the next section, this can be extended with little additional effort to any time-horizon of integer periods $T_f = nT$. Time-horizons that are not integer multiples of T, corresponding to transient phenomena within a forcing period, are not considered here.

Singular value decomposition of Φ' has been carried out for all flow configurations listed in table 3.1. The maximum gain values σ_1 are shown in figure 3.23 for fixed values of St_D and Re. Variations of σ_1 with the forcing amplitude A are given in table 3.3 for one setting $Re = 2000$ and $St_D = 0.6$. In all cases, the achievable transient amplification over one period is significantly higher than the maximum modal growth rate. A comparison with results of perturbed DNS flows (figure 3.16) is discussed in section 3.5.3.

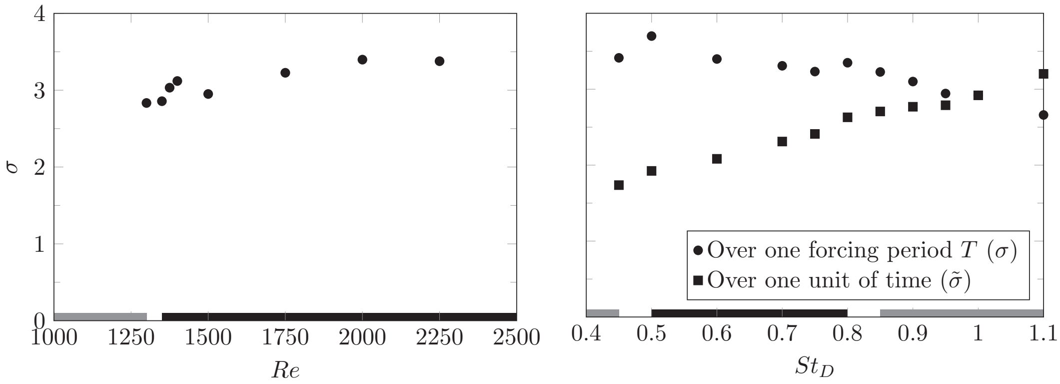

(a) $St_D = 0.6$.

(b) $Re = 2000$.

Figure 3.23: Norm of the time-shift operator for different Reynolds and Strouhal numbers, with a 5% forcing level and a normalised momentum thickness of 5%. The grey or black domains represent the parameters values for which DNS calculations show that the "natural" solution is unpaired or paired, as shown in figure 3.6. In figure 3.23b, the leading amplification rates are also depicted rescaled over one dimensionless time unit. Additional singular values for lower Reynolds number flows are discussed in section 3.5.4.

Forcing amplitude	1%	5%	10%
$\|\mathbf{u}_{opt}(T)\|$	3.96	3.40	3.32

Table 3.3: Evolution of the optimal perturbation gain over one period with the forcing amplitude for $Re = 2000$ and $St_D = 0.60$.

At fixed Strouhal number (figure 3.23a), the leading singular value changes weakly as a function of Reynolds number, even as the system goes from stable to unstable. Variations of σ_1 are within 20% as the value of Re is doubled.

At fixed Reynolds number (figure 3.23b), variations of the Strouhal number also do not affect σ_1 in a strong way. Doubling St_D from 0.45 to 0.9 is accompanied by a 10% decrease of the maximum gain over one flow period. However, when σ_1 is rescaled to give the mean amplification over a *constant time unit*, as $\tilde{\sigma}_1 = \sigma_1 St_D$, this rescaled gain increases by more than 30% over the investigated interval of St_D. This is consistent with Broze and Hussain (1994, 1996) : in their parametric study, as shown in figure 3.1, they found that when the Strouhal number is increased, the jet is more prone to experience non-T- or non-$2T$-periodic behaviour (periodic or not modulations, intermittency or chaos). Our study shows that the larger the Strouhal number, the more amplified random perturbations can be over a given time unit.

With increasing forcing amplitude, the maximum gain is moderately diminished (table 3.3). This may indicate that the receptivity to subharmonic perturbations is larger when the shear layer is not yet fully rolled up, since increasing forcing amplitude results in a faster roll-up of vortices, as shown in figure 3.8. Again, this is coherent with Broze and Hussain (1994, 1996): as shown in figure 3.1, with larger forcing levels, except at Strouhal numbers greater than those considered in our

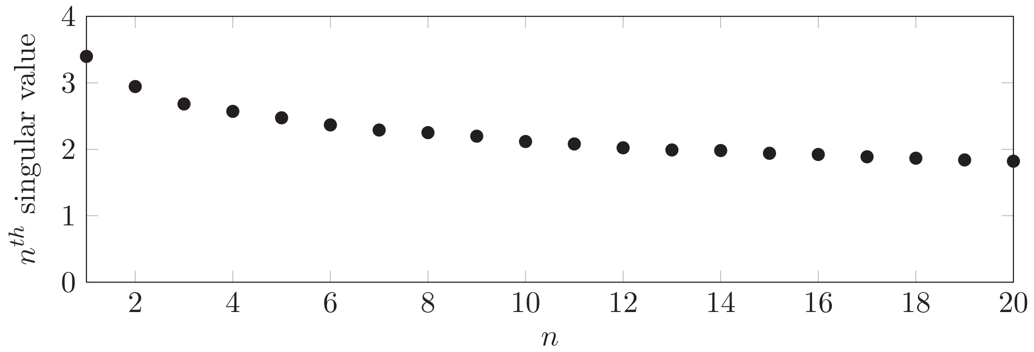

Figure 3.24: The twenty first singular values of Φ' for $Re = 2000$, $St_D = 0.6$ and $A = 5\%$.

study, the flow is less prone to non-periodic behaviour, which may be brought about by transient amplification of small disturbances.

The leading singular mode may not be the only relevant way to trigger transient growth. For the case $(Re = 2000, St_D = 0.6)$, the 20 largest singular values are represented in figure 3.24. Indeed, a strong dominance of the optimal perturbation cannot be affirmed: the first value is 15% larger than the second, 27% larger than the third, and only 87% larger than the twentieth.

The shapes of the optimal initial perturbation and response structures are shown for the case $(Re = 2000, St_D = 0.6)$ in figures 3.25a and 3.25b, respectively. In comparison with the Floquet mode discussed in section 3.4.4 (see figure 3.13), these perturbation structures are localised much closer to the inlet. Over the course of one period, the perturbation shape is largely conserved, while it is convected at the same pace as the rolled-up vortices. The manifestation of these perturbations in the total vorticity field is visualised in figure 3.26, where the linear optimal initial perturbation and response structures are superposed onto the periodic base state with a small amplitude of 5%. It can be observed that the optimal perturbation structures displace the vortices towards and away from the axis, in an alternating fashion. This displacement is furthermore oriented at an oblique angle, such that the distance between neighbouring vortices is modulated, thus initiating the pairing interaction.

The second singular mode pair in the same configuration, corresponding to σ_2, is displayed in figure 3.27. It exhibits a very similar structure as the first singular mode, the main difference being that the maximum amplitude is shifted downstream to the next vortex pair.

3.5.3 *Optimal linear perturbation growth over many cycles*

The technique that has been described in the previous section for optimisation over a single flow period T is easily extended in order to construct optimal perturbations for time horizons of *multiple* periods nT. Let $\mathbf{f}_n$ denote the optimal perturbation at $t = 0$ that leads to the largest possible flow response $\mathbf{r}_n$ at $t = nT$. The associated amplitude gain is then given by the norm $\|\mathbf{u}_{opt}(nT)\| = \|\mathbf{r}_n\| / \|\mathbf{f}_n\|$, which is identical to the largest singular value of the nth power of the operator Φ. Substituting Φ with its approximation $\tilde{\Phi}$, the SVD of $\tilde{\Phi}^n$ is straightforward to compute.

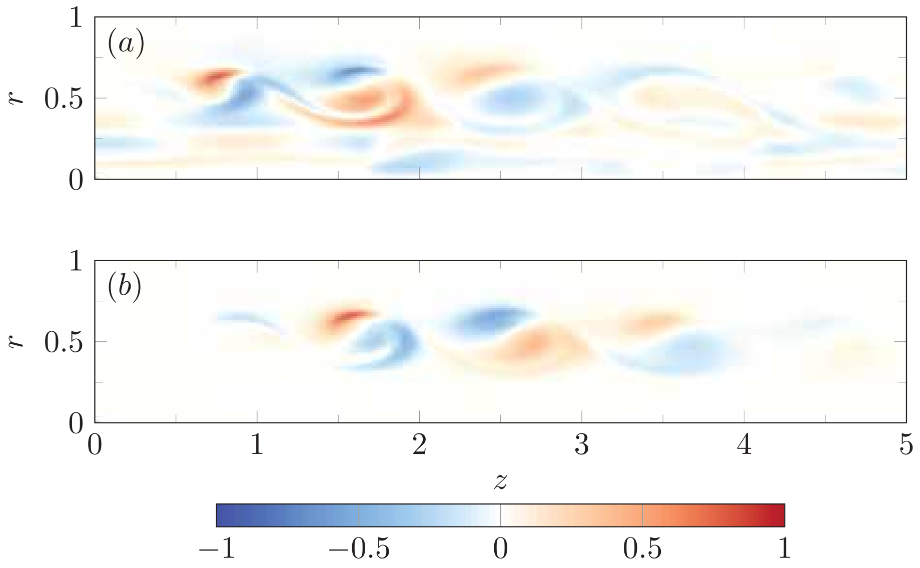

Figure 3.25: For $Re = 2000$ and $St_D = 0.6$, vorticity of (a) the optimal perturbation and (b) its response after one flow period. The maxima are located close to the inlet.

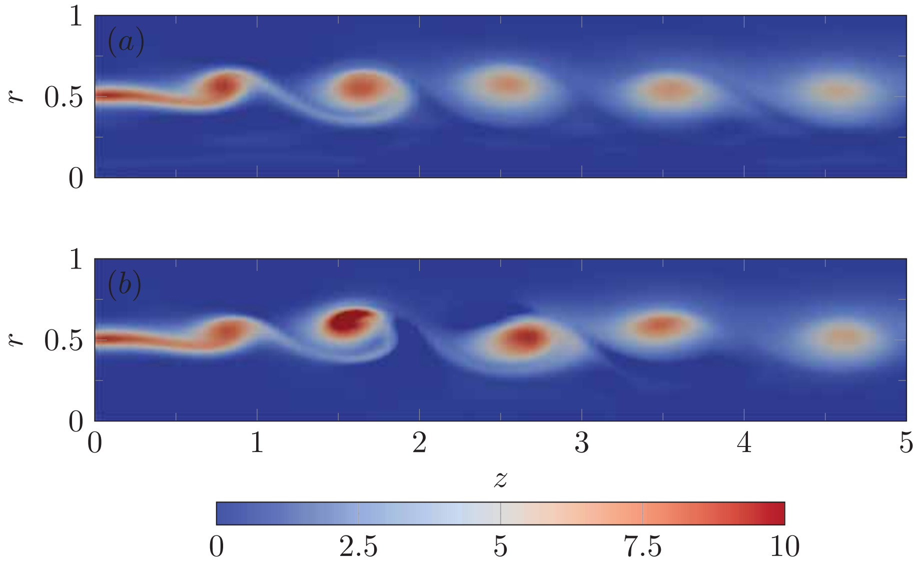

Figure 3.26: Superposition of the base flow and (a) the optimal perturbation, (b) the associated linear response after one flow period. The total vorticity is shown, for velocity fields $\mathbf{u}' = \mathbf{U^u} + 0.05\mathbf{u_1}$ and $\mathbf{u}' = \mathbf{U^u} + 0.05\sigma_1\mathbf{v_1}$, respectively, for the case $Re = 2000$ and $St_D = 0.6$. Both $\mathbf{u_1}$ and $\mathbf{v_1}$ have unit norm.

The ensuing variation of the optimal gain with nT is traced in figure 3.28, alongside the perturbation growth associated with the most unstable Floquet mode (section 3.4.4). Optimal perturbation at $t = 0$ enables a vigorous transient growth over short time horizons; at longer times, however, the optimal growth rate approaches that of the modal solution, given by the modulus of the dominant Floquet multiplier. This behaviour is identical to that of perturbation growth in steady base flows, which has been discussed theoretically by Trefethen and Embree (2005). In the present case, the transient non-modal growth provides a significant

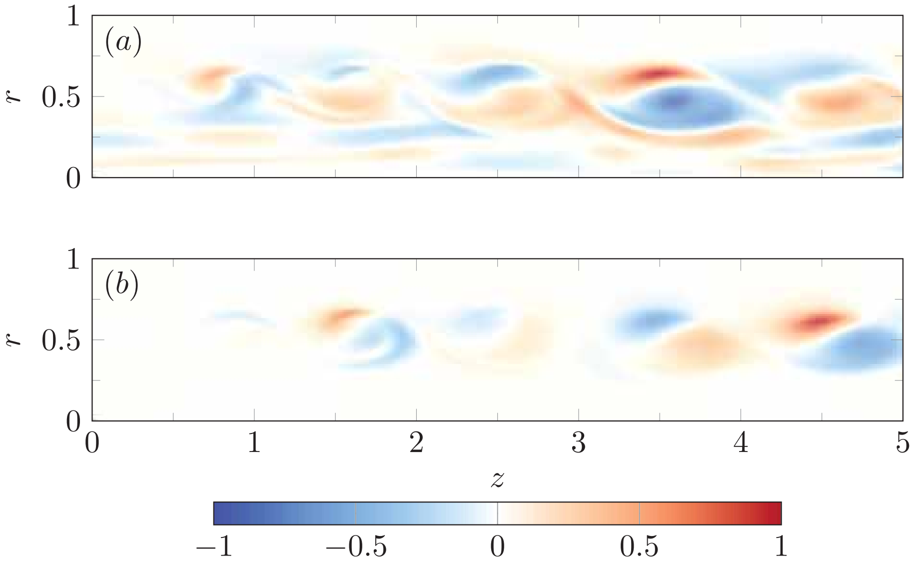

Figure 3.27: For $Re = 2000$ and $St_D = 0.6$, vorticity of (a) the second singular mode: (a) perturbation and (b) its response after one flow period. The maxima are located further downstream than in the optimal setting shown in figure 3.25.

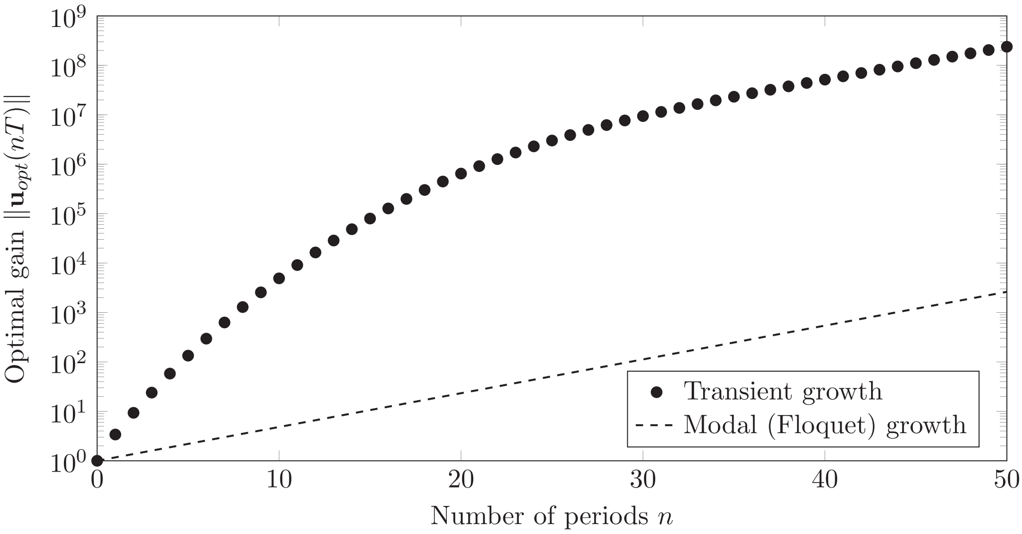

Figure 3.28: Transient growth gain achieved by a $(Re = 2000, St_D = 0.60)$ jet forced with 5% amplitude and comparison with modal growth.

boost, on the order of 10^5, of the overall long-time amplitude gain. This additional factor corresponds to 73 cycle periods of modal growth.

The evolution and convergence of the optimal initial perturbation and response *structures* are examined in figure 3.29 in terms of projections. The scalar products of the initial perturbation and response structures obtained for any number of cycles with those at $n = 1$ and $n = 50$ are represented. It is observed that the optimal initial perturbation structure does not evolve much with time, and that the shape determined for one single period is close to optimality for all time horizons. In contrast, the shape of the optimal response changes significantly through time; the optimal response at $t = 50T$ is indeed localised at a different location than

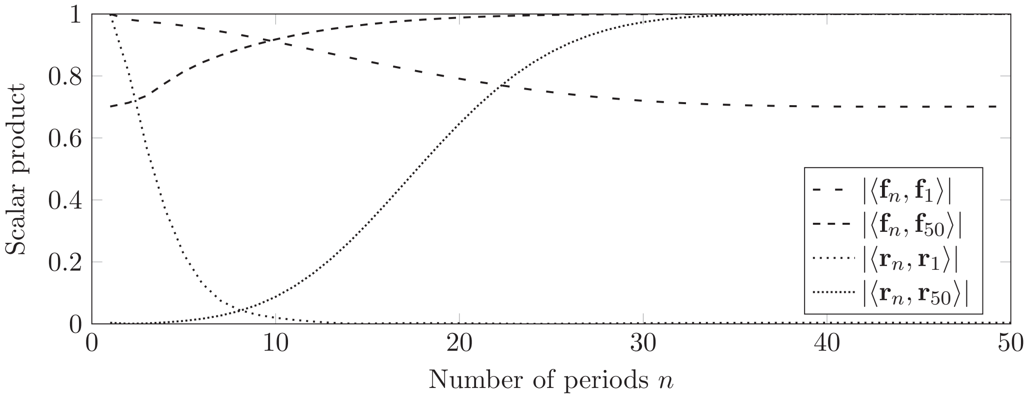

Figure 3.29: Projection of the optimal initial perturbation and response at time nT over the optimal initial perturbation and responses at times T and $50T$ for a jet at $Re = 2000$ and $St_D = 0.60$ forced with a 5% amplitude. While the optimal initial perturbation experiences little change, the optimal response changes drastically. All vectors considered have unit norm.

$\lvert\langle \mathbf{f}_1, \tilde{\mathbf{v}}_1 \rangle\rvert$	$\lvert\langle \mathbf{f}_{50}, \tilde{\mathbf{v}}_1 \rangle\rvert$	$\lvert\langle \mathbf{r}_1, \tilde{\mathbf{v}}_1 \rangle\rvert$	$\lvert\langle \mathbf{r}_{50}, \tilde{\mathbf{v}}_1 \rangle\rvert$
1.24×10^{-3}	1.10×10^{-5}	3.60×10^{-3}	9.9990×10^{-1}

Table 3.4: Scalar products (3.13) between the Floquet mode $\tilde{\mathbf{v}}_1$ and the optimal finite-time initial perturbations $\mathbf{f}_n$ and responses $\mathbf{r}_n$. All modes and perturbations have unit norm. Consistent with the notations introduced in section 3.5.2, $\mathbf{f}_1$ is identical to $\mathbf{v}_1$, and $\mathbf{r}_1$ to $\mathbf{u}_1$.

its counterpart at $t = T$. While the optimal initial perturbation structure always retains a nearly identical shape, the optimal response structure gradually shifts downstream with increasing time horizon, and eventually it converges towards the structure of the Floquet mode (see figure 3.13). The projection values in table 3.4 demonstrate this convergence. It is expected on theoretical grounds (Trefethen and Embree, 2005) that, at long time horizons, the optimal response structure corresponds to the dominant Floquet mode, whereas the optimal forcing is given by the associated *adjoint* mode of the time-shift operator.

The different evolution from different initial perturbations, documented in sections 3.5.1.1 and 3.5.1.2 can now be interpreted in terms of the optimal perturbation results.

In the two cases that were initialised with white noise perturbations, this initial condition contained significant components of strongly amplified optimal initial perturbation modes. After approximately five periods, these structures emerged from the background noise, as may be inferred from a qualitative comparison between figures 3.22, 3.25b and 3.27b. However, the maximum growth observed in figure 3.16 for $\sqrt{\epsilon^2} = (10^{-3}, 10^{-3})^T$ corresponds to a factor 2.16 per period, whereas the leading singular value was determined to be 3.40 in section 3.5.2 for the time horizon $t = T$. Yet, the optimal growth rate decreases with time; this is shown in

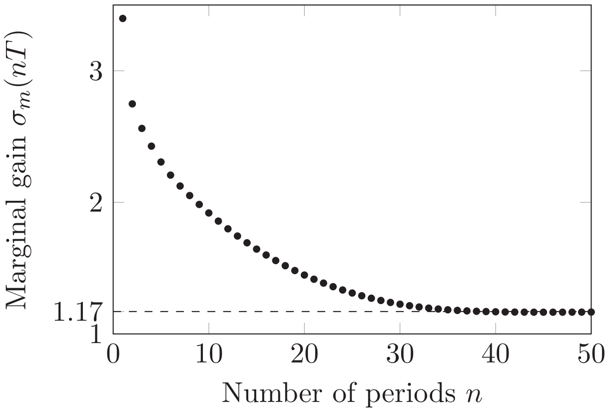

Figure 3.30: Marginal gain $\sigma_m(nT)$ of the optimal perturbation at the horizon time nT for $Re = 2000$, $St_D = 0.60$ and $A = 0.05$. The marginal growth rate asymptotically converges towards the modulus of the most unstable Floquet multiplier.

figure 3.30, which represents the marginal gain $\sigma_m(nT)$ at $t = nT$ of the nT-optimal perturbation:

$$\sigma_m(nT) = \frac{\|\mathbf{u}_{opt}[(n+1)T]\|}{\|\mathbf{u}_{opt}(nT)\|} \tag{3.23}$$

with $\|\mathbf{u}_{opt}(nT)\|$ plotted in figure 3.28. Therefore, the maximum growth value 2.16, observed in figure 3.16, is consistent with the marginal gains observed after 5 to 10 periods in figure 3.30.

In the case discussed in section 3.5.1.1, initialised without added noise, the exponential growth observed between $40T$ and $60T$ has been associated with the unstable Floquet mode. The initial perturbation (figure 3.18a) is spatially disjoint from optimal perturbations near the inflow. At $t = 20T$, a non-modal pairing perturbation is faintly visible in figure 3.18b, still in the process of transitionning towards the Floquet mode in figure 3.18c, the optimal linear response at long times.

Whether or not *transient* processes lead to a rapid onset of nonlinear vortex pairing depends on the energy level of oscillatory perturbations near the inflow, with appropriate wavelengths for subharmonic vortex modulation.

3.5.4 *Importance of transient dynamics at low Re*

In section 3.3.4.1, a Reynolds number threshold was determined below which pairing did no longer occur naturally. However, in section 3.3.4.3, it has been demonstrated that forcing a jet harmonically with a small noise level was able to trigger pairing for Reynolds numbers where pairing does not normally occur. It is now examined how this behaviour can be explained in the light of the transient growth analysis developed in the previous section. At $St_D = 0.6$ and $A = 5\%$, four Reynolds number values 1300, 1000, 750 and 500 are considered here. All these cases are modally stable, as seen in table 3.5. The transient growth of these cases is shown in figure 3.31.

Although in all cases, the gain decreases in the long term, the maximum achieved during the transient growth varies largely, between 4.5 after 6 periods for $Re = 500$, and 8.3×10^3 after 26 periods for $Re = 1300$. This change explains the different

Reynolds number	500	750	1000	1300
Floquet multiplier	$-0.51 \pm 0.031i$	-0.64	-0.82	-0.97
Leading singular value	1.85	2.28	2.58	2.83

Table 3.5: For $St_D = 0.6$ and $A = 0.05$, evolution of the least stable subharmonic Floquet multiplier and of the maximum growth rate over one period as a function of Re in the stable case.

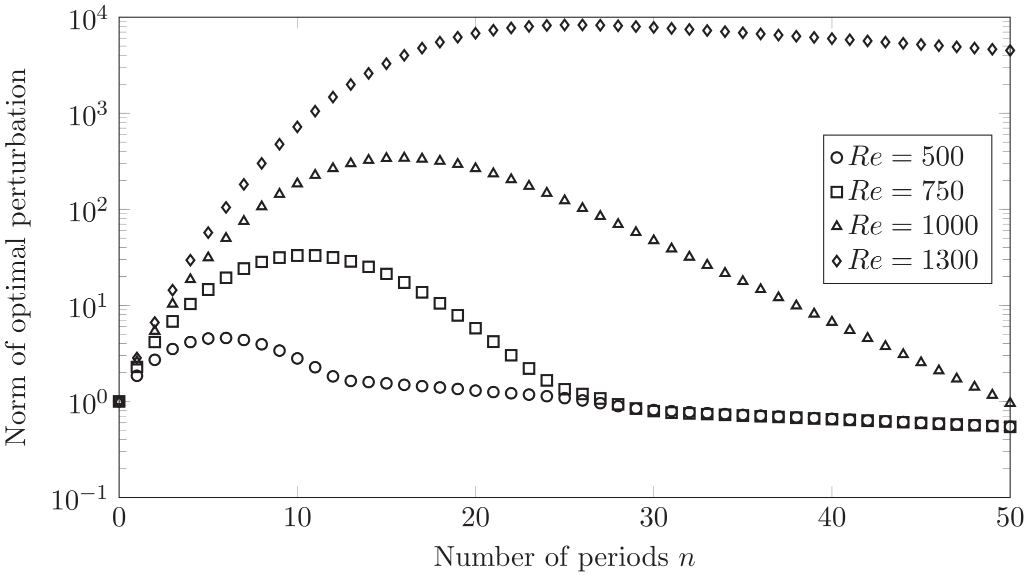

Figure 3.31: Transient growth gain for a jet forced at $St_D = 0.60$ with 5% amplitude at different subcritical Reynolds number values.

behaviour observed in section 3.3.4.3. At $Re = 500$, whatever the forcing level, the noise is not energetic enough to trigger pairing. On the other hand, at $Re = 1300$, even very small perturbations eventually initiate pairing via transient growth. At intermediate Reynolds numbers, the behaviour observed depends on the perturbation level.

3.6 CONCLUSION

The onset of sustained vortex pairing in the street of axisymmetric vortices in a laminar jet has been investigated by means of global instability analysis.

The numerical framework developed for this study is applicable to the instability analysis of any spatially developing time-periodic flow. It includes the computation of a strictly T-periodic base flow by means of DNS with added time-delay control (Shaabani-Ardali, Sipp, and Lesshafft, 2017), the identification of dominant linear Floquet modes, and a singular value decomposition of the propagator in order to characterise non-modal transient growth phenomena. The modal and non-modal analysis are both achieved via time-stepping of the linearised flow equations, without the need for adjoint calculations, in combination with a block-Arnoldi algorithm (Saad, 2011).

It has been demonstrated that self-sustained vortex pairing in a jet is the manifestation of a subharmonic linear Floquet instability of the underlying periodic vortex street. Direct numerical simulations of axisymmetric laminar jets, forced harmonically at Strouhal number St_D at the inlet, have been perfomed in order to delineate the region in the Re-St_D parameter plane where pairing in the ensuing vortex street arises spontaneously. This parameter regime has then been shown to be characterised by subharmonic Floquet instability. Furthermore, the phase velocities of fundamental and subharmonic fluctuations in the simulation results have been found to be consistent with the resonance model proposed by Monkewitz (1988). DNS results also show a strong influence of inflow forcing amplitude as well as random ambient noise on the onset of vortex pairing.

The spatial structure of the unstable linear Floquet mode, throughout the parameter regime considered in this study, reaches its maximum amplitude far downstream of the inlet, whereas the subharmonic perturbation amplitude in the nonlinear saturated paired flow state peaks a few diameters away from the inlet, where stationary vortex pairing occurs. When DNS calculations in the unstable regime are initiated with extremely low subharmonic perturbations, the Floquet mode structure and growth rate are indeed observed over a short time interval in the bifurcation process. However, when additional random noise is added to the initial condition, considerably faster subharmonic perturbation growth is observed, with spatial amplitudes concentrated near the inlet. This behaviour motivated a linear optimal perturbation analysis. It has been found that linear transient mechanisms may induce, for a standard configuration with $Re = 2000$ and $St_D = 0.6$, an additional amplitude gain of about five orders of magnitude with respect to purely modal growth. Furthermore, the spatial structure of the linear optimal perturbation response reflects the DNS observations at early times, when subharmonic perturbations may be assumed to be governed by linear dynamics.

While the asymptotic occurrence of vortex pairing is determined by modal Floquet instability, its emergence is dominated by non-modal transient growth mechanisms.

4

OPTIMAL TRIGGERING OF JET BIFURCATION, AN EXAMPLE OF OPTIMAL FORCING APPLIED TO A TIME-PERIODIC BASE FLOW

CONTEXT

In this final chapter, we study the bifurcating jet thanks to the tools developed for the axisymmetric pulsed jet in the previous chapter. In particular, we aim at optimising the forcing leading to the bifurcating jet.

Previous studies of the phenomenon generally focus on the response of a flow to an arbitrary spatiotemporal forcing, be it experimentally or numerically. Many choices are available for the forcing spatial shape – proportional to $\sin(\pi x/D)$, $\cos(\theta)$ or $\cos(\theta - \omega_f t/2)$–, for the forcing directions – axial or radial –, and for the forcing time-shift from the axisymmetric one. However, there is no clear conclusion about which choices are optimal. Because of the time-periodicity of the flow studied, and of the nonlinear behaviour of the Navier–Stokes equations, a brute-force optimisation of such phenomenon is very computationally expensive. Some attempts have been made in the past, but with poor spatial discretisation and parameter space scanned: instead of exploring all possible shapes, a parametrised forcing shape was optimised.

In order to tackle the optimisation of the bifurcating jet, the last building block needed in our toolbox is a physical bifurcation scenario. In this chapter, we use the mechanism proposed by Parekh, Leonard, and Reynolds (1988), which decouples in both space and time the respective roles of the axisymmetric and of the helical forcings. First, the axisymmetric forcing generates vortices after roll-up. Second, the helical forcing shifts and tilts the convected vortices off-axis. Then, by mutual nonlinear induction, they further depart from the axis, leading to the jet bifurcation.

This spatio-temporal dissociation, along with the stabilisation method developed in chapter 2, enables us to transform this nonlinear time-periodic $3D$ optimisation problem to a much computationally simpler linear time-periodic $2D$-helical optimisation problem. We do not impose any restriction on the spatial forcing, except that it must be of helical shape to enable two-dimensional calculations.

In summary, from the methodological point of view, the main contribution of this chapter consists in the derivation of a method for the long-time linear optimisation of periodic flow, that does not rely on direct-adjoint simulations.

An article presenting the results of this chapter is currently in preparation for the *Journal of Fluid Mechanics*.

ABSTRACT

The present chapter aims at optimising the spreading of a bifurcating jet – a jet that combines axisymmetric and helical forcings to achieve increased mixing in a preferential plane. Lee and Reynolds (1985) and Parekh, Leonard, and Reynolds (1988) explain such a bifurcation as the result of nonlinear interactions between ring vortices (triggered by $m = 0$ axisymmetric forcing) shifted off-axis in alternate directions (due to $m = 1$ helical forcing). Following this idea, we linearly optimise the periodic helical forcing to be applied at the inlet to optimally displace the ring vortices from an axisymmetric jet forced axially. Two norms are introduced to evaluate the effect of the $m = 1$ forcing onto the $m = 1$ response: the standard $\mathcal{L}_2$-norm and a semi-norm reflecting the $m = 0$ vortex displacements.

The linear results show a dominant forcing mode across the entire Strouhal band studied $[0.35; 0.80]$, with a large gain separation from suboptimals. The dominant forcing is mainly radial, independent of the chosen response norm, and provides a gain at least five times larger than the gain of previous helical forcing strategies. Superposition of base flow and linear results show the alternate shifting and twisting provoked by the the small-amplitude helical forcing, which is an essential ingredients to trigger jet bifurcation.

When plugged into $3D$ direct numerical simulations, a low amplitude helical forcing of 1% of the mean flow velocity, the optimal forcing achieves effective bifurcation across all Strouhal values studied. For large Strouhal numbers, an additional central branch emerges in the mean flow, leading to trifurcation. Across all frequencies, compared to simple forcing strategies, the optimal forcing triggers a much stronger and robust spreading, by moving upstream the bifurcation point. As a result, bifurcating jets are observed on a much larger Strouhal band ($[0.35; 0.80]$) compared to the band where simple forcing achieves bifurcation in our setting ($[0.40; 0.50]$).

4.1 INTRODUCTION

Jet control is a long-standing research problem motivated by two main purposes: increasing jet mixing, and reducing jet noise. These two objectives generally act in opposite directions.

One effective way of enhancing jet mixing is to increase the global jet spreading, and thus the size of its mixing layer region. To do so, one relies on the leading large global structures of the jet, the vortex rings (Hussain and Zaman, 1980; Zaman and Hussain, 1980). Imposing an axial forcing at the jet inlet defines the frequency at which the vortex rings are generated, and so their spacing. The subsequent control of the vortex rings dynamics then allows to further control the jet spreading and mixing. Several attempts that have been carried out in the literature are now detailed.

A first possibility is to rely on the pairing instability of vortices. In some parameter settings, the axisymmetric time-periodic array of vortices is globally unstable (Shaabani-Ardali, Sipp, and Lesshafft, 2018) in a Floquet sense (Floquet, 1883): ring vortices, while being advected downstream, merge two by two, leading to thicker

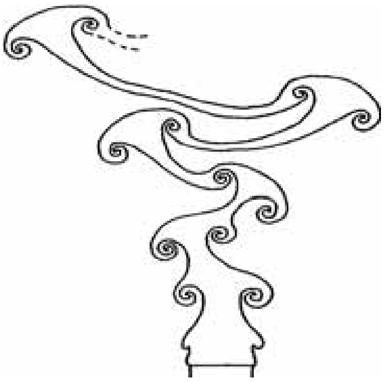

Figure 4.1: Schematic of a bifurcating jet, from Lee and Reynolds (1985).

ring vortices and to a larger mixing region. In stable cases, it is still possible to trigger the pairing instability of these vortices by adding an axisymmetric subharmonic forcing at the inlet (Hussain and Zaman, 1980; Zaman and Hussain, 1980). By choosing the phase shift between the fundamental and the subharmonic forcing, it is possible to control the occurrence or not of pairing, as done by Arbey and Ffowcs Williams (1984) or Raman and Rice (1991).

Another, more effective, possibility is to generate bifurcating and blooming jets. These jets, first studied by Lee and Reynolds (1985), are the result of a double forcing of the jet with axisymmetric and helical modes, at frequencies f_a and f_h. The difference between these two kinds of jets lies in the ratio of frequencies $R_f = f_a/f_h$. In the case of the bifurcating jet, this ratio is fixed at 2: each vortex generated is alternatively shed to the right and to the left, and then, by mutual induction, they further depart from the jet axis, leading to a bifurcating jet, as shown in figure 1.10. This jet strongly flares in the shedding plane, called hereafter the bifurcating plane, whereas this jet does not display any additional flaring in the normal plane, called the bisecting plane. This bifurcation scenario, introduced by Lee and Reynolds (1985) has been physically analysed by Parekh, Leonard, and Reynolds (1988) and Parekh, Reynolds, and Mungal (1987). They stated that *"the shear layer rolls up into a periodic array of vortex rings in response to the axial forcing. The helical or transverse forcing displaces these rings eccentrically. The resulting staggered array of rings is unstable. As a result, the rings tilt away from each other until initially adjacent rings eventually propagate along two different trajectories"*, as shown in figure 4.1. In their report, Parekh, Leonard, and Reynolds (1988) have shown that the bifurcating jet mechanism can also be triggered at large Reynolds number, and is not restricted to small Reynolds values. By fixing R_f to 3, trifurcating jets have been observed (Lee and Reynolds, 1985), but they do not display as much flaring as bifurcating jets.

This phenomenon, quite promising to enhance mixing, has been deeply analysed in a series of papers. A comprehensive review can be found in Reynolds et al. (2003). Some studies have tried to extend this method to compressible settings (Tyliszczak and Boguslawski, 2006, 2007) or to other methods of forcing, such as flapping motions (Danaila and Boersma, 1998, 2000; Gohil, Saha, and Muralidhar, 2010; Silva and Métais, 2002). From all these studies, it can be concluded that a convenient band of axisymetric forcing Strouhal numbers to observe bifurcating jets is $[0.4; 0.6]$, with a peak of bifurcation for $St_a = 0.50 - 0.55$. The existence of this band of Strouhal has been very early understood by Lee and Reynolds (1985): *"When the vortex rings are spaced far apart, the interaction between them is small. When the spacing is smaller, the interaction is stronger. When the rings are spaced closer and closer, a critical value is reached where the rings turn and run into each other without ever escaping."*

Nevertheless, other ways of achieving bifurcating jets have been developed in the 1990s. Pfizenmaier, Simon, and Monkewitz (1993) relied, with a single frequency forcing, on the spiral instability mode of a jet diffusion flame to achieve a flapping motion. One other method proposed relies on radial forcing. Experimentally, this corresponds to fluidic actuators placed along a ring around the jet inlet. These actuators pulse flow at a given frequency and are in phase opposition. Parekh et al. (1996) have shown experimentally in a compressible setting (Mach 1.47) that with a minimal mass flux, of about 1% of the mean flow flux, they were able to dramatically change the dynamics of the jet and its mixing properties. In similar settings, Freund and Moin (1998, 2000) have shown numerically that such a blowing was able to drastically reduce the size of the potential core and to enhance mixing for all the metrics they considered, such as mean mass flux or scalar disspation. Their instantaneous flow contours resemble traditional bifurcating jet flows, with vortices shed in a preferential plane entraining vortices. Simulations of this forcing have also been carried out for forcings behind real jet engines (Smith, Cain, and Chenault, 2001). In these studies, the most receptive Strouhal numbers St_h are of the order of 0.2 – 0.25. This frequency is similar to the helical forcing frequencies of the bifurcating jets with axial forcing (St_h of the order of 0.2 – 0.3), reinforcing the idea that similar mechanisms must play a role in these two flows. One other method relies on both passive and active control technique, by combining axisymmetric forcing (that triggers vortex rings) with nozzle modifications to induce non-axisymmetric perturbations on the rings. Several shapes have been tested, such as chevrons (vortex generators) in the nozzle (Zaman and Raman, 1997; Zaman, Reeder, and Samimy, 1994), stepped and sawtooth nozzles (Longmire and Duong, 1996), or inclined nozzles (Webster and Longmire, 1997).

For both of these methods – bifurcating two-frequency forcing and radial forcing – some studies have attempted to optimise the bifurcating and blooming jets. Koumoutsakos, Freund, and Parekh (1998) have tried to apply evolution strategies to optimise the bifurcating jet generated by a radial forcing. They also used vortex filament algorithms to optimise blooming jets. However, instead of carrying out global optimisation, they optimised the parameters (amplitude, frequency, phase) of a given forcing shape. Similarly, Hilgers and Boersma (2001) have applied genetic algorithms to flapping and bifurcating perturbations. In all of these studies, the computational cost was prohibitive, due to the cost of 3D-resolved DNS and the large numbers of runs needed for an optimisation. In both cases, several objective functions have been introduced: the volume integral of radial velocity, the passive scalar concentration in the outer domain or the radial displacement of vortices, and difficult compromises had to be made to mitigate the computational burden of such computations. In a later study, Tyliszczak and Geurts (2014) carried out a parametric analysis of the bifurcating jet, at $Re = 4300$ and 10000. They studied the influence of the amplitude, the forcing frequency and the phase of the forcing and of the turbulence level. Their main conclusions are, for the bifurcating jet, that the forcing amplitude must be larger than the inlet turbulence level and larger forcing amplitude leads to larger the Strouhal bifurcation band.

In the case of two-frequency forcing strategies, blooming jets occur when R_f is no longer integer: as f_a and f_h are no longer commensurate, there is no preferential plane for bifurcation, and the vortices are evolving in the full 3D space. Therefore, the jet envelope becomes conical, ensuring maximum mixing of the jet, as shown in figure 1.11. Lee and Reynolds (1985) have found that blooming, in their experimental setting, occurs for $1.6 < R_f < 3.2$ and $0.35 < St_a < 0.75$. This jet has gained attention recently with the articles of Tyliszczak (2015) and Gohil, Saha, and Muralidhar (2015). Both explain that, although at first glance the rings seem to cover uniformly all azimuthal directions, they form a distinct number of branches that can be directly linked to R_f. R_f determines also the spreading angle between two consecutive vortices; if these two consecutive vortices are on two sufficiently separated branches, these branches will not interact one with another, leading to a clear blooming.

In this study, our purpose is to find the optimal helical inlet forcing leading to jet bifurcation. To do so, we will rely on the bifurcation mechanism of Lee and Reynolds (1985) and Parekh, Leonard, and Reynolds (1988): in the vicinity of the inlet, the vortex rings do not undergo pairing and do not exhibit large displacement out of their axisymetric position. As a consequence, we consider the helical forcing induced displacements as linear perturbations from the axisymetric periodic state. We therefore seek the optimal linear helical inlet forcing that shifts the most the first vortex rings out of the axis. The base flow we consider is the time-periodic array of vortex rings generated with axisymetric forcing only. Then, we investigate which form of forcing is best suited to promote jet bifurcation — axial (Lee and Reynolds, 1985), or radial (Freund and Moin, 1998) — and the role of Strouhal number and optimisation parameters in the result. Throughout the study, the Reynolds number is fixed at 2000, moderate enough to assume a laminar flow, and large enough to be compared to experimental results, since it has been shown that the bifurcation phenomena prevails over a wide range of Reynolds numbers.

This chapter is organised as follows. In section 4.2, the optimisation procedure is detailed, with an emphasis on the base flow used and on the different norms selected for the optimisation. Then, in section 4.3, the results of the linear optimisation are discussed, emphasising the existence of one strong dominant forcing mode. The role of the different parameters involved and the implications for the physics of the bifurcating jet are also investigated. Finally, in section 4.4, the linear optimal results are plugged into $3D$ nonlinear simulations, and the results are then compared with non-optimal (simple) bifurcating forcing set-ups from the literature.

4.2 THE OPTIMISATION PROCEDURE

4.2.1 *Decomposition of the flow*

Fulfilling the idea of the bifurcation scenario of Lee and Reynolds (1985) and Parekh, Leonard, and Reynolds (1988) mentioned in section 4.1, we focus on the region close to the nozzle, where vortices are only slightly perturbed from an axisymmetric configuration. To account for this slight perturbation, we decompose the total flow $\mathbf{u}(r,\theta,z,t)$ as the sum of two components $\mathbf{U}(r,z,t)$ and $\mathbf{u}'(r,\theta,z,t)$.

On the one hand, $\mathbf{U}(r,z,t)$ represents the nonlinear axisymmetric unpaired flow that would occur without helical forcing at the jet inlet, such as displayed in figures 4.3b and 4.3c. This flow, triggered by an axisymmetric harmonic (at frequency ω) axial forcing at the inlet (plane $z=0$), is periodic. More details about its calculation are given in section 4.2.2.

On the other hand, $\mathbf{u}'(r,\theta,z,t)$ represents the real non-axisymmetric perturbations of the flow due to a given prescribed non-axisymmetric inlet forcing. In the optimisation, we will assume that $\mathbf{u}'$ is a linear perturbation forced helically, with both $m=1$ and $m=-1$ modes, at the jet inlet. By linearity, this implies that the perturbation is itself helical; we then introduce an $m=1$ complex part of the perturbation $\mathbf{u_1}(r,z,t)$, such that

$$\mathbf{u}'(r,\theta,z,t) = \mathbf{u_1}(r,z,t)e^{i\theta} + c.c. = \mathbf{u_1}(r,z,t)e^{i\theta} + \bar{\mathbf{u}}_\mathbf{1}(r,z,t)e^{-i\theta}. \tag{4.1}$$

For bifurcating jets, it is required that the frequency of the helical forcing is half the frequency ω_f of the axisymmetric forcing, as shown in section 4.1. Therefore, we can introduce the complex subharmonic helical inlet forcing functions $\mathbf{u_{1f,1}}(r)$ and $\mathbf{u_{1f,2}}(r)$ such that

$$\mathbf{u_1}(r,z=0,t) = \mathbf{u_{1f,1}}(r)\cos(\omega_f t/2) + \mathbf{u_{1f,2}}(r)\sin(\omega_f t/2), \text{ with } \mathbf{u_{1f,\cdot}}(r) \in \mathbb{C}^3. \tag{4.2}$$

This is equivalent to prescribing a total real perturbation field $\mathbf{u}'(r,\theta,z,t)$ equal to

$$\begin{aligned}\mathbf{u}'(r,\theta,z=0,t) \quad = \quad & 2\left[\mathcal{R}\left(\mathbf{u_{1f,1}}\right)\cos(\theta)\cos(\omega_f t/2) - \mathcal{I}\left(\mathbf{u_{1f,1}}\right)\sin(\theta)\cos(\omega_f t/2)\right.\\ & \left. + \mathcal{R}\left(\mathbf{u_{1f,2}}\right)\cos(\theta)\sin(\omega_f t/2) - \mathcal{I}\left(\mathbf{u_{1f,2}}\right)\sin(\theta)\sin(\omega_f t/2)\right],\end{aligned} \tag{4.3}$$

where $\mathcal{R}(\cdot)$ and $\mathcal{I}(\cdot)$ respectively denote real and imaginary parts. Therefore, each forcing component has four functional real degrees of freedom corresponding to two complex ones. More details on the optimisation are given in section 4.2.3.

To understand more physically the behaviour of such forcing, figure 4.2 represents some contours defined by iso-values of forcings that can be applied. We understand that when $\mathbf{u_{1f,1}}$ and $\mathbf{u_{1f,2}}$ have a constant and equal phase, a constant symmetry axis in the inlet plane is introduced. This symmetry axis defines the bifurcating and bisecting planes. In the following, it will be demonstrated that such a constant phase condition is enforced for the optimal forcing.

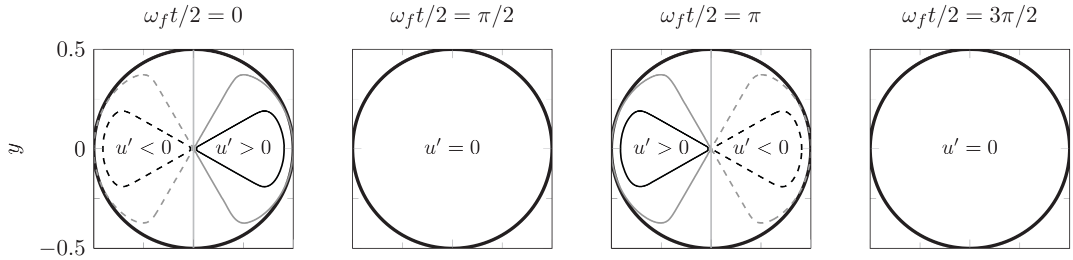

(a) $u'(r, \theta, z = 0, t) = U_0(r) \cos(\theta) \cos\left(\omega_f t/2\right)$. In this case, a constant vertical symmetry plane is observed.

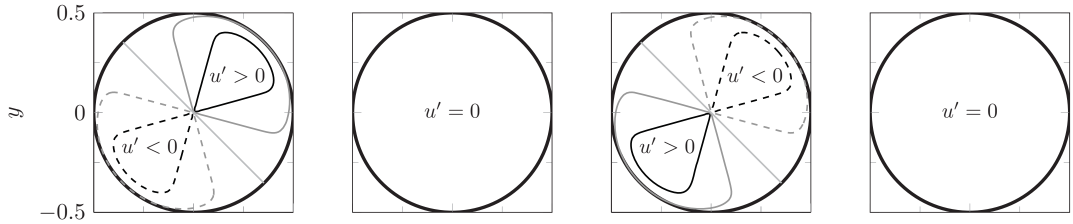

(b) $u'(r, \theta, z = 0, t) = U_0(r) \left(\cos(\theta) + \sin(\theta)\right) \cos\left(\omega_f t/2\right) / \sqrt{2}$, which can be simplified as $u'(r, \theta, z = 0, t) = U_0(r) \cos(\theta - \pi/4) \cos\left(\omega_f t/2\right)$. Compared to figure 4.2a, a $\pi/4$ azimuthal shift is introduced, shifting azimuthally the symmetry plane.

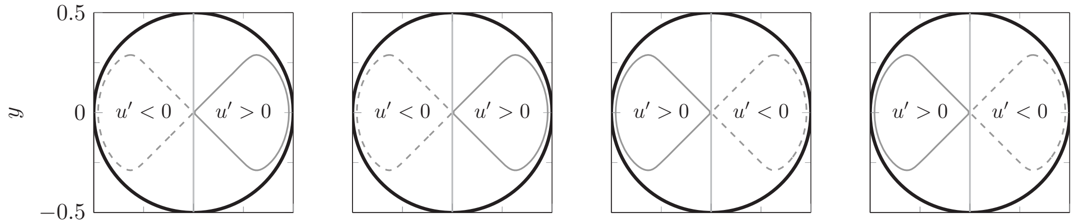

(c) $u'(r, \theta, z = 0, t) = U_0(r) \cos(\theta) \left(\cos\left(\omega_f t/2\right) + \sin\left(\omega_f t/2\right)\right) / \sqrt{2}$, which can be simplified as $u'(r, \theta, z = 0, t) = U_0(r) \cos(\theta) \cos\left(\omega_f t/2 - \pi/4\right)$. Compared to figure 4.2a, a $\pi/4$ time shift is introduced. The symmetry plane is left unchanged, constant in time.

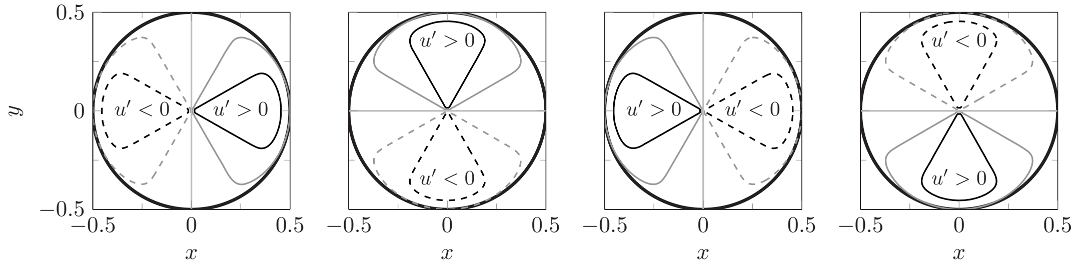

(d) $u'(r, \theta, z = 0, t) = U_0(r) \left(\cos(\theta) \cos\left(\omega_f t/2\right) + \sin(\theta) \sin\left(\omega_f t/2\right)\right) / \sqrt{2}$, which can be simplified as $u'(r, \theta, z = 0, t) = U_0(r) \cos\left(\theta - \omega_f t/2\right)$. Compared to figure 4.2a, the forcing is rotating in time. Hence, so does the symmetry plane.

Figure 4.2: Examples of isovalues of perturbation fields in the inlet plane. U_0 is defined in equation (4.7).

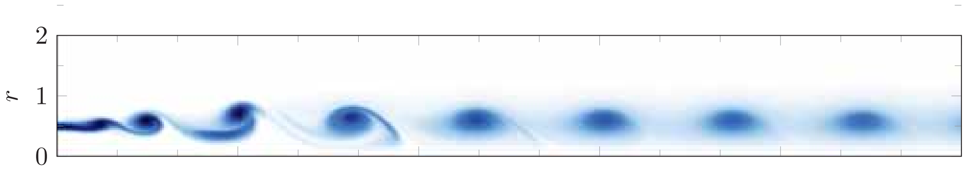

(a) Paired state ($2T_f$-periodic) at $St = 0.6$, $Re = 2000$ and $A = 5\%$ at $t = 3T_f/2$.

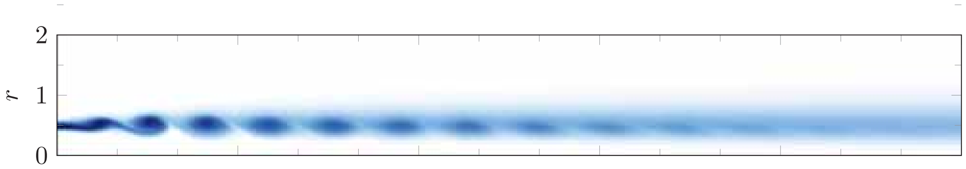

(b) Unpaired state (T_f-periodic) at $St = 0.6$, $Re = 1300$ and $A = 5\%$ at $t = T_f/2$.

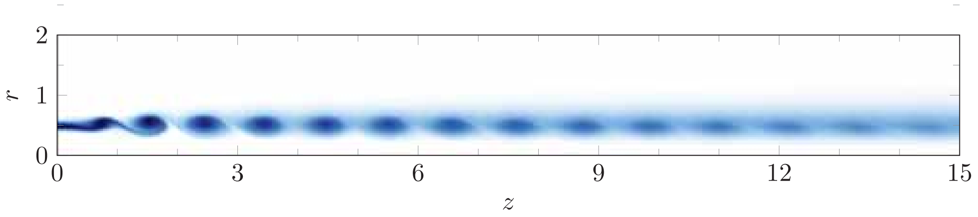

(c) Unpaired stabilised state (T_f-periodic) at $St = 0.6$, $Re = 2000$ and $A = 5\%$ at $t = T_f/2$.

Figure 4.3: Vorticity snapshots of the periodic paired and unpaired states, obtained naturally for two different parameter settings. Simulation details, forcing amplitude, Reynolds and Strouhal numbers are defined in section 4.2.2.2.

4.2.2 *Time-periodic base flow*

4.2.2.1 *Two different behaviours*

Axisymmetric harmonic forcing at the nozzle of a laminar round jet excites, over a wide range of frequencies, a shear instability of the steady flow state, leading to exponential growth of the perturbation amplitude along the axial direction. As the amplitude reaches nonlinear levels, the shear layer rolls up into a regular street of vortex rings, which form and convect at the frequency of the applied forcing. Depending on flow parameters and forcing frequency, these vortices may undergo subsequent pairing (Ho and Huerre, 1984; Hussain and Zaman, 1980; Shaabani-Ardali, Sipp, and Lesshafft, 2018; Zaman and Hussain, 1980), and if the ambient flow is sufficiently quiet and the harmonic forcing is well-controlled, this pairing takes place in a perfectly regular fashion.

In cases where pairing occurs, two neighboring vortices merge into one, such that the passage frequency of vortices downstream of the pairing location is exactly half that of the imposed forcing. If the forcing is characterised by the time period T_f, such that $\omega_f = 2\pi/T_f$, the "paired state" is globally $2T_f$-periodic (T_f-periodic upstream of the pairing and $2T_f$-periodic downstream). An example of this behaviour, obtained by direct numerical simulation, is shown in figure 4.3a.

Another case at different parameter settings, where no pairing is found to occur, is shown in figure 4.3b. Vortices roll up close to the nozzle and advect downstream, until they are dissipated by viscosity. Such a flow state is (globally) T_f-periodic and will be called hereafter an "unpaired state".

Shaabani-Ardali, Sipp, and Lesshafft (2018) have shown that the unpaired state exists for all values of parameters, but that this state may be linearly unstable in a Floquet way (Floquet, 1883). In particular, they found that, when unstable, the most unstable mode was always subharmonic at $\omega_f/2$ leading after destabilisation to a paired state.

In the case of a bifurcating jet, none of the vortices formed undergoes pairing, as shown in figures 1.10 and 4.1. In addition, the physical mechanism of Parekh, Leonard, and Reynolds (1988) explains bifurction by alternate shifting of the ring vortices achieved through helical forcing at half the vortex frequency. With pairing, paired vortices evolves at the same pace as the helical forcing, cancelling the alternate behaviour. Therefore, for the optimisation of the helical forcing, it seems natural to seek a base unpaired flow, even if this flow may be unstable with respect to axisymmetric perturbations (Shaabani-Ardali, Sipp, and Lesshafft, 2018). To do so, Shaabani-Ardali, Sipp, and Lesshafft (2017) describe a simple stabilisation tool to compute these unpaired states, which consists in adding a forcing term of the form

$$\mathbf{f} = -\lambda(\mathbf{U}(t) - \mathbf{U}(t - T_f)) \tag{4.4}$$

to the right-hand side of the Navier–Stokes equations (4.5). This allows to suppress $2T_f$-periodic fluctuations on T_f-periodic dynamics. In this framework, λ is a forcing parameter that needs to be prescribed; in this case, an optimal value of $0.044\omega_f$ has been found (Shaabani-Ardali, Sipp, and Lesshafft, 2017). In the same way as the selective frequency damping technique for steady flows (Åkervik et al., 2006), if the forced system converges towards a T_f-periodic unpaired state, the forcing will vanish, such that the recovered state is a consistent solution of the unforced Navier–Stokes equations. The results of this technique are shown in figure 4.3c, in which the stabilised flow is plotted.

4.2.2.2 *Configuration, governing equations and numerical discretisation*

Direct numerical simulations were carried out using *NEK5000*, an incompressible spectral element code. An axisymmetric laminar jet is described in cylindrical coordinates (z, r), z being the main flow direction and r being the radial distance from the jet axis. The flow is assumed to be governed by the incompressible Navier–Stokes equations with zero azimuthal velocity, written in dimensionless form as

$$\frac{\partial \mathbf{U}}{\partial t} + (\mathbf{U} \cdot \nabla)\,\mathbf{U} = -\nabla P + \frac{1}{Re}\Delta \mathbf{U}, \qquad \nabla \cdot \mathbf{U} = 0. \tag{4.5}$$

The velocity $\mathbf{U}$ has axial and radial components U and V, and P denotes pressure. The jet diameter D and the inlet centerline velocity $\overline{U}$ are used to render the flow problem nondimensional, defining the Reynolds number as $Re = \overline{U}D/\nu$, with ν the kinematic viscosity. The computational domain extends over 15×5 diameters respectively in the axial and radial directions and it is discretised with 6600 spectral elements, each containing 64 mesh points. Mesh convergence has been validated by comparing results for different spectral polynomial orders ($n = 4$, 6, 8 and 10; 8 being the standard value used hereafter). Boundary conditions are specified as follows.

1. In the inlet plane, $z = 0$, a hyperbolic-tangent velocity profile is imposed. In dimensionless form, its amplitude is modulated in time as

$$\begin{aligned} \mathbf{U}(r,t) &= \frac{1}{2}\left\{1 - \tanh\left[\frac{1}{4\theta_0}\left(r - \frac{1}{4r}\right)\right]\right\}\left(1 + A\cos\left(\omega_f t\right)\right)\mathbf{e_z} \quad (4.6)\\ &= U_0(r)\left(1 + A\cos\left(\omega_f t\right)\right)\mathbf{e_z}, \quad (4.7)\end{aligned}$$

   where A is the forcing amplitude of the jet, θ_0 is the initial dimensionless mixing layer thickness and ω_f is the axial forcing frequency. The forcing period is given by $T_f = 2\pi/\omega_f$, and the Strouhal number is defined as $St = \omega_f D/(2\pi\overline{U})$.

2. On the centerline of the jet, $r = 0$, axisymmetric boundary conditions are imposed,

$$\frac{\partial U}{\partial r} = V = \frac{\partial P}{\partial r} = 0. \quad (4.8)$$

3. In the outlet plane, $z = Z_m = 15$, and on the lateral boundary, $r = R_m = 5$, a stress-free outflow condition is applied:

$$-P\mathbf{n} + \frac{1}{Re}\left(\nabla\mathbf{U}\right)\mathbf{n} = 0, \quad (4.9)$$

   with $\mathbf{n}$ the normal vector at the boundary.

The flow configuration is thus characterised by the Reynolds number Re, the Strouhal number St, the dimensionless mixing layer thickness θ_0 and the forcing amplitude A. In this study, we keep the jet parameters fixed by considering a round jet at $Re = 2000$ with a mixing layer thickness of $\theta_0 = 0.025$. The amplitude of the axisymmetric forcing is also kept fixed to $A = 0.05$, but the forcing frequency (St) is a parameter of this study. For all Strouhal numbers considered, convergence towards a base periodic unpaired state has been achieved.

4.2.3 *Optimisation of the helical perturbation*

4.2.3.1 *Equations governing the helical perturbation*

Before writing the linearised Navier–Stokes equations, the $m = 1$ perturbation field $(\mathbf{u_1}, p_1)$ from equation (4.1) is rewritten as $(\mathbf{u_2}, p_2)$ with $\mathbf{u_2} = (u_{1,r}, iu_{1,\theta}, u_{1,z})^t$ and $p_2 = p_1$ in order to remove imaginary coefficients. The linearised Navier–Stokes equations for the perturbation $(\mathbf{u_2}, p_2)$ around the T-periodic base flow $\mathbf{U}(r,z,t)$ then read

$$\begin{aligned}
\frac{1}{r}\frac{\partial}{\partial r}(ru_{2,r}) + \frac{1}{r}u_{2,\theta} + \frac{\partial u_{2,z}}{\partial z} &= 0, && (4.10a)\\
\frac{\partial u_{2,r}}{\partial t} + U_r\frac{\partial u_{2,r}}{\partial r} + u_{2,r}\frac{\partial U_r}{\partial r} + U_z\frac{\partial u_{2,r}}{\partial z} + u_{2,z}\frac{\partial U_r}{\partial z} &= -\frac{\partial p_2}{\partial r} + \frac{1}{Re}\Delta_r\mathbf{u_2}, && (4.10b)\\
\frac{\partial u_{2,\theta}}{\partial t} + U_r\frac{\partial u_{2,\theta}}{\partial r} + U_z\frac{\partial u_{2,\theta}}{\partial z} + \frac{U_r u_{2,\theta}}{r} &= \frac{1}{r}p_2 + \frac{1}{Re}\Delta_\theta\mathbf{u_2}, && (4.10c)\\
\frac{\partial u_{2,z}}{\partial t} + U_r\frac{\partial u_{2,z}}{\partial r} + u_{2,r}\frac{\partial U_z}{\partial r} + U_z\frac{\partial u_{2,z}}{\partial z} + u_{2,z}\frac{\partial U_z}{\partial z} &= -\frac{\partial p_2}{\partial z} + \frac{1}{Re}\Delta_z\mathbf{u_2}, && (4.10d)
\end{aligned}$$

with the Laplacian in cylindrical coordinates

$$\begin{aligned}
\Delta_r\mathbf{u_2} &= \frac{1}{r}\frac{\partial}{\partial r}\left(r\frac{\partial u_{2,r}}{\partial r}\right) + \frac{\partial^2 u_{2,r}}{\partial z^2} - \frac{2u_{2,r}}{r^2} - \frac{2u_{2,\theta}}{r^2}, && (4.11a)\\
\Delta_\theta\mathbf{u_2} &= \frac{1}{r}\frac{\partial}{\partial r}\left(r\frac{\partial u_{2,\theta}}{\partial r}\right) + \frac{\partial^2 u_{2,\theta}}{\partial z^2} - \frac{2u_{2,\theta}}{r^2} - \frac{2u_{2,r}}{r^2}, && (4.11b)\\
\Delta_z\mathbf{u_2} &= \frac{1}{r}\frac{\partial}{\partial r}\left(r\frac{\partial u_{2,z}}{\partial r}\right) + \frac{1}{r^2}\frac{\partial^2 u_{2,z}}{\partial \phi^2} + \frac{\partial^2 u_{2,z}}{\partial z^2}. && (4.11c)
\end{aligned}$$

The following boundary and compatibility conditions are imposed:

$$\begin{aligned}
&\mathbf{u_2} = \mathbf{u_{2f,1}}(r)\cos(\omega_f t/2) + \mathbf{u_{2f,2}}(r)\sin(\omega_f t/2) \text{ at } z = 0, && (4.12a)\\
&\frac{\partial u_{2,r}}{\partial r} = \frac{\partial u_{2,\theta}}{\partial r} = u_{2,z} = 0 \text{ at } r = 0, && (4.12b)\\
&u_{2,r} + u_{2,\theta} = 0 \text{ at } r = 0, && (4.12c)\\
&\frac{1}{Re}\frac{\partial u_{2,r}}{\partial r} - p = \frac{\partial u_{2,\theta}}{\partial r} = \frac{\partial u_{2,z}}{\partial r} = 0 \text{ at } r = R_m, && (4.12d)\\
&\frac{1}{Re}\frac{\partial u_{2,z}}{\partial z} - p = \frac{\partial u_{2,r}}{\partial z} = \frac{\partial u_{2,\theta}}{\partial z} = 0 \text{ at } z = Z_m. && (4.12e)
\end{aligned}$$

with $\mathbf{u_{2f,1}}$ and $\mathbf{u_{2f,2}}$ the corresponding inlet forcings modified from $\mathbf{u_{1f,1}}$ and $\mathbf{u_{1f,2}}$. In this new formalism, equations for $\mathbf{u_2}$ only involve real coefficients, which is much more convenient for numerical computations.

4.2.3.2 *Optimisation procedure*

We aim at finding the optimal inlet forcing that maximally shifts the vortices off the axis, at a given optimisation time T_o, per unit of input energy. Formally, we want to solve

$$\max_{\|\mathbf{u}'(r,\theta,z=0,t)\|_f=1} \left\|\mathbf{u}'(r,\theta,z,t=T_o)\right\|, \tag{4.13}$$

with $T_o \longrightarrow \infty$. Again, the forcing $\mathbf{u}'(r,\theta,z=0,t)$ is assumed periodic of period $\omega_f/2$ (see eqn. (4.3)). The different norms used for forcing and response are detailed in section 4.2.4.

As will be demonstrated in section 4.3, this problem is well-posed, since the response converges towards an $\omega_f/2$-periodic limit cycle when $T_o \longrightarrow \infty$. This shows that the base flow is stable with respect to $m = 1$ subharmonic perturbations.

If the base flow were steady, the forced equations for linear perturbations could be written as

$$\frac{\partial \mathbf{u}'}{\partial t} = L\mathbf{u} + \hat{f}e^{i\omega t}, \tag{4.14}$$

which would lead to a traditional resolvent analysis (Schmid, 2007). However, because in our case L depends on t, this type of analysis is not possible.

Several algorithms are available for the problem at hand.

First, a classical direct-adjoint algorithm, already employed for periodic flow optimal perturbation analysis by Blackburn, Sherwin, and Barkley (2008), can be used. However, in the present optimisation, the flow perturbation field $\mathbf{u_2}$ is two-dimensional, while the prescribed inlet forcings $\mathbf{u_{2f,1}}(r)$ and $\mathbf{u_{2f,2}}(r)$ are only one-dimensional. Therefore, if a direct-adjoint calculation is carried out, the adjoint field needs eventually to be projected on the $1D$ inlet, and extra care needs to be taken to ensure this is done properly, as in Boujo and Gallaire (2015).

Another technique relies on the decomposition of the linearised operator, the forcing and response into Fourier components, and to solve the equations in Fourier space, as suggested by *harmonic-balance* methods. This has not been attempted here because of the considerable changes needed in the code compared to a standard time-stepping method, and the strong stiffness of these Newton-like problems.

In this work, the optimisation is instead carried out through a classical direct time-marching scheme detailed in section 4.2.3.3. A basis of forcing functions is chosen and time-stepped. Since the forcings only vary along the single radial dimension, a 300-dimensional basis is sufficient to accurately resolve the forcing space. Once time-stepping is carried out, thanks to linearity, the optimal combination of all 300 forcing vectors is calculated. This technique has several advantages compared to the two previous ones.

First, since the time-stepping step and the optimisation step are uncoupled in this process, many optimisation parameters, such as the final time T_o, the norm chosen for the optimisation or other norm-related parameters do not need to be fixed beforehand. They can be adjusted afterwards with the time-stepping results in order to make the results independent of these technical parameters. Changing these hyper-parameters can be done almost for free.

Then, in our case the time-marching step relies on an implicit scheme based on matrix inversions (see section 4.2.3.3); as the base flow changes at every time step, the matrix needs to be recalculated at every time-step, requiring a significant computation time. Therefore, time-marching $N \gg 1$ vectors simultaneously instead of 1 at a time for direct-adjoint optimisations saves computational time. In addition, our approach simply removes the need to compute the adjoint part, thereby saving time.

Finally, compared to the harmonic-balance techniques, which only capture the infinite time-horizon behaviour, our technique also allows to resolve transient dynamics.

4.2.3.3 *Implementation*

The evolution of the perturbation equations defined in section 4.2.3.1 is calculated using a fully implicit finite-difference time-stepping scheme of second order, implemented in the finite-element solver FreeFem++ (Hecht, 2012). The mesh has the same size and resolution as the one used in the Nek5000 calculations. $P2$ finite elements are used for the velocity perturbation, whereas $P1$ finite elements are used for the pressure.

Once time-stepping is completed, the calculation of the optimal forcing combination can be done easily with Octave/Matlab routines. The resulting optimal forcing and response fields from this combination can then be obtained in FreeFem++.

This study is carried out for 10 values of the Strouhal number, from 0.35 to 0.80 with a 0.05-step, at a Reynolds number of 2000.

4.2.4 *Forcing and response norms*

In equation (4.13), the norms used for forcing and response needs to be specified. For the forcing, we consider the energy ($\mathcal{L}_2$) norm, and for the response, two norms are introduced: the energy ($\mathcal{L}_2$) norm, and a norm based on the displacement of vortices.

Before going any further, let us remind notations on scalar products. The scalar product of two real numbers x, y reads $\langle x, y\rangle = xy$. In the complex case, the scalar product of two complex numbers z and z' is $\langle z, z'\rangle = \bar{z}z'$. Subsequently, if $\mathbf{a} = (a_i)_i$ and $\mathbf{b} = (b_i)_i$ are two vectors, their scalar product is $\langle \mathbf{a}, \mathbf{b}\rangle = \sum_i \langle a_i, b_i\rangle$. In the following, $\mathbf{u}'$ and $\mathbf{v}'$ are real vectors corresponding to real perturbation fields, whereas $\mathbf{u_2}$ and $\mathbf{v_2}$ are complex vectors corresponding to the helical mode $m = 1$.

4.2.4.1 *$\mathcal{L}_2$ norm for the forcing*

For the forcing $\mathbf{u}'$, the standard $\mathcal{L}_2$ energy norm is used. This norm is derived from the following scalar product, which involves an integration over a full forcing period:

$$\langle \mathbf{u}', \mathbf{v}'\rangle_f = \frac{1}{2T_f}\frac{1}{2\pi}\int_0^{2T_f}\int_0^{2\pi}\int_0^{R_m} r\langle \mathbf{u}'(r,\theta,z=0,t), \mathbf{v}'(r,\theta,z=0,t)\rangle \mathrm{d}r\,\mathrm{d}\theta\,\mathrm{d}t \tag{4.15a}$$

$$= \int_0^{R_m} r\left(\langle \mathcal{R}(\mathbf{u_{2f,1}}), \mathcal{R}(\mathbf{v_{2f,1}})\rangle + \langle \mathcal{I}(\mathbf{u_{2f,1}}), \mathcal{I}(\mathbf{v_{2f,1}})\rangle + \langle \mathcal{R}(\mathbf{u_{2f,2}}), \mathcal{R}(\mathbf{v_{2f,2}})\rangle + \langle \mathcal{I}(\mathbf{u_{2f,2}}), \mathcal{I}(\mathbf{v_{2f,2}})\rangle\right)\mathrm{d}r \tag{4.15b}$$

$$= \frac{1}{2}\int_0^{R_m} r\left(\langle \mathbf{u_{2f,1}}, \mathbf{v_{2f,1}}\rangle + \langle \overline{\mathbf{u_{2f,1}}}, \overline{\mathbf{v_{2f,1}}}\rangle + \langle \mathbf{u_{2f,2}}, \mathbf{v_{2f,2}}\rangle + \langle \overline{\mathbf{u_{2f,2}}}, \overline{\mathbf{v_{2f,2}}}\rangle\right)\mathrm{d}r. \tag{4.15c}$$

This scalar product is different from the standard scalar product for complex numbers. While this must be kept in mind during the optimisation process,the norm it induces for the forcing $\mathbf{u}'$ is the standard $\mathcal{L}_2$ norm:

$$\|\mathbf{u}'\|_f^2 = \int_0^{R_m} r\left(\langle \mathbf{u_{2f,1}}, \mathbf{u_{2f,1}}\rangle + \langle \mathbf{u_{2f,2}}, \mathbf{u_{2f,2}}\rangle\right)\mathrm{d}r. \tag{4.16}$$

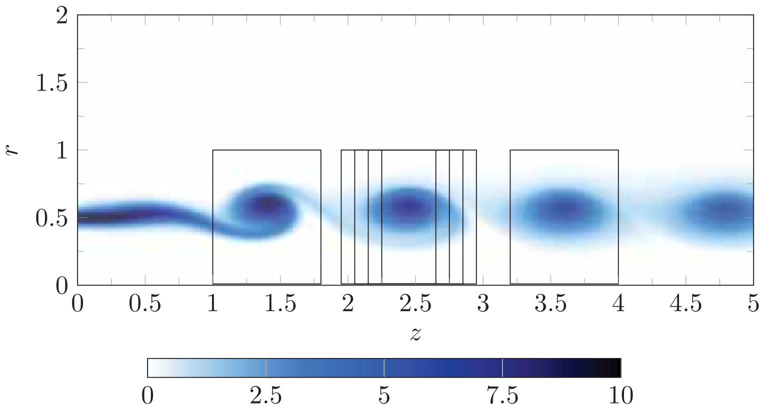

Figure 4.4: Vorticity cut of the $Re = 2000$, $St = 0.50$ base unpaired flow, with vortex domains represented for the first three vortices. For the second vortex, four δ_z sizes are sketched (0.4, 0.6, 0.8, 1.0), whereas for the first and third ones, only the $\delta_z = 0.8$ box is represented.

4.2.4.2 *$\mathcal{L}_2$ norm for response*

For the response, one possible norm is the energy norm based on the following scalar product:

$$\begin{aligned}
&\langle \mathbf{u}'(T_o), \mathbf{v}'(T_o)\rangle_2 \\
=&\frac{1}{2}\frac{1}{2\pi}\int_0^{Z_{opt}}\int_0^{2\pi}\int_0^{R_m} r\langle \mathbf{u}'(r,\theta,z,t=T_o), \mathbf{v}'(r,\theta,z,t=T_o)\rangle \mathrm{d}r\,\mathrm{d}\theta\,\mathrm{d}z && (4.17a)\\
=&\int_0^{Z_{opt}}\int_0^{R_m} r\left(\langle \mathcal{R}(\mathbf{u_2}), \mathcal{R}(\mathbf{v_2})\rangle + \langle \mathcal{I}(\mathbf{u_2}), \mathcal{I}(\mathbf{v_2})\rangle\right)\mathrm{d}r\,\mathrm{d}z && (4.17b)\\
=&\frac{1}{2}\int_0^{Z_{opt}}\int_0^{R_m} r\left(\langle \mathbf{u_2}(r,z,T_o), \mathbf{v_2}(r,z,T_o)\rangle + \langle \overline{\mathbf{u_2}}(r,z,T_o), \overline{\mathbf{v_2}}(r,z,T_o)\rangle\right)\mathrm{d}r\,\mathrm{d}z. && (4.17c)
\end{aligned}$$

Because we are interested in the evolution of perturbations close to the inlet, this scalar product is calculated on a reduced domain $(r,z) \in [0; R_m] \times [0; Z_{opt}]$. Unless specified otherwise, in the following, a value of $Z_{opt} = 5$ is chosen. The effect of this value is investigated in section 4.3.4.1. Once again, this scalar product is different from the standard scalar product for complex numbers. However, the corresponding $\mathcal{L}_2$ norm for the response remains the same:

$$\|\mathbf{u}'(T_o)\|_2^2 = \int_0^{Z_{opt}}\int_0^{R_m} r\langle \mathbf{u_2}(r,z,T_o), \mathbf{u_2}(r,z,T_o)\rangle \mathrm{d}r\,\mathrm{d}z. \tag{4.18}$$

Note that, for the response, both $\mathcal{L}_2$ scalar product and norm are not integrated over a full forcing period since this would require to store every time-step of every response field: storage is only done once every forcing period T_f. Therefore, a fixed time-shift with respect to the axisymmetric forcing is chosen equal to 0: T_o is taken as $2nT_f$, with $n \in \mathbb{N}$. The influence of this shift is investigated in section 4.3.4.4, while the influence of n is discussed in section 4.3.4.5.

4.2.4.3 *Displacement norm for response*

The bifurcation scenario (Lee and Reynolds, 1985; Parekh, Leonard, and Reynolds, 1988) relies on a slight tilt and shift of the vortices in the near field of the jet

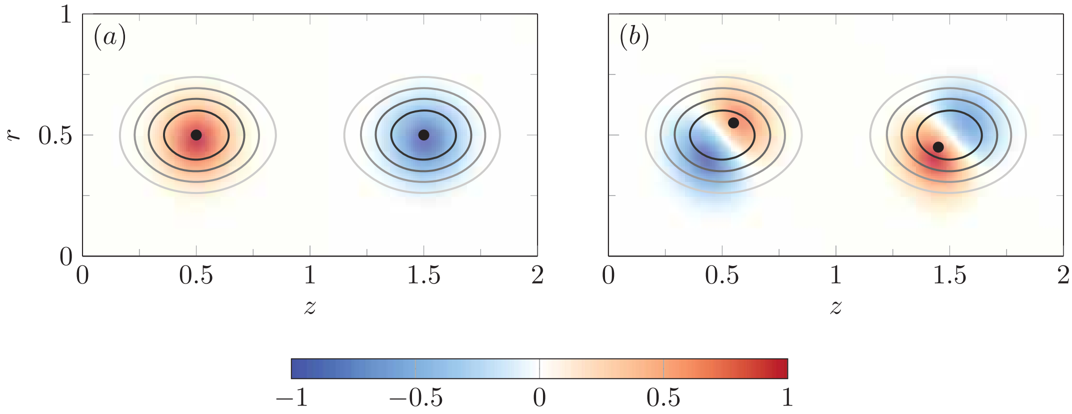

Figure 4.5: Schematic of base vortices (contour lines) superposed with a vorticity perturbation (colour field). The points represent the centroid of the superposition of the base flow and a finite-amplitude perturbation. (a), the perturbation does not change the centroid location, hence the displacement norm for this perturbation is zero. However, the perturbation is not identically zero, and so is not its $\mathcal{L}_2$ norm. (b), the perturbation moves the centroid, and thus both norms are non-zero in this case.

inlet. Therefore, in this section, we define an alternative norm that quantifies the displacement of vortices from a given configuration. The location of a given vortex i at T_o in a (r, z)-plane, cut at an angle θ_c, can be defined as the centroid of its vorticity ω_θ along θ

$$\mathbf{x}_i(\theta_c, T_o) = \frac{\iint_{r,z\in\mathbf{\Omega}_i} r\omega_\theta(r,\theta_c,z,T_o)\mathbf{x}\,\mathrm{d}r\,\mathrm{d}z}{\iint_{r,z\in\mathbf{\Omega}_i} r\omega_\theta(r,\theta_c,z,T_o)\,\mathrm{d}r\,\mathrm{d}z}, \tag{4.19}$$

with $\mathbf{\Omega}_i$ the domain of the i^{th}-vortex. This domain is defined as the rectangle $(z,r) \in [Z_i - \delta_z/2; Z_i + \delta_z/2] \times [0;1]$, with Z_i the axial component of the centroid of the i^{th}-vortex and δ_z conveniently fixed at 0.8. Examples of such boxes are represented in figure 4.4. The effect of δ_z on the optimisation is investigated in section 4.3.4.2.

The vorticity field ω_θ can be written as the sum of the vorticity Ω_θ induced by the base flow $\mathbf{U}(r,z,t)$ and an infinitesimal perturbation ω'_θ induced by the $m = 1$ perturbation $\mathbf{u}'$:

$$\Omega_\theta(r,z,t) = \frac{\partial U_r}{\partial z} - \frac{\partial U_z}{\partial r}, \tag{4.20}$$

$$\begin{aligned} \omega'_\theta(r,\theta,z,t) &= \frac{\partial u'_r}{\partial z} - \frac{\partial u'_z}{\partial r} \\ &= \left(\frac{\partial u_{2,r}}{\partial z} - \frac{\partial u_{2,z}}{\partial r}\right) e^{i\theta} + c.c. \\ &= \omega_{2,\theta}(r,z,t)e^{i\theta} + c.c. \end{aligned} \tag{4.21}$$

By specifying a perturbation amplitude $\epsilon \ll 1$, we get:

$$\begin{aligned} \omega_\theta(r,\theta,z,t) &= \Omega_\theta(r,z,t) + \epsilon\omega'_\theta(r,\theta,z,t) && (4.22a) \\ &= \Omega_\theta(r,z,t) + \epsilon\omega_{2,\theta}(r,z,t)e^{i\theta} + \epsilon\overline{\omega_{2,\theta}}(r,z,t)e^{-i\theta}. && (4.22b) \end{aligned}$$

The displacement norm with respect to the i^{th}-vortex $\mathbf{\Omega}_i$ can then be defined as:

$$\|\mathbf{u}'(T_o)\|^2_{disp,\mathbf{\Omega}_i} = \frac{1}{2}\frac{1}{2\pi}\int_0^{2\pi} \left\| \left.\frac{\mathrm{d}\mathbf{x}_i(\theta_c,T_o)}{\mathrm{d}\epsilon}\right|_{\epsilon=0} \right\|_2^2 \mathrm{d}\theta_c. \tag{4.23}$$

For each vortex considered, it is possible to define a corresponding displacement norm. In the present study, because of the bifurcation scenario (Parekh, Leonard, and Reynolds, 1988), the displacement norms for the first three vortices is considered. Then, the axial position of the third vortex, depending on the Strouhal number considered, approximately corresponds to 5 jet diameters, which is consistent with the optimisation domain chosen for the $\mathcal{L}_2$ norm (4.17b). Full details of on this norm are given in appendix 4.A.

Note that the displacement norm is not *strictly* a norm but a *semi-norm*: in other words, $\|\mathbf{u}'(T_o)\|_{disp,\mathbf{\Omega}_i} = 0$ does not necessarily imply that $\mathbf{u}'(T_o) = \mathbf{0}$. As can be seen in appendix 4.A and in figure 4.5, the displacement norm being equal to zero only implies that the vorticity centroid of the base flow and of the perturbation are at the same place, not that the perturbation is equal to zero. Therefore, the alternating pattern of figure 4.5b is a good candidate for a large displacement norm at fixed $\mathcal{L}_2$ norm. In this figure, one can easily understand that a large $\mathcal{L}_2$ norm does not necessarily imply a large displacement norm. Conversely, since the $\mathcal{L}_2$ norm is a true norm, a large displacement norm must imply a large $\mathcal{L}_2$ norm.

Eventually, because of the definition of this norm that focuses on a given vortex i, one displacement norm can be defined for each vortex ring. In our study, we assume the linear behaviour to be only valid in the vicinity of the inlet, where perturbations remains quite small; therefore we only consider the displacement norm for each of the first three vortex rings.

4.2.5 *Construction of a basis of forcings*

As explained in section 4.2.3.2, our purpose is to find the optimal forcing as the optimal linear combination of one-dimensional forcing functions. Both for convenience and to improve numerical accuracy, it is preferable to have a basis that is orthonormal with respect to the scalar product used for forcing (see section 4.2.4.1). This naturally suggests the use of Bessel functions, as the problem is formulated in cylindrical coordinates. As our problem is non-singular in $r = 0$, we focus on Bessel functions of the first kind J_k.

The Bessel functions J_0, J_1 and J_2, plotted in figure 4.6, verify the properties (Abramowitz and Stegun, 1964)

$$J_0(0) - 1 = J_1(0) = J_2(0) = J'_0(0) = J'_2(0) = 0. \tag{4.24}$$

Moreover, by denoting $\lambda_{i,n}$ the n^{th} root of J_i, these function verify the orthogonality property

$$\int_0^1 rJ_i(r\lambda_{i,n})\, J_i(r\lambda_{i,m})\,\mathrm{d}r = \frac{\delta_{mn}}{2}[J_{i+1}(\lambda_{i,n})]^2. \tag{4.25}$$

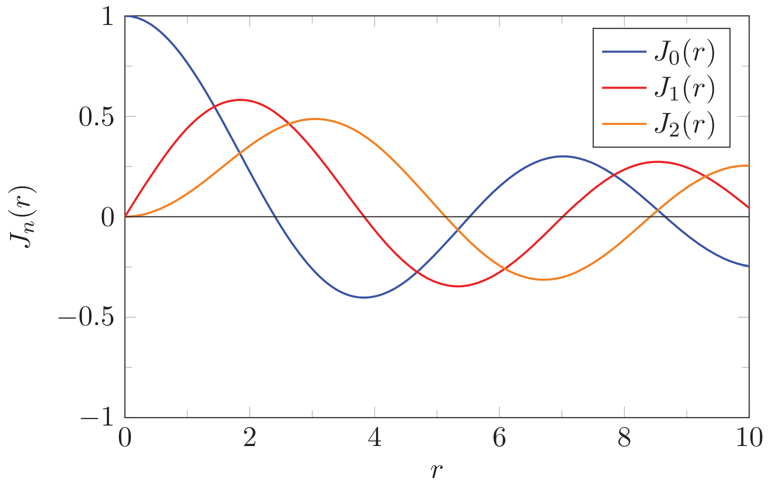

Figure 4.6: Bessel functions of the first kind J_0, J_1 and J_2.

j	$(u_{2f,1,r}, u_{2f,1,\theta}, u_{2f,1,z}, u_{2f,2,r}, u_{2f,2,\theta}, u_{2f,2,z})$
$1 \leq j \leq N$	$J_0(r\lambda_{0,j})\ (1,-1,0,0,0,0)\ \mathbb{1}_{[0;1]}/\lvert J_1(\lambda_{0,j})\rvert$
$N < j \leq 2N$	$J_2(r\lambda_{2,j-N})\ (1,1,0,0,0,0)\ \mathbb{1}_{[0;1]}/\lvert J_3(\lambda_{2,j-N})\rvert$
$2N < j \leq 3N$	$J_1(r\lambda_{1,j-2N}/2)\ (0,0,1,0,0,0)\ \mathbb{1}_{[0;2]}/\left(\sqrt{2}\lvert J_2(\lambda_{1,j-2N})\rvert\right)$
$3N < j \leq 4N$	$J_0(r\lambda_{0,j-3N})\ (0,0,0,1,-1,0)\ \mathbb{1}_{[0;1]}/\lvert J_1(\lambda_{0,j-3N})\rvert$
$4N < j \leq 5N$	$J_2(r\lambda_{2,j-4N})\ (0,0,0,1,1,0)\ \mathbb{1}_{[0;1]}/\lvert J_3(\lambda_{2,j-4N})\rvert$
$5N < j \leq 6N$	$J_1(r\lambda_{1,j-5N}/2)\ (0,0,0,0,0,1)\ \mathbb{1}_{[0;2]}/\left(\sqrt{2}\lvert J_2(\lambda_{1,j-5N})\rvert\right)$

Table 4.1: Description of the orthonormal basis of forcing functions used in the optimisation. The indicator function $\mathbb{1}_I$, where I is an interval, is 1 on I and 0 elsewhere.

We want to create a forcing basis that meets two criteria: first, it must be othogonal, and second, all basis functions must verify the boundary conditions at $r = 0$ (eqns. (4.12b) and (4.12c)).

We consider the N first Bessel functions $J_0(r\lambda_{0,m})$, $J_1(r\lambda_{1,m})$ and $J_2(r\lambda_{2,m})$ with which we can build a set of $6N$ basis functions. These orthonormal basis functions are defined in table 4.1. For both radial and azimuthal forcings, a r-support over $[0;1]$ is chosen, as their optimisation displayed in figure 4.10 reveals a quick decay after $r = 0.5$ of these components; conversely, for the axial component, an r-support over $[0;2]$ is chosen, since its decay is slower.

Any forcing function $(\mathbf{u}_{2f,1}, \mathbf{u}_{2f,2})$ can be decomposed onto this basis. Indeed, $u_{2f,1,r} - u_{2f,1,\theta}$ and $u_{2f,2,r} - u_{2f,2,\theta}$ are functions with a zero-derivative on the axis (see eqn. (4.12b)), and, by assuming that they have a compact support $[0;1]$, they can be decomposed into a $J_0(r\lambda_{0,j})\mathbb{1}_{[0;1]}$ series, where the indicator function $\mathbb{1}_{[0;1]}$ is 1 on $[0;1]$ and 0 elsewhere.

Moreover, $u_{2f,1,r} + u_{2f,1,\theta}$ and $u_{2f,2,r} + u_{2f,2,\theta}$ are functions with a zero-value and a zero-derivative on the axis (see eqn. (4.12b)-(4.12c)). By assuming again that they have a compact support $[0;1]$, they can be decomposed into a $J_2(r\lambda_{2,j})\mathbb{1}_{[0;1]}$ series.

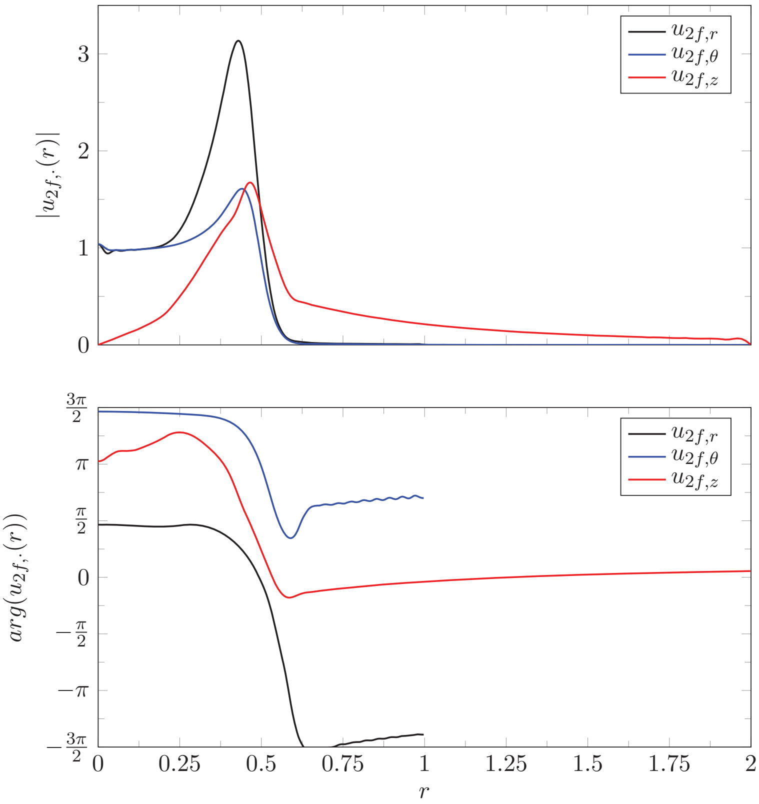

Figure 4.7: $\mathcal{L}_2$ norm optimal forcing modulus and phase for $Re = 2000$ and $St = 0.50$. The phase was unwrapped to remain continuous in r. $|\mathbf{u_{2f}}(r)|$ and $arg(\mathbf{u_{2f}}(r))$ are defined in equation (4.26b).

Finally, $u_{2f,1,z}$ and $u_{2f,2,z}$ have a zero-value at $r = 0$ (see eqn. (4.12b)). By assuming a compact support $[0;2]$, they can be decomposed into a $J_1(r\lambda_{1,j})\mathbb{1}_{[0;2]}$ series.

Further details of the optimisation procedure are given in appendix 4.B.

4.3 RESULTS OF THE OPTIMISATION

Throughout the entire section, except in section 4.3.4.5, the optimization time T_o used is chosen large enough such that the gain, forcing and response have reached thir asymptotic values ($T_o \to \infty$).

4.3.1 $St = 0.50$ *case*

In this subsection, the optimal $\mathcal{L}_2$ norm long-term forcing and response for the $Re = 2000$ and $St = 0.5$ case are discussed. This particular set of parameters is chosen since it leads to one of the largest vortex spreading in bifurcating jets, according to literature (Gohil, Saha, and Muralidhar, 2015; Parekh, Leonard, and Reynolds, 1988; Tyliszczak and Geurts, 2014).

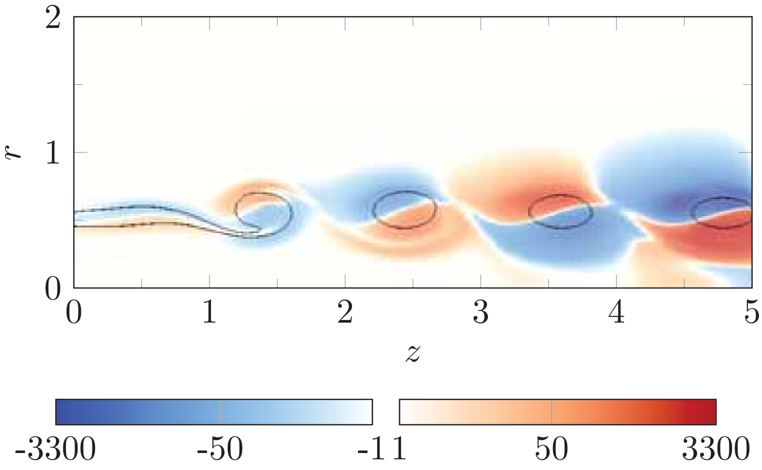

Figure 4.8: $\mathcal{L}_2$ norm optimal vorticity response $\omega'_{2,\theta,opt}$ snapshot $Re = 2000$ and $St = 0.50$ at a zero phase. A level-4 contours of base flow vorticity has been added to understand the response pattern. A truncated and sign-sensitive logarithmic scale has been used.

Concerning the optimal forcing, as shown in appendix 4.B.1, $\mathbf{u_{1f,1}}(r)$ and $\mathbf{u_{1f,2}}(r)$ can be chosen as real: choosing them complex is equivalent to shifting azimuthally the bifurcation plane. In this case, the optimal forcing can be rewritten as:

$$\begin{aligned} \mathbf{u_2}(r, z = 0, t) &= \mathbf{u_{2f,1}}(r)\cos(\omega_f t/2) + \mathbf{u_{2f,2}}(r)\sin(\omega_f t/2) && (4.26a)\\ &= |\mathbf{u_{2f}}(r)|\cos(\omega_f t/2 + arg(\mathbf{u_{2f}}(r))), && (4.26b) \end{aligned}$$

where the cosine function is evaluated component-wise.

The functions $|\mathbf{u_{2f}}(r)|$ and $arg(\mathbf{u_{2f}}(r))$ are displayed in figure 4.7. All three components of forcing peak in the jet mixing layer. It is well-known (Ho and Huerre, 1984) that this area is the most receptive area of jets. Moreover, the dominant forcing component is the radial one. This shows that it is much more effective to force in the radial direction than to force in the axial or azimuthal direction, the axial direction being the one mostly chosen for bifurcating jets in the literature (Hilgers and Boersma, 2001; Reynolds et al., 2003; Tyliszczak and Geurts, 2014). Finally, concerning the phase, in all three components, a phase shift is observed across the mixing layer. This phase shift is of roughly π for $u_{2f,\theta}$, 2π for $u_{2f,r}$ and of $\pi - 3\pi/2$ for $u_{2f,z}$. This induces additional shear in the mixing layer, strengthening or weakening locally the vortex to be formed.

Concerning the optimal response, represented in figure 4.8, we see the presence of alternating positive and negative vortcity patches. In the mixing layer where the vortices are not yet formed, the positive and negative patches fit closely the mixing layer sides. When vortices have rolled up, the patches spread on either side of the formed vortex rings in an alternate fashion. The intensity of the patches grows exponentially with the axial distance z. The contours of base flow vorticity show that the effect of these patches is to shift the vortex positions as expected. In an (r, z) cut, two consecutive vortices are therefore sent in opposite directions. For a given vortex ring, two opposed points (separated by π in the θ direction), are sent into opposite r and z directions, because of the helical nature of the perturbation. As

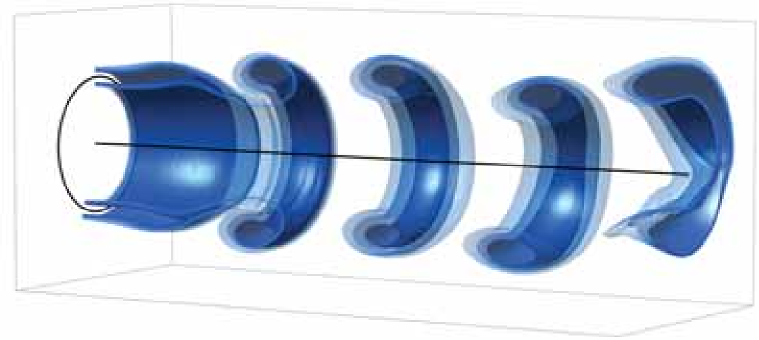

Figure 4.9: Snapshot of the superposition of the base flow and of the $\mathcal{L}_2$ norm optimal response with a finite amplitude at $Re = 2000$ and $St = 0.50$.

a consequence, in $3D$, consecutive vortex rings are globally shifted off the axis in alternate directions.

This is demonstrated in figure 4.9, where the axisymmetric unpaired base flow and the optimal $m = 1$ response are superposed. The vortices are alternatively shed towards the top and the bottom.

The optimal gain and the first suboptimal gain values are calculated. The first suboptimal forcing mode, and its corresponding gain and response, are defined as the optimal forcing mode that is also orthogonal (with respect to the forcing scalar product) to the optimal forcing mode. Although the optimal gain value in itself does not have a clear meaning, since we compare a $2D$-response to a $1D$-forcing, its large value (1.01×10^3) shows a strong receptivity of the flow to this kind of forcing. Also, the strong gain separation – the optimal gain being 102 times larger than the first suboptimal at $St = 0.50$ – shows that only the leading forcing mode is relevant in this study; the suboptimal ones only contribute marginally to the linear results.

4.3.2 *Effect of the Strouhal number St*

In this section, we investigate the effect of the Strouhal number on optimisation results, obtained with respect to the $\mathcal{L}_2$ norm.

Figure 4.10 represents the optimal forcing shapes – modulus and phase of each component – for four different Strouhal numbers (0.35, 0.50, 0.65, 0.80). A striking result is that we observe little change of the modulus shape by varying Strouhal number; however, the phases vary greatly. In fact, this latter change can be understood as an overall shift of the phase functions: for each Strouhal number, the phase variations remains the same, up to a constant shift.

In order to understand this shift quantitatively, we compare the values of two kinds of scalar products between optimal forcings. On the one hand, we compute the standard scalar product (4.15c) for all Strouhal numbers; results are displayed in table 4.2a. On the other hand, we calculate, for the four Strouhal numbers considered in figure 4.10, the scalar products between their forcing modulus, as displayed in table 4.2b. This latter scalar product only accounts for the modulus shape discrepancies of the forcing, not for the phase discrepancies. By comparing

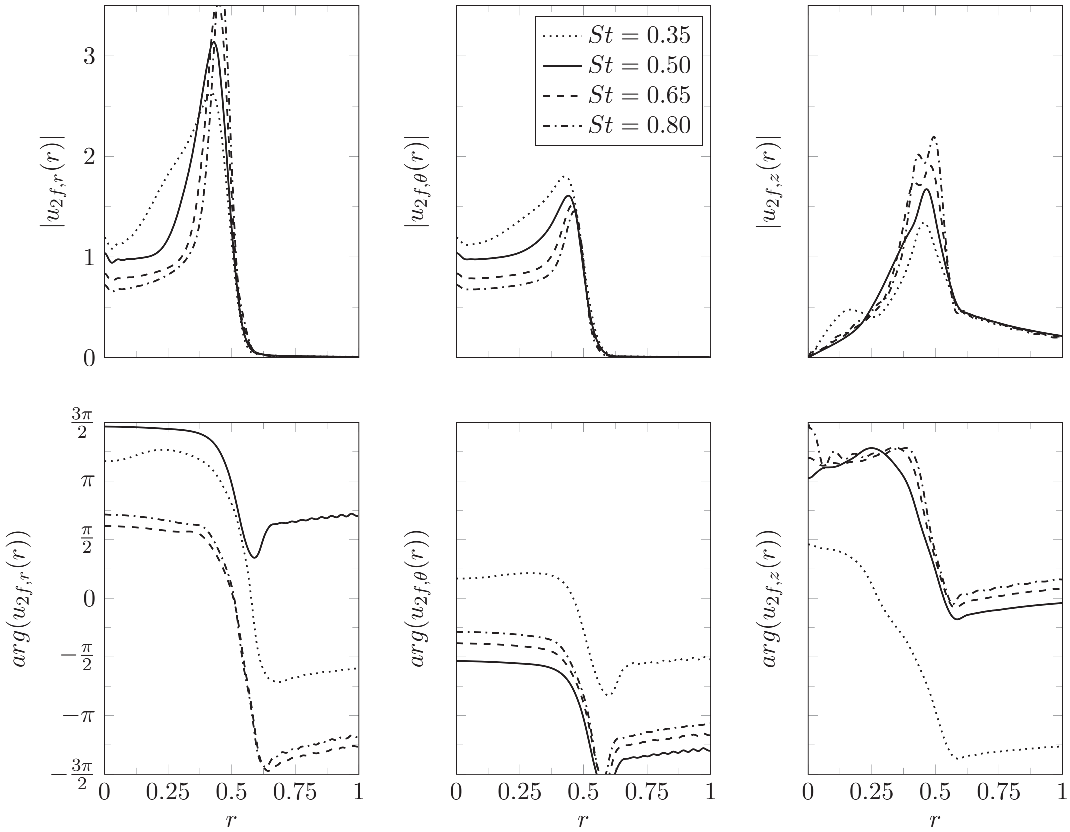

Figure 4.10: Evolution of the $\mathcal{L}_2$ norm optimal forcing modulus and phase for four different Strouhal numbers. $|\mathbf{u_{2f}}(r)|$ and $arg(\mathbf{u_{2f}}(r))$ are defined in equation (4.26b).

these two results, it can be easily found that most of the discrepancy is due to the phase difference, and not the shape difference. This is encouraging for practical applications of this method: if this optimal forcing shape were implemented in a physical device, this device could work efficiently for different Strouhal numbers by just varying the phase shift between forcings.

Optimal response shapes remain very similar to those represented in figure 4.8 across all Strouhal numbers. However, it is hard to derive precise quantitative comparisons of the responses, since these are located around base flow vortices, whose position varies with Strouhal number.

The evolution of the optimal and first suboptimal gains as a function of the Strouhal number is represented in figure 4.11. Concerning the optimal gain, we observe large variations across Strouhal numbers with an exponential growth as a function of Strouhal until 0.75, where it seems to reach a saturation point. These results are interesting since the literature on bifurcating jets (Danaila and Boersma, 1998, 2000; Gohil, Saha, and Muralidhar, 2010; Reynolds et al., 2003; Silva and Métais, 2002; Tyliszczak and Boguslawski, 2006, 2007) usually reports bifurcation in the Strouhal range [0.4; 0.6], whereas our optimal gain keeps growing for Strouhal numbers greater than 0.60. This discrepancy will be further discussed with nonlinear results, in section 4.4.3.

St	0.35	0.50	0.65	0.80
0.35	1.000	0.763	0.424	0.209
0.50	0.763	1.000	0.884	0.728
0.65	0.424	0.884	1.000	0.955
0.80	0.209	0.728	0.955	1.000

(a) $\mathcal{L}_2$ norm optimal forcings.

St	0.35	0.50	0.65	0.80
0.35	1.000	0.980	0.929	0.888
0.50	0.980	1.000	0.978	0.946
0.65	0.929	0.978	1.000	0.989
0.80	0.888	0.946	0.989	1.000

(b) $\mathcal{L}_2$ norm optimal forcings modulus.

Table 4.2: Comparison of $\mathcal{L}_2$ norm optimal forcings and their modulus for different Strouhal numbers.

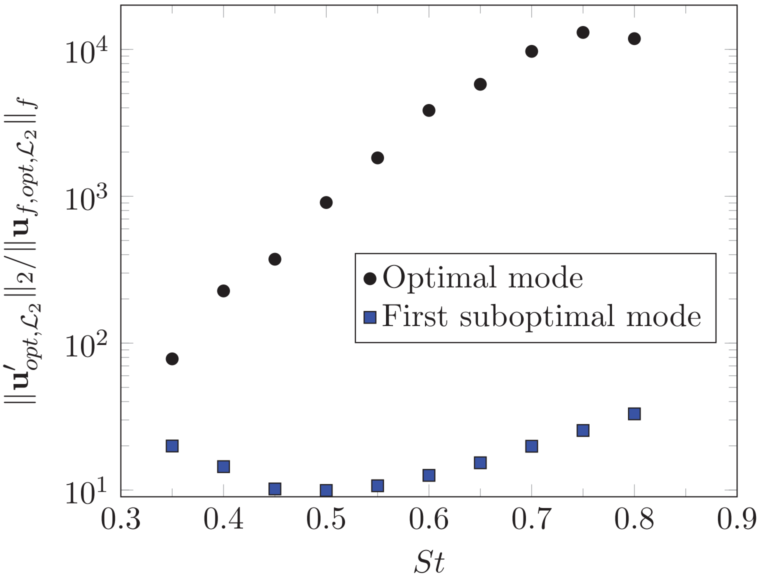

Figure 4.11: Evolution of the long-term ($T_o \longrightarrow \infty$) optimal and first suboptimal gains for the $\mathcal{L}_2$ norm optimisation as a function of Strouhal number.

The suboptimal gain does not vary as much as the optimal, remaining of the order of 10 at all Strouhal numbers. Therefore, the gain separation already mentioned in section 4.3.1 largely increases with Strouhal number. Its consequences are further discussed in section 4.3.3.

4.3.3 *Influence of the chosen norm*

We consider two distinct response norms: the $\mathcal{L}_2$ norm, defined in section 4.2.4.2, and the displacement norm, defined in section 4.2.4.3, the latter being based on the displacement of a given vortex ring. Up to this point, only results for the $\mathcal{L}_2$ norm have been shown. In this section, we investigate the influence of the norm by comparing optimisation results based on the $\mathcal{L}_2$ norm and the displacement norm of any of the first three vortex rings.

Optimisation norm	$\mathcal{L}_2$	$\boldsymbol{\Omega}_1$ disp.	$\boldsymbol{\Omega}_2$ disp.	$\boldsymbol{\Omega}_3$ disp.
$\mathcal{L}_2$	1.0	0.9846	0.9988	0.9999
$\boldsymbol{\Omega}_1$ disp.	0.9846	1.0	0.9885	0.9838
$\boldsymbol{\Omega}_2$ disp.	0.9988	0.9885	1.0	0.9989
$\boldsymbol{\Omega}_3$ disp.	0.9999	0.9838	0.9989	1.0

Table 4.3: Scalar product between the optimal unit-norm forcings for the different norms considered. $T_o = 18$, $Re = 2000$ and $St = 0.50$. Disp. is the abbreviation of displacement.

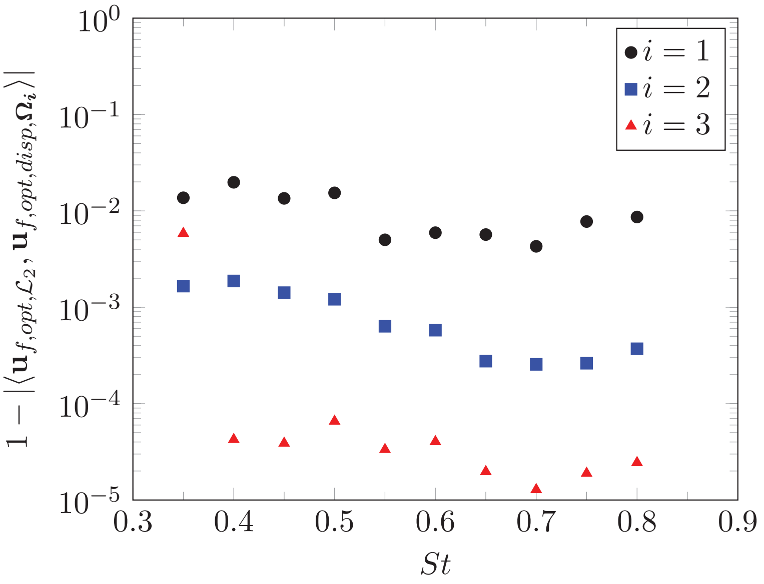

Figure 4.12: For every Strouhal number studied, scalar product between the optimal $\mathcal{L}_2$ forcing and the optimal displacement norm forcings, for any of the first three vortices considered.

At first, we focus on the $St = 0.50$ case. Table 4.3 compares the forcing shapes in this case for the different norms used. The main conclusion is that, in this case, irrespective of the vortex choice for the displacement norm, the results are almost independent of the response norm used, with a minimal scalar product of 0.9838 between two different unit-norm forcings.

For all Strouhal numbers studied, figure 4.12 compares the optimal $\mathcal{L}_2$ forcing with optimal forcings for displacement norms based on any of the first three vortices. Again, the results show an almost complete independence of the optimal forcing with respect to the chosen norm, with a minimal scalar product of 0.9802 between two different unit-norm forcings (for $St = 0.40$). However, we see that the $\mathcal{L}_2$ norm results are closer to the results of the third vortex displacement; this can be understood with the exponential spatial growth of the optimal linear response (see section 4.3.1) that obviously puts a larger emphasis on the situation at the end of the optimisation domain, where the third vortex is approximately located.

The independence of the forcing norm can be explained by two main reasons. First, comparing figures 4.5 and 4.8, one sees that the optimal $\mathcal{L}_2$ response shape, with its alternate pattern, is well-suited to shift the vortices off-axis, and therefore well-suited for the displacement norm. Second, the large separation gains that exists between the optimal forcing and its suboptimals reinforces this phenomenon. Indeed, considering the $\mathcal{L}_2$ norm, figure 4.11 shows that the optimal gain is 3.9 times larger than the first suboptimal at $St = 0.35$, and 513 times larger at $St = 0.75$. Therefore, although the two norms considered do not measure the exact same quantities, the large gain separation balances this potential discrepancy. Indeed, if the optimal $\mathcal{L}_2$ forcing has a much larger gain than any other orthogonal forcing, even though its corresponding unit-norm response shape might not shift the vortices optimally, this is compensated by its large gain.

4.3.4 *Effect of simulations parameters*

4.3.4.1 *Length of the optimisation box for the energy norm*

For the $\mathcal{L}_2$ norm, the optimisation is carried out by calculating the response norm on the domain $0 \leq r \leq R_m$ and $0 \leq z \leq Z_{opt}$, with $Z_{opt} = 5.0$. However, changing Z_{opt} could change the results. In this section, we investigate the effect of changing Z_{opt}, in the $(Re = 2000, St = 0.50)$ regime, by considering values of Z_{opt} from 3.0 to 7.5 separated by 0.5 increments. When all the optimal forcings are calculated, scalar products between each couple of them are subsequently computed, and the most distant optimal forcings are the one for $Z_{opt} = 3.0$ and $Z_{opt} = 7.5$, with a scalar product of 0.99961. The optimal forcing is thus independent of the domain length considered.

4.3.4.2 *Length of the boxes around vortices for displacement norm*

For the displacement norm, the optimal forcing is calculated by integrating perturbation quantities around the i^{th} vortex core ($i = 1$, 2 or 3). To perform this integration, a rectangular box $[Z_i - \delta_z/2; Z_i + \delta_z/2] \times [0; 1]$, with Z_i the axial position of the vortex (calculated as a centroid) and δ_z fixed to 0.8, is first chosen. However, the choice of δ_z could affect the results of the optimisation.

This effect is now studied for the $Re = 2000$ and $St = 0.50$ case. 4 different values of δ_z are tested: 0.4, 0.6, 0.8 and 1, as represented in figure 4.4. Above $\delta_z = 1$, boxes for consecutive vortices would overlap.The first three vortices are considered here.

The results show that the optimal forcing barely depends on the box size: by considering scalar products between optimal forcings on the same vortex for different δ_z, all scalar products are above 0.992.

4.3.4.3 *Effect of the size of the forcing space*

The convergence of the optimal forcing shape with respect to the number N of basis functions is now evaluated. Since these functions are orthonormal, the optimal forcing for a basis of dimension $N' < N$ can easily be computed by

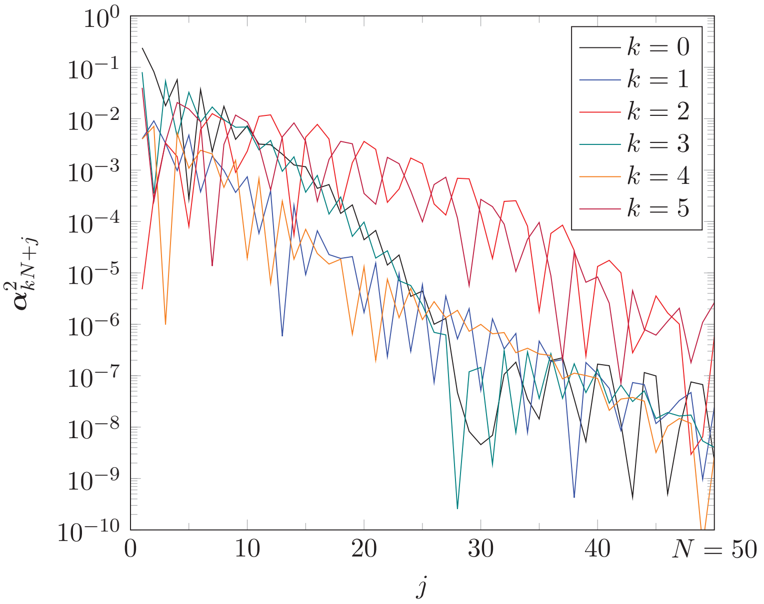

Figure 4.13: Energy component of the optimal forcing on each of the different basis forcing functions considered, for $Re = 2000$ and $St = 0.50$. In this case, $N = 50$.

taking the first N' components of the optimal N-forcing. Therefore, the evolution of energy component of the optimal forcing over each basis function, as represented in figure 4.13, shows the convergence of the algorithm as a function of N, for $Re = 2000$ and $St = 0.50$.

It can be stated that the quickest mode to converge are the $k = 0, 1, 3$ and 4 modes, corresponding to forcing in the radial and azimuthal directions. However, in all cases, convergence is properly achieved, with energy levels contained in the last modes about 10000 times lower than the ones in the first modes.

4.3.4.4 *Effect of the time-shift with respect to the axisymmetric forcing*

In this study, we carry out optimisation over a periodic flow with the cost function only calculated using data at $T_o = 2nT_f$. However, a large gain at these synchronized T_o does not necessarily imply large gain for different $T_o = (2n + \varphi)T_f$ phase-shifted of $2\pi\varphi$ with the fundamental forcing; in other words, there is no evidence that a forcing that shifts well the vortices at a given objective time will not perform poorly at another time.

Therefore, this section evaluates the influence of following optimisation time-shifts: $\varphi = 0$ (phase 0), $1/4$ (phase $\pi/2$), $1/2$ (phase π) and $3/4$ (phase $3\pi/2$). The different optimal $\mathcal{L}_2$ norm forcings found are then compared in table 4.4. Again, the optimal forcing is almost independent from the phase shift considered. This can be understood using the same arguments of the large gain separation as in section 4.3.3, but also physically by considering the jet bifurcation as a very receptive physical mechanism: in the interpretation of Parekh, Leonard, and Reynolds (1988), the vortices are shed out of the axis, and they do not oscillate around a fixed equilibrium. Therefore, there is no chance that at a particular time-shift, the forcing

Phase shift	0	$\pi/2$	π	$3\pi/2$
0	1.0	0.9896	0.9936	0.9941
$\pi/2$	0.9896	1.0	0.9831	0.9826
π	0.9936	0.9831	1.0	0.9923
$3\pi/2$	0.9941	0.9826	0.9923	1.0

Table 4.4: Scalar product of the $\mathcal{L}_2$ norm optimal forcings for different phase shifts. $T_o = (2n + \varphi)T$ with $2n = 18$ for phase 0 and 6 for others. $Re = 2000$ and $St = 0.50$.

has no effect on the vortices. If, at some time-step in the forcing period, the vortices are offset, then this offset continues through the entire cycle.

4.3.4.5 *Final objective time T_o*

The optimal forcing and response can be calculated for different objective times T_o. The shape of forcing functions and the associated gain evolves with time. At some point, the optimal forcing does not change and the gain reaches a plateau. In this study, the convergence condition we set for the final state is a variation of the gain by less than 0.5% compared to the gain achieved two forcing periods before. In this section, we discuss the evolution of these quantities for the $\mathcal{L}_2$ norm and the $St = 0.50$ case.

Figure 4.14a shows that after a transient time of exponential growth, the gain reaches a plateau. As mentioned in section 4.2.3.2, this confirms the stability of the axisymmetric unpaired base flow with respect to $m = 1$ perturbations.

Figure 4.14b displays the shape evolution with T_o of the optimal forcing and response by comparing each of those with the optimal quantities for $T_o = 2$ and 18. Regarding forcings, little change occurs between $T_o = 2$ and 18; the initial forcing is almost optimal, its shape is fixed. Therefore, if one is only interested in optimal forcings, there is no need to run the optimisation for long T_o. Concerning responses, because of the spatial development of the perturbation field (more than two forcing periods are necessary to fill the 5-diameter long optimisation domain, since the intial perturbation is zero), the initial shape of the response, at $T_o = 2$, has little resemblance with its final shape. But after 6 forcing periods, they are almost identical.

4.3.5 *Comparison with non-optimal simple forcing*

Previous studies (Danaila and Boersma, 1998, 2000) prescribe a helical forcing in the form:

$$\mathbf{u}(r, \theta, z = 0, t) = U_0(r)\left(1 + A\cos\left(\omega_f t\right) + C\cos\left(\omega_f t/2 + \phi\right)\cos(\theta)\left(\frac{2r}{D}\right)\right)\mathbf{e_z}, \tag{4.27}$$

with ϕ the phase shift prescribed and $(2r/D)$ a factor imposed to enforce the compatibility condition (4.12b) at $r = 0$. In Danaila and Boersma (1998, 2000) and

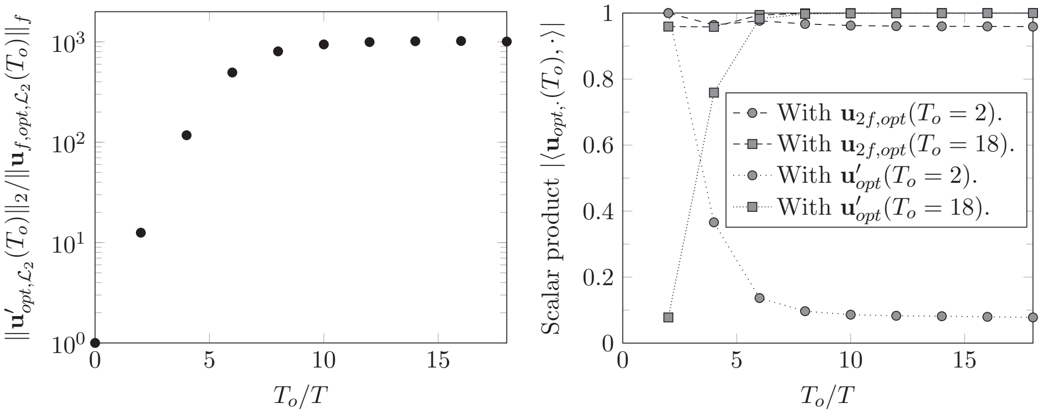

(a) Evolution of the optimal gain.

(b) Evolution of the optimal forcing and response, with scalar product comparisons with $T_o = 2$ and 18. The scalar products are all carried out over quantities normalized with respect to the relevant $\mathcal{L}_2$ norm.

Figure 4.14: Evolution of optimal forcing, response and gain as a function of optimisation time T_o for the $Re = 2000$, $St = 0.50$ case. All quantities are optimised with respect to the $\mathcal{L}_2$ norm.

St	0.35	0.50	0.65	0.80
$\lvert\langle \mathbf{u}_{2f,opt}, \mathbf{u}_{2f,simple}\rangle\rvert$	0.006	0.143	0.198	0.214

Table 4.5: Scalar product between normalised simple forcing from equation (4.27) and optimal forcing with respect to the $\mathcal{L}_2$ norm for four Strouhal number values.

Parekh, Leonard, and Reynolds (1988), the phase-shift ϕ is fixed at 0 to enforce simultaneous peaks (in time) of the axisymmetric and helical forcings.

The simple forcing (4.27) is now compared with the optimal one. This comparison is made by calculating the scalar product between this forcing and our optimal one for four Strouhal number values 0.35, 0.5, 0.65 and 0.8. Results are summarized in table 4.5. Because of the large gain separation shown in figure 4.11, these projection values approximately correspond to the ratio of the gains respectively achieved with simple and optimal forcing. Therefore, the increase of efficiency with the optimal forcing is significant.

4.4 THREE-DIMENSIONAL NONLINEAR RESULTS

In this section, the optimal forcing is implemented in three-dimensional nonlinear direct numerical simulations. The purpose is to assess the performance of the optimised forcing across a large Strouhal number band, in comparison with a conventional forcing shape that has been used in previous bifurcating jet, defined in section 4.3.5.

4.4.1 *Prescribed inflow forcing*

In order to compare the effects of optimal versus simple forcing in a meaningful way, a consistent normalisation of the input energy must be established. To this end, we calibrate the energy of helical forcing input with respect to the axisymmetric forcing (4.6). The latter is characterised by the fluctuation amplitude A, and its energy is measured from

$$\|\mathbf{U}\|_f^2 = \frac{1}{2T_f}\frac{1}{2\pi}\int_0^{2T_f}\int_0^{2\pi}\int_0^{R_m} r\langle \mathbf{U}(r,\theta,z=0,t), \mathbf{U}(r,\theta,z=0,t)\rangle \mathrm{d}r\,\mathrm{d}\theta\,\mathrm{d}t \quad (4.28a)$$

$$= \left(\int_0^{R_m} r\langle U_0(r)\mathbf{e_z}, U_0(r)\mathbf{e_z}\rangle \mathrm{d}r\right)\left(\frac{1}{2T_f}\int_0^{2T_f}\left(1+A\cos\left(\omega_f t\right)\right)^2\mathrm{d}t\right) \quad (4.28b)$$

$$= \|U_0\mathbf{e_z}\|_f^2\left(1+\frac{A^2}{2}\right), \quad (4.28c)$$

with R_m the outer radial boundary at the inlet in our simulations. Therefore, the energy of the base flow forcing is split between the mean component $\|U_0\mathbf{e_z}\|_f^2$ and the axisymmetric forcing $A^2\,\|U_0\mathbf{e_z}\|_f^2/2$.

4.4.1.1 *Amplitude and phase of the optimal forcing*

Adding the optimal helical forcing, with an amplitude of $B\Gamma$, the jet inlet velocity (4.3) is prescribed as

$$\begin{aligned}\mathbf{u}(r,\theta,z=0,t) \quad = \quad & U_0(r)\left(1+A\cos\left(\omega_f t\right)\right)\mathbf{e_z} + \\ & 2B\Gamma\left[\mathcal{R}\left(\mathbf{u_{1f,1}}\right)\cos(\theta)\cos(\omega_f t/2) - \mathcal{I}\left(\mathbf{u_{1f,1}}\right)\sin(\theta)\cos(\omega_f t/2) + \right. \\ & \left.\mathcal{R}\left(\mathbf{u_{1f,2}}\right)\cos(\theta)\sin(\omega_f t/2) - \mathcal{I}\left(\mathbf{u_{1f,2}}\right)\sin(\theta)\sin(\omega_f t/2)\right]. \end{aligned} \quad (4.29)$$

A normalisation factor Γ is introduced, with a numerical value determined as 0.239 for the present flow case, such that the energy ratio between axisymmetric and helical forcing is given by A^2/B^2.

Without loss of generality, the azimuthal phase of the bifurcation plane is set to $\theta = 0$ by imposing all coefficients $u_{2f,\cdot,\cdot}$ to be real-valued functions of r. This is possible since the perturbation equations for $\mathbf{u_2}$ only involve real coefficients (see appendix 4.B). Therefore, the total inflow forcing is finally recovered as

$$\mathbf{u}(r,\theta,z=0,t) \quad = \quad \left(1+A\cos\left(\omega_f t\right)\right)U_0(r)\mathbf{e_z} + 2B\Gamma\begin{bmatrix}\left(u_{2f,1,r}\cos(\omega_f t/2) + u_{2f,2,r}\sin(\omega_f t/2)\right)\cos(\theta) \\ \left(u_{2f,1,\theta}\cos(\omega_f t/2) + u_{2f,2,\theta}\sin(\omega_f t/2)\right)\sin(\theta) \\ \left(u_{2f,1,z}\cos(\omega_f t/2) + u_{2f,2,z}\sin(\omega_f t/2)\right)\cos(\theta)\end{bmatrix}, \quad (4.30)$$

In this study, the amplitude B is fixed at 0.01, five times lower than the amplitude of the axisymmetric forcing prescribed; if this helical forcing had a constant shape in the radial direction harmonically modulated with time (as the axisymmetric), this would have corresponded to a maximum velocity amplitude with respect to

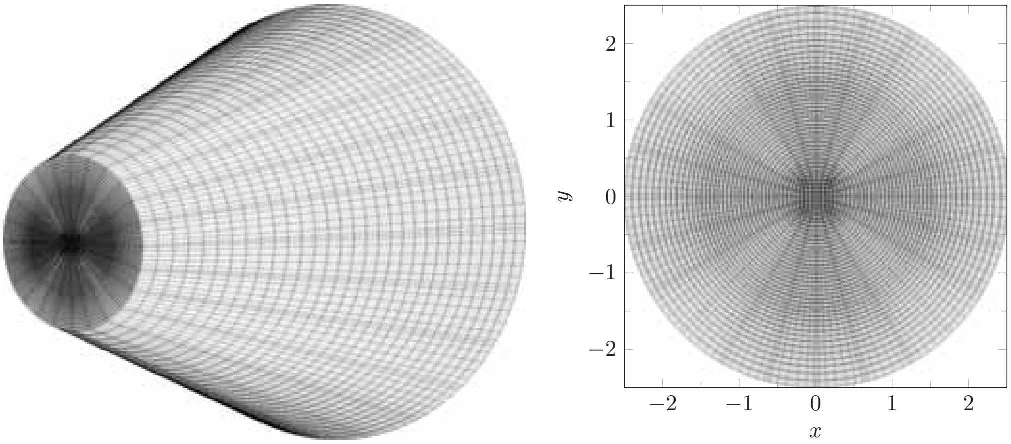

(a) Perspective view. (b) Cut in the inlet ($z = 0$) plane.

Figure 4.15: Mesh used for $3D$ nonlinear computation.

the infinity-norm of 1% of the mean-flow. This amplitude is much lower than what has been used in the literature: 5% of the mean-flow in Gohil, Saha, and Muralidhar (2015), 1 to 15% in Tyliszczak and Geurts (2014) or 15% in Danaila and Boersma (1998, 2000).

4.4.1.2 *Amplitude of the simple forcing*

The simple, non-optimal helical forcing (4.27) is accordingly cast in normalised form as

$$\mathbf{u}(r,\theta,z=0,t) = U_0(r)\left(1 + A\cos\left(\omega_f t\right) + B'\Gamma'\cos\left(\omega_f t/2\right)\cos(\theta)\left(\frac{2r}{D}\right)\right)\mathbf{e_z}, \tag{4.31}$$

with a fixed zero-phase shift. A value $\Gamma' = 1.850$ gives an energy ratio A^2/B'^2 between axisymmetric and helical components, which is consistent with the above parametrisation of the optimal forcing. To enable fair comparisons, B' is fixed at 0.01 as B in the previous section, much lower than forcing levels commonly used in the literature.

4.4.2 *Computational setup*

Nonlinear direct numerical simulations are again carried out using NEK5000 (*NEK5000*). In order to accommodate the spreading associated with bifurcation, a conical mesh is used, as represented in figure 4.15a. The domain is 15 diameters long and its circular cross-section grows linearly from 5 jet diameters at the inlet plane ($z = 0$) to 16 diameters at the outlet plane ($z = 15$). The mesh contains 27720 spectral elements, each containing 8 degrees of freedom in each direction ; there are 30 elements in the axial direction and each (x, y) plane contains 924 elements, as represented in the mesh cut in figure 4.15b.

The jet velocity is respectively prescribed in the inlet plane according to (4.30) or (4.31). An outflow condition (4.9) is applied at all other boundaries. In addition,

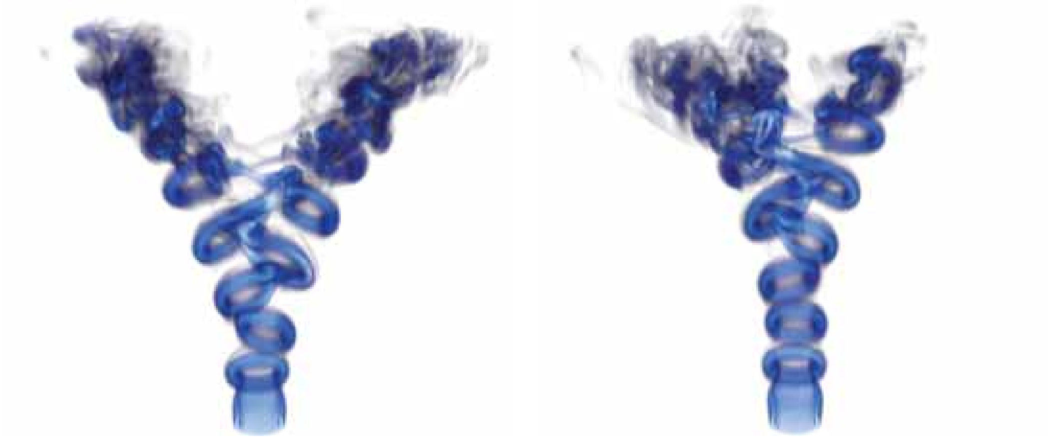

(a) Optimal forcing.

(b) Traditional forcing.

Figure 4.16: $3D$ vorticity magnitude snapshots of the nonlinearly forced bifurcating jet for $Re = 2000$ and $St = 0.50$. On the left, the jet is forced with the optimal forcing derived previously whereas on the right, it is forced with the simple forcing.

the radial boundary downstream of $z = 5$ is padded with absorbing layers of thickness 1. This is necessary in order to ensure numerical stability in some cases of particularly strong jet spreading. As a consequence, the entire flow region $z > 10$ is regarded as unphysical and is excluded from the following presentation of results.

A constant time-step of $\Delta t = 2.5 \times 10^{-3}$ is used hereafter. The simulations are run for at least one-hundred dimensionless time units, in order to evacuate transient dynamics. Average quantities are then calculated over the last 10 forcing periods of the simulation.

4.4.3 *Simulated jet bifurcation at various Strouhal numbers*

Simulations are performed at $Re = 2000$, with Strouhal numbers ranging from 0.35 to 0.8, in increments of 0.05, with the optimal forcing (4.30). For comparison, the nonlinear response to simple helical forcing (4.31) is computed for Strouhal numbers between 0.4 and 0.8, in increments of 0.1.

A vorticity snapshot of the optimally forced jet at $Re = 2000$ and $St = 0.5$ is shown in figure 4.16a. Close to the nozzle, axisymmetric vortex rings are seen to form rapidly, while the helical perturbation becomes appreciable about two jet diameters downstream of the inlet. The vortex rings are tilted and shifted off-axis, quickly resulting in bifurcation. In this process, the vortex rings are distorted on their inner side.

Comparing the nonlinear flow responses between optimised and simple forcings in figures 4.16a and 4.16b, we observe, without any ambiguity, that the optimal forcing leads to a much stronger and earlier bifurcation. Contrary to the optimised case, where the flow pattern is clearly symmetric with respect to the central plane, the effect of the simple forcing is too weak to enforce this symmetry.

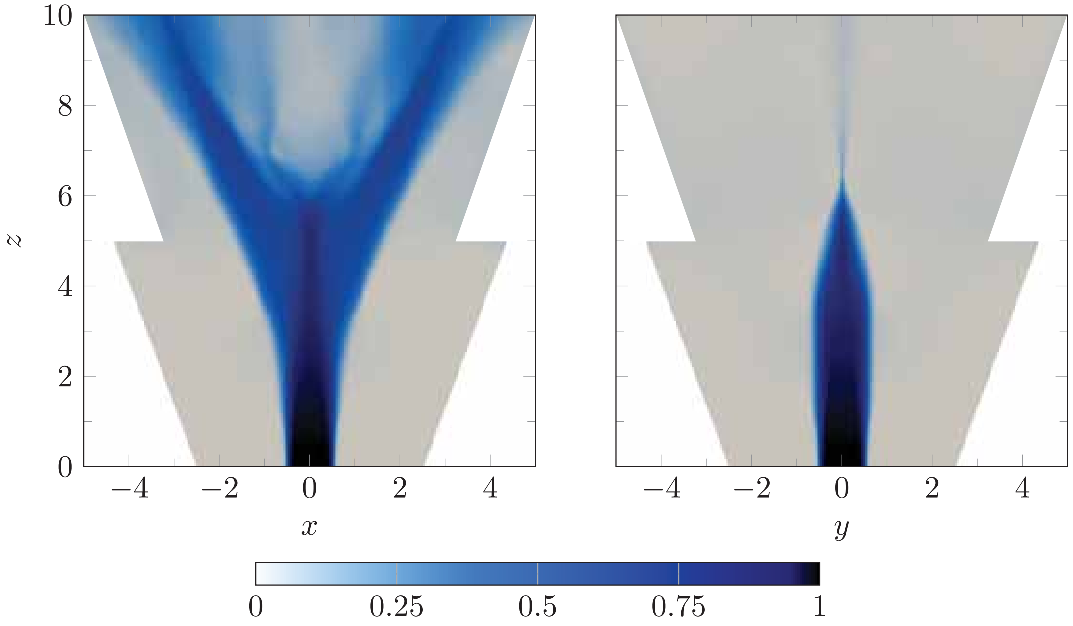

Figure 4.17: Mean axial velocity cut in the bifurcating ($y = 0$, left) and bisecting ($x = 0$, right) planes for the $Re = 2000$, $St = 0.50$ case optimally forced with a 1% amplitude. The sponge layers are not displayed.

The resulting time-averaged axial velocity is shown in figure 4.17. The symmetric bifurcation is clearly marked in the (x, z) plane, whereas the mean flow has entirely left the (y, z) plane at a streamwise distance of about six diameters. All these results validate our optimisation procedure.

Corresponding plots of the mean axial velocity in the bifurcation plane are shown in figure 4.18 for all Strouhal numbers. The response to optimal forcing is represented in the left and center columns, alongside the response to simple forcing in the right column. In addition, vorticity snapshots of the optimally forced jet for three different Strouhal numbers are displayed in figure 4.19.

In the optimally forced cases, a pronounced bifurcation is observed at all Strouhal numbers, despite the low helical forcing amplitude. Below $St = 0.55$, the cleavage between the two branches widens with the Strouhal number, which is fully consistent with the increase of the linear gain shown in figure 4.11. Below this threshold, vortices do not distort one another, as shown in figure 4.19a: such an interaction only starts around $St = 0.55$ (see figure 4.16a). Above this value, while the jet continues to display strong flaring, a third central structure emerges progressively, and the mean flow is more and more mixed in between the paths of the outer jets. Depending on the Strouhal number, this central structure resembles either a large central jet ($St = 0.75$ and 0.80), as shown in the mean flow cuts and in figure 4.19c, or resembles two smaller side jets ($St = 0.60$, 0.65 and 0.70), as shown in the mean flow cuts and in figure 4.19b. The occurrence of this central mixing seems to be linked to an observation by Parekh, Leonard, and Reynolds (1988): at high Strouhal number, associated with small spatial separation, the vortex rings interact and distort one another more intensely. This purely nonlinear effect, confirmed

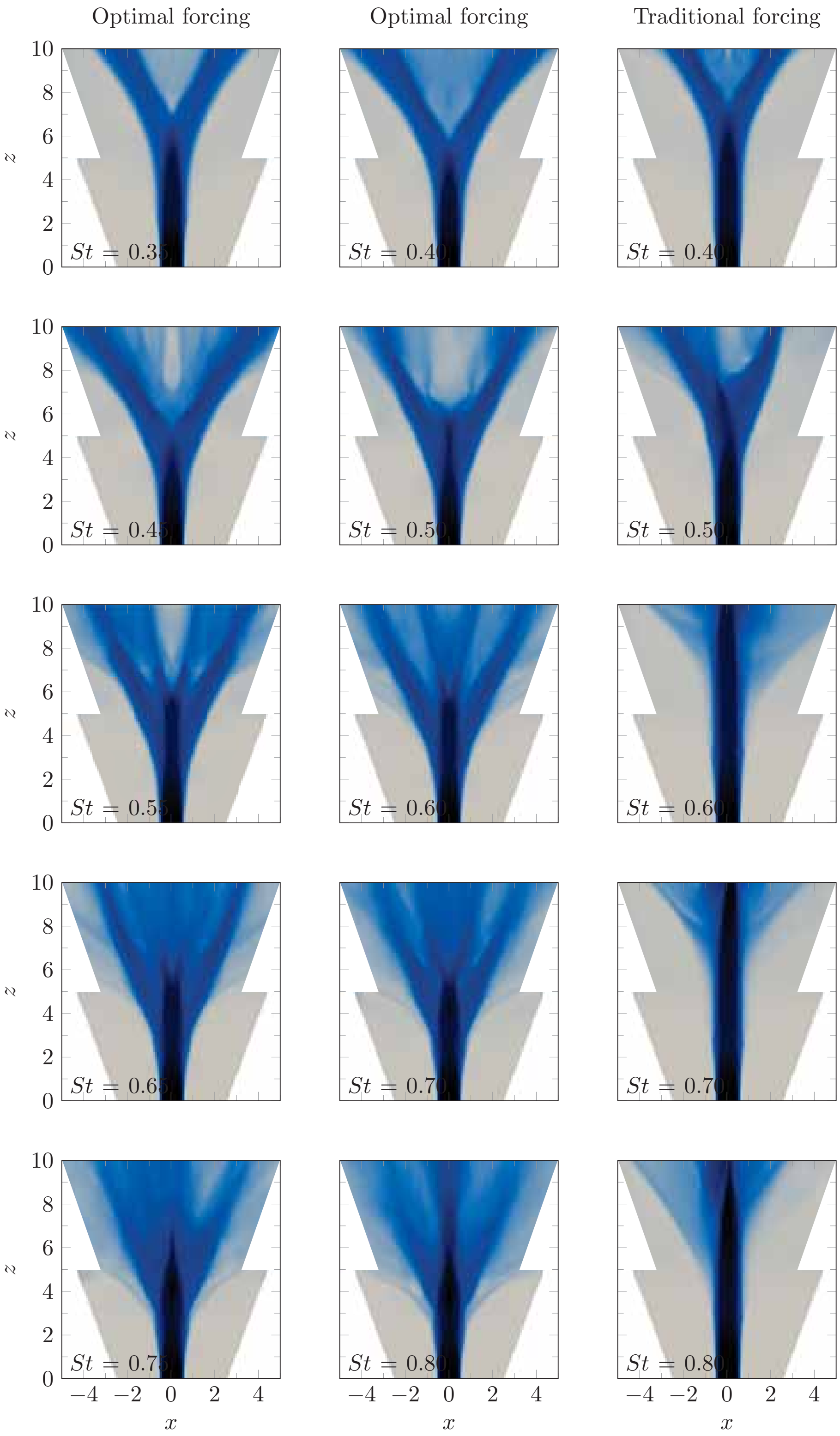

Figure 4.18: Mean axial velocity cuts in the bifurcating plane for various values of the Strouhal number in the range $[0.35; 0.80]$ and for both optimal (left and middle columns) and simple (right column) forcings. The forcing amplitude is fixed for B and B' at 1% and the colorbar can be found in figure 4.17. The sponge layers are not displayed.

(a) $St = 0.35$. (b) $St = 0.65$. (c) $St = 0.80$.

Figure 4.19: Three-dimensional vorticity magnitude snapshots of the nonlinearly optimally forced bifurcating jet for $Re = 2000$ and three different Strouhal values: 0.35, 0.65 and 0.80.

in figure 4.19, also leads to a stronger transition to turbulence in our simulations. Even though it is not captured by the analysis in §2, it provides a reasonable explanation for the blurring of the mean flow in the central region. However, the simulations clearly demonstrate that the continued exponential growth of the linear gain beyond $St = 0.55$ is not reflected in the nonlinear flow behaviour.

The simple helical forcing, as seen in the right column of figure 4.18, clearly is much less efficient in producing a bifurcation. First, the flaring, when occurring, sets in further downstream, typically with less pronounced branch formation, and the loss of symmetry in the 10-period mean indicates a much reduced efficiency to alternatively deviate the jet. Second, a clear bifurcation within ten diameters of the inlet is only observed in the narrow range $0.4 \leq St \leq 0.5$. Due to the low helical forcing amplitude of 1% in our simulations, this band of St is consistent with the literature (Reynolds et al., 2003; Tyliszczak and Geurts, 2014). Conversely, optimised forcing resulting in bifurcation over the entire range of Strouhal numbers considered in this study have been achieved here.

4.5 CONCLUSION

Optimal forcing of jet bifurcation, as an example of forced symmetry breaking of a time-periodic base flow, has been investigated in a linear framework. Results have been validated in three-dimensional DNS calculations.

This study relies on the bifurcation scenario originally described by Lee and Reynolds (1985) and Parekh, Leonard, and Reynolds (1988). Following their physical insight, we have proposed to optimise the bifurcating jet by maximising a linear helical perturbation of an array of axisymmetric ring vortices in a jet. Due to pairing instabilities, the axisymmetric unpaired base flow has been computed through a time-delayed feedback technique (Shaabani-Ardali, Sipp, and Lesshafft, 2017). Then, the optimisation framework has been derived, with two maximisation norms introduced: the classical $\mathcal{L}_2$ norm and a norm based on vortex displacement. Numerically, this optimisation is performed through time-stepping of a basis of inlet forcing functions ($1D$) and the selection of the best linear combination of these forcings.

After carrying out the optimisation, it has been found that irrespective of the Strouhal number, chosen between 0.35 and 0.80, one should mostly force around the mixing layer position and mainly along the radial direction, which contradicts previous studies that mainly forced along the axial direction. By varying the Strouhal number, the shape of the modulus of the optimal forcing does not vary much, but it undergoes global shifts in phase. For practical applications, this shows that optimal perturbations can be easily provided by a unique setup along a large band of Strouhal numbers just by varying the phase difference with the axisymmetric forcing. Moreover, the forcing found is extremely robust: it is independent on both the norm and the hyperparameters chosen, such as the domain size or the time-shift. This robustness can be explained by a large gain separation with suboptimal: varying the optimisation parameters (norms used, domain length) as well as the physical parameters (time horizons T_o chosen, phase difference of the chosen T_o, vortex chosen to optimise around) has little influence on the final result. The gain obtained grows exponentially with the Strouhal number, before saturating around $St = 0.75$, and is at least five times larger than the one achieved with simple forcing strategies.

Eventually, $3D$ DNS calculations have been carried out to validate the results. A low forcing amplitude of 1% has been chosen for the helical forcing. It has been found that the optimal forcings perform extremely well along the entire band of Strouhal numbers studied ($[0.35; 0.80]$), leading to a large flaring of the jet and, therefore, a large improvement of its mixing properties. Two kinds of flow topology have been found: for lower Strouhal values (below 0.55), a classical bifurcating jet is obtained whereas for larger Strouhal values (above 0.55), a third central structure emerges. In all cases, comparisons with simple forcing strategies show that the optimisation triggers bifurcation much more efficiently, by moving upstream the bifurcation point and displaying a stronger displacement of vortices ; further, that this triggering can occur over a very large Strouhal band, compared to the narrow band in which bifurcation is found for simple forcing strategies.

Mathematically, in this study, we have derived a framework to carry out linear optimisation over periodic flows for long time-horizons. Physically, our work provides a better understanding of the bifurcating jet phenomenon. Even though our study focuses on a laminar bifurcating jet at a moderate Reynolds number, previous results (Tyliszczak and Geurts, 2014) have shown that the turbulence level in bifurcating jet becomes important only when it exceeds the axisymmetric and helical forcings levels. This implies that an optimal forcing for a laminar flow would remain close-to-optimal for turbulent flows with a forcing amplitude adjusted so that it exceeds the turbulence level. Moreover, Parekh, Leonard, and Reynolds (1988) have shown that bifurcating jet could be essentially triggered in similar ways both at moderate and large Reynolds numbers.

An interesting question, outside the scope of this study, would be to precisely understand the effect of turbulence and Reynolds number on our results. To do so, one could rely on a linear optimisation over the base flow of a turbulent phase-averaged axisymmetric pulsed jet. This analysis, of great interest, would transpose the resolvent analysis to the time-periodic (in an averaged sense) turbulent flows, and would be useful for many other flows.

4.A FURTHER DETAILS ON THE DISPLACEMENT NORM

From equation (4.23), the displacement norm can be written as:

$$\left\|\mathbf{u}'(T_o)\right\|^2_{disp,\mathbf{\Omega}_i} = \frac{1}{2}\frac{1}{2\pi}\int_0^{2\pi}\left\|\left.\frac{\mathrm{d}\mathbf{x}_i(\theta_c,T_o)}{\mathrm{d}\epsilon}\right|_{\epsilon=0}\right\|_2^2 \mathrm{d}\theta_c. \tag{4.32}$$

By introducing the original vortex position $\mathbf{X}_i(T_o)$ and the total vorticity of the base i^{th}-vortex $\Omega_{i,tot}(T_o)$:

$$\begin{aligned}\mathbf{X}_i(T_o) = R_i(T_o)\mathbf{e_r} + Z_i(T_o)\mathbf{e_z} &= \frac{\iint_{\mathbf{\Omega}_i} r\Omega_\theta(r,z,T_o)\mathbf{x}\,\mathrm{d}r\,\mathrm{d}z}{\iint_{\mathbf{\Omega}_i} r\Omega_\theta(r,z,T_o)\,\mathrm{d}r\,\mathrm{d}z}, && (4.33)\\ \Omega_{i,tot}(T_o) &= \iint_{\mathbf{\Omega}_i} r\Omega_\theta(r,z,T_o)\,\mathrm{d}r\,\mathrm{d}z, && (4.34)\end{aligned}$$

the displacement norm can be rewritten as

$$\begin{aligned}&\left\|\mathbf{u}'(T_o)\right\|^2_{disp,\mathbf{\Omega}_i}\\ &= \frac{1}{4\pi}\int_0^{2\pi}\left\|\frac{\left(\iint_{\mathbf{\Omega}_i} r\omega'_\theta(r,\theta_c,z,T_o)(\mathbf{x}-\mathbf{X}_i(T_o))\,\mathrm{d}r\,\mathrm{d}z\right)}{\Omega_{i,tot}(T_o)}\right\|_2^2 \mathrm{d}\theta_c && (4.35)\\ &= \left\|\frac{\left(\iint_{\mathbf{\Omega}_i} r\omega_{2,\theta}(r,z,T_o)\mathbf{x}\,\mathrm{d}r\,\mathrm{d}z\right) - \left(\iint_{\mathbf{\Omega}_i} r\omega_{2,\theta}(r,z,T_o)\,\mathrm{d}r\,\mathrm{d}z\right)\mathbf{X}_i(T_o)}{\Omega_{i,tot}(T_o)}\right\|_2^2, && (4.36)\end{aligned}$$

with $\omega_{2,\theta} \in \mathbb{C}$ *a priori*.

4.B OPTIMISATION DETAILS

4.B.1 *Optimization for the $\mathcal{L}_2$-norm*

Let's denote $\mathbf{f_j}$ the orthonormal basis of forcing functions ($1 \leq j \leq 6N$) in the "2" framework (see table 4.1):

$$\mathbf{f_j} = \left(u_{2f,1,r,j}, u_{2f,1,\theta,j}, u_{2f,1,z,j}, u_{2f,2,r,j}, u_{2f,2,\theta,j}, u_{2f,2,z,j}\right)^t, \tag{4.37}$$

each of those associated with a response vector $\mathbf{r_j}$ in the "2" framework:

$$\mathbf{r_j} = \left(u_{2,r,j}, u_{2,\theta,j}, u_{2,z,j}\right)^t. \tag{4.38}$$

All these forcings and responses are real. We want to find an optimal linear combination $\sum_j \left(\alpha_j + i\beta_j\right) \mathbf{f_j}$ such that:

$$\begin{aligned}
\begin{bmatrix}\boldsymbol{\alpha}\\ \boldsymbol{\beta}\end{bmatrix} &= \underset{\|\boldsymbol{\alpha}+i\boldsymbol{\beta}\|=1}{\arg\max} \left\| \sum_j \left(\alpha_j + i\beta_j\right) \mathbf{r_j}(T_o) \right\|_2^2 && (4.39a)\\
&= \underset{\|\boldsymbol{\alpha}+i\boldsymbol{\beta}\|=1}{\arg\max} \langle \sum_j \left(\alpha_j + i\beta_j\right) \mathbf{r_j}(T_o), \sum_k \left(\alpha_k + i\beta_k\right) \mathbf{r_k}(T_o)\rangle && (4.39b)\\
&= \underset{\|\boldsymbol{\alpha}+i\boldsymbol{\beta}\|=1}{\arg\max} \sum_{j,k} \left(\alpha_j\alpha_k + \beta_j\beta_k\right) \langle \mathbf{r_j}(T_o), \mathbf{r_k}(T_o)\rangle, \text{ from equation (4.17b)} && (4.39c)\\
&= \underset{\|\boldsymbol{\alpha}+i\boldsymbol{\beta}\|=1}{\arg\max} \begin{bmatrix}\boldsymbol{\alpha}\\ \boldsymbol{\beta}\end{bmatrix}^t \begin{bmatrix}A & 0\\ 0 & A\end{bmatrix} \begin{bmatrix}\boldsymbol{\alpha}\\ \boldsymbol{\beta}\end{bmatrix}, && (4.39d)
\end{aligned}$$

with A the matrix such that $A_{j,k} = \langle \mathbf{r_j}(T_o), \mathbf{r_k}(T_o)\rangle$. The leading eigenvector of A, a real-symmetric positive semidefinite matrix (Gram matrix), gives the coefficients a_i of the optimal linear combination of $\mathbf{f_i}$ and $\mathbf{r_i}$. The corresponding leading eigenvalue gives the optimal gain squared of the operator. Then the optimal forcing can be written $\boldsymbol{\alpha} = \cos(\phi)\mathbf{a}$ and $\boldsymbol{\beta} = \sin(\phi)\mathbf{b}$, for any $\phi \in \mathbb{R}$.

This phase ϕ is totally arbitrary, and will determine the angle of the bifurcating plane. Indeed, with $\phi = 0$, i.e. real $\boldsymbol{\alpha} + i\boldsymbol{\beta}$, the forcing applied is proportional to $\cos(\theta)$ in the axial and radial directions, and proportional to $\sin(\theta)$ in the azimuthal one, leading to a $\theta = 0$ bifurcating plane since the linearised equations for $\mathbf{u_2}$ (4.10a)-(4.10d) only involve real coefficients, preserving this forcing plane. With another ϕ, this bifurcating plane is shifted by $-\phi$, as shown in figure 4.2.

4.B.2 *Optimisation for the displacement norm*

Each of the responses $\mathbf{r_j}$ induces a corresponding vorticity perturbation $\omega_{2,\theta}$ that will be denoted $\tilde{\omega}_j$. Since all the forcings and responses are real in the $(\mathbf{u_2}, p2)$-framework, the $\tilde{\omega}_j(r, z, T_o)$ are real too. Therefore, again, we want to find an optimal linear combination $\sum_j \left(\alpha_j + i\beta_j\right) \mathbf{f_j}$ such that:

$$\begin{bmatrix}\boldsymbol{\alpha}\\ \boldsymbol{\beta}\end{bmatrix} = \underset{\|\boldsymbol{\alpha}+i\boldsymbol{\beta}\|=1}{\arg\max} \left\| \sum_j \left(\alpha_j + i\beta_j\right) \mathbf{r_j}(T_o) \right\|_{disp,\boldsymbol{\Omega}_i}^2 . \qquad (4.40)$$

Let's introduce the $6N$-size vectors $\tilde{\mathbf{R}}$, $\tilde{\mathbf{Z}}$ and $\tilde{\mathbf{Tot}}$ such that:

$$\begin{aligned}
\tilde{R}_j(T_o) &= \frac{\iint_{\boldsymbol{\Omega}_i} r^2 \tilde{\omega}_j(r, z, T_o)\, \mathrm{d}r\, \mathrm{d}z}{\Omega_{i,tot}(T_o)}, && (4.41)\\
\tilde{Z}_j(T_o) &= \frac{\iint_{\boldsymbol{\Omega}_i} rz \tilde{\omega}_j(r, z, T_o)\, \mathrm{d}r\, \mathrm{d}z}{\Omega_{i,tot}(T_o)}, && (4.42)\\
\tilde{Tot}_j(T_o) &= \frac{\iint_{\boldsymbol{\Omega}_i} r \tilde{\omega}_j(r, z, T_o)\, \mathrm{d}r\, \mathrm{d}z}{\Omega_{i,tot}(T_o)}. && (4.43)
\end{aligned}$$

Therefore,

$$\left\| \sum_j \left(\alpha_j + i\beta_j\right) \mathbf{r_j}(T_o) \right\|^2_{disp,\boldsymbol{\Omega}_i}$$

$$= \left\| \sum_j \left(\alpha_j + i\beta_j\right) \left(\tilde{R}_j(T_o)\mathbf{e_r} + \tilde{Z}_j(T_o)\mathbf{e_z} - \tilde{Tot}_j(T_o)\mathbf{X}_i(T_o)\right) \right\|^2_2 \tag{4.44a}$$

$$= \left\| \sum_j \left(\alpha_j + i\beta_j\right) \begin{bmatrix} \tilde{R}_j(T_o) - \tilde{Tot}_j(T_o)R_i(T_o) \\ \tilde{Z}_j(T_o) - \tilde{Tot}_j(T_o)Z_i(T_o) \end{bmatrix} \right\|^2_2 \tag{4.44b}$$

$$\begin{aligned} = \; & \sum_{j,k} \left(\alpha_j\alpha_k + \beta_j\beta_k\right) [\\ & \left(\tilde{R}_j(T_o) - \tilde{Tot}_j(T_o)R_i(T_o)\right)\left(\tilde{R}_k(T_o) - \tilde{Tot}_k(T_o)R_i(T_o)\right) + \\ & \left(\tilde{Z}_j(T_o) - \tilde{Tot}_j(T_o)Z_i(T_o)\right)\left(\tilde{Z}_k(T_o) - \tilde{Tot}_k(T_o)Z_i(T_o)\right)] \end{aligned} \tag{4.44c}$$

$$= \langle \boldsymbol{\alpha}, \mathbf{R}' \rangle^2 + \langle \boldsymbol{\alpha}, \mathbf{Z}' \rangle^2 + \langle \boldsymbol{\beta}, \mathbf{R}' \rangle^2 + \langle \boldsymbol{\beta}, \mathbf{Z}' \rangle^2, \tag{4.44d}$$

with $\mathbf{R}' = \tilde{\mathbf{R}} - R_i(T_o)\tilde{\mathbf{Tot}}$ and $\mathbf{Z}' = \tilde{\mathbf{Z}} - Z_i(T_o)\tilde{\mathbf{Tot}}$. Therefore, we want:

$$\begin{bmatrix} \boldsymbol{\alpha} \\ \boldsymbol{\beta} \end{bmatrix} = \underset{\|\boldsymbol{\alpha}+i\boldsymbol{\beta}\|=1}{\arg\max} \left(\langle \boldsymbol{\alpha}, \mathbf{R}' \rangle^2 + \langle \boldsymbol{\alpha}, \mathbf{Z}' \rangle^2 + \langle \boldsymbol{\beta}, \mathbf{R}' \rangle^2 + \langle \boldsymbol{\beta}, \mathbf{Z}' \rangle^2 \right). \tag{4.45}$$

Let's define $\boldsymbol{\gamma}$ as the solution of

$$\boldsymbol{\gamma} = \underset{\|\boldsymbol{\gamma}\|=1}{\arg\max} \left(\langle \boldsymbol{\gamma}, \mathbf{R}' \rangle^2 + \langle \boldsymbol{\gamma}, \mathbf{Z}' \rangle^2 \right). \tag{4.46}$$

This is is a $2D$-optimisation problem in the $(\mathbf{R}', \mathbf{Z}')$-plane. Because $\mathbf{R}'$ and $\mathbf{Z}'$ are not collinear *a priori*, the problem (4.46) has a unique solution (up to the sign). Then, the argument of the maximisation problem (4.45) can be bounded as

$$\begin{aligned} & \langle \boldsymbol{\alpha}, \mathbf{R}' \rangle^2 + \langle \boldsymbol{\alpha}, \mathbf{Z}' \rangle^2 + \langle \boldsymbol{\beta}, \mathbf{R}' \rangle^2 + \langle \boldsymbol{\beta}, \mathbf{Z}' \rangle^2 \\ \leq \; & \left(\|\boldsymbol{\alpha}\|^2 + \|\boldsymbol{\beta}\|^2 \right) \left(\langle \boldsymbol{\gamma}, \mathbf{R}' \rangle^2 + \langle \boldsymbol{\gamma}, \mathbf{Z}' \rangle^2 \right) \end{aligned} \tag{4.47a}$$

$$\leq \langle \boldsymbol{\gamma}, \mathbf{R}' \rangle^2 + \langle \boldsymbol{\gamma}, \mathbf{Z}' \rangle^2, \tag{4.47b}$$

since $\|\boldsymbol{\alpha} + i\boldsymbol{\beta}\| = 1$ in the maximisation. This bound is also achieved if and only if both $\boldsymbol{\alpha}$ and $\boldsymbol{\beta}$ are collinear to $\boldsymbol{\gamma}$. Therefore, there exists $\psi \in [0, 2\pi]$ such that

$$\boldsymbol{\alpha} = \cos(\psi)\,\boldsymbol{\gamma} \quad \text{and} \quad \boldsymbol{\beta} = \sin(\psi)\,\boldsymbol{\gamma}. \tag{4.48}$$

To solve the problem (4.46), the $(\mathbf{R}', \mathbf{Z}')$-basis is orthonormalised. We construct $\mathbf{W}$ such that $(\mathbf{R}'/\|\mathbf{R}'\|, \mathbf{W})$ is orthonormal as

$$\mathbf{W} = \frac{\mathbf{W}'}{\|\mathbf{W}'\|}, \text{ with } \mathbf{W}' = \frac{\mathbf{Z}'}{\|\mathbf{Z}'\|} - \left\langle \frac{\mathbf{R}'}{\|\mathbf{R}'\|}, \frac{\mathbf{Z}'}{\|\mathbf{Z}'\|} \right\rangle \frac{\mathbf{R}'}{\|\mathbf{R}'\|}. \tag{4.49}$$

Then, $\langle \mathbf{W}, \mathbf{R}' \rangle = 0$, $\langle \mathbf{W}, \mathbf{W} \rangle = 1$ and the $(\mathbf{R}'/\|\mathbf{R}'\|, \mathbf{W})$ basis spans the same space as $(\mathbf{R}', \mathbf{Z}')$. By writing:

$$\boldsymbol{\gamma} = \cos(\phi)\frac{\mathbf{R}'}{\|\mathbf{R}'\|} + \sin(\phi)\mathbf{W}, \tag{4.50}$$

we get

$$\phi = \frac{1}{2} \arctan \left(\frac{2 \left\| \mathbf{Z}' - \left\langle \frac{\mathbf{R}'}{\|\mathbf{R}'\|}, \mathbf{Z}' \right\rangle \frac{\mathbf{R}'}{\|\mathbf{R}'\|} \right\| \left\langle \frac{\mathbf{R}'}{\|\mathbf{R}'\|}, \mathbf{Z}' \right\rangle}{\|\mathbf{R}'\|^2 + 2 \left\langle \frac{\mathbf{R}'}{\|\mathbf{R}'\|}, \mathbf{Z}' \right\rangle^2 - \|\mathbf{Z}'\|^2} \right) \left[\frac{\pi}{2} \right] . \tag{4.51}$$

This gives four possible values for ϕ, but solutions ϕ and $\phi + \pi$ refers to the same vector (one and its opposite). With the two remaining values, one corresponds to a minimum and is dropped off, and the other to a maximum. Then, any combination of $(\alpha, \beta) = (\cos(\psi)\gamma, \sin(\psi)\gamma)$ is an optimal solution, and as in figures 4.2 and appendix 4.B.1, the choice of ψ fixes the bifurcation plane.

5

CONCLUSION

5.1 SUMMARY OF MAIN CONTRIBUTIONS

This thesis describes a comprehensive framework for the analysis of instabilities in time-periodic flow; it provides a toolbox that includes a numerical stabilisation technique for the computation of unstable periodic orbits, an algorithm for the efficient calculation of Floquet instability modes based on time-stepping, and for the identification of optimal linear initial flow perturbations and optimal sustained forcing. This toolbox has been applied in order to analyse the instability dynamics of pulsed jets, in view of two distinct phenomena: *vortex pairing*, as an intrinsic Floquet instability, and *jet bifurcation*, which exploits an extrinsic instability in the flow response to subharmonic helical forcing.

5.1.1 *A time-delayed feedback technique for the numerical stabilisation of unstable periodic orbits*

In chapter 2, a technique has been presented that allows to stabilise unstable periodic orbits. This method relies on a time-delayed feedback to filter all frequency components that are not equal to or multiples of the frequency of the desired stabilised flow. This technique is very easy to implement, but it requires the storage, in RAM, of a complete flow period in order to perform the feedback. An optimal parametrisation of the feedback amplitude has been derived from a model problem.

The technique has been validated for the case of a laminar axisymmetric pulsed jet, which is prone to pairing. In all cases studied, it has been possible to recover a fully periodic unpaired flow. A parametric analysis over all optimal feedback amplitudes has confirmed the amplitude value obtained from the model problem.

Two extensions of this technique have been provided. First, we have been able to drastically reduce the memory footprint required to perform this stabilisation, by storing only an equispaced fraction of flow state snapshots and their time-derivatives (“check-pointing”). Between these snapshots, the flow states are reconstructed through spline-interpolation. Despite a significantly lowered memory burden, the final residual level achieved with check-pointing is of the same order as with full storage.

Second, we have been able to stabilise periodic orbits of unknown frequency. Starting from a rough estimate for this frequency, the algorithm is able to adjust to its actual value and to stabilise the flow. The effectiveness of this technique was demonstrated for the case of flow over a three-dimensional lid-driven cavity.

5.1.2 *Modal and non-modal analysis of vortex pairing in pulsed jets*

Chapter 3 provides a toolbox for both modal and non-modal instability analysis of a time-periodic flow. The pairing instability encountered in pulsed jets is interpreted as a global bifurcation from the unpaired flow, calculated in chapter 2, emphasising the respective roles of both modal and non-modal mechanisms for the bifurcation process.

After a literature review of the phenomenon, a parametric analysis of the occurrence of pairing in pulsed jets has been carried out, by means of direct numerical simulations. The effects of the Reynolds number, the Strouhal number, the inlet forcing amplitude and of the inlet noise levels have been investigated. A global trend has emerged: pairing occurs above a critical Reynolds number in a restricted Strouhal band that widens with increasing Re. A higher forcing amplitude shifts the pairing regime towards lower Reynolds number values, whereas added inlet noise mainly has the effect of triggering transient growth dynamics.

A modal stability analysis has been carried out next, relying on the Floquet framework (section 1.3.2). The base flow is the unpaired axisymmetric flow calculated in chapter 2. This analysis allowed us to accurately predict the parameter domain in which pairing occurs. The unstable Floquet mode reaches its amplitude maximum about 20 diameters downstream of the jet inlet, much further than the pairing location observed in the DNS.

Finally, a non-modal transient growth analysis has been performed, motivated by striking differences between DNS results of the transition scenario from unpaired to paired flow states, when starting with unperturbed or randomly perturbed unpaired flows. Transient effects induce a much faster growth of initial perturbations, leading to amplitude growth of about 200% per flow period, as opposed to modal growth factors on the order of 10%. The corresponding optimal perturbations are located close to the inlet, triggering much earlier pairing than in the modal scenario. This linear transient growth phenomenon was found to be in good agreement with the nonlinear DNS results.

In conclusion, the *occurrence* of sustained pairing in vortex streets has been shown to be determined by modal Floquet instability, whereas the transition path is dominated by transient phenomena.

5.1.3 *The optimal triggering of jet bifurcation*

In chapter 4, a framework for the identification of optimal sustained forcing in a periodic flow is provided. The *bifurcating jet*, the second instability encountered in jet vortex arrays, is chosen as an example. The bifurcating jet displays a strong flaring in one plane, resulting from a combination of axisymmetric and subharmonic helical forcing. In this chapter, the subharmonic forcing component has been optimised such as to maximise the jet spreading and mixing rate. As in chapter 3, the base flow used for this optimisation is the unpaired jet stabilised by means of the method described in chapter 2.

Jet bifurcation exploits the nonlinear mechanism described by Parekh, Leonard, and Reynolds (1988): following the roll-up of vortices induced by the axisymmetric forcing, the helical forcing component shifts the vortices away from the axis. Subsequently, by mutual induction, the vortices further depart from the jet axis, leading to bifurcation. Close to the inlet, the helical dynamics can be assumed to be linear, and an optimisation framework for this helical inlet forcing has been employed in order to provide maximal spreading. The time-periodic unpaired vortex array obtained in chapter 2 has been chosen as a base flow. Two responses norms have been considered: the standard $\mathcal{L}_2$ (energy) norm and a norm based on the vortex displacements.

The linear optimisation has been carried out over the Strouhal band $[0.35; 0.8]$. Across this band, the optimal $\mathcal{L}_2$ forcing peaks in the mixing layer and is mainly radial, in contrast with some previous studies that used an axial helical forcing. The optimal forcing shape is mainly phase-shifted between the different Strouhal values; if this forcing were implemented in a physical device, changing the Strouhal number would only require to change the phase difference with the axisymmetric forcing. In addition, the forcing found is very robust, being almost independent of the optimisation norm, and of the hyperparameters chosen.

The performance of the optimal forcing has been evaluated in three-dimensional DNS, and compared to a simple *ad hoc* force distribution used in the literature. A low forcing amplitude of 1% has been used in the present nonlinear simulations. First, the optimal forcing leads to much stronger spreading, and triggers the bifurcation further upstream. Second, the optimal forcing widens drastically the Strouhal band where bifurcation is encountered: while this only occurs in a narrow range for the simple forcing, spreading was observed at all tested Strouhal numbers ($[0.35; 0.8]$) with optimal forcing.

5.2 PERSPECTIVES

In this section, two physical natural extensions of this thesis, regarding blooming jets and the study of phase-averaged periodic turbulent flows, are presented, along with a comparison attempt of time-marching and spectral techniques for periodic flows.

5.2.1 *Blooming jets*

The optimisation carried out for bifurcating jets could be expanded to blooming jets Reynolds et al. (2003), represented in figure 1.11. These jets exhibit uniform flaring in all azimuthal directions, and improving both this spreading and the parameter range in which it occurs would be promising.

In such jets, the axisymmetric and the helical forcing are no longer in simple proportions; for instance, Tyliszczak (2015) use frequency ratios between axisymmetric and helical forcing between 1.6 and 3.2. Physically, this means that, contrary to the bifurcating jet, where one tends to keep a constant symmetry plane for the inlet helical forcing such as in figures 4.2a or 4.2b, in this case, one tends to have a rotating symmetry plane, such as in figure 4.2d, such that vortices are shifted in many different directions. These directions are fixed by the instantaneous azimuthal location of this helical peak at the moment when the axisymmetric forcing peak (Gohil, Saha, and Muralidhar, 2015; Tyliszczak, 2015).

The impact of this non-simple proportion between axisymmetric and helical forcings on the optimisation procedure needs to be assessed. Indeed, choosing the optimisation time T_o as $2nT_f$ ($n \in \mathbb{N}$), with the axisymmetric forcing period T_f, corresponds to a fixed zero-phase for the axisymmetric forcing, but to a varying phase for the helical one. In both bifurcating and blooming jets, we are interested in the vortex displacement with respect to its axisymmetrical equilibrium, *i.e.* its unpaired position. Following the insight developed in section 4.3.4.4, we can assume that, irrespective of the phase difference between the axisymmetric and the helical forcing, at a given optimisation time T_o, all vortices will be shifted from their axisymmetric position not in a fixed plane, but along an azimuthal direction that changes constantly in time and between vortices. Therefore, both the $\mathcal{L}_2$ and the displacement norms defined in section 4.2.4, which integrate the perturbation for a given vortex along all azimuthal positions, are well-suited for such a study.

In the end, it would be interesting to compare the shape of the optimal blooming forcing to the optimal bifurcating forcing: does this forcing mainly rely on radial or axial components? How does it evolve with the axisymmetric Strouhal number and with the frequency ratio?

5.2.2 *Extension of the mean flow analysis to turbulent phase-averaged periodic flows*

The ideas in this subsection have been developed in collaboration with Luis Benetti Ramos, Lucas Franceschini and Johann Moulin, PhD candidates at ONERA.

As stated in chapter 1, few instability investigations have been carried out over periodic phase-averaged turbulent flows. Much effort has been made to compute these phase-averaged limit cycles, through Harmonic Balance or Time Spectral Methods, as discussed in section 2.1, but little has been done to assess the stability of the resulting orbits.

Therefore, in a similar way as what mean-flow analysis provided for turbulent flows without dominating frequencies (Barkley, 2006; Beneddine et al., 2016; Sipp and Lebedev, 2007), it would be interesting to study both the stability and the response to perturbations of such phase-averaged flows. The stability analysis would give an insight into the “unnatural” frequencies that could appear in such configurations, whereas the optimal perturbation analysis would give an insight into the perturbation that could initiate large transient growth.

However, to apply the resolvent analysis methodology in phase-averaged flows, extra care is needed. Indeed, let us consider a base flow evolving at frequency ω_f and forced at a frequency ω', such as in

$$\partial_t \mathbf{q} + \mathcal{L}(t)\mathbf{q} = \hat{\mathbf{f}} e^{i\omega' t}, \tag{5.1}$$

with $\mathcal{L}(t)$ periodic of period $2\pi/\omega_f$. The resulting flow perturbation $\mathbf{q}$ contains more than one frequency, but it involves an infinite sum of Fourier components:

$$\mathbf{q}(t) = \sum_k \hat{\mathbf{q}}_{\mathbf{k}} e^{i(k\omega_f + \omega')t} = \tilde{\mathbf{q}}(t) e^{i\omega' t}, \tag{5.2}$$

with $\tilde{\mathbf{q}}(t)$ time-periodic of period $2\pi/\omega_f$. If ω_f and ω' are not commensurable, the resulting flow is aperiodic. By injecting this formulation into the periodic resolvent equation (5.1), one obtains:

$$\left(\partial_t + i\omega' + \mathcal{L}(t)\right) \tilde{\mathbf{q}}(t) = \hat{\mathbf{f}}. \tag{5.3}$$

Therefore, even if there is no well-defined phase shift between the base flow at ω_f and the forcing at ω', the forcing $\hat{\mathbf{f}} e^{i\omega' t}$ and the response $\tilde{\mathbf{q}}(t) e^{i\omega' t}$ are phase-locked. As $\tilde{\mathbf{q}}(t)$ is time-periodic, the resolvent analysis can be rewritten as

$$\max_{(\partial_t + i\omega' + \mathcal{L}(t))\tilde{\mathbf{q}}(t) = \hat{\mathbf{f}}} \frac{\displaystyle\int_0^{\frac{2\pi}{\omega_f}} \|\tilde{\mathbf{q}}(t)\|^2 \mathrm{d}t}{\|\hat{\mathbf{f}}\|^2}. \tag{5.4}$$

The problem (5.4) can then be solved by direct time-stepping, if the forcing space $\hat{\mathbf{f}}$ has a lower dimension than the entire flow space and can be spanned by a reduced basis, such as in chapter 4 or by a direct-adjoint analysis in a more general case.

Another method relies on the use of the Harmonic Balance Technique, or Time Spectral Method, described in section 1.2.1.2, which substitutes CPU-intensive time-stepping with memory-intensive matrix computations.

5.2.3 *Comparing spectral methods with time-stepping techniques*

In this thesis, for both the stabilisation of unstable orbits and the stability analysis, two different families of methods were available. On the one hand, methods relying on time-stepping, such as the time-delayed feedback (see chapter 2) or the Floquet analysis through time-stepping (see chapter 3) and, on the other hand, spectral methods, decomposing the flow in Fourier components, described in section 1.3.3 and in section 2.1. It would be interesting to compare the performance of both methods applied to both problems. To do so, I describe some parameters that may motivate the choice of one or the other kind of methods.

The computational cost in the two group of methods are constrained by two related, albeit different, parameters: spectral methods become more expensive when more *Fourier components* are needed to resolve the time-periodicity, whereas the numerical burden of time-stepping techniques increases with the *number of time-steps in a given flow period*. A large number of Fourier components imposes a minimal number of time-steps per period (at least because of the Nyquist criterion); on the contrary, a large number of time-steps in a flow period does not necessarily correspond to numerous Fourier components; this number of time-steps can be imposed by a CFL condition, such as a mesh refinement close to an obstacle.

To compute unstable orbits, different characteristics of the flow influence the results. Concerning the time-delayed feedback method, one of the most important criteria determining the algorithm performance is the relative position of the frequency to be damped compared to the frequency to be resolved (figure 2.2): a subharmonic frequency is well-targeted by the algorithm, whereas quasi-periodic frequencies $\omega_f \pm \delta\omega$ are poorly controlled. In private conversations with Damien Jallas and Olivier Marquet (ONERA), we discussed on how to improve this technique to target frequencies that are not subharmonic. We proposed to modify the feedback term, either to add combinations of previous flow snapshots, such as $\mathbf{u}(t-2T)$ or $\mathbf{u}(t-4T)$ or to add combinations of phase-shifted flow snapshots, such as $\mathbf{u}(t-T/3)$ or $\mathbf{u}(t-T/4)$. The purpose is, again, to design a feedback which filters only the targeted frequency $e^{i\omega' t}$ with the right phase.

When it comes to spectral methods, the dominant criterion would be the quality of the initial guess of the algorithm; these methods rely on Newton techniques or pseudo-time marching to damp residuals, and the closer one is to the unstable orbit, the easier it is to converge the flow.

To study their stability, the hardware available for the computation and its architecture are also very important. A clear trade-off between CPU and memory limitations emerges. On the one hand, time-marching techniques require less RAM memory than frequency methods because of the lower number of components involved; however they rely on the propagation over many time-steps, hence requiring more CPU time.

On the other hand, performing Floquet analysis in the harmonic balance or the time-spectral frameworks requires large RAM memory to compute the eigenvalues of the propagation operator (Lazarus and Thomas, 2010), but not so much computation time. As a consequence, on a cluster, even if the latter methods require less CPU, one might end up using many more cluster nodes than necessary in order to obtain the required RAM.

To conclude, it would be interesting to compare the performance of both algorithms on a variety of problems. I believe that there is no definite reason to prefer one method over others in general, and that both are well suited in certain cases.

A

STABILITY OF VICINAL SURFACES: BEYOND THE QUASISTATIC APPROXIMATION

CONTEXT

In the following Appendices, we report a work coming from a collaboration with Laurent Guin, PhD candidate in the *Laboratoire de Mécanique des Solides* of École Polytechnique and Professors Michel Jabbour and Nicolas Triantafyllidis from the same laboratory.

It is an interesting example where the stability methods of hydrodynamics prove to be useful in other scientific fields, specifically the field of surface science.

The problem, which is part of the thesis work of Laurent Guin concerns the stability of vicinal surfaces. A vicinal surface is the surface that results from a crystal cut in a plane deliberately misaligned from a high symmetry crystal plane. At the atomic level, this results in a sequence of atomic terraces separated by a regular array of atomic steps with an interstep distance controlled by the cutting angle (see figure A.1). Vicinal surfaces are used to perform *epitaxy* — the growth of a crystalline structure on top of a crystalline substrate. In particular, we focus on the step flow regime where, as atoms arriving from the vapour end up attaching to the steps, crystal growth occurs through the propagation of these atomic steps. Depending on the growth conditions, the regular array of steps can undergo two major kind of instabilities: *step bunching*, when straight steps propagating at different speeds forms a alternating pattern of wide atomic terraces and step bunches, and *step meandering*, when these steps gets deformed in the spanwise direction, transitioning from rectilinear to wavy steps.

The propagation of such steps can be modelled by a system of partial differential equations with moving interfaces. The widespread approach in the physics literature to study the stability of this system relies on the so-called quasistatic approximation which simplifies the stability analysis by neglecting some time-dependent terms in the governing equations. In our collaboration, drawing on methods of hydrodynamic stability we perform the stability analysis without resorting to the quasistatic approximation and show that for several growth conditions the stability results derived under the quasistatic approximations are not valid. In addition, the new results brought by the general analysis provide possible explanations for some experimental observations of step bunching.

From these collaboration, two articles are in preparation. The first one gives an overview of the methods and the main results while the second one provides a detailed description of the stability analysis and a comprehensive discussion of the new features revealed by the general stability analysis. For a comprehensive presentation of the problem, we fully reproduce in the following the first article in its provisional version and include in appendix B the sections of the second article related to the stability analysis itself.

While the subsequent material furnishes a self-contained presentation of this work, I specifically contributed to the following aspects. First, the derivation of the linear stability problem that fully encompasses the moving interfaces (section B.1 of appendix B). Second, its numerical implementation using Chebychev spectral methods (section B.2 of appendix B).

ABSTRACT

The quasistatic approximation is the framework within which the existing theoretical studies of step stability at low deposition/evaporation rate are carried out. Using fluid flow stability methods, we compute the linear stability of the step dynamics without resorting to that approximation and show that the regimes of stability against step bunching are modified even in the domain where the quasistatic analysis was thought sufficient. It appears that for pure deposition and slow step kinetics (attachment/detachment limited regime), the steps are naturally unstable against step bunching. Without appealing to any sophisticated mechanism, this provides a possible simple explanation for the occurrence of that instability in the epitaxial growth of several materials.

MAIN ARTICLE

Epitaxial crystal growth is often accompanied by surface morphology changes such as island nucleation or atomic step bunching and meandering (Michely and Krug, 2012). Understanding the microscopic mechanisms underlying surface patterning is a problem of fundamental interest with technological applications like the use of the patterns as templates for growing nanostructures. Whereas the first crystal growth model of the atomic steps dynamics was introduced by Burton, Cabrera, and Frank (1951) before any direct observation of atomic step, the advent a few decades later of atomic scale microscopy imaging, fostered theoretical works on the step flow model.

One of the widely observed instabilities of step flow growth is step bunching, explained in the early days as a consequence of the inverse Ehrlich-Schwoebel (ES) effect (Schwoebel, 1969; Schwoebel and Shipsey, 1966), whereby adatom attachment to descending steps is more favorable than to ascending ones. As cases were encountered where the ES effect is more likely not inverse but rather negligible or direct, other mechanisms for step bunching have been proposed such as the coupling between two diffusing species (Pimpinelli and Videcoq, 2000) or step-edge diffusion (Politi and Krug, 2000).

With a few exceptions (Dufay, Frisch, and Debierre, 2007; Ghez, Cohen, and Keller, 1993; Keller, Cohen, and Merchant, 1993; Liu and Metiu, 1994; Ranguelov and Stoyanov, 2007), the classical stability analyses (Pierre-Louis, 2003; Sato, Uwaha, and Saito, 2000; Schwoebel, 1969), whereby step bunching under deposition is associated to an inverse ES effect, have been carried out in the framework of the

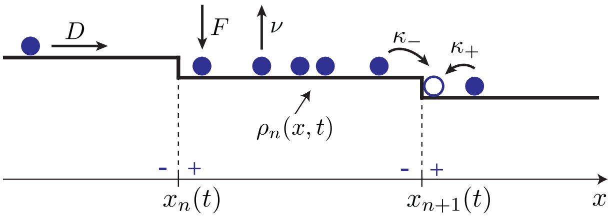

Figure A.1: Sequence of two successive atomic steps displaying the microscopic mechanisms involved in step flow.

quasistatic approximation (Ghez and Iyer, 1988; Krug, 2005; Michely and Krug, 2012). This mathematical simplifications, detailed below, is usually considered appropriate in regimes of low deposition rate. In this letter, we develop a linear stability analysis of the general governing equations without resorting to that simplification and surprisingly find that the stability results are modified, even in the regime of slow deposition. While this result questions the validity of the quasistatic approximation, it also provides a new mechanism for step bunching which might be pertinent for the understanding of its occurrence in epitaxial growth of GaAs(001) and Si(111)-7×7.

For studying the step bunching instability, steps can be assumed straight and described in a one-dimensional framework by their position x_n on the x-axis (see figure A.1), while the adatom density on the terrace n is denoted ρ_n. The asymmetry of the attachment/detachment (a/d) of adatoms to the descending (ascending) steps is accounted for by the kinetic coefficients κ_- (κ_+). In addition, elastic interactions between the steps, of magnitude α, are embedded in the elastic configurational force $f_n := -\alpha/(x_{n+1}-x_n)^3 + \alpha/(x_n - x_{n-1})^3$ exerted on step n by the nearest-steps (Krug, 2005). The governing equations for the fields $\rho_n(x,t)$ and $x_n(t)$, derived with methods of continuum thermodynamics (Cermelli and Jabbour, 2005) consist of: the diffusion equation on terraces

$$\partial_t \rho_n = D\partial_{xx}\rho_n + F - \nu\rho_n, \tag{A.1}$$

with D the diffusion coefficient, F the deposition rate and ν the evaporation probability; the boundary conditions at steps

$$\begin{aligned} -\rho_n^- \dot{x}_{n+1} - D(\partial_x\rho_n)^- - a^2\rho_{eq}^* &= \kappa_-\left[\rho_n^- - \rho_{eq}^*\left([\![\rho]\!]_{x_{n+1}} - \frac{f_{n+1}}{k_B T}\right)\right] =: J_{n+1}^-, \\ \rho_n^+ \dot{x}_n + D(\partial_x\rho_n)^+ - a^2\rho_{eq}^* &= \kappa_+\left[\rho_n^+ - \rho_{eq}^*\left([\![\rho]\!]_{x_n} - \frac{f_n}{k_B T}\right)\right] =: J_n^+, \end{aligned} \tag{A.2}$$

with ρ_{eq}^* the adatom density in equilibrium with an isolated step, a the lattice parameter, $[\![\rho]\!]_{x_n}$ the jump $\rho_{n+1}(x_n,t) - \rho_n(x_n,t)$, k_B the Boltzmann constant and T the absolute temperature; and the step velocity equation

$$\dot{x}_n = a^2(J_n^+ + J_n^-), \tag{A.3}$$

where $J_n^\pm$ are the net attachment rates to the steps as defined in (A.2).

While (A.1)-(A.3) embed only the basic physical mechanisms (ES effect, elastic interactions), they can be easily completed to account for other processes such as step permeability or electromigration if appropriate.

In the framework of continuum step models, step bunching is investigated through a stability analysis of the steady-state fundamental solution with equidistant steps,

$$\overset{o}{x}_n(t) = nL_0 + \overset{o}{V}t \quad ; \quad \overset{o}{\rho}_n(x,t) = \overset{o}{\varrho}(x - \overset{o}{x}_n(t)), \tag{A.4}$$

where L_0 denotes the initial terrace width and $\overset{o}{V}$ and $\overset{o}{\varrho}$ are the unknown uniform step velocity and adatom density function, respectively. which is, as a first step, investigated with a linear stability analysis. Invoking the quasistatic approximation, most existing stability analyses are performed neglecting the dynamic terms which consist of the advective currents $\rho_n^{\pm}\dot{x}_n$ in (A.2) —only included in recent theoretical works (Cermelli and Jabbour, 2005; Dufay, Frisch, and Debierre, 2007; Pierre-Louis, 2003)— and the term $\partial_t\rho_n$ in (A.1). This approximation is traditionally justified by noting that under low deposition (or evaporation) rate, the time scale for the diffusion of an adatom across a terrace is small compared to the time taken by a step for the same displacement which, in the context of deposition, reads (Ghez and Iyer, 1988; Krug, 2005; Michely and Krug, 2012)

$$FL_0^2a^2/D \ll 1. \tag{A.5}$$

As noticed by some authors (Michely and Krug, 2012; Pierre-Louis and Misbah, 1998), the slow deposition condition (A.5) is actually always satisfied in step flow growth as it coincides with the one for island nucleation which is another regime. Note that the quasistatic approximation brings considerable simplification to the stability analysis by transforming a partial differential system strongly coupling $\rho_n(x,t)$ and $x_n(t)$ in a weakly coupled ordinary differential system. A few studies (Dufay, Frisch, and Debierre, 2007; Ghez, Cohen, and Keller, 1993; Keller, Cohen, and Merchant, 1993; Liu and Metiu, 1994; Ranguelov and Stoyanov, 2007) considered the stability against step bunching while including partly the dynamic terms. However, either because of the lack of some of the dynamic terms (Ghez, Cohen, and Keller, 1993; Keller, Cohen, and Merchant, 1993; Liu and Metiu, 1994) or approximations in the mathematical treatment of the stability problem (Dufay, Frisch, and Debierre, 2007; Ranguelov and Stoyanov, 2007), the important implications of the dynamic terms on the stability results were not drawn. Furthermore, in these work the purpose is to address the step stability beyond the condition (A.5), while we are concern by all deposition rates.

In this letter, making use of stability methods of fluid dynamics, we address the linear stability of the general system (A.1)-(A.3) without neglecting the dynamic terms, and show that, while the effect on stability of these terms is major at relatively high deposition rate, it is also important in the limit of slow deposition, hence questioning the validity of the quasistatic approximation. In addition, stability changes brought by the dynamic terms provide possible explanations for the observed step bunching in epitaxial growth of Si(111)-7×7 and GaAs(001).

The sytem (A.1)-(A.3) is nondimensionalised with L_0, L_0^2/D and ρ_{eq}^* as the characteristic length, time and adatom density respectively. Introducing the dimensionless deposition rate $\overline{F} := FL_0^2/(\rho_{eq}^*D)$ and evaporation probability $\overline{\nu} := \nu L_0^2/D$, the diffusion equation is rewritten

$$\partial_t\rho_n = \partial_{xx}\rho_n - \overline{\nu}\rho_n + \overline{F}, \tag{A.6}$$

along with the boundary conditions

$$\begin{aligned} -\rho_n^- \dot{x}_{n+1} - (\partial_x \rho_n)^- &= \overline{\kappa}(\rho_n^- - 1 - \Theta[\![\rho]\!]_{x_{n+1}} + \overline{f}_{n+1}) =: \overline{J}^-_{n+1}, \\ \rho_n^+ \dot{x}_n + (\partial_x \rho_n)^+ &= \overline{\kappa} S(\rho_n^+ - 1 - \Theta[\![\rho]\!]_{x_n} + \overline{f}_n) =: \overline{J}^+_n, \end{aligned} \tag{A.7}$$

and the step velocity equation

$$\dot{x}_n = \Theta(\overline{J}^+_n + \overline{J}^-_n), \tag{A.8}$$

where the parameter $\overline{\kappa} := \kappa_- L_0/D$ expresses the ratio of a/d kinetics to terrace diffusion kinetics, $S := \kappa_+/\kappa_-$ gives the nature of the Schwoebel effect, $\overline{f}_n := -\overline{\alpha}/(x_{n+1} - x_n)^3 + \overline{\alpha}/(x_n - x_{n-1})^3$ is the dimensionless elastic configurational force with $\overline{\alpha} := a^2\alpha/(k_B T L_0^3)$ and $\Theta := a^2 \rho^*_{eq}$ denotes the equilibrium adatom coverage. For simplicity, we do not relabel the dimensionless space, time and adatom density.

The linear stability analysis of (A.6)-(A.8) is outlined as follows. Consider a sequence of an infinite number of steps, the principal solution, written as the dimensionless form of (A.4) is solved for $\overset{o}{V}$ and the function $\overset{o}{\varrho}$. Note that in the case of pure deposition ($\overline{\nu} = 0$, relevant for crystal growth at relatively low temperature) they have analytical expressions: $\overset{o}{V} = \overline{F}\Theta$ and $x \mapsto \overset{o}{\varrho}(x)$ is a quadratic function. When perturbing $(x_n, \rho_n)_{n\in\mathbb{N}}$ about the principal solution, (A.6)-(A.8) form a partial differential system with freely moving interfaces at $(x_n)_{n\in\mathbb{N}}$. Since domain boundaries are time-varying unknowns, using an arbitrary Lagrangian-Eulerian approach, we map for each terrace n the spatial variable $x \in (x_n, x_{n+1})$ to $u = g_n(x,t) := (x - x_n(t))/(x_{n+1}(t) - x_n(t)) \in (0,1)$ and with the reciprocal function g_n^{-1} introduce the *Lagrangian adatom densities*

$$\tilde{\rho}_n(u,t) := \rho_n(g_n^{-1}(u,t),t) \tag{A.9}$$

defined, for all n, on $(0,1) \times \mathbb{R}^+$.

Rewriting (A.6)-(A.8) in terms of variables $(x_n, \tilde{\rho}_n)$ and denoting the perturbations by $\mathbf{q}_n = (\delta x_n, \delta\tilde{\rho}_n)$, the linear perturbation equation for $(\mathbf{q}_n)_{n\in\mathbb{N}}$ about the principal solution reads in abstract form

$$\mathcal{A}\big[\mathbf{q}_{n-1}, \mathbf{q}_n, \mathbf{q}_{n+1}, \mathbf{q}_{n+2}\big] = \mathcal{B}\big[\dot{\mathbf{q}}_n, \dot{\mathbf{q}}_{n+1}\big], \tag{A.10}$$

where superimposed dot denote the partial time derivative and $\mathcal{A}$ and $\mathcal{B}$ are linear operators involving u-derivatives of $\delta\tilde{\rho}_n$. Due to the linearity, of the operators $\mathcal{A}$ and $\mathcal{B}$, their time-independence and invariance with respect to 1-terrace translation —which lies on the 1-terrace periodicity of the principal solution— the solutions of (A.10) can be sought as a combination of *Bloch waves* whose component of wave number $k \in (-\pi, \pi)$ reads

$$\begin{aligned} \delta x_n(t) &= \delta\hat{x}\exp(ikn + \lambda t), \\ \delta\tilde{\rho}_n(u,t) &= \delta\hat{\rho}(u)\exp(ikn + \lambda t), \end{aligned} \tag{A.11}$$

where λ is the unknown complex growth rate associated to k. Inserting the Bloch wave expression (A.11) in the linear perturbation equation (A.10) yields for a given wave number k, a generalised eigenvalue problem of the form

$$\hat{\mathcal{A}}_k \hat{\mathbf{q}} = \lambda \hat{\mathcal{B}}_k \hat{\mathbf{q}}, \tag{A.12}$$

Mechanism	Direct ES $(S > 1)$	Inverse ES $(S < 1)$	Elasticity f_n	Diff. CF $\Theta[\![\rho]\!]$
Growth	$\mathcal{S}$	$\mathcal{D}$	$\mathcal{S}$	$\mathcal{D}$
Evaporation	$\mathcal{D}$	$\mathcal{S}$	$\mathcal{S}$	$\mathcal{S}$

Table A.1: Effect on stability under deposition and evaporation of the mechanisms in the quasistatic approximation: inverse and direct Ehrlich-Schwoebel effect (ES), elasticity, diffusion-mediated configurational force (Diff. CF). Notations $\mathcal{S}$ and $\mathcal{D}$ are used for stabilising and destabilising mechanisms, respectively.

where $\hat{\mathbf{q}} := (\delta\hat{x}, \delta\hat{\rho}) \in \mathbb{C} \times \mathbb{C}^{(0,1)}$ and $\hat{\mathcal{A}}_k$ and $\hat{\mathcal{B}}_k$ denote the linear operators deriving from $\mathcal{A}$ and $\mathcal{B}$, respectively. Solving (A.12) numerically by means of *Chebychev spectral methods* (Peyret, 2002), we obtain for a given k a set of eigenmodes $\hat{\mathbf{q}}$ and associated growth rate λ, among which the maximum of $\mathcal{R}(\lambda)$ is the critical growth rate of mode k, where $\mathcal{R}(\lambda)$ is the real part of λ.

In summary, we have devised a method to compute the dispersion relation $\mathcal{R}(\lambda)[k]$ that provides the critical growth rate of a perturbation of wave number k for a step dynamics governed by the general system (A.6)-(A.8) not subject to any simplification. The system is stable if for any mode k, $\mathcal{R}(\lambda)[k] \leq 0$. This new method by comparison of its results with the analytical dispersion relations derived under the quasistatic approximation (Pierre-Louis, 2003) allows to directly quantify the effect of the dynamic terms on the stability, whereby addressing the validity of that approximation.

A relevant approach to make sense of the stability behaviour of the system (A.6)-(A.8) consists, as summarised in table A.1 for the quasistatic results, in looking at the contribution to stability of each mechanism it contains. The dynamic terms can be seen as another mechanism (though naturally present) whose influence on stability is studied, *per se*, by disabling the other phenomena($S = 1$, $\Theta[\![\rho]\!] = 0$ and $\overline{\alpha} = 0$) so that, the quasistatic model having neutral stability ($\lambda = 0$ for all k), the dispersion relation of the system (A.6)-(A.8) shown in figure A.2 accounts solely for the effect of the dynamic terms. It appears that the relevant parameters that determine the stability influence of these terms is $\overline{\kappa}$: dynamic terms rather destabilising for $\overline{\kappa} < 1$ (tend to the a/d limited regime as $\overline{\kappa} \ll 1$) and stabilising for $\overline{\kappa} > 1$ (tend to the diffusion limited regime as $\overline{\kappa} \gg 1$). Furthermore note that the magnitude of the effect of the dynamic terms roughly scales as a linear function of $\overline{F}$ —like the other kinetics mechanisms— and as a quadratic function of Θ, implying a more significant dynamic effect for materials with an high adatom coverage.

In turn, the quasistatic stability predictions for various continuum step models found in the literature appear to be significantly modified when including the dynamic terms. Furthermore, we illustrate in the following how these modifications provide possible explanations to some experimental results, in particular to the step bunching observed in growth of GaAs(001) (Hata et al., 1993; Ishizaki, Ohkuri, and Fukui, 1996; Ishizaki et al., 1994; Kasu and Fukui, 1992; Pond, 1994; Shinohara and Inoue, 1995) and Si(111)-7×7 (Omi et al., 2005) in the temperature ranges of 600°C-700°C and 700°C-780°C, respectively.

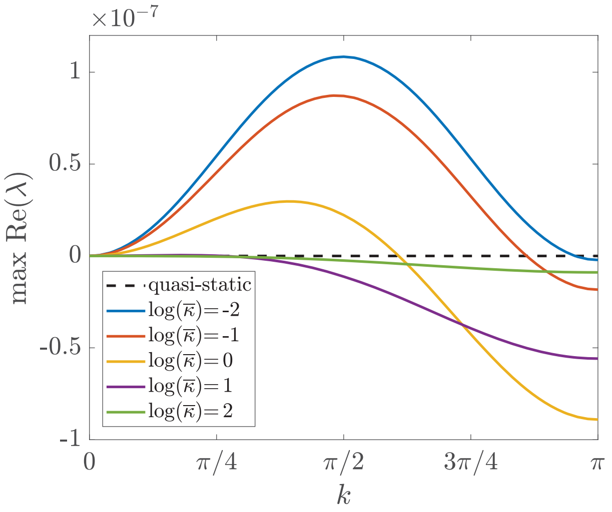

Figure A.2: Dispersion curves giving the critical growth rate max $\mathcal{R}(\lambda)$ associated to the wave number k under pure deposition ($\overline{v} = 0$, $\overline{F} = 10^{-3}$, $\Theta = 0.01$). The dotted line shows the neutral stability under the quasistatic approximation and the continuous lines give the stability results with dynamic terms for different values of $\overline{\kappa}$. Apart from dynamic effect, other mechanisms are disabled ($S = 1$, $\overline{\alpha} = 0$, and $\Theta[\![\rho]\!] = 0$).

The elastic interactions between the steps being stabilising, the unique way within the classical step continuum model —which does not include the term $\Theta[\![\rho]\!]$— to account for step bunching under growth is to invoke an inverse ES effect. However, as noticed in Pimpinelli and Videcoq (2000) and Vladimirova, De Vita, and Pimpinelli (2001), although such a barrier favouring attachment from the upper terrace is conceivable, it is, regarding the microscopic picture of a step, counterintuitive. Studies in Si(111)-7×7, based on observations such as the denuded zones around steps (Rogilo et al., 2013; Voigtlander et al., 1995), the decay rates of islands and holes (Ichimiya, Tanaka, and Ishiyama, 1996) or the distributions of island nucleations (Chung and Altman, 2002) resulted in contradictory results, namely a direct (Ichimiya, Tanaka, and Ishiyama, 1996), inverse (Chung and Altman, 2002; Rogilo et al., 2013) and the absence of a Schwoebel barrier (Voigtlander et al., 1995). On the other hand, work on the growth of mound (Krug, 1997; Šmilauer and Vvedensky, 1995) and direct *ab initio* computations concluded that the ES barrier is direct in GaAs(001) (Salmi et al., 1999). Giving the limited evidence of an inverse Schwoebel effect to explain step bunching, new physical mechanisms —which are plausible but without clear evidence of their existence— have been invoked such as coupling between diffusing precursors and adatoms (Pimpinelli and Videcoq, 2000) in vapour phase epitaxy of GaAs or step edge diffusion (Politi and Krug, 2000) for Si(111) molecular beam epitaxy.

Giving the undetermined nature of the Schwoebel barrier in Si(111)-7×7 , we study, in the absence of it ($S = 1$), the stability under deposition which results from the interplay of the dynamic terms and the stabilising elastic interactions. While in such a case, the classical model (where $\Theta[\![\rho]\!]$ is absent), involving only the elastic interactions, predicts a stable growth for all set of parameters, the stability diagram,

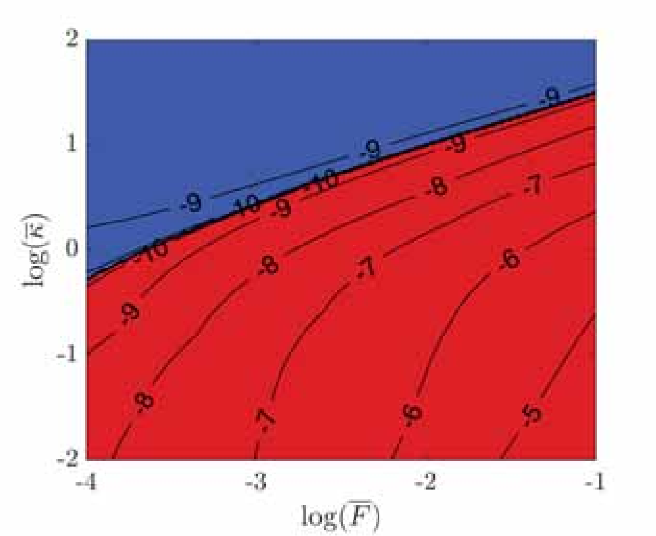

Figure A.3: Stability diagram under deposition ($\overline{\nu} = 0$) when including elasticity ($\overline{\alpha} = 10^{-4}$) and dynamic terms and without ES barrier ($S = 1$) nor diffusion-mediated configurational force ($\Theta[\![\rho]\!] = 0$). Blue and red domains correspond to the stable ($\max_{k\in(-\pi,\pi)} \mathcal{R}(\lambda) < 0$) and unstable ($\max_{k\in(-\pi,\pi)} \mathcal{R}(\lambda) > 0$) regions, respectively. For the latter, isolines display $\max_{k\in(-\pi,\pi)} \log\left(\mathcal{R}(\lambda)\right)$, indicating the magnitude of the most critical growth rate. Note for comparison that the stability diagram corresponding to the classical model (only elastic interaction, no dynamic terms) is stable (blue domain) everywhere.

when including the dynamic terms is shown in figure A.3. Here, the coefficient $\overline{\alpha}$ of the elastic interaction (Marchenko and Parshin, 1980) has been derived from dipole computation (Stewart, Pohland, and Gibson, 1994) in Si(111)-7×7. The range of $\overline{\kappa}$ covers both a/d limited and diffusion limited regimes while values of $\overline{F}$ corresponds to different deposition rates below one, typical value at which step flow would break for island growth (Michely and Krug, 2012).

It appears that the dynamic terms create a large domain of instability essentially for low values of $\overline{\kappa}$ (inclination for a/d limited regime), hence revealing a possible mechanism responsible for the unstable growth of Si(111)-7×7. In sum, we show that step bunching under deposition can be exhibited simply by performing a proper stability analysis on the original system that includes dynamic terms. This complements our previous work (Cermelli and Jabbour, 2005; Cermelli and Jabbour, 2007) where a thermodynamically consistent derivation of the governing equations revealed the existence of the configurational force $\Theta[\![\rho]\!]$ which is another mechanism whereby step bunching under growth may happen. Furthermore, figure A.3 shows that the dynamic terms have an effect even for $\overline{F}\Theta \ll 1$, regime where the quasistatic approximation was considered appropriate in the literature, which interestingly questions its domain of validity. Note that qualitatively, we observe the same trend as in the work of Ranguelov and Stoyanov (2007), i.e., an instability above a certain value of step velocity —step velocity being proportional to $\overline{F}$ can be read on the x-axis of figure A.3— while unlike them we are not considering especially high deposition rate as we stay in the regime where (A.5) is satisfied.

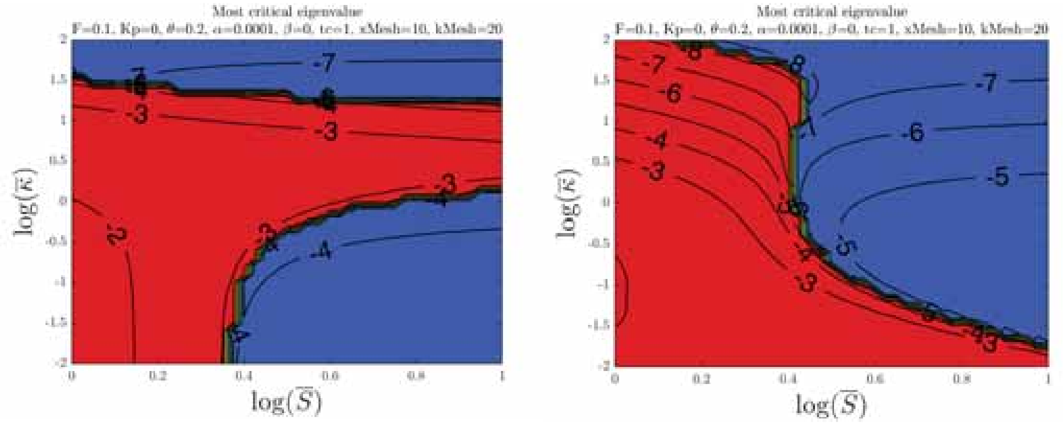

Figure A.4: Stability diagram for pure deposition ($\overline{F} = 0.1, \overline{v} = 0$) with elasticity ($\overline{\alpha} = 10^{-5}$), direct Ehrlich-Schwoebel barrier ($1 < S < 10$) and diffusion-mediated configurational force ($\Theta = 0.2$) under the quasistatic approximation (a) and with dynamic terms (b). For the legend of colours and isolines see caption of figure A.3.

The importance of keeping the dynamic terms for the stability analysis appears as well when the model including the various likely relevant mechanisms which are, in addition to elasticity, both a ES barrier and the diffusion-mediated configurational force. Here we have in mind the growth of GaAs(001) for which estimation of the direct ES barrier are between $S = 2$ and $S = 10$ and the particularly high equilibrium adatom coverage ($\Theta \sim 0.2$ (Johnson et al., 1996; Tersoff, Johnson, and Orr, 1997)) suggests a strong effect of the dynamic terms. As can be seen in table A.1, in the case of growth with a direct Schwoebel barrier, an unstable region may result from the diffusion-mediated configurational force as shown in figure A.4(a) under the quasistatic approximation. By comparison, results with dynamic terms (figure A.4(b)) show a strong modification of the stability domains.

The two cases described above illustrate the fact that the dynamic terms cannot be neglected *a priori* in the linear stability analysis of the continuum step model. In the first example, figure A.3, the dynamic terms might provide a simple explanations for step bunching in a situation where, as an analysis in the quasistatic case predicted stable growth, theoreticians were lead to invoke new physical mechanisms to account for the experimental results. The second example, shown on figure A.4, gives a case where a complex stability diagram which results from the interplay of various mechanisms is modified by the dynamic terms in a non-trivial manner.

While we show that keeping the dynamic terms is important regarding the linear stability analysis, it is also likely to have an effect on the nonlinear dynamic evolution of the bunches of steps. The numerical resolution of the nonlinear partial differential system (A.1)-(A.3) with moving interfaces represents an interesting challenge. Indeed, to better determine the mechanism behind step bunching in a specific experimental cases, recent works (Krug et al., 2005; Pimpinelli et al., 2002) have undertaken, under the quasistatic approximation, a classification based on the spatial patterns of the step bunches. The numerical resolution of (A.1)-(A.3), by providing how the dynamic effect affects the patterns of the bunched surfaces would help to identify the experimental cases where bunching is related to this effect.

B

DETAILS ON THE STEP BUNCHING STABILITY ANALYSIS

CONTEXT

This second appendix provides a more thorough analysis on the step bunching stability analysis. In particular, it highlights the physics behind the computed equations (section B.1) and explains in details the stability analysis conducted (section B.2).

B.1 STEP DYNAMICS MODEL

B.1.1 *Overview of the governing equations*

Consider, in a 1D framework, an infinite sequence of straight atomic steps (see figure A.1) and denote by $x_n(t)$ the position of the n^{th} step. The dynamics of these steps results from the attachment to the steps and detachment from the steps of adatoms that diffuse on the atomic terraces. With the objective of investigating the influence on the stability against step bunching of various physical ingredients added in the last decades to the original step model of Burton, Cabrera, and Frank (1951) we consider a model based on the thermodynamically consistent derivation of Cermelli and Jabbour (2005) and which includes:

1. An asymmetry in the attachment/detachment (a/d) rates from the upper and lower terraces (i.e., direct or inverse Ehrlich-Schwoebel (ES) barrier (Schwoebel, 1969; Schwoebel and Shipsey, 1966)).
2. The elastically mediated step-step interactions of homoepitaxy and heteroepitaxy (Tersoff et al., 1995).
3. Finite permeability of steps allowing for direct hopping of adatoms between terraces (Ozdemir and Zangwill, 1992; Pierre-Louis, 2003).
4. The diffusion-mediated configurational force exhibited in the work of Cermelli and Jabbour (2005).
5. The advection terms accounting for the adatom current induced by the motion of steps included in recent works (Cermelli and Jabbour, 2005; Dufay, Frisch, and Debierre, 2007; Pierre-Louis, 2003).

Note that we do not include the effect of electromigration of adatoms which restrict the present study to situations with radiative heating of the substrate (by opposition to electric current heating). Indeed, regarding the stability results, electromigration adds another layer of complexity which should be addressed after a good understanding of the stability in the absence of electromigration.

Nevertheless, the extension of the stability analysis developed in section B.2 to situations with electromigration is straightforward.

The dynamics of the vicinal surface is governed by the adatom diffusion on the terrace along with the corresponding boundary conditions for the adatom flux at the steps completed by the step velocity equation. The governing equations for the adatom density $\rho_n(x,t)$ on terrace n and the step position $x_n(t)$ can be categorised in the class of free boundary problem where the "boundaries" are the infinitely many interfaces constituted by the steps. We derive these governing equations using concepts of continuum thermodynamics, in line with the work of Cermelli and Jabbour (2005) that we complete by including elastic interactions between steps and step permeability. For conciseness, this section summarizes the governing equations whose full derivation can be obtained from Cermelli and Jabbour (2005).

The dynamics of adatoms on all terraces (for all n in $\mathbb{Z}$) is governed by a reaction-diffusion equation, which derives from the adatom balance law and the constitutive relations for the adatom diffusion flux and deposition-evaporation rate as a function of the appropriate chemical potentials (see Cermelli and Jabbour, 2005). Denoting by ρ_{eq}^* the equilibrium adatom density (for an equilibrium with a straight isolated step) and assuming small departures of the adatom density from its equilibrium value, i.e., $|\rho_n - \rho_{eq}^*| \ll \rho_{eq}^*$, it reduces to

$$\partial_t\rho_n = D\partial_{xx}\rho_n + F - \nu\rho_n, \tag{B.1}$$

where D is the diffusion coefficient of adatoms, ν their evaporation probability and F the deposition flux of atoms. Equation (B.1) is completed by boundary conditions on the adatom current at both sides of each step. Denoting by κ_- (κ_+) the kinetic coefficients for attachment/detachment of adatoms to the step from the upper (lower) terrace and κ_p the kinetic coefficient for adatom hopping between terraces (related to permeability), the combination of the adatom balance at the n^{th} step and the constitutive relations for the a/d and hopping fluxes, yields under the near-equilibrium condition the following boundary conditions:

$$\begin{aligned}
-\rho_n^-\dot{x}_{n+1} - D(\partial_x\rho_n)^- &= \underbrace{\kappa_-\left[\rho_n^- - \rho_{eq}^* - a^2\rho_{eq}^*\left([\![\rho]\!]_{x_{n+1}} - \frac{f_{n+1}}{k_BT}\right)\right]}_{J_{n+1}^-} - \kappa_p[\![\rho]\!]_{x_{n+1}},\\
\rho_n^+\dot{x}_n + D(\partial_x\rho_n)^+ &= \underbrace{\kappa_+\left[\rho_n^+ - \rho_{eq}^* - a^2\rho_{eq}^*\left([\![\rho]\!]_{x_n} - \frac{f_n}{k_BT}\right)\right]}_{J_n^+} - \kappa_p[\![\rho]\!]_{x_n},
\end{aligned} \tag{B.2}$$

with $\dot{x}_n(t)$ the velocity of step n, a^2 the surface area occupied by a crystal atom, $f_n(t)$ the elastic configurational force exerted by the other steps on step n, k_B the Boltzmann constant and T the absolute temperature. For any field φ, the φ^- (φ^+) denotes the limit values of φ approaching the step from above (below) and $[\![\rho]\!]_{x_n}$ denotes the jump $\rho_{n+1}(x_n,t) - \rho_n(x_n,t)$. The current J_n^- (J_n^+) denote the net attachment flux from the upper (lower) terrace to the step n.

Finally, the velocity of the n^{th} step, deriving from the adatom balance at steps which involves the net attachment flux of adatoms to them reads

$$\dot{x}_n = a^2(J_n^- + J_n^+). \tag{B.3}$$

Equations (B.1)-(B.3) written for all $n \in \mathbb{Z}$ constitute a complete time-evolution system for the unknowns fields $\rho_n(x,t)$ and $x_n(t)$.

B.1.2 *Nondimensionalisation*

We nondimensionalise the free-boundary value problem (B.1)-(B.3) with the initial terrace width L_0 as a characteristic length, ρ^*_{eq} for the adatom density and L_0^2/D as a characteristic time, and consequently identify eight dimensionless parameters in the dimensionless formulation of the problem. The equilibrium adatom coverage is described by

$$\Theta := a^2 \rho^*_{eq}, \tag{B.4}$$

as a fraction of the available lattice sites, clearly $0 \leq \Theta \leq 1$. The deposition and evaporation of adatoms are characterised by their dimensionless counterparts

$$\overline{F} := \frac{F L_0^2}{\rho^*_{eq} D} = \frac{L_0^2}{\left(L_d^{dep}\right)^2}, \tag{B.5}$$

which quantifies the ratio of the initial terrace width to the diffusion length under deposition and

$$\overline{\nu} := \frac{\nu L_0^2}{D} = \frac{L_0^2}{\left(L_d^{eva}\right)^2}, \tag{B.6}$$

that conversely gives the ratio of the initial terrace width to the diffusion length under evaporation. Note that the natural requirement that $\rho \leq 1/a^2$ and the more compelling assumption that ρ deviates little from ρ^*_{eq} implies upper bounds on the values of $\overline{F}$ and $\overline{\nu}$. Given that the adatom a/d from above and below are related to similar atomistic mechanisms, they shall have comparable orders of magnitude, hence the kinetic coefficients are rewritten in terms of

$$\overline{\kappa} = \frac{\kappa_- L_0}{D}, \tag{B.7}$$

expressing the ratio of the initial terrace width to the a/d kinetic length D/κ_- and

$$S = \frac{\kappa_+}{\kappa_-}, \tag{B.8}$$

giving the nature and the strength of the Ehrlich-Schwoebel effect. The case $0 < S < 1$ ($S > 1$) correspond to an inverse (direct) ES effect, while $S = 1$ is for a symmetric a/d. Similarly, the importance of adatom hopping between terraces is given by the dimensionless permeability kinetic coefficient

$$\overline{\kappa}_p = \frac{\kappa_p L_0}{D}. \tag{B.9}$$

The strength of the elastic interactions is represented by the dimensionless counterpart of α and β

$$\overline{\alpha} = \frac{a^2 \alpha}{k_B T L_0^3} \quad \text{and} \quad \overline{\beta} = \frac{a^2 \beta}{k_B T L_0}. \tag{B.10}$$

Without relabelling the dimensionless variables, the governing equations for the adatom diffusion problem (B.1)-(B.3) reads in their dimensionless form

$$\begin{cases} \partial_t \rho_n = \partial_{xx}\rho_n - \overline{\nu}\rho_n + \overline{F}, \\ -\rho_n^- \dot{x}_{n+1} - (\partial_x \rho_n)^- = \underbrace{\overline{\kappa}(\rho_n^- - 1 - \Theta[\![\rho]\!]_{x_{n+1}} + f_{n+1})}_{J^-_{n+1}} - \overline{\kappa}_p [\![\rho]\!]_{x_{n+1}}, \\ \rho_n^+ \dot{x}_n + (\partial_x \rho_n)^+ = \underbrace{\overline{\kappa} S(\rho_n^+ - 1 - \Theta[\![\rho]\!]_{x_n} + f_n)}_{J^+_n} + \overline{\kappa}_p [\![\rho]\!]_{x_n}, \\ \dot{x}_n = \Theta(J_n^+ + J_n^-), \end{cases} \tag{B.11}$$

where f_n is rewritten as a dimensionless quantity

$$f_n = \sum_{\substack{r \in \{-R,\ldots,R\} \\ r \neq 0}} \left(\frac{\overline{\beta}}{x_{n+r} - x_n} - \frac{\overline{\alpha}}{(x_{n+r} - x_n)^3} \right). \tag{B.12}$$

B.1.3 *The quasistatic approximation*

B.1.3.1 *Definition of the quasistatic approximation*

Throughout subsequent sections, the step bunching phenomenon is investigated by computing the stability of the steady-state solution defined in appendix A ($\overset{o}{\rho}(x,t) = \overset{o}{\rho}(x - \overset{o}{x}_n(t))$ and $\overset{o}{x}_n(t) = n + \overset{o}{V}t$ for all $n \in \mathbb{Z}$) against perturbation in step position and adatom densities.

Stability analyses of step dynamics on systems of the type of (B.11) have been carried out in numerous works (see e.g. Bales and Zangwill, 1990; Pierre-Louis, 2003; Pierre-Louis and Misbah, 1998; Pimpinelli et al., 1994), however up to a few exceptions (Dufay, Frisch, and Debierre, 2007; Ghez, Cohen, and Keller, 1993; Keller, Cohen, and Merchant, 1993; Ranguelov and Stoyanov, 2007) these analyses have been performed under the so-called *quasistatic approximation* (QSA). This approximation, which consists in neglecting the dynamic terms $\partial_t \rho_n$ in $(\text{B.11})_1$ and $\rho_n^\pm \dot{x}_n$ in $(\text{B.11})_{2,3}$, considerably simplifies the stability analysis. Although this simplification is classically said appropriate in the regimes of slow deposition/evaporation rates (Krug, 2005; Michely and Krug, 2012) with a quantitative criteria

$$\overline{F}\Theta \ll 1 \qquad \text{and} \qquad \overline{\nu}\Theta \ll 1 \tag{B.13}$$

for pure deposition and pure evaporation respectively, we bring two arguments raising doubts about its validity in the regime considered. The first one, detailed in section B.1.3.2, is an analysis, *a priori*, of the weaknesses of the argument traditionally used for justifying the approximation in the stability analysis. The second one, based on results of section B.2, is an *a posteriori* discussion of the QSA whereby comparing the stability results with and without the QSA of examples[1] in the slow deposition regime we show significant modifications brought by the dynamics terms.

---

[1] By *example* we mean a given set of parameters $\overline{F}$, $\overline{\nu}$, $\overline{\kappa}$, $\overline{\kappa}_p$, $\overline{\alpha}$, $\overline{\beta}$, Θ for the system (B.11).

B.1.3.2 *Classical justification for the quasistatic approximation*

In this section, we discuss the justification given in the literature for the quasistatic approximation and distinguish between its use for the computation of the steady-state solution and for the stability analysis.

First a quantitative criterion should express the idea of slow step motion and second one shall show that under that criterion the dynamics terms are negligible compared to the other terms of the equations that govern the problem addressed.

To this regard, note that there are two distinct problems usually addressed, the first one is the computation of the steady-state solution (i.e., step velocity and adatom density profile of the equidistant step propagation: $\overset{o}{x}_n(t) = n + \overset{o}{V}t$ and $\overset{o}{\rho}(x,t) = \overset{o}{\rho}(x - \overset{o}{x}_n(t))$) of (B.11), while the second one concerns the stability of that solution with respect to step bunching. While the first problem is governed by the system (B.11), the second one is ruled, as far as the linear stability is concerned, by the linear perturbation equations. An *a priori* justification of the quasistatic approximation for the first problem shall show that the dynamics terms are negligible compared to the other terms of (B.11). Likewise, such a justification for the second problem implies that the terms issued from the dynamics terms in (B.21) are negligible, which is not the case.

We shall see that the *a priori* justification of the quasistatic approximation works only for the computation of the steady-state solution, which have not been pointed out in the literature. With the classcial argument invoking a small step velocity, a difficulty comes from the fact that the step velocity should be compared to some characteristic diffusion velocity not well determined. On the one hand, Ghez and Iyer (1988) take as a characteristic diffusion velocity $v_d^G = \sqrt{D\nu}$ while Michely and Krug (2012) and Krug (2005) choose $v_d^K = D/L_0$.

quasistatic approximation for the steady-state solution We shall see that with regards to the computation of the steady state solution, a careful analysis of the equations shows that the quasisatic approximation works when comparing the step velocity to Krug's diffusion velocity v_d^K.

Indeed, we can estimate of the order of magnitude of the dynamics terms in the dimensional governing equations (B.1)-(B.3). For the steady-state solution, the term $\partial_t \rho_n$ in (B.1) can be rewritten $\overset{o}{V}\partial_x \overset{o}{\rho}$ which, noting that ρ_n is of order ρ_{eq}^* and typically varies over L_0, is of order $\overset{o}{V}\rho_{eq}^*/L_0$. The question is whether this non-equilibrium term is small compared to the diffusive adatom source $D\partial_{xx}\rho_n$ which is of order $D\rho_{eq}^*/L_0^2$. Hence we define $\mathcal{P}$ estimating the ratio of the dynamics term over its diffusive counterpart and find $\mathcal{P} = \overset{o}{V}L_0/D$. Similarly the terms $-\rho_n^- \dot{x}_{n+1}$ and $\rho_n^+ \dot{x}_n$ are both of order $\rho_{eq}^* \overset{o}{V}$, to be compared to the diffusion currents $D(\partial_x \rho_n)^\pm$ of order $D\rho_{eq}^*/L_0$. Again the ratio of these two term is the same quantity $\mathcal{P} = \overset{o}{V}L_0/D$.

These estimates[2] reveal that the "diffusion velocity" to which the step's velocity should be compared to qualifies the regime for the quasistatic approximation is v_d^K. Hence a computation of the steady-state solution under the quasistatic approximation is justified in the regime were the *Péclet number* $\mathcal{P} = \overset{o}{V} L_0 / D$ is small compared to one. In addition, we have checked *a posteriori* that this Péclet number is the pertinent one by comparing the steady-state diffusion field obtained with and without the quasistatic approximation.

For situations where deposition prevails over evaporation (i.e., $F \ll \nu \rho_{eq}^*$) —which is often the case for MBE or CVD at low enough temperature— the steady-state step velocity is $\overset{o}{V} = F a^2 L_0$. Conversely when evaporation prevails —typical examples are the numerous experiments of pure evaporation without deposition — the step velocity is not explicit but one can show that it is upper bounded in absolute value by its limit value $\overset{o}{V}_{SE} = \nu \rho_{eq}^* L_0 a^2$ in the Slow Evaporation (SE) regime ($\nu \to 0$). This provides *a priori* estimates of the Péclet number in the two limit regimes where deposition or evaporation prevail, which we rewrite in terms of the dimensionless coefficients of section B.1.2:

$$\mathcal{P}^{dep} = \frac{F a^2 L_0^2}{D} = \overline{F} \Theta, \tag{B.14}$$

for deposition, —which appears in Krug (2005) and (Michely and Krug, 2012)— and

$$\mathcal{P}^{eva} = \frac{\nu \rho_{eq}^* L_0^2 a^2}{D} = \overline{\nu} \Theta, \tag{B.15}$$

for evaporation.

QUASISTATIC APPROXIMATION FOR THE STABILITY ANALYSIS Note that, in this discussion, we have estimated the order of magnitude of the dynamics terms in the governing equations for adatom density and step velocity for the particular steady-state solution. Regarding the problem of stability of the steady-state solution, one should be concerned by the size of the terms issued from the dynamic term in the linear perturbation equation It is not clear here that the dynamic contribution to the linear perturbation equation derived subsequently (B.21) is negligible in the limit $\mathcal{P} \to 0$, all the more that the operator $\mathcal{B}$ full with dynamic terms becomes singular in the quasistatic assumption.

INTEREST OF A QUASISTATIC ANALYSIS While these elements shall show that the QSA is not valid simply under the slow deposition/evaporation condition (B.13), there are still particular cases where the stability results with and without the QSA converges. Consequently, the QSA remains a worthwhile approach, especially as it brings, contrary to a general stability analysis, stability results with analytical form, hence yielding material to understand the effect of the various physical mechanisms on the stability of step dynamics.

---

[2] These estimates can still be discussed as for instance, depending on the value of the parameters ρ may typically vary over a distance smaller than L_0 to be identified with some diffusion length.

B.1.3.3 *Review of the works beyond the quasistatic approximation*

In terms of mathematical method, the linear stability analysis of (B.11) with all dynamics terms is well more intricate than under the quasistatic approximation. A few works (Dufay, Frisch, and Debierre, 2007; Ghez, Cohen, and Keller, 1993; Keller, Cohen, and Merchant, 1993; Liu and Metiu, 1994; Pierre-Louis, 2003; Ranguelov and Stoyanov, 2007) have addressed such a problem on systems of the type of (B.11). The governing equations in these works essentially differ from (B.11) through the physical mechanisms included is the model (Schwoebel effect, elastic interactions, permeability, diffusion-mediated configurational force) which does not change fundamentally the problem. Note also that in the early work of Ghez, Cohen, and Keller (1993), Keller, Cohen, and Merchant (1993), and Liu and Metiu (1994) the dynamics terms are absent of the boundary conditions $(B.11)_{2,3}$ and only included in the step velocity equation $(B.11)_4$. The dynamics terms in all four governing equations (B.11) only appear in the more recent works (Dufay, Frisch, and Debierre, 2007; Pierre-Louis, 2003; Ranguelov and Stoyanov, 2007) as expected from a continuum thermodynamics derivation of these equations (Cermelli and Jabbour, 2005).

Note that the motivation of above cited works is to investigate the stability in the high deposition/evaporation regime where the quasistatic condition (B.13) is violated. By contrast, our motivation for addressing the stability of the system with dynamic terms lies in a questioning regarding the validity of the quasistatic approach in the regime (B.13) where it is supposedly valid.

Of course, this analysis can also be used in the regime beyond (B.13), however, if the dimensionless deposition/evaporation rate can be of order one —at the limit where (B.13) is not satisfied anymore— it seems that values several order of magnitudes higher than one are,for two reasons, not relevant. First, with such values, the near-equilibrium assumption on which relies the governing equations (B.11) is not satisfied anymore, and one would need to come back to the diffusion equation and boundary conditions before linearisation of the chemical potential (see section B.1.1 and Cermelli and Jabbour (2005)). Second, at such high deposition (evaporation) rate the 2D growth in the step flow regime is likely to break down for a 3D growth with island (holes) nucleation.

In terms of method of the linear stability analysis, the approach developed in this section is similar in the spirit to the work of Ghez, Cohen, and Keller (1993) and Keller, Cohen, and Merchant (1993), as we both derive linear perturbation equation by perturbing both the adatom density and the step position about the steady-state solution. However, in their work, Ghez. *et al.* decompose the adatom density as a sum of the steady-state solution and perturbation without noting that, the step positions being also perturbed, the adatom steady-state and perturbed adatom densities are not defined on the same domain. We address that issue by rewriting the governing equations on a fixed domain, whereby using a *Lagrangian formulation* of the problem for deriving the perturbation equations.

The work of Liu and Metiu (1994) adopts a very different approach based on a formulation of the step dynamics as integral-differential equations.

On the other hand Dufay, Frisch, and Debierre (2007) and Pierre-Louis (2003), in between a quasistatic and a complete treatment of the problem have only considered the contribution of the steady-state solution to the dynamics terms, which allows to carry out a stability analysis in the spirit of the quasistatic one. We have verified, *a posteriori* that this approach does not fully account for the effect of the dynamics term.

Finally, Ranguelov and Stoyanov (2007) addressed the problem of step dynamics in the simplified framework of infinite terrace diffusion which as they say "provides a relatively simple way to study the linear stability of a step train beyond the quasistatic approximation". This simplified problem takes a very different form, however regarding the results we shall see that our general treatment is, when applied to the particular case they consider (interplay between dynamics and elasticity), in qualitative agreement with this work.

B.2 STABILITY WITH DYNAMIC TERMS

One can demonstrate that the stability analysis under the quasistatic approximation provides analytical expressions for the growth rate of instabilities, which are very helpful to understand the effect of each mechanism. However as discussed in section B.1.3, these results rely on an approximation whose scope of validity is not clear *a priori*, which requires to go beyond to clarify it. In this section we develop a linear stability analysis for the general system (B.11) and use its results to discuss the validity of the quasistatic approximation.

For the clarity of the discussion developed throughout this section,the reader should note that we call *the dynamics terms* the three terms $\partial_t \rho$, $-\rho_n^- \dot{x}_{n+1}$ and $\rho_n^+ \dot{x}_n$ in $(B.11)_1$, $(B.11)_2$ and $(B.11)_3$ respectively. They are the terms neglected in a quasistatic linear stability analysis while conserved in the present section.

B.2.1 *Steady-state solution*

The steady-state solution is formed by an equispaced array of steps with a spatially periodic base adatom density between steps. Therefore, the steady-state solution is written $\overset{o}{x}_n(t) = n + \overset{o}{V} t$ for all $n \in \mathbb{Z}$ and $\overset{o}{\rho}(x,t) = \overset{o}{\hat{\rho}}(x - \overset{o}{x}_n(t))$ for $x \in \left]\overset{o}{x}_n(t), \overset{o}{x}_n(t) + 1\right[$. Inserting these expressions in (B.11), one can obtain, by solving $(B.11)_{1-3}$, an analytical expression of $\overset{o}{\hat{\rho}}$ which nevertheless involves the unknown step velocity $\overset{o}{V}$. As a second step, inserting the currents J_n^- and J_n^+ in $(B.11)_4$ yields an equation for $\overset{o}{V}$. In the particular case of pure deposition ($\overline{\nu} = 0$), this equation can be solved analytically and one recover the quasistatic steady-state velocity $\overset{o}{V} = \overline{F}\Theta$. However, in the general case, this is a transcendental equation with a unique physically sound solution computed numerically using Newton's method.

B.2.2 *Linear stability analysis*

In this section, we develop a method to derive the linear stability of the steady-state solution of (B.11).

lagrangian formulation The problem under consideration being a free boundary problem, the perturbation of the adatom density is not defined on the same domain as the principal solution. Thus, the partial differential system (B.11)$_{1-3}$ is rewritten on a fixed domain by introducing the *Lagrangian* space variable u related to x on (x_n, x_{n+1}) by the diffeomorphism g_n defined by

$$u = g_n(x,t) := \frac{x - x_n(t)}{x_{n+1}(t) - x_n(t)}. \tag{B.16}$$

Denoting by g_n^{-1} its reciprocal function, let for all $n \in \mathbb{Z}$, $\tilde{\rho}_n$ be the *Lagrangian adatom density* defined on $(0,1) \times \mathbb{R}^+$ by

$$\tilde{\rho}_n(u,t) := \rho_n(g_n^{-1}(u,t),t). \tag{B.17}$$

Using the relations between the partial derivatives of ρ_n and of $\tilde{\rho}_n$[3], (B.11) is rewritten with Lagrangian variables

$$\begin{cases} s_n^2 \partial_t \tilde{\rho}_n = \partial_{uu}\tilde{\rho}_n + s_n\big[\dot{x}_n + [\dot{x}_{n+1} - \dot{x}_n]u\big]\partial_u\tilde{\rho}_n + s_n^2\big[-\overline{\nu}\tilde{\rho}_n + \overline{F}\big], \\ -s_n\tilde{\rho}_n^-\dot{x}_{n+1} = s_n\Big[\tilde{J}_{n+1}^- - \overline{\kappa}_p\big(\tilde{\rho}_{n+1}^+ - \tilde{\rho}_n^-\big)\Big] + (\partial_u\tilde{\rho}_n)^-, \\ s_n\tilde{\rho}_n^+\dot{x}_n = s_n\Big[\tilde{J}_n^+ + \overline{\kappa}_p\big(\tilde{\rho}_n^+ - \tilde{\rho}_{n-1}^-\big)\Big] - (\partial_u\tilde{\rho}_n)^+, \\ \dot{x}_n = \Theta(\tilde{J}_n^+ + \tilde{J}_n^-), \end{cases} \tag{B.18}$$

where $\tilde{J}_{n+1}^-$ and $\tilde{J}_n^+$ are

$$\begin{cases} \tilde{J}_{n+1}^- = \overline{\kappa}\Big(\tilde{\rho}_n^- - 1 - \Theta\big(\tilde{\rho}_{n+1}^+ - \tilde{\rho}_n^-\big) + f_{n+1}\Big), \\ \tilde{J}_n^+ = \overline{\kappa}S\Big(\tilde{\rho}_n^+ - 1 - \Theta\big(\tilde{\rho}_n^+ - \tilde{\rho}_{n-1}^-\big) + f_n\Big), \end{cases} \tag{B.19}$$

and $s_n = 1 + x_{n+1} - x_n$ and the superscript plus and minus denote evaluations at 0 and 1, respectively: $\tilde{\rho}_n^+ := \tilde{\rho}_n(0,t)$, $\tilde{\rho}_n^- := \tilde{\rho}_n(1,t)$, $(\partial_u\tilde{\rho}_n)^+ := \partial_u\tilde{\rho}_n|_{(0,t)}$ and $(\partial_u\tilde{\rho}_n)^- := \partial_u\tilde{\rho}_n|_{(1,t)}$.

linear perturbation equation Noting that, for the steady-state solution the variable u coincides with the variable $x - \overset{o}{x}_n(t)$, the Lagrangian form of the principal solution reads $\overset{o}{\tilde{\rho}}(u) = \overset{o}{\rho}(u)$. To derive the linear perturbation equation, consider the perturbed state

$$\begin{cases} x_n(t) = n + \overset{o}{V}t + \varepsilon\delta x_n(t) + o(\varepsilon), \\ \tilde{\rho}_n(u,t) = \overset{o}{\tilde{\rho}}(u) + \varepsilon\delta\tilde{\rho}_n(u,t) + o(\varepsilon), \end{cases} \tag{B.20}$$

where ε is a small parameters and $\mathbf{q} := (\delta x_n, \delta\tilde{\rho}_n)$ denote the perturbation and collect terms of order ε after inserting (B.20) in (B.18). This yields a linear system for $\mathbf{q}$, which reads in abstract form

$$\mathcal{A}\big[\mathbf{q}_{n-1}, \mathbf{q}_n, \mathbf{q}_{n+1}, \mathbf{q}_{n+2}\big] = \mathcal{B}\big[\dot{\mathbf{q}}_n, \dot{\mathbf{q}}_{n+1}\big], \tag{B.21}$$

where and $\mathcal{A}$ and $\mathcal{B}$ denote linear operators involving u-derivatives of $\delta\tilde{\rho}_n$ whose complete expressions are given in section B.A.

---

[3] These relations, directly deriving from (B.16) and (B.17) are: $\partial_t\tilde{\rho}_n = \big(\dot{x}_n + (\dot{x}_{n+1} - \dot{x}_n)u\big)\partial_x\rho_n + \partial_t\rho_n$, $\partial_u\tilde{\rho}_n = (1 + x_{n+1} - x_n)\partial_x\rho_n$ and $\partial_{uu}\tilde{\rho}_n = (1 + x_{n+1} - x_n)^2\partial_{xx}\rho_n$.

BLOCH-WAVE ANALYSIS Following the stability method of hydrodynamics, an arbitrary perturbation $\mathbf{q}$ is written as a combination of normal modes and the stability of the system is obtained by checking the stability with respect to each of these modes. Using the linearity of (B.21) and noting that the operators $\mathcal{A}$ and $\mathcal{B}$ are independent of n (i.e., invariant by 1-terrace translation[4]), the perturbations, solutions of (B.21), can be written as a combination of the normal modes given by the *Bloch waves*

$$\begin{aligned} \delta x_n(t) &= \delta\hat{x}\exp(ikn+\lambda t), \\ \delta\tilde{\rho}_n(u,t) &= \delta\hat{\rho}(u)\exp(ikn+\lambda t), \end{aligned} \tag{B.22}$$

where $k \in (-\pi,\pi)$ is the wave number and λ the associated growth rate.

Inserting (B.22) in (B.21) yields for a given wave number k, the following generalised eigenvalue problem:

$$\hat{\mathcal{A}}_k\hat{\mathbf{q}} = \lambda\hat{\mathcal{B}}_k\hat{\mathbf{q}}, \tag{B.23}$$

where $\hat{\mathbf{q}} = (\delta\hat{x},\delta\hat{\rho})$ and $\hat{\mathcal{A}}_k$ and $\hat{\mathcal{B}}_k$ are linear operators deriving from $\mathcal{A}$ and $\mathcal{B}$ whose complete expressions are given in appendix B.A.

B.2.3 *Numerical method*

The eigenvalue problem (B.23) involves two operators $\hat{\mathcal{A}}_k$ and $\hat{\mathcal{B}}_k$ acting on the scalar variable $\delta\hat{x}$ and on the function $\delta\hat{\rho}$ and its derivatives defined on $(0,1)$. This problem is solved numerically, using the Chebyshev collocation method (Peyret, 2002), a spectral method adapted to nonperidic problems such as (B.23).

Consider a function $f \in \mathbb{C}^{(0,1)}$ and let its Chebychev series approximation f_N truncated at order N:

$$f_N := \sum_{n=0}^{N}\check{f}_n\check{T}_n, \tag{B.24}$$

where $\check{f}_n$ are the Chebychev coefficients and $\check{T}_n$ denote the Chebyshev polynomials[5] represented on figure B.1 and defined on (0,1) by

$$\check{T}_0(u) = 1, \quad \check{T}_1(u) = 2u-1, \tag{B.26}$$

and the recurrence relationship

$$\check{T}_n - (4u-2)\check{T}_{n-1} + \check{T}_{n-2} = 0, \text{ for } n \leq 2. \tag{B.27}$$

To compute the Chebychev coefficients $\check{f}_n$, two main methods are available. First,

---

[4] The Bloch wave decomposition of $\tilde{\rho}_n$ can be seen differently by introducing the variable $v = u+n \in \mathbb{R}$ where $u \in (0,1)$ and $n \in \mathbb{Z}$ and letting $\delta\tilde{\rho}(v,t)$ defined on $\mathbb{R}\times\mathbb{R}^+$ by $\delta\tilde{\rho}(v,t) := \tilde{\rho}_n(v-n,t)$ when $v \in (n,n+1)$. With these definitions, the operators $\mathcal{A}$ and $\mathcal{B}$ rewritten as acting on $\left(\delta x_n,\delta\tilde{\rho}\right)$ satisfy $\mathcal{A}\left[\delta x_{n+1}(t),\delta\tilde{\rho}(v+1,t)\right] = \mathcal{A}\left[\delta x_n(t),\delta\tilde{\rho}(v,t)\right]$ and a similar relation for $\mathcal{B}$. This make explicit the space periodicity of the differential operators allowing to write the solutions of (B.21) as a combinations of Bloch waves reading for $\delta\tilde{\rho}$: $\delta\tilde{\rho}(v,t) = \delta\check{\rho}(v)\exp(ikv+\lambda t)$ where $\delta\check{\rho}$ is a 1-periodic function. $\delta\hat{\rho}$ is related to $\check{\rho}$ by $\delta\hat{\rho}(u) = \delta\check{\rho}(u)\exp(iku)$ on $(0,1)$.

[5] Note that the Chebychev polynomials $\check{T}_n$ defined on $(0,1)$ that we used here are obtained by rescaling the traditional Chebyshev polynomials T_n defined on $(-1,1)$ with

$$\check{T}_n(u) = T_n\left(2u-1\right), \text{ for } u \in (0,1). \tag{B.25}$$

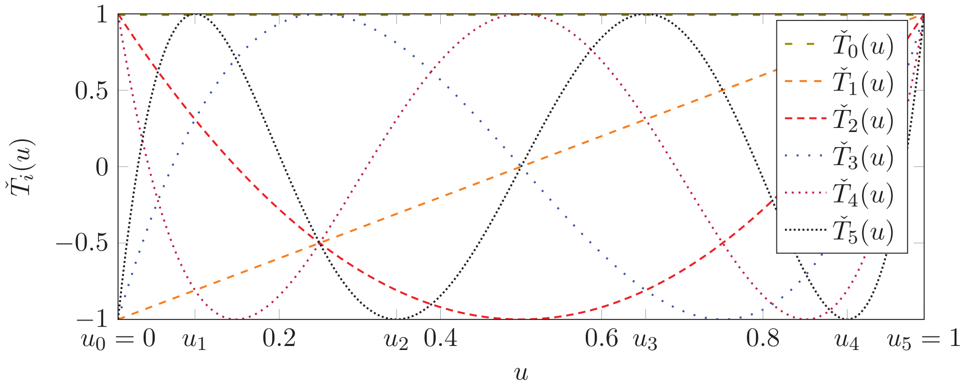

Figure B.1: Representation of the first six Chebyshev polynomials $\check{T}_n$ along with the six Gauss-Lobatto points for $N = 5$.

the *tau*-method, whereby the coefficients $\check{f}_n$ are obtained by projection of f on the basis $(\check{T}_n)$:

$$\check{f}_n = \int_0^1 \frac{f(u)\check{T}_n(x)}{\sqrt{u(1-u)}} \mathrm{d}u. \tag{B.28}$$

Second, the *collocation* method where the coefficients $\check{f}_n$ are obtained from the $N+1$ equation deriving from the interpolation of f on the Gauss-Lobatto points $(u_0, \ldots, u_N)$:

$$f_N(u_n) = \sum_{j=0}^{N} \check{f}_j \check{T}_j(u_n) = f(u_n), \tag{B.29}$$

where the Gauss-Lobatto mesh is composed of the $N+1$ points defined by

$$u_n = \frac{1}{2}\left(\cos\left(\frac{\pi(N-n)}{N}\right) + 1\right), \text{ for } n = 0 \ldots N, \tag{B.30}$$

illustrated on figure B.1 for $N = 5$. Note that the points are not uniformly distributed on $(0, 1)$ but denser close to the edges.

These two methods, although leading to different discretisation schemes, have the same rate of convergence in the approximation (Peyret, 2002). In the present case, as (B.23) involves functions (such as the steady-state solution $\overset{o}{\tilde{\rho}}$) whose evaluation on the points u_i is straightforward while their projection on the functions T_i require some numerical work, the collocation method is used.

With the Chebychev approximation, the first and second derivatives of f are approximated by

$$f'_N = \sum_{n=0}^{N} \check{f}_n \check{T}'_n \text{ and } f''_N = \sum_{n=0}^{N} \check{f}_n \check{T}''_n. \tag{B.31}$$

In addition, using the collocation techniques, the values of f'_N and f''_N on are obtained witout resorting to the $\check{f}_n$. Indeed it is possible to define a differentiation matrix $\check{\mathbf{D}}$, that directly relate the values, on the Gauss-Lobato points, of the function and its first deivatives through $f'_N(u_n) = \check{D}_{n,j} f_N(u_j)$.[6] Note that, with the Chebyshev

---

[6] The coefficients of the $\check{\mathbf{D}}$ are obtained by adaptating the differentiation matrix $\mathbf{D}$ found in Peyret (2002) to the Chebychev approximation reformulated on $(0, 1)$.

method, the derivative at one point does not only depend on the neighbouring points but on all the points of the domain which makes $\check{\mathbf{D}}$ a full matrix. Similarly, the second-order derivative is approximated using $(\check{\mathbf{D}})^2$.

To derive the discrete form of (B.23), the operators $\hat{\mathcal{A}}_k$ and $\hat{\mathcal{B}}_k$ are decomposed as a sum of operators acting separately on $\delta\hat{x}$, $\delta\hat{\rho}$ and its derivatives:

$$\hat{\mathcal{A}}_k(\delta\hat{x},\delta\hat{\rho}) = \hat{\mathcal{A}}_k^1\delta\hat{x} + \hat{\mathcal{A}}_k^2\delta\hat{\rho} + \hat{\mathcal{A}}_k^3\delta\hat{\rho}' + \hat{\mathcal{A}}_k^4\delta\hat{\rho}'' \text{ and } \hat{\mathcal{B}}_k(\delta\hat{x},\delta\hat{\rho}) = \hat{\mathcal{B}}_k^1\delta\hat{x} + \hat{\mathcal{B}}_k^2\delta\hat{\rho}, \tag{B.32}$$

where the full expressions of the $\hat{\mathcal{A}}_k^p$, $p = 1\ldots4$ and $\hat{\mathcal{B}}_k^m$, $m = 1,2$ are given in appendix B.A.

Using the decomposition (B.32), the operators $\hat{\mathcal{A}}_k$ and $\hat{\mathcal{B}}_k$ are approximated using the $(N+2)\times(N+2)$ matrices $\check{\mathbf{A}}^k$ and $\check{\mathbf{B}}^k$ written as

$$\check{\mathbf{A}}_k\check{\mathbf{q}} = \check{\mathbf{A}}_k^1(\check{\mathbf{D}})^2\delta\check{\boldsymbol{\rho}} + \check{\mathbf{A}}_k^2\check{\mathbf{D}}\delta\check{\boldsymbol{\rho}} + \check{\mathbf{A}}_k^3\delta\check{\boldsymbol{\rho}} + \check{\mathbf{A}}_k^4\delta\hat{x}, \tag{B.33}$$

$$\check{\mathbf{B}}_k\check{\mathbf{q}} = \check{\mathbf{B}}_k^1\delta\check{\boldsymbol{\rho}} + \check{\mathbf{B}}_k^2\delta\hat{x}, \tag{B.34}$$

where $\delta\check{\boldsymbol{\rho}} = \big(\delta\hat{\rho}(u_0),\ldots,\delta\hat{\rho}(u_N)\big)$, $\check{\mathbf{q}} = (\delta\hat{x},\delta\check{\boldsymbol{\rho}})$ and $\check{\mathbf{A}}_k^p$, $p = 1\ldots4$ and $\check{\mathbf{B}}_k^m$, $m = 1,2$ are the discretisation of the corresponding operators $\hat{\mathcal{A}}_k^p$ and $\hat{\mathcal{B}}_k^m$ on the Gauss-Lobatto mesh $\{u_i, 0 \le i \le N\}$.

This allow to write (B.23) as a $(N+2)\times(N+2)$ generalised eigenvalue problem: For a given $k \in (-\pi,\pi)$, find $(\lambda,\check{\mathbf{q}}) \in (\mathbb{C}\times\mathbb{C}^{N+2})$ with $\check{\mathbf{q}} \neq \mathbf{0}$ such that

$$\check{\mathbf{A}}_k\check{\mathbf{q}} = \lambda\check{\mathbf{B}}_k\check{\mathbf{q}}. \tag{B.35}$$

After solving (B.35) numerically, we consider the leading eigenvalue λ (the eigenvalue with largest real part) which correspond to the most critical growth rate.

Note that as $\check{\mathbf{B}}_k$ is not inversible, (B.23) has less than $N+2$ solutions. Indeed as can be seen from (B.40) in appendix B.A, the last three rows of $\hat{\mathcal{B}}_k$ being linearly dependent, its kernel is of dimension 2. As a result, and noting that $\check{\mathbf{A}}^k$ is invertible, (B.35) has only N solutions.

CONVERGENCE We evaluate the convergence of the numerical method by considering the leading eigenvalue, and determine an satisfactory number of discretisation points $N+1$.

For a given set of parameters ($\overline{F} = 10^{-2}$, $\overline{\nu} = 0$, $S = 1$, $\overline{\kappa} = 10$, $\overline{\kappa}_p = 0$, $\Theta = 0.01$, $\overline{\alpha} = 0$, $\overline{\beta} = 0$ and $k = \pi/2$), the leading eigenvalue with $N = 50$ is $-1.1271 \cdot 10^{-7} + 1.0000 \cdot 10^{-4} i$. Because of the spectral convergence properties of Chebyshev methods (Peyret, 2002), full convergence with five significant digits of the leading eigenvalue is achieved with N as low as 5. This fast convergence has been verified for various set of parameters and we select the value $N = 10$ for the subsequent analysis.

A superposition of eigenvalue spectra for different values of N is shown in figure B.2. On top of the leading eigenvalue previously discussed, we observe the progressive formation of two branches of constant imaginary part in the stable spectral plane. Note that, although these branches are not of particular interest for the linear stability analysis, as expected from a consistent numerical method they get more and more resolved as N increases.

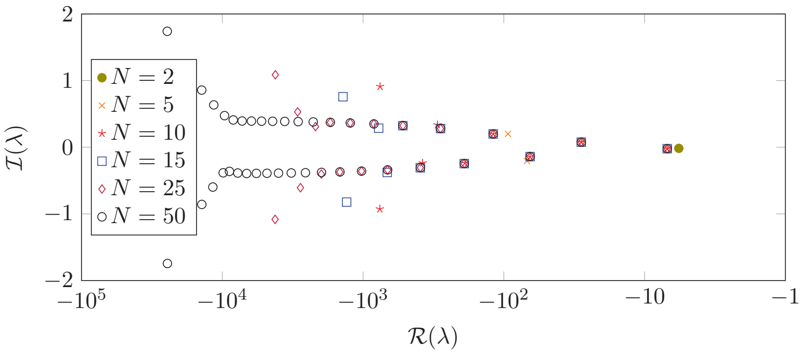

Figure B.2: Evolution of the eigenvalue spectrum with the number N of discretisation points for the set of parameters $\overline{F} = 10^{-2}$, $\overline{v} = 0$, $S = 1$, $\overline{\kappa} = 10$, $\overline{\kappa}_p = 0$, $\Theta = 0.01$, $\overline{\alpha} = 0$, $\overline{\beta} = 0$ and $k = \pi/2$. The logarithmic scale used on the abscissa is not wide enough to include the leading eigenvalue $-1.1271 \cdot 10^{-7} + 1.0000 \cdot 10^{-4} i$.

B.2.4 *Results*

An overview of the results is provided in appendix A.

B.A DETAILS OF THE LINEAR STABILITY ANALYSIS WITH DYNAMICS TERMS

In section B.2.2 the linear operators $\mathcal{A}$ and $\mathcal{B}$ reads as follows

$$\begin{aligned}\mathcal{A}\left[\mathbf{q}_{n-1}, \mathbf{q}_n, \mathbf{q}_{n+1}, \mathbf{q}_{n+2}\right] = &\begin{pmatrix} A_1^{1\prime}\,\delta x_n + A_1^{1\prime\prime}\,\delta x_{n+1} \\ A_2^{1\prime}\,\delta x_n + A_2^{1\prime\prime}\,\delta x_{n+1} + A_2^{1\prime\prime\prime}\,\delta x_{n+2} \\ A_3^{1}\,\delta x_{n-1} + A_3^{1\prime}\,\delta x_n + A_3^{1\prime\prime}\,\delta x_{n+1} \\ A_4^{1}\,\delta x_{n-1} + A_4^{1\prime}\,\delta x_n + A_4^{1\prime\prime}\,\delta x_{n+1} \end{pmatrix} + \begin{pmatrix} A_1^{2}\,\delta\tilde{\rho}_n \\ A_2^{2}\,\delta\tilde{\rho}_{n+1}^{+} + A_2^{2\prime}\,\delta\tilde{\rho}_n^{-} \\ A_3^{2}\,\delta\tilde{\rho}_n^{+} + A_3^{2\prime}\,\delta\tilde{\rho}_{n-1}^{-} \\ A_4^{2}\,\delta\tilde{\rho}_n^{+} + A_4^{2\prime}\,\delta\tilde{\rho}_{n-1}^{-} \end{pmatrix} \\ &+ \begin{pmatrix} A_1^{3}\,\partial_u\delta\tilde{\rho}_n \\ A_2^{3}\,(\partial_u\delta\tilde{\rho}_n)^{-} \\ A_3^{3}\,(\partial_u\delta\tilde{\rho}_n)^{+} \\ 0 \end{pmatrix} + \begin{pmatrix} A_1^{4}\,\partial_{uu}\delta\tilde{\rho}_n \\ 0 \\ 0 \\ 0 \end{pmatrix},\end{aligned} \tag{B.36}$$

and

$$\mathcal{B}\left[\dot{\mathbf{q}}_n, \dot{\mathbf{q}}_{n+1}\right] = \begin{pmatrix} (u-1)\overset{o}{\tilde{\rho}}{}'\delta\dot{x}_n - u\overset{o}{\tilde{\rho}}{}'\delta\dot{x}_{n+1} \\ \overset{o}{\tilde{\rho}}(1)\delta\dot{x}_{n+1} \\ \overset{o}{\tilde{\rho}}(0)\delta\dot{x}_n \\ \delta\dot{x}_n \end{pmatrix} + \begin{pmatrix} \partial_t\delta\tilde{\rho}_n \\ 0 \\ 0 \\ 0 \end{pmatrix}, \tag{B.37}$$

where

$$\begin{cases} A_1^{1\prime} =- A_1^{1\prime\prime} = 2\nu\overset{o}{\tilde{\rho}} - 2F - \overset{o}{V}\overset{o}{\tilde{\rho}}{}', \\ A_2^{1\prime} =\overline{\kappa}(1+3\overline{\alpha}-\overline{\beta}) + (\overline{\kappa}_p + \overline{\kappa}\Theta)\overset{o}{\tilde{\rho}}(0) - \big(\overline{\kappa}(1+\Theta) + \overline{\kappa}_p + \overset{o}{V}\big)\overset{o}{\rho}(1), \\ A_2^{1\prime\prime} =- \overline{\kappa}(1+6\overline{\alpha}-2\overline{\beta}) - (\overline{\kappa}_p + \overline{\kappa}\Theta)\overset{o}{\tilde{\rho}}(0) + \big(\overline{\kappa}(1+\Theta) + \overline{\kappa}_p + \overset{o}{V}\big)\overset{o}{\rho}(1), \\ A_2^{1\prime\prime\prime} =\overline{\kappa}(3\overline{\alpha}-\overline{\beta}), \quad A_3^1 = \overline{\kappa}S(3\overline{\alpha}-\overline{\beta}), \\ A_3^{1\prime} =\overline{\kappa}S(1-6\overline{\alpha}+2\overline{\beta}) + (\overline{\kappa}_p - \overline{\kappa}S\Theta)\overset{o}{\tilde{\rho}}(1) \\ \qquad + \big(\overline{\kappa}S + (\Theta-1) - \overline{\kappa}_p + \overset{o}{V}\big)\overset{o}{\rho}(0), \\ A_3^{1\prime\prime} =- \overline{\kappa}S(1-3\overline{\alpha}+\overline{\beta}) - (\overline{\kappa}_p - \overline{\kappa}S\Theta)\overset{o}{\tilde{\rho}}(1) \\ \qquad + \big(\overline{\kappa}S + (1-\Theta) + \overline{\kappa}_p - \overset{o}{V}\big)\overset{o}{\rho}(0), \\ 2A_4^1 =- A_4^{1\prime} = 2A_4^{1\prime\prime} = 2\Theta\overline{\kappa}(1+S)(\overline{\beta}-3\overline{\alpha}), \\ A_1^2 =- \overline{\nu}, \quad A_2^2 = -\overline{\kappa}\Theta - \overline{\kappa}_p, \quad A_2^{2\prime} = \overline{\kappa}(1+\Theta) + \overline{\kappa}_p + \overset{o}{V}, \\ A_3^2 =\overline{\kappa}S(1-\Theta) + \overline{\kappa}_p - \overset{o}{V}, \quad A_3^{2\prime} = \overline{\kappa}S\Theta - \overline{\kappa}_p, \\ A_4^2 =\Theta\overline{\kappa}\big(\Theta(1+S) - S\big), \quad A_4^{2\prime} = -\Theta\overline{\kappa}\big(\Theta(1+S)+1\big), \\ A_1^3 =\overset{o}{V}, \quad A_2^3 = 1, \quad A_3^3 = -1, \quad A_1^4 = 1. \end{cases} \tag{B.38}$$

The operators $\hat{\mathcal{A}}_k$ and $\hat{\mathcal{B}}_k$ after the Bloch wave decomposition have the following expressions:

$$\begin{aligned} \hat{\mathcal{A}}_k\hat{\mathbf{q}} &= \hat{\mathcal{A}}_k^1(u)\delta\hat{x} + \hat{\mathcal{A}}_k^2\delta\hat{\rho}(u) + \hat{\mathcal{A}}_k^3\delta\hat{\rho}'(u) + \hat{\mathcal{A}}_k^4\delta\hat{\rho}''(u) \\ &= \begin{pmatrix} \hat{A}_1^1\,(u)\delta\hat{x} \\ \hat{A}_2^1\,\delta\hat{x} \\ \hat{A}_3^1\,\delta\hat{x} \\ \hat{A}_4^1\,\delta\hat{x} \end{pmatrix} + \begin{pmatrix} \hat{A}_1^2\,\delta\hat{\rho}(u) \\ \hat{A}_2^2\,\delta\hat{\rho}(0) + \hat{A}_2^{2\prime}\,\delta\hat{\rho}(1) \\ \hat{A}_3^2\,\delta\hat{\rho}(0) + \hat{A}_3^{2\prime}\,\delta\hat{\rho}(1) \\ \hat{A}_4^2\,\delta\hat{\rho}(0) + \hat{A}_4^{2\prime}\,\delta\hat{\rho}(1) \end{pmatrix} + \begin{pmatrix} \hat{A}_1^3\,\delta\hat{\rho}'(u) \\ \hat{A}_2^3\,\delta\hat{\rho}'(1) \\ \hat{A}_3^3\,\delta\hat{\rho}'(0) \\ 0 \end{pmatrix} + \begin{pmatrix} \hat{A}_1^4\,\delta\hat{\rho}''(u) \\ 0 \\ 0 \\ 0 \end{pmatrix}, \end{aligned} \tag{B.39}$$

and

$$\begin{aligned} \hat{\mathcal{B}}_k\hat{\mathbf{q}} &= \hat{\mathcal{B}}_k^1(u)\delta\hat{x} + \hat{\mathcal{B}}_k^2\delta\hat{\rho}(u) \\ &= \begin{pmatrix} \hat{B}_1^1\,(u)\delta\hat{x} \\ \hat{B}_2^1\,\delta\hat{x} \\ \hat{B}_3^1\,\delta\hat{x} \\ \hat{B}_4^1\,\delta\hat{x} \end{pmatrix} + \begin{pmatrix} \hat{B}_1^2\,\delta\hat{\rho}(u) \\ 0 \\ 0 \\ 0 \end{pmatrix}, \end{aligned} \tag{B.40}$$

where

$$
\left\{
\begin{aligned}
\hat{A}_1^1 =& \left(-1+\mathrm{e}^{ik}\right)\left(2\overline{F}-2\overline{v}\overset{o}{\hat{\rho}}(u)+\overset{o}{V}\overset{o}{\hat{\rho}}'(u)\right),\\
\hat{A}_2^1 =& \left(-1+\mathrm{e}^{ik}\right)\left(\overline{\kappa}\left((\mathrm{e}^{ik}-1)(3\overline{\alpha}-\overline{\beta})+(\overset{o}{\hat{\rho}}(1)-\overset{o}{\hat{\rho}}(0))\Theta+\overset{o}{\hat{\rho}}(1)-1\right)\right.\\
&\qquad\left.+\overset{o}{\hat{\rho}}(1)(\overline{\kappa}_p+\overset{o}{V})-\overline{\kappa}_p\overset{o}{\hat{\rho}}(0)\right),\\
\hat{A}_3^1 =& \left(-1+\mathrm{e}^{ik}\right)\left(\overline{\kappa}S\left((1-\mathrm{e}^{-ik})(3\overline{\alpha}-\overline{\beta})-\overset{o}{\hat{\rho}}(0)(\Theta-1)+\overset{o}{\hat{\rho}}(1)\Theta-1\right)\right.\\
&\qquad\left.+\overset{o}{\hat{\rho}}(0)(\overline{\kappa}_p-\overset{o}{V})-\overline{\kappa}_p\overset{o}{\hat{\rho}}(1)\right),\\
\hat{A}_4^1 =& -2\overline{\kappa}(S+1)\Theta(3\overline{\alpha}-\overline{\beta})(\cos(k)-1),\\
\hat{A}_1^2 =& -\overline{v},\quad \hat{A}_2^2=-\mathrm{e}^{ik}(\overline{\kappa}\Theta+\overline{\kappa}_p),\quad \hat{A}_2^{2\prime}=\overline{\kappa}+\overline{\kappa}_p+\overline{\kappa}\Theta+\overset{o}{V},\\
\hat{A}_3^2 =& -\overline{\kappa}S\Theta+\overline{\kappa}S+\overline{\kappa}_p-\overset{o}{V},\quad \hat{A}_3^{2\prime}=\mathrm{e}^{-ik}(\overline{\kappa}S\Theta-\overline{\kappa}_p),\\
\hat{A}_4^2 =& \overline{\kappa}\Theta\big((S+1)\Theta-S\big),\quad \hat{A}_4^{2\prime}=-\mathrm{e}^{-ik}\overline{\kappa}\Theta\big((S+1)\Theta+1\big),\\
\hat{A}_1^3 =& \overset{o}{V},\quad \hat{A}_2^3=1,\quad \hat{A}_3^3=-1,\quad \hat{A}_1^4=1,\\
\hat{B}_1^1 =& -\left(1+\left(-1+\mathrm{e}^{ik}\right)u\right)\overset{o}{\hat{\rho}}'(u),\quad \hat{B}_2^1=-\mathrm{e}^{ik}\overset{o}{\hat{\rho}}(1),\\
\hat{B}_3^1 =& \overset{o}{\hat{\rho}}(0),\quad \hat{B}_4^1=-1,\quad \hat{B}_1^2=1.
\end{aligned}
\right.
\tag{B.41}
$$

BIBLIOGRAPHY

Abdessemed, N., S.J. Sherwin, and V. Theofilis (2009). "Linear instability analysis of low-pressure turbine flows." In: *J. Fluid Mech.* 628, pp. 57–83.

Abramowitz, M. and I.A. Stegun (1964). *Handbook of mathematical functions: with formulas, graphs, and mathematical tables*. Courier Corporation.

Åkervik, E., L. Brandt, D.S. Henningson, J. Hœpffner, O. Marxen, and P. Schlatter (2006). "Steady solutions of the Navier–Stokes equations by selective frequency damping." In: *Phys. Fluids* 18.6, p. 068102.

Alben, S. and M. Shelley (2005). "Coherent locomotion as an attracting state for a free flapping body." In: *P. Natl. Acad. Sci. USA* 102.32, pp. 11163–11166.

Alizard, F., S. Cherubini, and J.-C. Robinet (2009). "Sensitivity and optimal forcing response in separated boundary layer flows." In: *Phys. Fluids* 21.6, p. 064108.

Arbey, H. and J.E. Ffowcs Williams (1984). "Active cancellation of pure tones in an excited jet." In: *J. Fluid Mech.* 149, pp. 445–454.

Arnold, V.I. (1973). *Ordinary Differential Equations*. The MIT Press.

Arratia, C., C.P. Caulfield, and J.-M. Chomaz (2013). "Transient perturbation growth in time-dependent mixing layers." In: *J. Fluid Mech.* 717, pp. 90–133.

Åström, K.J. and R.M. Murray (2008). *Feedback systems: an introduction for scientists and engineers*. Princeton university press.

Bales, G.S. and A. Zangwill (1990). "Morphological instability of a terrace edge during step-flow growth." In: *Phys. Rev. B* 41.9, pp. 5500–5508.

Barkley, D. (2006). "Linear analysis of the cylinder wake mean flow." In: *EPL (Europhysics Letters)* 75.5, p. 750.

Barkley, D., H.M. Blackburn, and S.J. Sherwin (2008). "Direct optimal growth analysis for timesteppers." In: *Int. J. Numer. Meth. Fl.* 57.9, pp. 1435–1458.

Barkley, D. and R.D. Henderson (1996). "Three-dimensional Floquet stability analysis of the wake of a circular cylinder." In: *J. Fluid Mech.* 322, pp. 215–241.

Becker, H.A. and T.A. Massaro (1968). "Vortex evolution in a round jet." In: *J. Fluid Mech.* 31.03, pp. 435–448.

Beneddine, S., D. Sipp, A. Arnault, J. Dandois, and L. Lesshafft (2016). "Conditions for validity of mean flow stability analysis." In: *J. Fluid Mech.* 798, pp. 485–504.

Blackburn, H.M. and G.J. Sheard (2010). "On quasiperiodic and subharmonic Floquet wake instabilities." In: *Physics of Fluids* 22.3, p. 031701.

Blackburn, H.M., S.J. Sherwin, and D. Barkley (2008). "Convective instability and transient growth in steady and pulsatile stenotic flows." In: *J. Fluid Mech.* 607, pp. 267–277.

Bogey, C. and C. Bailly (2010). "Influence of nozzle-exit boundary-layer conditions on the flow and acoustic fields of initially laminar jets." In: *J. Fluid Mech.* 663, pp. 507–538.

Borisov, A.V., A.A. Kilin, and I.S. Mamaev (2013). "The dynamics of vortex rings: Leapfrogging, choreographies and the stability problem." In: *Regul. Chaotic Dyn.* 18.1-2, pp. 33–62.

Borisov, A.V., A.A. Kilin, I.S. Mamaev, and V.A. Tenenev (2014). "The dynamics of vortex rings: leapfrogging in an ideal and viscous fluid." In: *Fluid Dyn. Res.* 46.3, p. 031415.

Boujo, E. and F. Gallaire (2015). "Sensitivity and open-loop control of stochastic response in a noise amplifier flow: the backward-facing step." In: *J. Fluid Mech.* 762, pp. 361–392.

Bourget, B., T. Dauxois, S. Joubaud, and P. Odier (2013). "Experimental study of parametric subharmonic instability for internal plane waves." In: *J. Fluid Mech.* 723, pp. 1–20.

Bradley, T.A. and T.T. Ng (1989). "Phase-locking in a jet forced with two frequencies." In: *Exp. Fluids* 7.1, pp. 38–48.

Brancher, P. and J.-M. Chomaz (1997). "Absolute and convective secondary instabilities in spatially periodic shear flows." In: *Phys. Rev. Lett.* 78.4, p. 658.

Bridges, J.E. and A.K.M.F. Hussain (1987). "Roles of initial condition and vortex pairing in jet noise." In: *J. Sound Vib.* 117.2, pp. 289–311.

Broze, G. and F. Hussain (1994). "Nonlinear dynamics of forced transitional jets: periodic and chaotic attractors." In: *J. Fluid Mech.* 263, pp. 93–132.

Broze, G. and F. Hussain (1996). "Transitions to chaos in a forced jet: intermittency, tangent bifurcations and hysteresis." In: *J. Fluid Mech.* 311, pp. 37–71.

Burton, W.K., N. Cabrera, and F.C. Frank (1951). "The Growth of Crystals and the Equilibrium Structure of their Surfaces." In: *Philos. T. Roy. Soc. A* 243.866, pp. 299–358.

Campobasso, M. S. and M.B. Giles (2004). "Stabilization of a linear flow solver for turbomachinery aeroelasticity using recursive projection method." In: *AIAA J.* 42.9, pp. 1765–1774.

Cermelli, P. and M. Jabbour (2005). "Multispecies epitaxial growth on vicinal surfaces with chemical reactions and diffusion." In: *P. Roy. Soc. A-Math. Phy.* 461.2063, pp. 3483–3504.

Cermelli, P. and M.E. Jabbour (2007). "Possible mechanism for the onset of step-bunching instabilities during the epitaxy of single-species crystalline films." In: *Phys. Rev. B* 75 (16), p. 165409.

Cheng, M. and H.-C. Chang (1992). "Subharmonic instabilities of finite-amplitude monochromatic waves." In: *Phys. Fluids A-Fluid* 4.3, pp. 505–523.

Cheng, M., J. Lou, and T.T. Lim (2015). "Leapfrogging of multiple coaxial viscous vortex rings." In: *Phys. Fluids* 27.3, p. 031702.

Chomaz, J.-M. (2005). "Global instabilities in spatially developing flows: non-normality and nonlinearity." In: *Annu. Rev. Fluid Mech.* 37, pp. 357–392.

Chung, W.F. and M.S. Altman (2002). "Kinetic length, step permeability, and kinetic coefficient asymmetry on the Si(111) (7×7) surface." In: *Phys. Rev. B* 66.7.

Corless, R.M., G.H. Gonnet, D.E.G. Hare, D.J. Jeffrey, and D.E. Knuth (1996). "On the Lambert W function." In: *Adv. Comput. Math.* 5.1, pp. 329–359.

Danaila, I. and B.J. Boersma (1998). "Mode interaction in a forced homogeneous jet at low Reynolds numbers." In: *Proceedings of the summer program*, pp. 141–158.

Danaila, I. and B.J. Boersma (2000). "Direct numerical simulation of bifurcating jets." In: *Phys. Fluids* 12.5, pp. 1255–1257.

Delbende, I., B. Piton, and M. Rossi (2015). "Merging of two helical vortices." In: *Eur. J. Mech. B-Fluids* 49, pp. 363–372.

Dowling, A.P. and A.S. Morgans (2005). "Feedback control of combustion oscillations." In: *Annu. Rev. Fluid Mech.* 37, pp. 151–182.

Doyle, J.C., B.A. Francis, and A.R. Tannenbaum (1992). *Feedback control theory*. Macmillan Publishing Company.

Drazin, P.G. and W.H. Reid (2004). *Hydrodynamic Stability*. Cambridge University Press.

Dufay, M., T. Frisch, and J.-M. Debierre (2007). "Role of step-flow advection during electromigration-induced step bunching." In: *Phys. Rev. B* 75.24.

Duprat, C., C. Ruyer-Quil, S. Kalliadasis, and F. Giorgiutti-Dauphiné (2007). "Absolute and convective instabilities of a viscous film flowing down a vertical fiber." In: *Phys. Rev. Lett.* 98.24, p. 244502.

Duprat, C., F. Giorgiutti-Dauphiné, D. Tseluiko, S. Saprykin, and S. Kalliadasis (2009). "Liquid film coating a fiber as a model system for the formation of bound states in active dispersive-dissipative nonlinear media." In: *Phys. Rev. Lett.* 103.23, p. 234501.

Ekici, K. and K.C. Hall (2008). "Nonlinear frequency-domain analysis of unsteady flows in turbomachinery with multiple excitation frequencies." In: *AIAA J.* 46.8, pp. 1912–1920.

Feldman, Y. and A.Y. Gelfgat (2010). "Oscillatory instability of a three-dimensional lid-driven flow in a cube." In: *Phys. Fluids* 22.9, p. 093602.

Floquet, G. (1883). "Sur les équations différentielles linéaires à coefficients périodiques." In: *Ann. Sci. École Norm. Sup.* 12, pp. 47–88.

Freund, J.B. and P. Moin (1998). "Mixing enhancement in jet exhaust using fluidic actuators: direct numerical simulations." In: *ASME: FEDSM98* 5235.

Freund, J.B. and P. Moin (2000). "Jet mixing enhancement by high-amplitude fluidic actuation." In: *AIAA J.* 38.10, pp. 1863–1870.

Garnaud, X., L. Lesshafft, P.J. Schmid, and P. Huerre (2013). "Modal and transient dynamics of jet flows." In: *Phys. Fluids* 25.4, p. 044103.

Ghez, R., H.G. Cohen, and J.B. Keller (1993). "The stability of growing or evaporating crystals." In: *J. Appl. Phys.* 73.8, pp. 3685–3693.

Ghez, R. and S.S. Iyer (1988). "The kinetics of fast steps on crystal surfaces and its application to the molecular beam epitaxy of silicon." In: *IBM J. Res. Dev.* 32.6, pp. 804–818.

Gioria, R.S., P.J.S. Jabardo, B.S. Carmo, and J.R. Meneghini (2009). "Floquet stability analysis of the flow around an oscillating cylinder." In: *J. Fluid. Struct.* 25.4, pp. 676–686.

Gohil, T.B., A.K. Saha, and K. Muralidhar (2010). "Control of flow in forced jets: a comparison of round and square cross sections." In: *J. Visual.* 13.2, pp. 141–149.

Gohil, T.B., A.K. Saha, and K. Muralidhar (2015). "Simulation of the blooming phenomenon in forced circular jets." In: *J. Fluid Mech.* 783, pp. 567–604.

Gopinath, A. and A. Jameson (2005). "Time spectral method for periodic unsteady computations over two-and three-dimensional bodies." In: *AIAA Paper* 1220, pp. 10–13.

Gopinath, A. and A. Jameson (2006). "Application of the time spectral method to periodic unsteady vortex shedding." In: *AIAA Paper* 449.

Hajj, M.R., R.W. Miksad, and E.J. Powers (1992). "Subharmonic growth by parametric resonance." In: *J. Fluid Mech.* 236, pp. 385–413.

Hajj, M.R., R.W. Miksad, and E.J. Powers (1993). "Fundamental–subharmonic interaction: effect of phase relation." In: *J. Fluid Mech.* 256, pp. 403–426.

Hall, K.C., J.P. Thomas, and W.S. Clark (2002). "Computation of unsteady nonlinear flows in cascades using a harmonic balance technique." In: *AIAA J.* 40.5, pp. 879–886.

Han, X., J. Li, and A.S. Morgans (2015). "Prediction of combustion instability limit cycle oscillations by combining flame describing function simulations with a thermoacoustic network model." In: *Combust. Flame* 162.10, pp. 3632–3647.

Hata, K., A. Kawazu, T. Okano, T. Ueda, and M. Akiyama (1993). "Observation of step bunching on vicinal GaAs(100) studied by scanning tunneling microscopy." In: *Appl. Phys. Lett.* 63.12, pp. 1625–1627.

Hecht, F. (2012). "New development in FreeFem++." In: *J. Numer. Math.* 20.3-4, pp. 251–265.

Henderson, R.D. and D. Barkley (1996). "Secondary instability in the wake of a circular cylinder." In: *Phys. Fluids* 8.6, pp. 1683–1685.

Hilgers, A. and B.J. Boersma (2001). "Optimization of turbulent jet mixing." In: *Fluid Dyn. Res.* 29.6, pp. 345–368.

Hinze, M., A. Walther, and J. Sternberg (2006). "An optimal memory-reduced procedure for calculating adjoints of the instationary Navier-Stokes equations." In: *Optim. Contr. Appl. Met.* 27.1, pp. 19–40.

Ho, C.-M. and L.-S. Huang (1982). "Subharmonics and vortex merging in mixing layers." In: *J. Fluid Mech.* 119, pp. 443–473.

Ho, C.-M. and P. Huerre (1984). "Perturbed free shear layers." In: *Annu. Rev. Fluid Mech.* 16.1, pp. 365–422.

Huerre, P. and P.A. Monkewitz (1990). "Local and global instabilities in spatially developing flows." In: *Annu. Rev. Fluid Mech.* 22.1, pp. 473–537.

Husain, H.S. and F. Hussain (1989). "Subharmonic resonance in a shear layer." In: *Advances in Turbulence* 2. Springer, pp. 96–101.

Husain, H.S. and F. Hussain (1995). "Experiments on subharmonic resonance in a shear layer." In: *J. Fluid Mech.* 304, pp. 343–372.

Hussain, A.K.M.F. and K.B.M.Q. Zaman (1980). "Vortex pairing in a circular jet under controlled excitation. Part 2. Coherent structure dynamics." In: *J. Fluid Mech.* 101.03, pp. 493–544.

Ichimiya, A., Y. Tanaka, and K. Ishiyama (1996). "Quantitative Measurements of Thermal Relaxation of Isolated Silicon Hillocks and Craters on the Si(111)-(7×7) Surface by Scanning Tunneling Microscopy." In: *Phys. Rev. Lett.* 76.25, pp. 4721–4724.

Inoue, O. (2002). "Sound generation by the leapfrogging between two coaxial vortex rings." In: *Phys. Fluids* 14.9, pp. 3361–3364.

Ishizaki, J., K. Ohkuri, and T. Fukui (1996). "Simulation and Observation of the Step Bunching Process Grown on GaAs (001) Vicinal Surface by Metalorganic Vapor Phase Epitaxy." In: *Jpn. J. Appl. Phys.* 35.2S, p. 1280.

Ishizaki, J., S. Goto, M. Kishida, T. Fukui, and H. Hasegawa (1994). "Mechanism of Multiatomic Step Formation during Metalorganic Chemical Vapor deposition Growth of GaAs on (001) Vicinal Surface Studied by Atomic Force Microscopy." In: *Jpn. J. Appl. Phys.* 33.1S, p. 721.

Jacobs, R. G. and P. A. Durbin (2001). "Simulations of bypass transition." In: *J. Fluid Mech.* 428, pp. 185–212.

Jallas, D., O. Marquet, and D. Fabre (2017). "Linear and nonlinear perturbation analysis of the symmetry breaking in time-periodic propulsive wakes." In: *Phys. Rev. E* 95.6, p. 063111.

Johnson, H.G., V. Brion, and L. Jacquin (2016). "Crow instability: nonlinear response to the linear optimal perturbation." In: *J. Fluid Mech.* 795, pp. 652–670.

Johnson, M.D., K.T. Leung, A. Birch, B.G. Orr, and J. Tersoff (1996). "Adatom concentration on GaAs(001) during MBE annealing." In: *Surf. Sci.* 350.1, pp. 254 –258.

Jordan, P. and T. Colonius (2013). "Wave packets and turbulent jet noise." In: *Annu. Rev. Fluid Mech.* 45, pp. 173–195.

Juniper, M.P. and R.I. Sujith (2018). "Sensitivity and nonlinearity of thermoacoustic oscillations." In: *Annu. Rev. Fluid Mech.* 50, pp. 661–689.

Kasu, M. and T. Fukui (1992). "Multi-Atomic Steps on Metalorganic Chemical Vapor Deposition-Grown GaAs Vicinal Surfaces Studied by Atomic Force Microscopy." In: *Jpn. J. Appl. Phys.* 31.7A, p. L864.

Keller, J.B., H.G. Cohen, and G.J. Merchant (1993). "The stability of rapidly growing or evaporating crystals." In: *J. Appl. Phys.* 73.8, pp. 3694–3697.

Kercher, D.S., J.-B. Lee, O. Brand, M.G. Allen, and A. Glezer (2003). "Microjet cooling devices for thermal management of electronics." In: *IEEE T. Compon. Pack. T.* 26.2, pp. 359–366.

Keynes, J.M. (1923). *A tract on monetary reform*. Pickle Partners Publishing.

Kibens, V. (1980). "Discrete noise spectrum generated by acoustically excited jet." In: *AIAA J.* 18.4, pp. 434–441.

Klostermeyer, J. (1982). "On parametric instabilities of finite-amplitude internal gravity waves." In: *J. Fluid Mech.* 119, pp. 367–377.

Koumoutsakos, P., J. Freund, and D. Parekh (1998). "Evolution strategies for parameter optimization in jet flow control." In: *Proceedings of the Summer Program, Center for Turbulent Research, Stanford University*, pp. 121–132.

Krug, J. (1997). "Origins of scale invariance in growth processes." In: *Adv. Phys.* 46.2, pp. 139–282.

Krug, J. (2005). "Introduction to Step Dynamics and Step Instabilities." In: *Multiscale Modeling in Epitaxial Growth*. Ed. by Axel Voigt. Basel: Birkhäuser Basel, pp. 69–95.

Krug, J., V. Tonchev, S. Stoyanov, and A. Pimpinelli (2005). "Scaling properties of step bunches induced by sublimation and related mechanisms." In: *Phys. Rev. B* 71.4.

Ku, D.N. (1997). "Blood flow in arteries." In: *Annu. Rev. Fluid Mech.* 29.1, pp. 399–434.

Kuhlmann, H.C. and S. Albensoeder (2014). "Stability of the steady three-dimensional lid-driven flow in a cube and the supercritical flow dynamics." In: *Phys. Fluids* 26.2, p. 024104.

Lazarus, A. and O. Thomas (2010). “A harmonic-based method for computing the stability of periodic solutions of dynamical systems.” In: *C. R. Mécanique* 338.9, pp. 510–517.

Lee, M. and W.C. Reynolds (1985). *Bifurcating and blooming jets. Report TF-22*. Tech. rep. Thermosciences Division, Department of Mechanical Engineering, Stanford University.

Liu, F. and H. Metiu (1994). “Stability and kinetics of step motion on crystal surfaces.” In: *Phys. Rev. E* 49.4, pp. 2601–2616.

Loiseau, J.-C., J.-C. Robinet, and E. Leriche (2016). “Intermittency and transition to chaos in the cubical lid-driven cavity flow.” In: *Fluid Dyn. Res.* 48.6.

Loiseau, J.-C., J.-C. Robinet, S. Cherubini, and E. Leriche (2014). “Investigation of the roughness-induced transition: global stability analyses and direct numerical simulations.” In: *J. Fluid Mech.* 760, pp. 175–211.

Longmire, E.K. and L.H. Duong (1996). “Bifurcating jets generated with stepped and sawtooth nozzles.” In: *Phys. Fluids* 8.4, pp. 978–992.

Lopez, J.M., B.D. Welfert, K. Wu, and J. Yalim (2017). “Transition to complex dynamics in the cubic lid-driven cavity.” In: *Phys. Rev. Fluids* 2.7, p. 074401.

Lust, K. and D. Roose (1998). “An adaptive Newton–Picard algorithm with subspace iteration for computing periodic solutions.” In: *SIAM J. Sci. Comput.* 19.4, pp. 1188–1209.

Mankbadi, R.R. (1985). “On the interaction between fundamental and subharmonic instability waves in a turbulent round jet.” In: *J. Fluid Mech.* 160, pp. 385–419.

Marchenko, V.I. and A.Y. Parshin (1980). “Elastic properties of crystal surfaces.” In: *Sov. Phys. JETP* 52.1, pp. 129–131.

Marquet, O. and M. Larsson (2015). “Global wake instabilities of low aspect-ratio flat-plates.” In: *Eur. J. Mech. B-Fluids* 49, pp. 400–412.

McMullen, M., A. Jameson, and J. Alonso (2006). “Demonstration of nonlinear frequency domain methods.” In: *AIAA J.* 44.7, pp. 1428–1435.

McMullen, M., A. Jameson, and J.J. Alonso (2002). “Application of a non-linear frequency domain solver to the Euler and Navier–Stokes equations.” In: *AIAA Paper* 13625.

Meunier, P., U. Ehrenstein, T. Leweke, and M. Rossi (2002). “A merging criterion for two-dimensional co-rotating vortices.” In: *Phys. Fluids* 14.8, pp. 2757–2766.

Meynart, R. (1983). “Speckle velocimetry study of vortex pairing in a low-Re unexcited jet.” In: *Phys. Fluids* 26.8, pp. 2074–2079.

Michalke, A. (1971). “Instabilität eines kompressiblen runden Freistrahls unter Berücksichtigung des Einflusses der Strahlgrenzschichtdicke.” In: *Z. Flugwiss.* 19. English translation: NASA Tech. Memo. 75190 (1977), pp. 319–328.

Michely, T. and J. Krug (2012). *Islands, mounds and atoms*. Vol. 42. Springer Science & Business Media.

Michiels, W. and S.-I. Niculescu (2007). *Stability and Stabilization of Time-Delay Systems (Advances in Design & Control)*. Philadelphia, PA, USA: SIAM.

Mied, R.P. (1976). “The occurrence of parametric instabilities in finite-amplitude internal gravity waves.” In: *J. Fluid Mech.* 78.4, pp. 763–784.

Monkewitz, P.A. (1988). “Subharmonic resonance, pairing and shredding in the mixing layer.” In: *J. Fluid Mech.* 188, pp. 223–252.

Morgans, A.S. and S.R. Stow (2007). “Model-based control of combustion instabilities in annular combustors.” In: *Combust. Flame* 150.4, pp. 380–399.

NEK5000. Version 1.0 rc1/SVN r1094, Argonne National Laboratory, Illinois. Available at `https://nek5000.mcs.anl.gov`.

Nadarajah, S. K., M. S. McMullen, and A. Jameson (2003). “Optimum Shape Design for Unsteady Flow Using Time Accurate and Nonlinear Frequency Domain Methods.” In: *AIAA Paper* 3875.2003-3875.

Nadarajah, S. and A. Jameson (2007). “Optimum shape design for unsteady three-dimensional viscous flows using a nonlinear frequency-domain method.” In: *J. Aircraft* 44.5, pp. 1513–1527.

Narayanan, S. and F. Hussain (1997). “Chaos control in open flows–experiments in a circular jet.” In: *AIAA Paper* 97-1822.

Nichols, J.W. and S.K. Lele (2011). “Global modes and transient response of a cold supersonic jet.” In: *J. Fluid Mech.* 669, pp. 225–241.

Omi, H., Y. Homma, V. Tonchev, and A. Pimpinelli (2005). “New Types of Unstable Step-Flow Growth onSi(111)-(7×7)during Molecular Beam Epitaxy: Scaling and Universality.” In: *Phys. Rev. Lett.* 95.21.

Ozdemir, M. and A. Zangwill (1992). “Morphological equilibration of a facetted crystal.” In: *Phys. Rev. B* 45 (7), pp. 3718–3729.

Parekh, D.E., A. Leonard, and W.C. Reynolds (1988). *Bifurcating jets at high Reynolds numbers. Report TF-35*. Tech. rep. Thermosciences Division, Department of Mechanical Engineering, Stanford University.

Parekh, D.E., W.C. Reynolds, and M.G. Mungal (1987). “Bifurcation of round air jets by dual-mode acoustic excitation.” In: *25th AIAA Aerospace Sciences Meeting*.

Parekh, D.E., V. Kibens, A. Glezer, J.M. Wiltse, and D.M. Smith (1996). “Innovative jet flow control: mixing enhancement experiments.” In: *AIAA Paper* 308, p. 1996.

Paschereit, C.O., I. Wygnanski, and H.E. Fiedler (1995). “Experimental investigation of subharmonic resonance in an axisymmetric jet.” In: *J. Fluid Mech.* 283, pp. 365–407.

Petersen, R.A. (1978). “Influence of wave dispersion on vortex pairing in a jet.” In: *J. Fluid Mech.* 89.03, pp. 469–495.

Peyret, R. (2002). *Spectral methods for incompressible viscous flow*. Vol. 148. Springer-Verlag.

Pfizenmaier, E., J. Simon, and P.A. Monkewitz (1993). “Bouquet with bifurcating jet diffusion flame.” In: *Phys. Fluids A-Fluid* 5.9.

Pierre-Louis, O. (2003). “Step bunching with general step kinetics: stability analysis and macroscopic models.” In: *Surf. Sci.* 529.1, pp. 114 –134.

Pierre-Louis, O. and C. Misbah (1998). “Dynamics and fluctuations during MBE on vicinal surfaces. I. Formalism and results of linear theory.” In: *Phys. Rev. B* 58.4, pp. 2259–2275.

Pimpinelli, A. and A. Videcoq (2000). “Novel mechanism for the onset of morphological instabilities during chemical vapour epitaxial growth.” In: *Surf. Sci.* 445.1, pp. L23–L28.

Pimpinelli, A., I. Elkinani, A. Karma, C. Misbah, and J. Villain (1994). “Step motions on high-temperature vicinal surfaces.” In: *J. Phys.-Condens Mat.* 6.14, pp. 2661–2680.

Pimpinelli, A., V. Tonchev, A. Videcoq, and M. Vladimirova (2002). “Scaling and Universality of Self-Organized Patterns on Unstable Vicinal Surfaces.” In: *Phys. Rev. Lett.* 88.20.

Politi, P. and J. Krug (2000). “Crystal symmetry, step-edge diffusion, and unstable growth.” In: *Surf. Sci.* 446.1-2, pp. 89–97.

Pond, K. (1994). “Step bunching and step equalization on vicinal GaAs(001) surfaces.” In: *J. Vac. Sci. Technol. B* 12.4, p. 2689.

Pyragas, K. (1992). “Continuous control of chaos by self-controlling feedback.” In: *Phys. Lett. A* 170.6, pp. 421–428.

Raman, G. and E.J. Rice (1991). “Axisymmetric jet forced by fundamental and subharmonic tones.” In: *AIAA J.* 29.7, pp. 1114–1122.

Ranguelov, B. and S. Stoyanov (2007). “Evaporation and growth of crystals: Propagation of step-density compression waves at vicinal surfaces.” In: *Phys. Rev. B* 76.3.

Reynolds, W.C., D.E. Parekh, P.J.D. Juvet, and M.J.D. Lee (2003). “Bifurcating and blooming jets.” In: *Annu. Rev. Fluid Mech.* 35.1, pp. 295–315.

Rogilo, D.I., L.I. Fedina, S.S. Kosolobov, B.S. Ranguelov, and A.V. Latyshev (2013). “Critical Terrace Width for Two-Dimensional Nucleation during Si Growth on Si(111)-(7×7) Surface.” In: *Phys. Rev. Lett.* 111.3.

Roose, D., K. Lust, A. Champneys, and A. Spence (1995). “A Newton-Picard shooting method for computing periodic solutions of large-scale dynamical systems.” In: *Chaos Soliton Fract.* 5.10, pp. 1913–1925.

Saad, Y. (2011). *Numerical Methods for Large Eigenvalue Problems: Revised Edition*. SIAM.

Saffman, P.G. (1992). *Vortex dynamics*. Cambridge University Press.

Salmi, M.A., M. Alatalo, T. Ala-Nissila, and R.M. Nieminen (1999). “Energetics and diffusion paths of gallium and arsenic adatoms on flat and stepped GaAs(001) surfaces.” In: *Surf. Sci.* 425.1, pp. 31–47.

Sánchez, J. and M. Net (2010). “On the multiple shooting continuation of periodic orbits by Newton–Krylov methods.” In: *Int. J. Bifurcat. Chaos* 20.01, pp. 43–61.

Sánchez, J., M. Net, B. Garcıa-Archilla, and C. Simó (2004). “Newton–Krylov continuation of periodic orbits for Navier–Stokes flows.” In: *J. Comput. Phys.* 201.1, pp. 13–33.

Sato, M., M. Uwaha, and Y. Saito (2000). “Instabilities of steps induced by the drift of adatoms and effect of the step permeability.” In: *Phys. Rev. B* 62.12, pp. 8452–8472.

Schmid, P.J. (2007). “Nonmodal stability theory.” In: *Annu. Rev. Fluid Mech.* 39, pp. 129–162.

Schram, C. (2003). “Aeroacoustics of subsonic jets: prediction of the sound produced by vortex pairing based on Particle Image Velocimetry.” PhD thesis. Technische Universiteit Eindhoven.

Schram, C., S. Taubitz, J. Anthoine, and A. Hirschberg (2005). “Theoretical/empirical prediction and measurement of the sound produced by vortex pairing in a low Mach number jet.” In: *J. Sound Vib.* 281.1, pp. 171–187.

Schwoebel, R.L. (1969). “Step Motion on Crystal Surfaces. II.” In: *J. Appl. Phys.* 40.2, pp. 614–618.

Schwoebel, R.L. and E.J. Shipsey (1966). "Step Motion on Crystal Surfaces." In: *J. Appl. Phys.* 37.10, pp. 3682–3686.

Selçuk, C., I. Delbende, and M. Rossi (2017a). "Helical vortices: Quasiequilibrium states and their time evolution." In: *Phys. Rev. Fluids* 2.8, p. 084701.

Selçuk, C., I. Delbende, and M. Rossi (2017b). "Helical vortices: linear stability analysis and nonlinear dynamics." In: *Fluid Dyn. Res.* 50.1, p. 011411.

Semeraro, O., V. Jaunet, P. Jordan, A. V. Cavalieri, and L. Lesshafft (2016). "Stochastic and harmonic optimal forcing in subsonic jets." In: *22nd AIAA/CEAS Aeroacoustics Conference*, p. 2935.

Shaabani-Ardali, L., D. Sipp, and L. Lesshafft (2017). "Time-delayed feedback technique for suppressing instabilities in time-periodic flow." In: *Phys. Rev. Fluids* 2.11, p. 113904.

Shaabani-Ardali, L., D. Sipp, and L. Lesshafft (2018). "Vortex pairing in jets as a global Floquet instability: modal and transient dynamics." In: *submitted to the J. Fluid Mech.*

Shankar, P.N. and M.D. Deshpande (2000). "Fluid mechanics in the driven cavity." In: *Annu. Rev. Fluid Mech.* 32.1, pp. 93–136.

Shariff, K. and A. Leonard (1992). "Vortex rings." In: *Annu. Rev. Fluid Mech.* 24.1, pp. 235–279.

Sharma, A.S., N. Abdessemed, S.J. Sherwin, and V. Theofilis (2011). "Transient growth mechanisms of low Reynolds number flow over a low-pressure turbine blade." In: *Theor. Comp. Fluid Dyn.* 25.1-4, pp. 19–30.

Sherwin, S.J. and H.M. Blackburn (2005). "Three-dimensional instabilities and transition of steady and pulsatile axisymmetric stenotic flows." In: *J. Fluid Mech.* 533, pp. 297–327.

Shinohara, M. and N. Inoue (1995). "Behavior and mechanism of step bunching during metalorganic vapor phase epitaxy of GaAs." In: *Appl. Phys. Lett.* 66.15, pp. 1936–1938.

Shroff, G.M. and H.B. Keller (1993). "Stabilization of unstable procedures: the recursive projection method." In: *SIAM J. Numer. Anal.* 30.4, pp. 1099–1120.

Sicot, F. (2009). "Simulation efficace des écoulements instationaires périodiques en turbomachines." PhD thesis. École Centrale de Lyon.

Sicot, F., G. Dufour, and N. Gourdain (2012). "A time-domain harmonic balance method for rotor/stator interactions." In: *J. Turbomach.* 134.1, p. 011001.

Silva, C.B. da and O. Métais (2002). "Vortex control of bifurcating jets: A numerical study." In: *Phys. Fluids* 14.11, pp. 3798–3819.

Sipp, D. and A. Lebedev (2007). "Global stability of base and mean flows: a general approach and its applications to cylinder and open cavity flows." In: *J. Fluid Mech.* 593, pp. 333–358.

Šmilauer, P. and D.D. Vvedensky (1995). "Coarsening and slope evolution during unstable spitaxial growth." In: *Phys. Rev. B* 52.19, pp. 14263–14272.

Smith, T.D., A.B. Cain, and C.F. Chenault (2001). "Numerical simulation of enhanced mixing in jet plumes using pulsed blowing." In: *J. Aircraft* 38.3, pp. 458–463.

Spiker, M.A., J.P. Thomas, R.E. Kielb, K.C. Hall, and E.H. Dowell (2006). "Modeling cylinder flow vortex shedding with enforced motion using a harmonic balance approach." In: *AIAA Paper* 1965, p. 2006.

Staquet, C. and J. Sommeria (2002). “Internal gravity waves: from instabilities to turbulence.” In: *Annu. Rev. Fluid Mech.* 34.1, pp. 559–593.

Stewart, J., O. Pohland, and J.M. Gibson (1994). “Elastic-displacement field of an isolated surface step.” In: *Phys. Rev. B* 49 (19), pp. 13848–13858.

Tersoff, J., M.D. Johnson, and B.G. Orr (1997). “Adatom Densities on GaAs: Evidence for Near-Equilibrium Growth.” In: *Phys. Rev. Lett.* 78 (2), pp. 282–285.

Tersoff, J., Y.H. Phang, Z. Zhang, and M.G. Lagally (1995). “Step-Bunching Instability of Vicinal Surfaces under Stress.” In: *Phys. Rev. Lett.* 75 (14), pp. 2730–2733.

Theofilis, V. (2011). “Global linear instability.” In: *Annu. Rev. Fluid Mech.* 43, pp. 319–352.

Thomas, J.P., E.H. Dowell, and K.C. Hall (2002). “Nonlinear inviscid aerodynamic effects on transonic divergence, flutter, and limit-cycle oscillations.” In: *AIAA J.* 40.4, pp. 638–646.

Tophøj, L. and H. Aref (2013). “Instability of vortex pair leapfrogging.” In: *Phys. Fluids* 25.1, p. 014107.

Trefethen, L.N., A.E. Trefethen, S.C. Reddy, and T.A. Driscoll (1993). “Hydrodynamic stability without eigenvalues.” In: *Science* 261.5121, pp. 578–584.

Trefethen, Lloyd N. and M. Embree (2005). *Spectra and pseudospectra: the behavior of nonnormal matrices and operators*. Princeton University Press.

Tyliszczak, A. (2015). “Multi-armed jets: A subset of the blooming jets.” In: *Phys. Fluids* 27.4, p. 041703.

Tyliszczak, A. and A. Boguslawski (2006). “LES of the jet in low Mach variable density conditions.” In: *Direct and Large-Eddy Simulation VI*, pp. 575–582.

Tyliszczak, A. and A. Boguslawski (2007). “LES of variable density bifurcating jets.” In: *Complex Effects in Large Eddy Simulations*. Springer, pp. 273–288.

Tyliszczak, A. and B.J. Geurts (2014). “Parametric analysis of excited round jets-numerical study.” In: *Flow Turbul. Combust.* 93.2, pp. 221–247.

Van Der Weide, E., A. Gopinath, and A. Jameson (2005). “Turbomachinery applications with the time spectral method.” In: *AIAA paper* 4905.

Vandenberghe, N., J. Zhang, and S. Childress (2004). “Symmetry breaking leads to forward flapping flight.” In: *J. Fluid Mech.* 506, pp. 147–155.

Vassberg, J.C., A.K. Gopinath, and A. Jameson (2005). “Revisiting the Vertical-Axis Wind-Turbine Design using Advanced Computational Fluid Dynamics.” In: *AIAA Paper* 0047.

Vermeer, L.J., J.N. Sørensen, and A. Crespo (2003). “Wind turbine wake aerodynamics.” In: *Prog. Aerosp. Sci.* 39.6-7, pp. 467–510.

Vladimirova, M., A. De Vita, and A. Pimpinelli (2001). “Dimer diffusion as a driving mechanism of the step bunching instability during homoepitaxial growth.” In: *Phys. Rev. B* 64.24.

Voigtlander, B., A. Zinner, T. Weber, and H.P. Bonzel (1995). “Modification of growth kinetics in surfactant-mediated epitaxy.” In: *Phys. Rev. B* 51.12, pp. 7583–7591.

Webster, D.R. and E.K. Longmire (1997). “Vortex dynamics in jets from inclined nozzles.” In: *Phys. Fluids* 9.3, pp. 655–666.

Williamson, C.H.K. (1996). “Three-dimensional wake transition.” In: *J. Fluid Mech.* 328, pp. 345–407.

Winant, C.D. and F.K. Browand (1974). "Vortex pairing: the mechanism of turbulent mixing-layer growth at moderate Reynolds number." In: *J. Fluid Mech.* 63.2, pp. 237–255.

Zaman, K.B.M.Q. and A.K.M.F. Hussain (1980). "Vortex pairing in a circular jet under controlled excitation. Part 1. General jet response." In: *J. Fluid Mech.* 101.03, pp. 449–491.

Zaman, K.B.M.Q. and G. Raman (1997). "Reversal in spreading of a tabbed circular jet under controlled excitation." In: *Phys. Fluids* 9.12, pp. 3733–3741.

Zaman, K.B.M.Q., M.F. Reeder, and M. Samimy (1994). "Control of an axisymmetric jet using vortex generators." In: *Phys. Fluids* 6.2, pp. 778–793.

Zhao, D. and A.S. Morgans (2009). "Tuned passive control of combustion instabilities using multiple Helmholtz resonators." In: *J. Sound Vib.* 320.4-5, pp. 744–757.

COLOPHON

This document was typeset using the adapted typographical `classicthesis` package developed by André Miede and Ivo Pletikosić. `classicthesis` is available for both LaTeX and LyX:

`https://bitbucket.org/amiede/classicthesis/`

Final Version as of September 26, 2018 (classicthesis v4.6).

université
PARIS-SACLAY

ÉCOLE DOCTORALE
Sciences mécaniques et énergétiques, matériaux et géosciences (SMEMAG)

Titre : Stabilité et optimisation d’écoulements périodiques en temps — Application au jet pulsé

Mots clés : Jet, stabilité, optimisation, périodicité temporelle, appariement tourbillonaire, jet bifurqué.

Résumé : Cette thèse étudie la stabilité et l’optimisation d’écoulements périodiques en temps. Le cadre développé a été appliqué au cas du jet rond pulsé.

Dans la couche de mélange d’un jet, du fait de sa grande réceptivité aux perturbations, des anneaux de vorticité se forment spontanément. Ces derniers sont contrôlés en imposant une pulsation axisymétrique au niveau de la buse. Dans cette configuration, deux types d’instabilités surgissent. D’une part, de façon intrinsèque, un *appariement tourbillonnaire* peut parfois survenir : les anneaux fusionnent deux par deux, conduisant à un épaississement du jet et à un mélange accru. D’autre part, si un terme hélicoïdal sous-harmonique est ajouté au forçage axisymétrique, les anneaux formés sont alternativement excentrés de part et d’autre de l’axe, conduisant à un *jet bifurqué*. L’induction mutuelle des anneaux permet un large évasement du jet dans un plan préférentiel de bifurcation.

Dans un premier chapitre, nous avons développé une méthode de stabilisation d’orbites périodiques instables basée sur un contrôle volumique avec un terme de retard. Cette méthode a été appliquée au cas du jet axisymétrique pulsé pour obtenir un écoulement non-apparié. Cette partie fournit l’écoulement de base qui sera utilisé pour les études de stabilité et d’optimisation des parties suivantes.

Dans un deuxième chapitre, nous avons étudié la stabilité modale et non-modale de ce jet non-apparié à l’aide de la théorie de Floquet. La stabilité modale prédit avec précision la présence ou non d’un appariement tourbillonnaire tandis que la croissance non-modale fournit un mécanisme de transition très intense entre l’état non-apparié et l’état apparié.

Dans un troisième chapitre, le forçage hélicoïdal appliqué au jet bifurqué a été optimisé pour améliorer ses propriétés de mélange et d’évasement. Nous avons ensuite comparé par simulation numérique directe les jets bifurqués issus de forçages optimaux avec ceux issus de forçages plus simples précédemment utilisés dans la littérature. Le forçage optimal déclenche la bifurcation beaucoup plus tôt, ce qui permet un évasement bien plus marqué du jet qu’avec un forçage simple. En outre, le forçage optimal augmente considérablement la gamme de nombres de Strouhal dans laquelle cette bifurcation a lieu.

Enfin, en annexe, des travaux effectués en collaboration avec le Laboratoire de Mécanique des Solides (LMS, École polytechnique) sur la stabilité et la croissance des surfaces vicinales sont présentés.

Title : Stability and optimisation of time-periodic flows — Application to the pulsed jet

Keywords : Jet, stability, optimisation, time-periodicity, vortex pairing, bifurcating jet.

Abstract : This thesis focuses on the stability and the optimisation of time-periodic flows. The resulting framework has been applied to the pulsed jet study.

In a laminar round jet, due to its large noise amplification properties, ring vortices are generated spontaneously. This generation can be controlled by imposing an axisymmetric forcing at the inlet. In this configuration, two kinds of instabilities arise. On the one hand, in an intrinsic way, these vortices, can undergo *vortex pairing*: rings merge two by two, increasing the jet thickness and mixing. On the other hand, if an additional subharmonic helical term is superimposed to the axisymmetric forcing, ring vortices can be shifted off-axis in an alternate fashion, leading to a *bifurcating jet*. The mutual induction between rings leads to a large spreading in a preferential bifurcating plane.

First, a stabilisation technique for unstable periodic orbits, based on a time-delayed feedback, has been developed. This method has been applied to the axisymmetric pulsed jet to recover unpaired periodic states. This chapter provides the base flow used for stability and optimisation studies in the following.

Second, the modal and non-modal stability of the unpaired jet has been investigated using Floquet theory. While modal stability accurately predicts vortex pairing occurrence, transient growth provides a vigorous transition mechanism from unpaired to paired state.

Then, an optimisation of the helical forcing applied to bifurcating jets has been carried out to improve their spreading and mixing. The optimal forcing has been plugged in direct numerical simulations and results have been compared with those obtained with simpler forcing used in the literature. Optimal forcing moves strongly upstream the bifurcation point, triggering a larger flaring of the jet. In addition, optimal forcing dramatically increases the Strouhal number domain in which jet bifurcation can be encountered.

Finally, as an Appendix, results from a collaboration with the Laboratoire de Mécanique des Solides (LMS, École polytechnique) on the stability of the growth of vicinal surfaces are presented.

Université Paris-Saclay
Espace Technologique / Immeuble Discovery
Route de l’Orme aux Merisiers RD 128 / 91190 Saint-Aubin, France